

CHIRAL NEMATIC MESOPOROUS MATERIALS
TEMPLATED BY NANOCRYSTALLINE CELLULOSE

by

Kevin Eric Shopsowitz

B.Sc., McGill University, 2007

A Thesis Submitted in Partial Fulfillment of the
Requirements for the Degree of

DOCTOR OF PHILOSOPHY

in

The Faculty of Graduate Studies

(CHEMISTRY)

The University of British Columbia

(Vancouver)

August 2012

© Kevin Eric Shopsowitz, 2012

Abstract

The synthesis, characterization, and application of the first examples of chiral nematic mesoporous materials are reported. Nanocrystalline cellulose (NCC) was used as a liquid crystal template to generate NCC/silica composite films through evaporation induced self-assembly. The NCC was removed from the composite films by calcination to generate mesoporous silica films with high specific surface areas and chiral nematic structures. The chiral nematic ordering in these films gives rise to photonic properties that can be tuned depending on the synthetic conditions. Thus mesoporous silica films with colours spanning the visible spectrum were synthesized. The combination of mesoporosity and chiral nematic ordering in these materials causes them to change colour in response to liquids and show strong circular dichroism signals that depend on the refractive index within the mesopores. Chiral nematic mesoporous silica can also be used as a hard template to generate nanocrystalline films of anatase titanium dioxide. The titanium dioxide replicas are mesoporous and show chiral nematic ordering and photonic properties that mimic the original silica films.

By exploring different methods to remove NCC from the composite films, the procedure used to synthesize chiral nematic mesoporous silica films was expanded to organosilica. The resulting chiral nematic mesoporous organosilica films show similar properties to the mesoporous silica films but have superior flexibility in some cases. Methods to control the pore size of the mesoporous silica and organosilica materials were developed.

Nanocrystalline cellulose/silica composite films were also used as a starting point to synthesize chiral nematic mesoporous carbon films. This was achieved by pyrolyzing NCC/silica composite films followed by dissolving the silica in strong base. The silica

used in this procedure was shown to be necessary for both the retention of chiral nematic ordering and the introduction of mesoporosity into the carbonaceous material. Finally, chiral nematic mesoporous carbon (CNMC) was shown to be a promising material as a supercapacitor electrode material both on its own and as a composite with polyaniline.

Preface

In all chapters, Prof. Mark MacLachlan acted in a supervisory role. Chapters 2-5 involved collaboration with Dr. Wadood Hamad of FPInnovations, Vancouver, BC, Canada, who provided us with the nanocrystalline cellulose that was used throughout this thesis.

Portions of Chapter 2 have been previously published as: K. E. Shopsowitz, H. Qi, W. Y. Hamad, M. J. MacLachlan, “Free-Standing Mesoporous Silica Films with Tunable Chiral Nematic Structures.” *Nature* **2010**, *468*, 422-425. I was the principal author of this work and co-edited it with Prof. Mark MacLachlan, Dr. Wadood Hamad, and Dr. Hao Qi. I carried out all of the experiments reported in Chapter 2 (with the exception of the synthesis of NCC, which was provided by Dr. Wadood Hamad).

Portions of Chapter 3 have been previously published as: K. E. Shopsowitz, W. Y. Hamad, M. J. MacLachlan, “Flexible and Iridescent Chiral Nematic Organosilica Films.” *J. Am. Chem. Soc.* **2012**, *134*, 867-870. I was the principal author of this work and co-edited it with Prof. Mark MacLachlan and Dr. Wadood Hamad. Alan Manning performed the solid-state NMR experiments reported in Chapter 3. Andrea Terpstra synthesized and characterized **Me-CNMO** and **Hex-CNMO**, and Camille Gregory synthesized and characterized **Bz-CNMO**. I performed all of the other experiments reported in Chapter 3.

Portions of Chapter 4 have been published as: K. E. Shopsowitz, A. Stahl, W. Y. Hamad, M. J. MacLachlan, “Hard Templating of Nanocrystalline Titanium Dioxide with Chiral Nematic Ordering.” *Angew. Chem. Int. Ed.* **2012**, *51*, 6886-6890. I was the principal author of this work and co-edited it with Prof. Mark MacLachlan and Dr. Wadood Hamad. The synthesis and nitrogen adsorption measurements of **Si-Acid** and **Ti-**

Acid were carried out by Alexander Stahl. I performed all of the other experiments reported in Chapter 4.

Portions of Chapter 5 have been published as: K. E. Shopsowitz, W. Y. Hamad, M. J. MacLachlan, “Chiral Nematic Mesoporous Carbon Derived from Nanocrystalline Cellulose.” *Angew. Chem. Int. Ed.* **2011**, *50*, 10991-10995. I was the principal author of this work and co-edited it with Prof. Mark MacLachlan and Dr. Wadood Hamad. Simon Law synthesized and characterized (with the exception of electron microscopy) all of the **PANI@CNMC3** samples reported in Chapter 5. I performed all of the other experiments reported in Chapter 5.

Table of Contents

Abstract	ii
Preface	iv
Table of Contents	vi
List of Tables	ix
List of Figures	x
List of Schemes	xvii
List of Symbols and Abbreviations	xviii
Acknowledgements	xxi
Chapter 1 Introduction	1
1.1 Nanomaterials	1
1.1.1 Overview	1
1.1.2 Self-Assembly	1
1.1.3 Synthesis of Nanomaterials	2
1.1.4 Biological Nanomaterials	3
1.2 Chiral Nematic Liquid Crystals	5
1.2.1 Photonic Crystals	5
1.2.2 Introduction to Liquid Crystals	6
1.2.3 The Chiral Nematic Phase	7
1.2.4 Photonic Properties of Chiral Nematic Liquid Crystals	10
1.3 Nanocrystalline Cellulose	12
1.3.1 Introduction to Cellulose	12
1.3.2 Introduction to Cellulose Nanomaterials	13
1.3.3 Preparation of Nanocrystalline Cellulose	15
1.3.4 Chiral Nematic Self-Assembly of Nanocrystalline Cellulose	16
1.3.5 Mechanisms for NCC Chiral Nematic Phase Formation	18
1.3.6 Potential Applications Involving NCC	21
1.4 Mesoporous Materials	22
1.4.1 Overview	22
1.4.2 Liquid Crystal Templating	23
1.4.3 Mesoporous Silica	27
1.4.4 Mesoporous Organosilica	28
1.4.5 Mesoporous Carbon	30
1.4.6 Other Mesoporous Materials	33
1.5 Goals and Scope of the Thesis	35
Chapter 2 Mesoporous Silica Films with Tunable Chiral Nematic Structures	37
2.1 Introduction	37

2.2 Experimental.....	40
2.2.1 General.....	40
2.2.2 Spectroscopic Characterization.....	40
2.2.3 Microscopy	41
2.2.4 Preparation of Nanocrystalline Cellulose	41
2.2.5 Preparation of NCC/Silica Composite Films.....	42
2.2.6 Preparation of Mesoporous Silica.....	43
2.3 Results and Discussion	43
2.3.1 Preparation of Chiral Nematic NCC/Silica Composite Films	43
2.3.2 Optical Characterization of NCC/Silica Composite Films	49
2.3.3 Influence of pH on the Formation of NCC-Silica Composite Films	51
2.3.4 Removal of the NCC Template by Calcination	53
2.3.5 Mesoporosity of Calcined Silica Films.....	55
2.3.6 Optical Characterization of Mesoporous Silica Films.....	59
2.3.7 Addition of Isotropic Liquids to Chiral Nematic Mesoporous Silica	62
2.4 Conclusions.....	65
Chapter 3 Chiral Nematic Mesoporous Organosilica Films	67
3.1 Introduction.....	67
3.2 Experimental.....	68
3.2.1 General.....	68
3.2.2 Spectroscopic Characterization.....	69
3.2.3 Sucrose Sensing Experiments	70
3.2.4 Microscopy	70
3.2.5 Preparation of NCC/Silica and NCC/Organosilica Composite Films	71
3.2.6 Preparation of Mesoporous Silica and Organosilica.....	72
3.3 Results and Discussion	73
3.3.1 Preparation of NCC/Organosilica Composite Films.....	73
3.3.2 Removal of NCC from Ethylene-Bridged NCC-Organosilica Composite Films	75
3.3.3 Chiral Nematic Optical and Structural Properties of Ethylene-Bridged Organosilica	78
3.3.4 Porosity Characterization of Chiral Nematic Organosilica and Silica Samples Prepared by Acid Hydrolysis of NCC	81
3.3.5 Mechanical Properties of Et-CNMO Films	87
3.3.6 Refractive Index Sensing with Et-CNMO Films.....	88
3.3.7 Synthesis of Additional Organosilica Samples.....	91
3.4 Conclusions.....	96
Chapter 4 Hard Templating of Nanocrystalline TiO₂ with Chiral Nematic Ordering.....	97
4.1 Introduction.....	97
4.2 Experimental.....	99
4.2.1 General.....	99
4.2.2 Microscopy	99
4.2.3 Preparation of NCC/Silica Composite Films.....	100
4.2.4 Preparation of Mesoporous Silica.....	100
4.2.5 Preparation of TiO ₂	100
4.3 Results and Discussion	101

4.3.1 Synthesis of Mesoporous Silica Films.....	101
4.3.2 Synthesis of TiO ₂ Replicas via Hard Templating.....	102
4.3.3 Nitrogen Adsorption Studies of TiO ₂ Replicas.....	105
4.3.4 Chiral Nematic Optical and Structural Properties of TiO ₂ Replicas.....	106
4.4 Conclusions.....	110
Chapter 5 Chiral Nematic Mesoporous Carbon Derived from Nanocrystalline Cellulose.....	112
5.1 Introduction.....	112
5.2 Experimental.....	114
5.2.1 General.....	114
5.2.2 Microscopy.....	115
5.2.3 Preparation of NCC/silica Composite Films.....	115
5.2.4 Preparation of Mesoporous Carbon Films.....	115
5.2.5 Conductivity and Electrochemical Measurements of Mesoporous Carbon Films.....	116
5.2.6 Synthesis and Electrochemical Characterization of PANI@CNMC Films.....	116
5.3 Results and Discussion.....	117
5.3.1 Synthesis of Mesoporous Carbon from NCC/Silica Composite Films.....	117
5.3.2 Comparison of the Porosity of Carbon Obtained from Different NCC/Silica Compositions.....	121
5.3.3 SEM Structural Studies of NCC-Derived Carbon.....	125
5.3.4 Chiral Nematic Mesoporous Carbon as a Hard Template for Silica.....	127
5.3.5 Application of Chiral Nematic Mesoporous Carbon as a Supercapacitor Electrode.....	128
5.3.6 Electropolymerization of Polyaniline within Chiral Nematic Mesoporous Carbon.....	130
5.4 Conclusions.....	136
Chapter 6 Conclusions and Future Directions.....	138
6.1 Conclusions.....	138
6.2 Future Directions.....	142
References.....	146
Appendix A Additional Characterization for Chapter 2.....	163
Appendix B Additional Characterization and Discussion for Chapter 3	165
Appendix C Additional Characterization for Chapter 4.....	168

List of Tables

Table 2-1. Compositions and peak reflected wavelengths of NCC/silica composite films	47
Table 2-2. Nitrogen adsorption data for selected samples.	57
Table 2-3. Peak reflected wavelengths for chiral nematic mesoporous silica samples....	60
Table 3-1. Ethylene-bridged NCC/organosilica composite films.	74
Table 3-2. Nitrogen adsorption characterization of acid hydrolyzed samples.	83
Table 3-3. Elemental analysis and N ₂ adsorption data for different organosilica samples	93
Table 4-1. Nitrogen adsorption data.....	106
Table 5-1. Compositions of NCC/silica and carbon/silica films.....	119
Table 5-2. Nitrogen adsorption data for porous carbon.	123
Table 5-3. Characterization data for PANI@CNMC3 samples.	135

List of Figures

- Figure 1-1.** Examples of hierarchically structured biological nanomaterials. (a) The nanostructure of spider silk gives it its incredible strength. (b) The nanostructured setae present on gecko feet give them remarkable adhesive properties. (a) was reproduced in part by permission from Macmillan Publishers Ltd: Nature Materials,^[19] copyright 2010. (b) was reproduced in part from reference 26. Copyright 2005 National Academy of Sciences, USA..... 4
- Figure 1-2.** Representative examples of photonic crystal structures. (a) The different coloured layers represent materials with different refractive indices. (b) The opal structure consists of spheres arranged in an fcc lattice. 6
- Figure 1-3.** (a) Schematic representation of a CN-LC. Discrete layers are shown (left) to illustrate the structure, although in a real CN-LC the rotation of the nematic director is continuous. The right side shows the orientation of the nematic director in each layer as it makes a full 360° rotation corresponding to the distance P . (b) Polarized optical micrograph of a CN-LC showing characteristic fingerprint texture (scale bar = 30 μm)... 9
- Figure 1-4.** Schematic representation of diffraction from a left-handed CN-LC with P of ~ 300 nm. Left-handed circularly polarized blue light is selectively reflected while the remaining incoming light is transmitted. 11
- Figure 1-5.** Molecular structure of cellulose. (a) Chemical structure of an individual cellulose polymer chain. (b) Possible hydrogen-bonding patterns for cellulose I found in plants. (b) was reproduced in part with permission from reference 47. Copyright 2004 American Chemical Society. 13
- Figure 1-6.** TEM micrographs of negatively stained NCC. (a) NCC prepared by sulfuric acid hydrolysis of cotton. (b) NCC prepared by sulfuric acid hydrolysis of tunicate. Reproduced in part with permission from reference 50. Copyright 2008 American Chemical Society. 15
- Figure 1-7.** Schematic illustration of NCC synthesis by sulfuric acid hydrolysis 16
- Figure 1-8.** Different packing arrangements of screw-shaped rods. (a) Parallel arrangement. (b) Chiral arrangement, which can facilitate closer packing. 19
- Figure 1-9.** Synthesis of ordered mesoporous materials by cooperative self-assembly and “true” liquid crystal templating pathways..... 26
- Figure 1-10.** Chemical structures of typical alkoxy silanes used to synthesize mesoporous silica and organosilica materials. R = alkyl group (typically $-\text{CH}_3$ or $-\text{CH}_2\text{CH}_3$). R' = any organic group. 29
- Figure 1-11.** Scheme outlining the synthesis of mesoporous carbon through hard templating. 31
- Figure 1-12.** Ragone plot comparing performance of different energy storage devices.. 33

Figure 2-1. POM micrograph of a drop taken from an NCC/TMOS mixture during evaporation on a glass slide. The right side of the image (closer to the edge of the drop) displays a fingerprint texture indicative of a chiral nematic LC phase (scale bar = 100 μm)..... 46

Figure 2-2. SEM images of chiral nematic NCC and NCC/silica films. (a) Low magnification image of pure NCC film CN-NCC (scale bar = 200 μm). (b) Cross-sectional image of CN-NCC shows periodic structure perpendicular to the film surface (scale bar = 10 μm). (c) Cross-sectional image of CN-NCC at higher magnification (scale bar = 2 μm). (d) Cross-sectional image of NCC/silica composite film Comp2 at the same magnification as (c) shows a similar periodic structure but with a larger repeating distance (scale bar = 2 μm). (e) Cross-sectional image of NCC/silica composite film Comp5 (scale bar = 2 μm). (f) Cross-sectional image of NCC/silica composite film Comp8 (scale bar = 2 μm). 48

Figure 2-3. (a) POM micrograph of a free-standing chiral nematic NCC film (CN-NCC, scale bar = 100 μm). (b) POM micrograph of free-standing NCC/silica composite film Comp3 (scale bar = 100 μm). 50

Figure 2-4. UV-Vis spectra for chiral nematic NCC and selected NCC/silica composite films. 51

Figure 2-5. Disruption of chiral nematic ordering by the addition of HCl. (a) POM micrograph of Comp3-pH2.0 (scale bar = 100 μm). (b) Cross-sectional SEM micrograph of Comp3-pH2.0 (scale bar = 1 μm)..... 53

Figure 2-6. IR spectra and PXRD patterns before and after calcination of an NCC-silica composite film. (a) IR spectrum of Comp1. Arrows indicate characteristic NCC peaks (O-H, C-H, and C-C stretching modes, respectively, from left to right). (b) IR spectrum of CNMS1. (c) PXRD pattern of Comp1. (d) PXRD pattern for CNMS1. 54

Figure 2-7. SEM images of calcined silica CNMS2. (a) Top view looking down the edge of a fractured film (scale bar = 10 μm). (b) Cross-sectional micrograph of film showing repeating structure with fingerprint defect (scale bar = 10 μm). (c) Cross-sectional view at higher magnification (scale bar = 2 μm). (d) High magnification micrograph looking down the chiral nematic helical axis (scale bar = 200 nm)..... 55

Figure 2-8. Nitrogen adsorption data for selected calcined samples (a) N_2 isotherm for CNMS1. (b) N_2 isotherm for CNMS3. (c) N_2 isotherm for MS3-pH2.0. (d) N_2 isotherm for MS3-pH12.5. (e) BJH pore size distribution for CNMS1. (f) BJH pore size distribution for CNMS6. 58

Figure 2-9. SEM comparison of chiral nematic film before and after calcination. (a) Cross-sectional micrograph of Comp2 (scale bar = 2 μm). (b) Cross-sectional micrograph of CNMS2 (scale bar = 2 μm)..... 59

Figure 2-10. TEM micrographs of CNMS3. (a) View looking down the helical axis of a film fragment (scale bar = 100 nm). (b) Film fragment with the helical axis in the plane of the image as indicated (scale bar = 100 nm)..... 59

Figure 2-11. POM micrographs of chiral nematic silica films CNMS3-CNMS6 (a-d respectively, all scale bars = 100 μm).....	60
Figure 2-12. Photographs of iridescent silica films. (a) Silica films CNMS3-6. The dime is included for scale (d = 18 mm). (b) Photograph of CNMS6 taken at normal incidence. (c) Photograph of CNMS6 taken at oblique incidence.	61
Figure 2-13. Optical characterization of iridescent silica films CNMS3-6. (a) UV-Vis spectra of CNMS3-6. (b) CD spectra of CNMS3-6.....	62
Figure 2-14. Photograph of CNMS3-6 after the addition of water.....	63
Figure 2-15. Water infiltration of CNMS4. (a) UV-Vis spectra of CNMS4 before and after the addition of water. (b) POM micrograph of CNMS4 after the addition of water (scale bar = 200 μm). The green area in the top-left region of the image is still dry.....	64
Figure 2-16. Circular dichroism spectra of CNMS5 after infiltration with different liquids.....	65
Figure 3-1. UV-Vis/NIR spectra of Et-Comp1-4.....	74
Figure 3-2. ^{13}C CP/MAS solid-state NMR of ethylene-bridged organosilica before (green) and after (blue) the removal of NCC.....	76
Figure 3-3. ^{29}Si CP/MAS solid-state NMR spectra of (a) Et-Comp3 and (b) Et-CNMO3.	77
Figure 3-4. TGA of (a) Et-CNMO3 and (b) CNMS3- H_2SO_4	78
Figure 3-5. Optical characterization of Et-CNMO films. (a) Photograph of Et-CNMO2 (left) and Et-CNMO3 (right, scale bar = 18 mm). (b) UV-Vis/NIR (solid lines) and CD spectra (dashed lines) of Et-CNMO1-4.	79
Figure 3-6. SEM images of Et-CNMO films. (a) Top view of fracture for Et-CNMO3 (scale bar = 30 μm). (b) High magnification micrograph of Et-CNMO3 (scale bar = 1 μm). (c) Cross-sectional micrograph of Et-CNMO1 (scale bar = 2 μm). (d) Cross-sectional micrograph of Et-CNMO4 (scale bar = 2 μm).	80
Figure 3-7. Nitrogen adsorption data for selected ethylene-bridged mesoporous organosilica samples. (a) N_2 isotherm for Et-CNMO1. (b) BJH pore size distribution for Et-CNMO1. (c) N_2 isotherm for Et-CNMO3. (d) BJH pore size distribution for Et-CNMO3. (e) N_2 isotherm for Et-CNMO3-Cal. (f) BJH pore size distribution for Et-CNMO3-Cal.....	82
Figure 3-8. Helium ion micrograph of Et-CNMO3 (scale bar = 200 nm). The inset shows a blown-up section taken from the middle of the image.....	84
Figure 3-9. Nitrogen adsorption data for mesoporous silica films prepared by acid hydrolysis of Comp3. (a) N_2 isotherm for CNMS3- H_2SO_4 . (b) BJH pore size distribution for CNMS3- H_2SO_4 . (c) N_2 isotherm for CNMS3-HCl. (d) BJH pore size distribution for	

CNMS3-HCl. (e) N₂ isotherm for CNMS3-HCl-Cal. (f) BJH pore size distribution for CNMS3-HCl-Cal. 86

Figure 3-10. Improved flexibility of Et-CNMO films. (a) Photograph of a film from sample Et-CNMO2 being bent with tweezers. (b) Comparison of stress-strain curves obtained from tensile testing of mesoporous silica (CNMS3-HCl) and organosilica (Et-CNMO2) samples. 87

Figure 3-11. POM micrographs of Et-CNMO2 taken at different time points after wetting with acetone. (a) Et-CNMO2 immediately after wetting with acetone. (b) Et-CNMO2 15 seconds after wetting with acetone. (c) Et-CNMO2 17 seconds after wetting with acetone. (d) Et-CNMO2 30 seconds after wetting with acetone. All scale bars = 200 μm. 88

Figure 3-12. CD spectra of Et-CNMO2 after wetting with different liquids..... 89

Figure 3-13. (a) CD spectra for Et-CNMO2 after soaking with different aqueous sucrose solutions. (b) Plot of max CD signal vs. refractive index based on the spectra shown in (a). 90

Figure 3-14. The different organosilica precursors used in this chapter..... 92

Figure 3-15. SEM images of organosilica samples with different bridging groups. (a) Side view of Me-CNMO film at edge (scale bar = 20 μm). (b) Edge of Me-CNMO film at higher magnification (scale bar = 1 μm). (c) Top view of Bz-CNMO film at edge (scale bar = 10 μm). (d) Edge of Bz-CNMO film at higher magnification (scale bar = 1 μm). (e) Low magnification image of Hex-MO (scale bar = 50 μm). (f) Hex-MO viewed at higher magnification (scale bar = 500 nm). 94

Figure 3-16. N₂ adsorption data for organosilica samples with different bridging groups. (a) N₂ adsorption isotherm and BJH pore size distribution (inset) for Me-CNMO. (b) N₂ adsorption isotherm and BJH pore size distribution (inset) for Bz-CNMO. (c) N₂ adsorption isotherm and BJH pore size distribution (inset) for Hex-MO. (d) N₂ adsorption isotherm and BJH pore size distribution (inset) for Et-CNMO3. 95

Figure 4-1. N₂ adsorption isotherms before and after TiO₂ loading. (a) Isotherms for Si-Cal and the corresponding silica/titania composite obtained after the final TiCl₄ loading step and calcination at 600 °C. (b) Isotherms for Si-Acid and the corresponding silica/titania composite obtained after the final TiCl₄ loading step and calcination at 600 °C. 103

Figure 4-2. Data showing the removal of SiO₂ by NaOH treatment of SiO₂/TiO₂ composite. (a) IR spectra before (Si/Ti-Acid) and after (Ti-Acid) NaOH treatment of SiO₂/TiO₂ composite. (b) EDX spectrum of Ti-Acid. 104

Figure 4-3. PXRD patterns for (a) Ti-Acid and (b) Ti-Control. Ti-Cal is not shown but gives a pattern virtually identical to Ti-Acid. 105

Figure 4-4. N₂ adsorption isotherms for mesoporous titania (a) Ti-Cal and (b)Ti-Acid.106

- Figure 4-5.** Circular polarized iridescence of Ti-Acid. (a) Ti-Acid photographed using a left-handed circular polarizing filter (scale bar = 2 cm). (b) Ti-Acid photographed using a right-handed circular polarizing filter (scale bar = 2 cm). 107
- Figure 4-6.** SEM images of Si-Acid, Ti-Acid, and Ti-Cal. (a) Top view of Si-Acid film at edge (scale bar = 1 μm). (b) Cross-section of Si-Acid at high magnification (scale bar = 500 nm). (c) Top view of Ti-Acid film at edge (scale bar = 1 μm). (d) Cross-section of Ti-Acid at high magnification (scale bar = 500 nm). (e) Side view of Ti-Cal film at edge (scale bar = 5 μm). (f) Edge of Ti-Cal film at higher magnification (scale bar = 2 μm). 109
- Figure 4-7.** (a) POM micrographs Ti-Acid. (a) Micrograph of a dry Ti-Acid film (scale bar = 400 μm). (b) Micrograph of the same film after wetting with ethanol (scale bar = 400 μm). 110
- Figure 5-1.** (a) TGA of Comp3. (b) TGA of Comp3 after carbonization at 900 $^{\circ}\text{C}$. Both samples were run under air. 119
- Figure 5-2.** Photographs of carbon films before and after the removal of silica. (a) Carbon/silica composite films derived from Comp3 (scale bar = 2 cm). (b) Mesoporous carbon sample CNMC3 (scale bar = 2 cm). 120
- Figure 5-3.** TGA and EDX characterization of mesoporous carbon. (a) TGA of CNMC3 (10 $^{\circ}\text{C}/\text{min}$, air). (b) EDX spectrum of CNMC3. The two unlabeled peaks at 1.25 and 1.5 keV correspond to Mg and Al found in the SEM stub. 120
- Figure 5-4.** Spectroscopic characterization of mesoporous carbon. (a) PXRD pattern of CNMC3. (b) Raman spectrum of CNMC3. 121
- Figure 5-5.** Nitrogen adsorption isotherms for selected carbon samples. (a) N_2 isotherm measured for MC1. (b) N_2 isotherm measured for CNMC2. (c) N_2 isotherm measured for CNMC3. (d) N_2 isotherm measured for CNMC5. 122
- Figure 5-6.** (a) BJH pore size distribution for CNMC3. (b) BJH pore size distribution for MC3-pH2.0. 124
- Figure 5-7.** TEM micrographs of porous carbon samples. (a) TEM micrograph of CNMC3. (b) TEM micrograph of MC3-pH2.0. (c) TEM micrograph of MC1. Scale bars all = 200 nm. 124
- Figure 5-8.** SEM micrographs of CNMC3. (a) Top view of film at low magnification (scale bar = 500 μm). (b) Side view at fracture (scale bar = 5 μm). (c) Cross-sectional view of film (scale bar = 2 μm). (d) High magnification image of cross-section (scale bar = 500 nm). 126
- Figure 5-9.** SEM micrographs of MC1 and CNMC2. (a) Top view of fracture of MC1 film (scale bar = 1 μm). (b) Top view of fracture of CNMC2 film (scale bar = 1 μm)... 126
- Figure 5-10.** Optical characterization of silica templated by CNMC3. (a) POM micrograph (scale bar = 200 μm). (b) CD spectrum. 128

Figure 5-11. SEM micrographs of silica templated by CNMC3. (a) Cross-sectional view (scale bar = 2 μm). (b) Cross-sectional view at higher magnification (scale bar = 500 nm).
..... 128

Figure 5-12. Electrochemical characterization of CNMC3. (a) Photograph of mesoporous carbon film on a stainless steel current collector (scale bar = 1.5 cm). (b) Galvanostatic charge/discharge curve for CNMC3 at a current load of 230 mA/g. (c) Cyclic voltammogram of CNMC3 at a scan rate of 2 mV/s. (d) Cyclic voltammogram of CNMC3 at scan rates ranging from 10-100 mV/s. All measurements were carried out using a symmetrical two-electrode setup in a 1M $\text{H}_2\text{SO}_{4(\text{aq})}$ electrolyte solution. 130

Figure 5-13. SEM micrographs of selected samples. (a) Top surface of a CNMC3 film before PANI deposition. (b) Top surface of a PANI@CNMC3 film after 100 second electropolymerization. (c) Top surface of a PANI@CNMC3 film after 300 second electropolymerization. (d) Edge of PANI@CNMC3 film after 300 second electropolymerization. Scale bars all = 500 nm. 132

Figure 5-14. SEM images and photographs of different coloured PANI@CNMC3 films. (a) Top view of a PANI@CNMC3 film after 350 second electropolymerization (scale bar = 500 nm). (b) Side view of a PANI@CNMC3 film after 350 second electropolymerization (scale bar = 1 μm). (c) Top view of a PANI@CNMC3 film after 400 second electropolymerization (scale bar = 500 nm). (d) Side view of a PANI@CNMC3 film after 400 second electropolymerization (scale bar = 1 μm). (e) Top view of a PANI@CNMC3 film after 900 second electropolymerization (scale bar = 500 nm). (f) Side view of a PANI@CNMC3 film after 900 second electropolymerization (scale bar = 1 μm). The insets show photographs of the corresponding films. 133

Figure 5-15. Nitrogen adsorption isotherms for PANI@CNMC3 electropolymerized for 50, 100, and 300 seconds. 135

Figure 5-16. Electrochemical characterization of selected PANI@CNMC3 samples. (a) Current vs. time curve during a 900 s PANI electropolymerization carried out at 0.8 V vs. Ag/AgCl. (b) CV curves for selected samples obtained at a scan rate of 2 mV/s (all CVs were run with a three electrode setup, potential is vs. Ag/AgCl). 136

Figure A-1. TEM micrograph of negatively stained NCC template. 163

Figure A-2. TEM micrograph of negatively stained NCC template at higher magnification. 164

Figure A-3. Width distribution calculated from Figure A-2 (total count = 67, avg. width = 9 nm). 164

Figure B-1. TGA run under air for different organosilica samples: (a) Me-CNMO, (b) Bz-CNMO, and (c) Hex-CNMO. 165

Figure B-2. ^{13}C CP/MAS solid-state NMR of Me-CNMO. The single peak corresponds to the methylene bridge of the organosilica. 165

Figure B-3. ^{13}C CP/MAS solid-state NMR of Bz-CNMO. Peak labeled benzene corresponds to the phenylene bridge of the organosilica. Peaks labeled SS are spinning sidebands, artifacts from spinning the rotor that are often large for aromatic samples. Small additional peaks that may come from residual NCC or glucose are also present..166

Figure B-4. UV-Vis/NIR spectra for (a) Me-CNMO and (b) Bz-CNMO.....166

Figure C-1. TGA of Ti-Acid run under air.....168

Figure C-2. SEM images showing the surface of Ti-Acid films. (a) Image showing a region without any surface crust. (b) Image showing a region with a surface crust.....168

List of Schemes

Scheme 2-1. Outline of the synthesis of chiral nematic NCC/silica composite films and chiral nematic mesoporous silica (CNMS).....	45
Scheme 4-1. Schematic representation of the synthesis of chiral nematic mesoporous titania. (a) Chiral nematic mesoporous silica used as a hard template. (b) Chiral nematic mesoporous titania replica.	103
Scheme 5-1. Conversion of chiral nematic NCC/silica composite film to chiral nematic mesoporous carbon. (a) NCC/silica composite film. (b) Carbon/silica composite film obtained after pyrolysis of (a) at 900 °C under an N ₂ atmosphere. (c) Mesoporous carbon obtained after the treatment of (b) with 2M NaOH.	118

List of Symbols and Abbreviations

@	encapsulated in
Δn	birefringence
λ	wavelength
λ_{\max}	wavelength with maximum intensity
n	refractive index
n_{avg}	average refractive index
P	helical pitch
Q	chalcogenide
ATR	attenuated total reflectance
BET	Brunauer-Emmett-Teller
BJH	Barrett-Joyner-Halenda
BNC	bacterial nanocellulose
BTESB	1,4-bis(triethoxysilyl)benzene
BTESM	bis(triethoxysilyl)methane
BTMSE	1,2-bis(trimethoxysilyl)ethane
BTMSH	1,6-bis(trimethoxysilyl)hexane
CD	circular dichroism
CN-LC	chiral nematic liquid crystal
CNMC	chiral nematic mesoporous carbon
CNMO	chiral nematic mesoporous organosilica
CNMS	chiral nematic mesoporous silica
CP/MAS	cross-polarization / magic angle spinning

CTAB	cetyl trimethylammonium bromide
CV	cyclic voltammetry
D_{eff}	effective diameter
DI	de-ionized
DMSO	dimethyl sulfoxide
DSS	4,4-dimethyl-4-silapentane-1-sulfonic acid
EDLC	electrical double-layer capacitor
EDX	energy dispersive X-ray
EISA	evaporation induced self-assembly
FT-IR	Fourier transform infrared
GLAD	glancing angle deposition
i-PrOH	isopropanol
IR	infrared
IUPAC	International Union for Pure and Applied Chemistry
LC	liquid crystal
LHP	left-handed circular polarizer
MFC	microfibrillated cellulose
NCC	nanocrystalline cellulose
NIR	near infrared
NMR	nuclear magnetic resonance
NP	nanoparticle
PANI	polyaniline
PEG	polyethylene glycol
PMO	periodic mesoporous organosilica
POM	polarized optical microscopy

PXRD	powder X-ray diffraction
RHP	right-handed circular polarizer
SEM	scanning electron microscopy
TEM	transmission electron microscopy
TEMPO	2,2,6,6-tetramethylpiperidin-1-yl)oxidanyl
TEOS	tetraethyl orthosilicate
TGA	thermal gravimetric analysis
TMOS	tetramethyl orthosilicate
UV-Vis	ultraviolet-visible

Acknowledgements

First and foremost, I would like to thank my PhD supervisor, Mark MacLachlan, who has been an incredible mentor. Mark's passion for research and his devotion to his students is truly amazing and I am forever grateful for the opportunities that he has provided me with. I am also very appreciative of his prompt editing of this thesis.

I would also like to thank Dr. Wadood Hamad, without whom none of this work would have been possible. Not only did he save me the trouble of having to make any starting materials, he has also provided me with valuable guidance over the years. I would also like to thank Professor Mike Wolf, who kindly agreed to read my thesis given the unlikely circumstance that all of my committee members are currently on sabbatical.

I have been extremely fortunate to have been surrounded with excellent coworkers and friends throughout my time at UBC. All of the past and present members of the MacLachlan and Wolf groups (amongst others) have been intelligent, friendly, and fun people to be around. The many trips to the village for lunch, ski days at Whistler, and nights drinking beer really made the past five years enjoyable.

I had the privilege to supervise many excellent undergraduates throughout my PhD, some of whose work is directly incorporated into this thesis. Camille Gregory, Simon Law, Alex Stahl, Si Rim Kim, Cooper Johnston, Anthony Bryson, and Emily Hopkins, it was a lot of fun working with all of you and I really appreciate your hard work.

Lastly, and most importantly, I would like to thank my family, who has always been extremely supportive of me. Catherine, you have made me the happiest and luckiest guy in the world.

Chapter 1

Introduction

1.1 Nanomaterials

1.1.1 Overview

Broadly defined, nanomaterials have at least one spatial dimension in the size range of 1-100 nm,^{*} which consequently gives them properties that differ from their bulk analogues.^[1, 2] For example, the brilliant colours of noble metal and semi-conductor nanoparticles (NPs) are caused by quantum confinement effects.^[3, 4] Another important feature of nanomaterials is their high surface area compared to bulk materials. High surface area nanomaterials can be used to efficiently store gases at moderate temperatures and pressures,^[5] deliver high loadings of therapeutic agents to cells for targeted therapies,^[6] and catalyze reactions at rates that are orders of magnitudes higher than what is observed for bulk materials.^[7] Taken as a whole, nanomaterials are an incredibly vast and active research area; the following sections are only meant to provide a brief overview of several key concepts that are relevant to the overall scope of this thesis.

1.1.2 Self-Assembly

Self-assembly is a term used to describe the spontaneous formation of ordered structures from initially disordered systems.^[8] This process occurs extensively in both natural and synthetic systems, often producing functional, nanostructured materials. Self-assembled structures form based on reversible, local interactions between individual components that lead to thermodynamic energy minimization.^[9] The resulting structures

^{*} Although this is the most common definition, nanomaterials are sometimes defined as having dimensions of 1-1000 nm.

are therefore encoded by the building blocks based on their shape, size, and specific interactions, making self-assembly very attractive from a design perspective; by precisely controlling the properties of relatively simple components, much larger and more complicated structures can be obtained. In the context of molecular systems, self-assembly is generally considered to involve relatively weak and reversible interactions between molecules such as hydrogen bonding, van der Waals, hydrophobic, and Coulombic interactions.^[8, 10] In addition to molecular systems, the principles of self-assembly can also be applied to larger building blocks such as nanoparticles and even macroscopic components.^[11]

1.1.3 Synthesis of Nanomaterials

Nanomaterials are synthesized using strategies that can generally be classified as top-down or bottom-up approaches.^[2, 12] Top-down approaches start from larger structures and convert them into nanomaterials. Examples are the use of fabrication methods, such as lithography, to pattern nanostructures onto surfaces, and the stripping down of biological materials into their constituent nanostructures. Bottom-up approaches, on the other hand, use atomic or molecular precursors as the starting point to build up nanomaterials.

Self-assembly has proven to be a useful strategy for producing ordered nanomaterials, either starting from molecular or nano-sized building blocks.^[12, 13] Although self-assembly is inherently a bottom-up approach, it can also be used in a complementary fashion with top-down approaches, as in soft lithography.^[14] Self-assembly is used extensively for the synthesis of nanoporous materials. Highly porous metal organic frameworks are formed by the self-assembly of metal ions with ligands^[15]

and the spontaneous ordering of lyotropic liquid crystals can be used to template mesoporous materials with diverse compositions.^[16]

1.1.4 Biological Nanomaterials

Biological materials often have hierarchical nanostructures that are integral to their function. These materials range in size from discrete molecular assemblies (e.g., enzymes and lipid vesicles), to nanostructured solids like wood and bone.^[17] Biological nanomaterials can form through basic molecular self-assembly processes (e.g., protein folding) or more complex pathways like biomineralization. Proteins provide an excellent example of biomaterials that derive specific functions from hierarchical nanostructures. Linear polypeptide chains, which are typically non-functional, self-assemble to form ordered secondary structures (e.g., α -helices and β -sheets) that further organize into folded tertiary structures. The three-dimensional architectures of folded proteins allow them to function with unparalleled efficiency. For example, enzymes can selectively catalyze chemical reactions with up to 10^{19} fold rate enhancements.^[18]

Many materials in biology that appear to be bulk solids are in fact nanostructured, which often explains their excellent physical properties.^[17] Silk is one of the toughest materials known in spite of the fact that it is composed entirely of proteins held together by weak hydrogen bonds. It has recently been demonstrated that the strength of silk, which exceeds that of steel, is the result of nanoconfinement effects exhibited by its constituent β -sheet nanocrystals.^[19] Another example is the incredible ability of geckos to stick to almost any surface, which is due entirely to the shape and size of nanofilaments present on their feet. The extremely high surface area of these nanofilaments allows gecko feet to achieve their stickiness solely using van der Waals interactions.^[20] Nanostructured biomaterials can also have interesting optical properties. The eyes of

moths contain a subwavelength periodic nanostructure that acts as an anti-reflective coating and improves their vision in low-light conditions^[21] while the beautiful iridescent colours of many insects, including certain beetles^[22] and butterflies,^[23] are caused by periodic chitin nanostructures that cause Bragg diffraction of visible light. The nanostructures present in biology are not limited to organic materials; there exist many examples of almost purely inorganic (e.g., the shells of diatoms)^[24] and organic/inorganic composite materials (e.g., bone) that have intricate nanostructures as well.^[25]

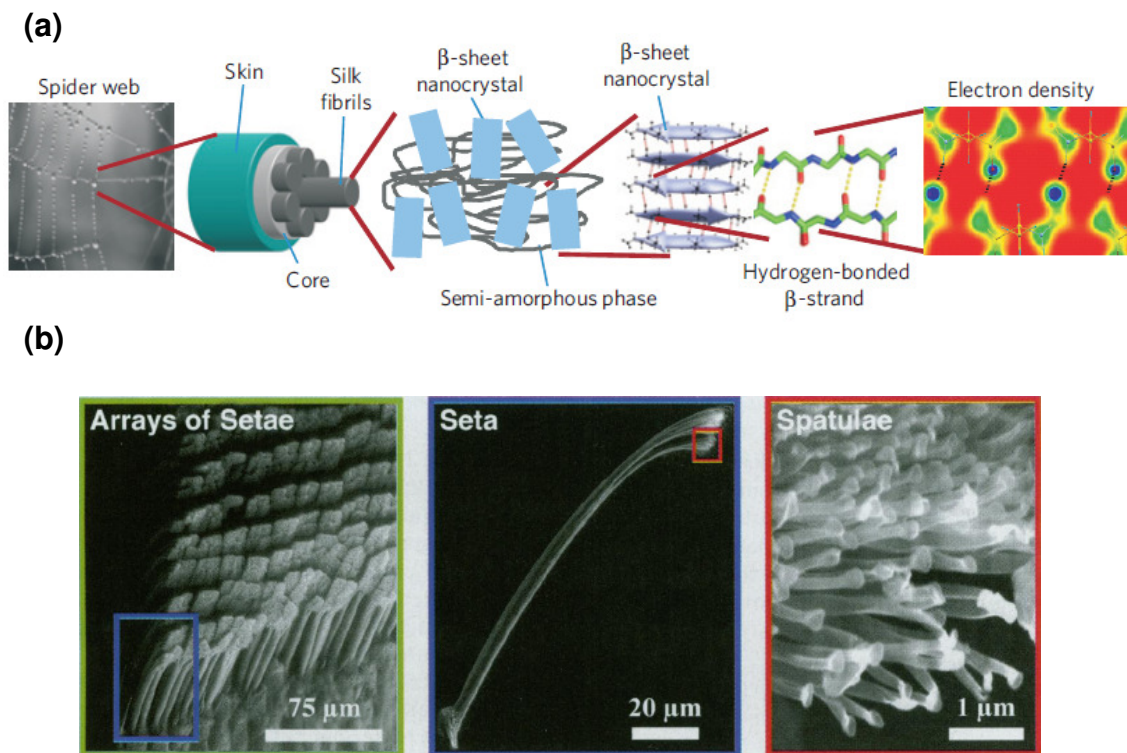


Figure 1-1. Examples of hierarchically structured biological nanomaterials. (a) The nanostructure of spider silk gives it its incredible strength. (b) The nanostructured setae present on gecko feet give them remarkable adhesive properties. (a) was reproduced in part by permission from Macmillan Publishers Ltd: Nature Materials,^[19] copyright 2010. (b) was reproduced in part from reference 26. Copyright 2005 National Academy of Sciences, USA.

1.2 Chiral Nematic Liquid Crystals

1.2.1 Photonic Crystals

Photonic crystals are materials with periodically changing refractive indices that give rise to a range of wavelengths of electromagnetic radiation, known as the photonic band gap, for which propagation within the material is forbidden.^[27] The position and size of a photonic band gap generally depends on the repeating distance and refractive index contrast of the photonic crystal, although the exact band structure depends on its specific ordering. Light incident on a photonic crystal that falls within the photonic band gap is selectively reflected from the material due to Bragg diffraction, whereas light that is outside of the photonic band gap is transmitted. As a result, when the repeating distance is on the length scale of the wavelengths of visible light, photonic crystals appear coloured.

Photonic crystals can be classified as one-dimensional, two-dimensional, or three-dimensional, depending on the dimensionality of their periodicity (see Figure 1-2 for examples). An example of a one-dimensional photonic crystal is a Bragg reflector, which simply consists of alternating layers of materials with different refractive indices (e.g., SiO₂ and TiO₂) with a characteristic repeating distance.^[28] An example of a two-dimensional photonic crystal is a periodic array of holes on a surface.^[29] Examples of three-dimensional photonic crystals include opals, which are colloidal crystals formed by monodispersed spherical particles, and inverse opals, which are formed by condensing a material around an opal template.^[30]

The unique optical properties of photonic crystals have been effectively utilized for a number of different applications. For example, photonic crystals with engineered defects are excellent materials for controlling the propagation of light in fibre optics and waveguides, and can also be used as gain media for low-threshold lasing.^[31-33] Because

photonic band gaps depend on refractive index contrast, porous photonic crystals can be made to change colour in response to different stimuli (e.g., vapor infiltration and biomolecule adsorption) making them useful as colour changing pigments and sensors.^[34, 35] The continued development of new synthetic routes to photonic crystals with novel structures and compositions is an exciting area with many promising outlets for future applications.

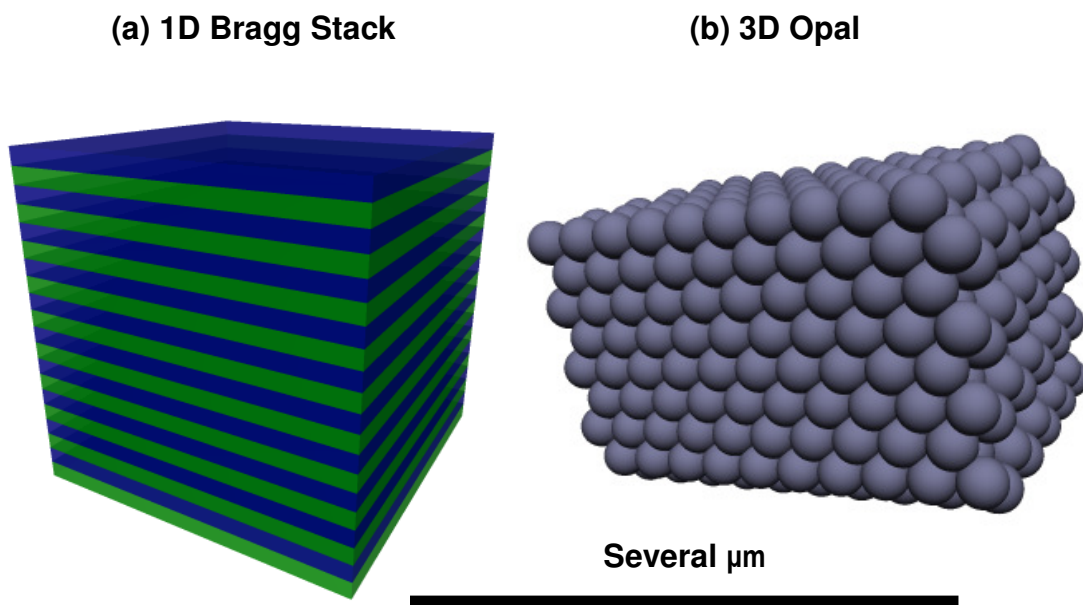


Figure 1-2. Representative examples of photonic crystal structures. (a) The different coloured layers represent materials with different refractive indices. (b) The opal structure consists of spheres arranged in an fcc lattice.

1.2.2 Introduction to Liquid Crystals

Liquid crystals (LCs, also referred to as mesophases) are a state of matter with the fluid properties of liquids but also with varying degrees of orientational and positional ordering.^[36] Liquid crystals can be divided into two general types: thermotropic and lyotropic. Thermotropic liquid crystals occur within a certain temperature range, below which a solid is formed, and above which an isotropic liquid is formed. Lyotropic liquid

crystals consist of molecules or particles in a solvent that show liquid crystal phase transitions dependent on concentration, temperature, and other factors.

The formation of liquid crystals is a self-assembly process that largely depends on the shape of the molecular building blocks, or mesogens. Thermotropic liquid crystals are most commonly formed by either rod-shaped or disc-shaped molecules, which can organize to form LC phases with different types of positional and orientational ordering. Various aspects of mesogens can be engineered, such as the length of alkyl substituents, to influence the specific LC phase that forms and the temperature range over which it forms. In addition to being sensitive to temperature, thermotropic LCs are also generally sensitive to electric fields, which forms the basis of most modern display technologies.

Perhaps the most well-known examples of lyotropic LCs are amphiphilic molecules or polymers (e.g., surfactants and block copolymers). Above a critical concentration in water, these molecules will self-assemble to form micelles in order to shield their hydrophobic regions. At higher concentrations, the micelles can further organize to form highly ordered hexagonal, cubic, or lamellar LC phases depending on concentration and other factors.^[37] In addition to amphiphilic molecules, various polymers and colloidal particles can also form lyotropic LC phases above critical concentrations in different solvents.^[38]

1.2.3 The Chiral Nematic Phase

Rod-shaped molecules have a tendency to align along their molecular axis, which can give rise to several distinct LC phases depending on the degree of ordering. The nematic phase is the simplest of these, showing long-range orientational ordering but no positional ordering.^[36] The average direction of the long molecular axes of mesogens in a nematic liquid crystal is termed the nematic director, and when chirality is introduced

into nematic systems, this can cause an intrinsic helical structure of the director field.^[39] This type of liquid crystal is referred to as a chiral nematic (CN-LC, also often referred to as a cholesteric LC for historical reasons), and has a helical axis that runs perpendicular to the plane of the nematic director (see Figure 1-3a).

In a CN-LC structure, the orientation of the nematic director rotates continuously along the direction of the helical axis with a handedness that depends on the chirality of the mesogens. This gives rise to a characteristic repeating distance, or pitch, every time the director makes a full 360° rotation. CN-LCs are known for both thermotropic and lyotropic systems. Thermotropic CN-LCs can either be formed by pure rod-shaped chiral molecules (e.g., derivatives of cholesterol) or by adding a chiral dopant to an achiral system that would otherwise form a nematic phase.^[39] In the latter case, the helical pitch is inversely proportional to the concentration of chiral dopant. As might be expected, the helical pitch of thermotropic CN-LCs strongly depends on temperature. Lyotropic CN-LC phases have been observed for many chiral biomolecules or bioparticles such as cellulose derivatives, DNA, and certain rod-shaped viruses.^[40-42] For lyotropic CN-LCs, the helical pitch generally depends upon concentration, however, many other factors can also play a role.

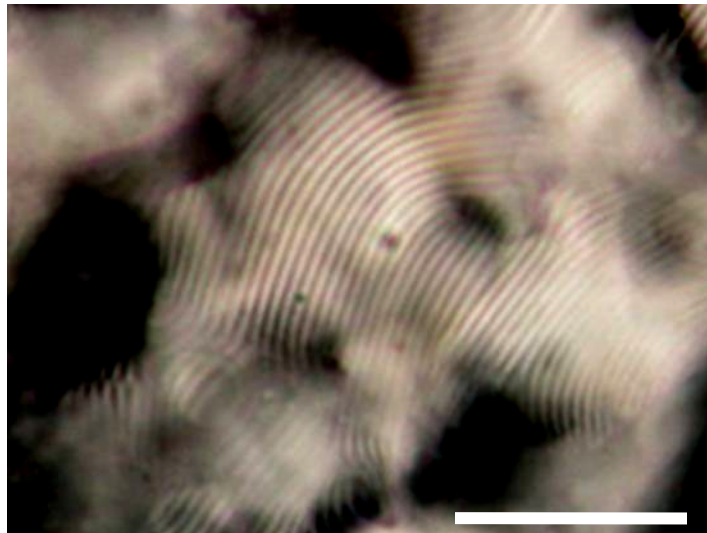
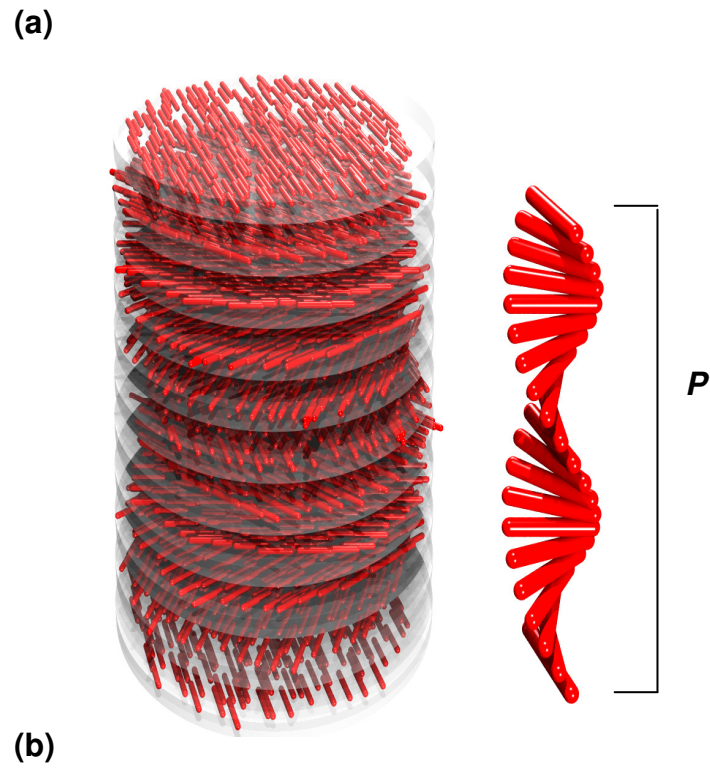


Figure 1-3. (a) Schematic representation of a CN-LC. Discrete layers are shown (left) to illustrate the structure, although in a real CN-LC the rotation of the nematic director is continuous. The right side shows the orientation of the nematic director in each layer as it makes a full 360° rotation corresponding to the distance P . (b) Polarized optical micrograph of a CN-LC showing characteristic fingerprint texture (scale bar = $30\ \mu\text{m}$).

1.2.4 Photonic Properties of Chiral Nematic Liquid Crystals

The observation made in the late 1800s that the colourless compound cholesteryl benzoate displays brilliant iridescence when heated within a certain temperature range helped lead to the discovery of liquid crystals.^[43] It is now known that the optical properties of cholesteryl benzoate are caused by a chiral nematic structure. The helical ordering of the nematic director within CN-LCs results in a periodically changing refractive index, which causes them to behave as one-dimensional photonic crystals. When the helical pitch is on the length scale of several microns and oriented parallel to a light source, the periodic structure can be observed by polarized optical microscopy as a characteristic fingerprint texture (Figure 1-3b). When the helical pitch of CN-LCs is on the length scale of several hundred nanometers, they appear coloured due to the selective reflection of visible light according to the following equation:

$$\lambda = P \cdot n_{\text{avg}} \cdot \sin\theta \quad (1)$$

From equation 1, it can be seen that the wavelength of light reflected from a CN-LC is related to the helical pitch (P), average refractive index (n_{avg}), and angle of incidence (θ) relative to the plane perpendicular to P .^[44] In equation 1, λ corresponds to the center of the reflection peak, while the width of the reflection peak is given by:

$$\Delta\lambda = P\Delta n \quad (2)$$

where Δn corresponds to the birefringence of the liquid crystal. An additional feature of reflection from a CN-LC is that it only occurs for light with circular polarization that matches the handedness of the helical structure. This means that for a left-handed chiral nematic structure, only left-handed circularly polarized light will be reflected while right-handed circularly polarized will be transmitted (Figure 1-4). It is therefore possible to determine the handedness of a CN-LC by measuring the polarization of light that it reflects or transmits. Finally, the handedness of the polarization does not flip after

reflection as is the case for reflection of circularly polarized light from conventional mirrors. The optical properties of CN-LCs make them useful for applications including thermometers, polarizing mirrors, and reflective displays.^[39]

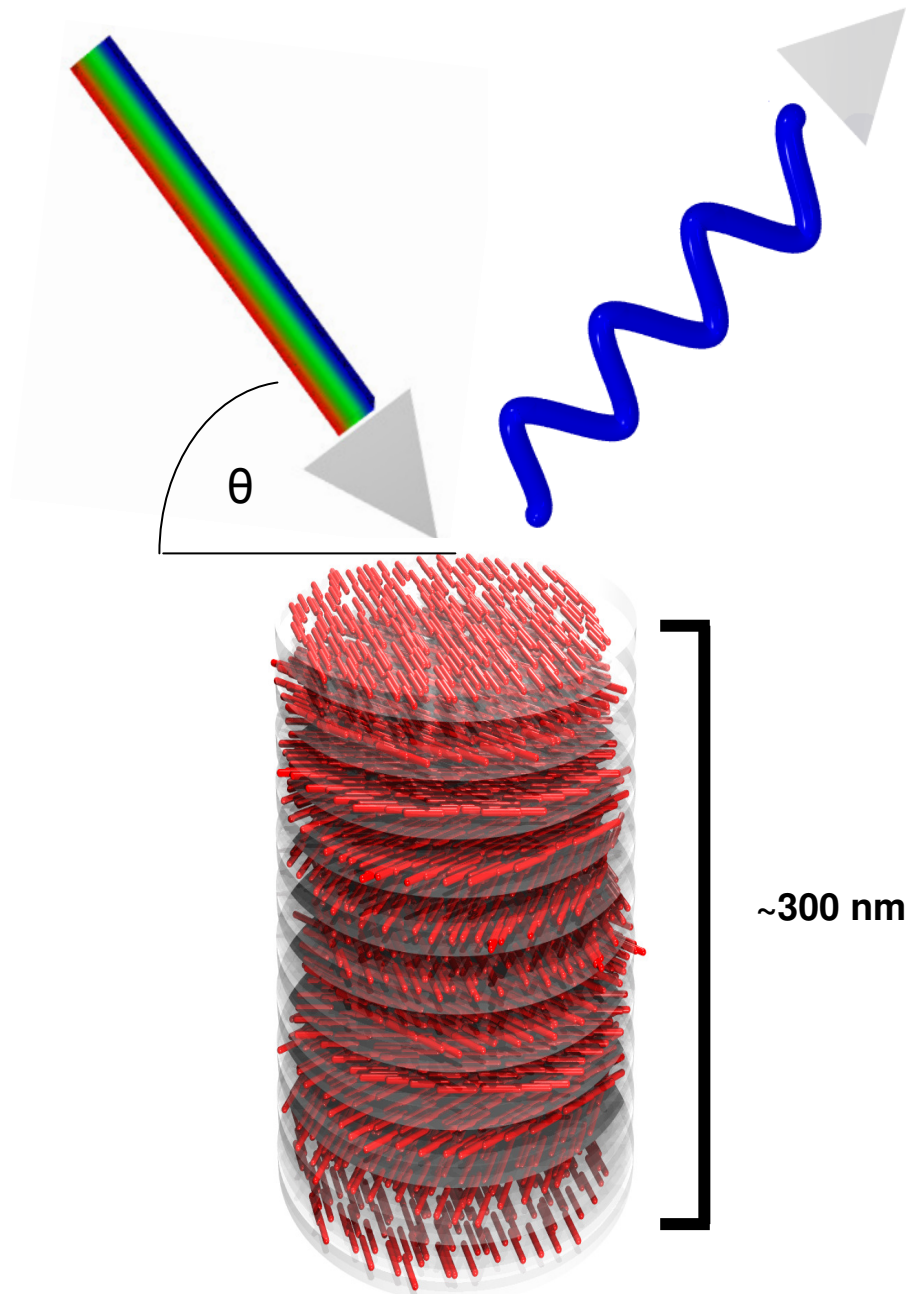


Figure 1-4. Schematic representation of diffraction from a left-handed CN-LC with P of ~ 300 nm. Left-handed circularly polarized blue light is selectively reflected while the remaining incoming light is transmitted.

1.3 Nanocrystalline Cellulose

1.3.1 Introduction to Cellulose

Cellulose is a simple linear polymer composed of D-glucose linked through 1,4-glycosidic bonds that acts as the major structural component of plant cell walls. In addition, cellulose is also produced by some bacteria, fungi, and in rare cases, by animals (e.g., tunicate). As a result, cellulose is the most abundant renewable material on Earth.^[45] In plants, cellulose is synthesized by the rosette terminal complex found in the plasma membrane and spun into microfibrils with diameters of ~2-20 nm that go on to form larger fibres that make up the plant cell wall.^[46] Cellulose microfibrils are held together through extensive intra- and interchain hydrogen bonding and are highly crystalline. Although cellulose can form several distinct crystalline structures, the cellulose found within plants is exclusively cellulose I, which consists of a parallel arrangement of cellulose chains (Figure 1-5).^[47] In plants, cellulose microfibrils are embedded within an amorphous matrix of predominantly lignin and hemicellulose, with compositions that vary significantly between different parts of plants and plant species. The lignocellulosic material found in plants has evolved to form a wide array of complex hierarchical structures with different physical properties depending on their chemical composition and precise nanostructure.^[48]

Due to its wide abundance, excellent mechanical properties, and stability, cellulose is one of the most ubiquitous materials used in modern society. Currently, the extraction of cellulose fibres from wood forms the basis of the pulp and paper industry and cellulose is the major constituent of many materials used in the textiles industry such as cotton and rayon. Although interchain hydrogen bonding makes cellulose fibres quite insoluble, cellulose can be derivatized to form soluble polymers such as cellulose acetate,

nitrocellulose, and hydroxypropyl cellulose, which are used for industrial applications ranging from membranes to explosives.

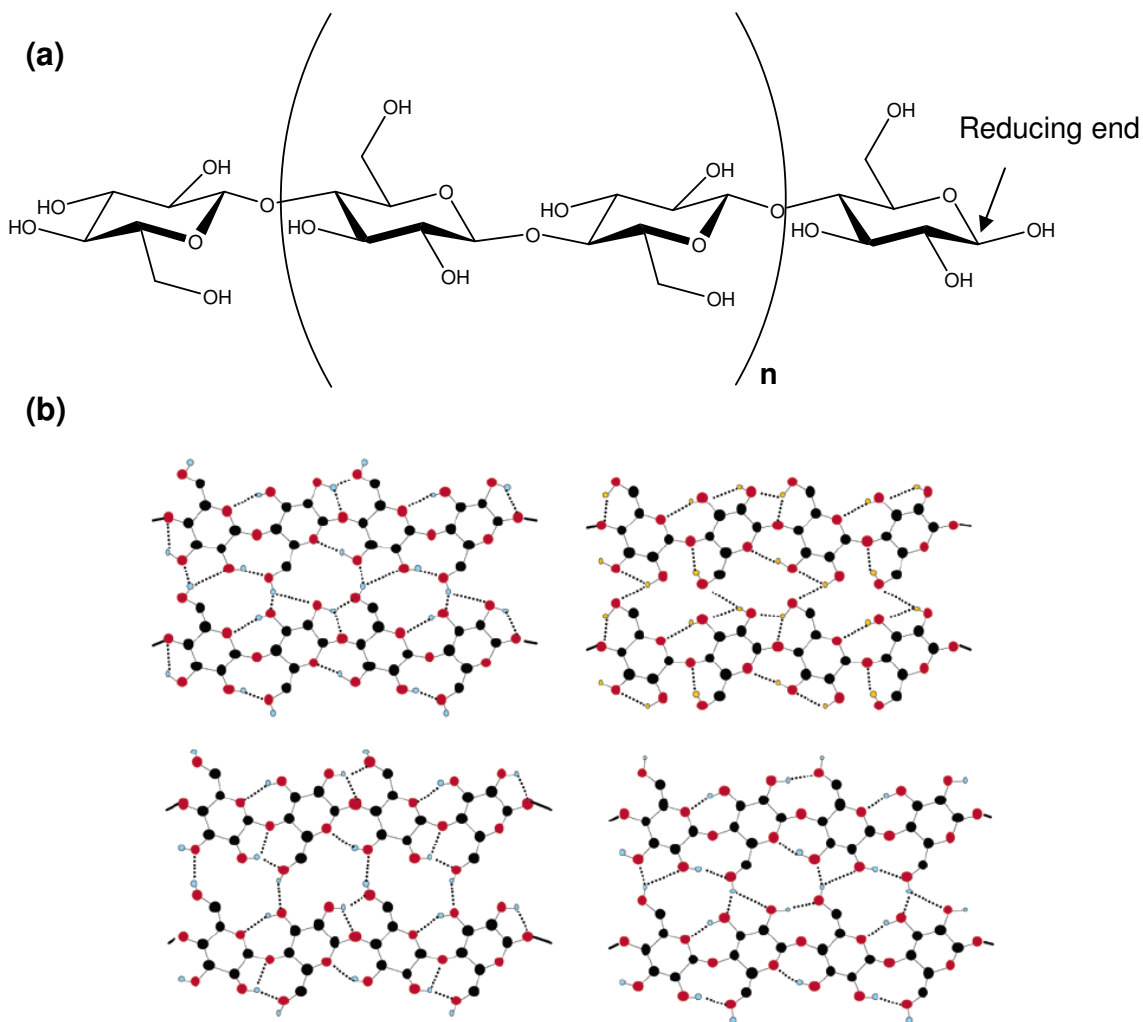


Figure 1-5. Molecular structure of cellulose. (a) Chemical structure of an individual cellulose polymer chain. (b) Possible hydrogen-bonding patterns for cellulose I found in plants. (b) was reproduced in part with permission from reference 47. Copyright 2004 American Chemical Society.

1.3.2 Introduction to Cellulose Nanomaterials

Cellulose nanomaterials show promise for a range of applications due to their excellent mechanical properties, biocompatibility, high surface areas, and unique self-assembly properties.^[49] Whereas the plant-derived cellulose fibres used in paper products and textiles have typical widths of 10-30 μm , and lengths ranging from several millimeters

to several centimeters, cellulose nanomaterials have widths below 100 nm and lengths ranging from ~100 nm to several microns depending on the cellulose source and method of preparation.^[49]

Cellulose nanomaterials can be produced by top-down approaches, which involve the isolation of fibrils or crystallites from extracted cellulose fibres, or by bottom-up methods that use bacteria to assemble them directly from glucose. As proposed by Klemm *et al.*,^[49] the resulting materials can be classified into three main categories depending on their method of preparation: nanocrystalline cellulose (NCC) is produced by acid hydrolysis of bulk cellulose, microfibrillated cellulose (MFC) is produced by the mechanical treatment of bulk cellulose, and bacterial nanocellulose (BNC) is synthesized directly by bacteria. These different preparation methods lead to cellulose nanomaterials with different sizes and morphologies. NCC consists of rigid, rod-like particles with diameters of ~5-30 nm and lengths of ~100-250 nm, when derived from plant sources (significantly larger particles can be obtained from other sources such as tunicate, algae, and bacteria). MFC and BNC, on the other hand, have more flexible fibrous morphologies with widths of 5-100 nm and lengths of several microns.

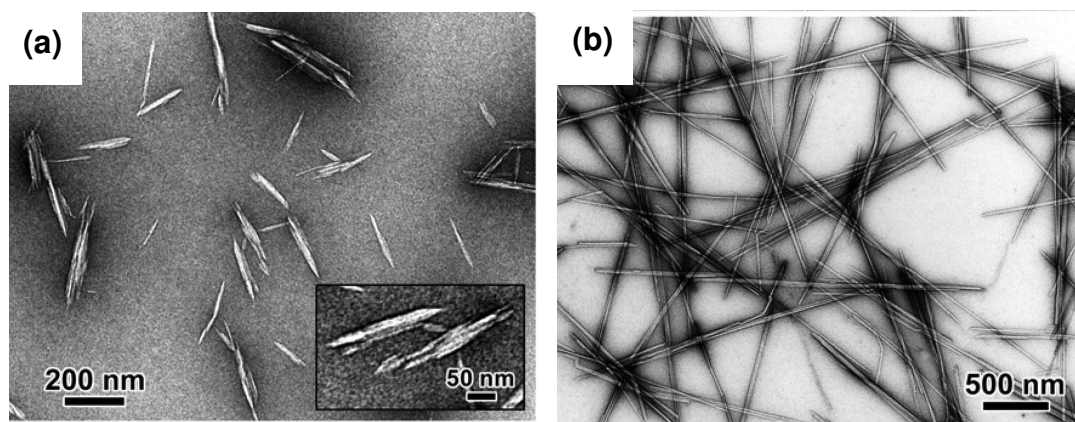


Figure 1-6. TEM micrographs of negatively stained NCC. (a) NCC prepared by sulfuric acid hydrolysis of cotton. (b) NCC prepared by sulfuric acid hydrolysis of tunicate. Reproduced in part with permission from reference 50. Copyright 2008 American Chemical Society.

1.3.3 Preparation of Nanocrystalline Cellulose

Cellulose microfibrils can be tens of microns long and contain nanocrystalline regions of cellulose I separated by amorphous regions that arise due to defects along the fibril axis.^[46] The amorphous regions of cellulose are more susceptible to acid catalyzed hydrolysis than the highly crystalline regions, and under the appropriate conditions, it is possible to selectively remove them and isolate rigid, spindle-shaped nanocrystalline cellulose particles. This is a kinetically controlled process and the size of the NCC particles depends on the exact conditions used (acid, concentration, temperature) and duration of the treatment.^[51] The dimensions of NCC also depend largely upon the cellulose source. Cotton and wood-based cellulose are ~50-80% crystalline and give relatively small NCC particles with diameters of 5-20 nm and lengths of 100-250 nm.^[46, 49-51] Other cellulose sources, such as tunicate and algae, can be more crystalline and give considerably larger, more polydisperse particles.^[46, 49, 50] After the acid hydrolysis reaction is quenched, the NCC is typically purified by centrifugation and dialysis to remove byproducts and excess acid.

The first synthesis of colloidal cellulose particles by controlled hydrolysis was

reported by Rånby in the early 1950s, who used sulfuric acid as the catalyst.^[52] When sulfuric acid is employed, sulfate ester groups are covalently attached to the surface of NCC particles giving them a negative charge in water. The charge of sulfated NCC causes electrostatic repulsion between the particles allowing them to form stable aqueous suspensions. Hydrochloric and hydrobromic acid can also be used to produce NCC, although this results in almost neutral NCC particles that are much harder to disperse and prone to flocculation.^[49] NCC prepared by HCl can be further treated, however, to introduce surface charge and improve its dispersibility. For example, TEMPO can be used to selectively oxidize the primary alcohol groups of NCC to carboxylic acids, thereby introducing a negative surface charge.^[53]

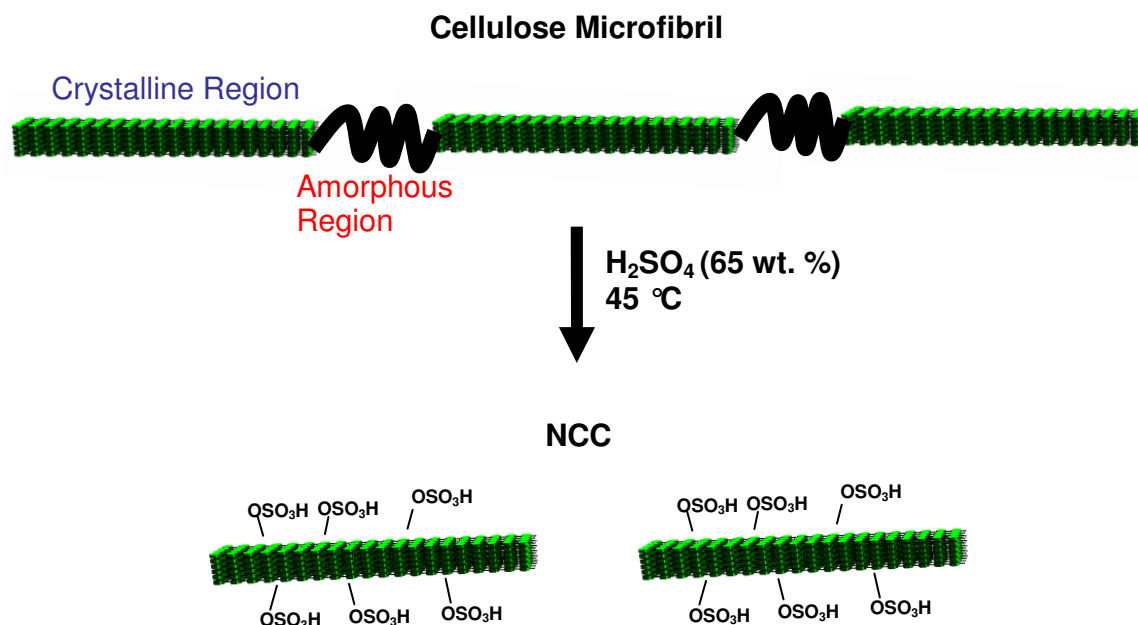


Figure 1-7. Schematic illustration of NCC synthesis by sulfuric acid hydrolysis.

1.3.4 Chiral Nematic Self-Assembly of Nanocrystalline Cellulose

Lyotropic chiral nematic phases of concentrated cellulose derivatives in water were first reported for hydroxypropyl cellulose,^[54] and have since been observed for

many additional cellulose derivatives in water and other solvents.^[40] The CN-LC phases observed for cellulose derivatives consist of dissolved polymeric species that can form either left- or right-handed structures depending on the substitution pattern, solvent, and temperature.^[49]

The chiral nematic phase of colloidal nanocrystalline cellulose suspensions was first reported in 1992 by Revol *et al.* and occurs at much lower concentrations (~3-6 wt. %) than what is seen for dissolved cellulose derivatives (ca. 40 wt. %).^[55] Below the critical concentration, NCC suspensions are completely isotropic, while above it, there exists a biphasic region where the chiral nematic phase is in equilibrium with the isotropic phase. The relative volumes of the two phases in this region depend on concentration, and at a high enough concentration, the isotropic phase disappears completely.^[56] Whereas left- and right-handed structures have been reported for dissolved cellulose derivatives, to date only left-handed structures have been observed for NCC.

There are many factors that influence the chiral nematic self-assembly of NCC. One of the major parameters that determines the anisotropic phase formation of NCC is the aspect ratio, with longer nanocrystals tending to gel before establishing a chiral nematic phase.^[49] Other factors that affect chiral nematic phase formation are ionic strength,^[56] the nature of the counterion,^[57] and the preparation conditions of the NCC.^[58] The anisotropic phase of NCC can also be influenced by external fields. Magnetic fields have been used to orient NCC, which may be useful for applications in NMR spectroscopy.^[59]

The slow evaporation of NCC suspensions can result in solid chiral nematic films.^[60] While the helical pitch of NCC suspensions is typically on the order of microns, the increase in concentration that occurs upon evaporation results in a decrease in pitch with the resulting films frequently reflecting visible wavelengths of light. A variety of

methods have been explored to influence the final helical pitch, and hence colour, of the dried films. These include the addition of salt (blue shift),^[61] ultrasonication of the suspension prior to drying (higher energies lead to a red shift),^[62] and drying temperature (increased temperature causes a blue shift).^[61] It should be noted that all of these methods used to influence the colours of NCC films must be performed prior to or during the preparation process. Once the films are formed, their optical properties are essentially locked in place.

1.3.5 Mechanisms for NCC Chiral Nematic Phase Formation

The phase separation of rod-shaped colloidal particles above a critical concentration was first explained by Onsager.^[63] The underlying reason for this behaviour relates to the competition between orientational entropy, which favors disorder, and the entropy effect associated with excluded volume, which favors orientational ordering. In the case of perfectly rigid, neutral particles, the critical concentration simply depends on the aspect ratio L/D . For polyelectrolyte particles, electrostatic interactions play an important role and certain modifications must be made to Onsager's original theory.^[64] One of the major differences for charged systems is that there is an increased effective diameter (D_{eff}) of the particles due to electrostatic repulsion, which depends on the size of the electric double layer and hence on the ionic strength (i.e., D_{eff} decreases with increasing ionic strength).

It has been proposed that NCC rods have a screw-like shape that gives rise to their chiral interactions.^[53, 65, 66] This hypothesis was supported by neutron diffraction experiments on chiral nematic NCC suspensions that showed closer packing along the direction of the helical axis than in the nematic planes perpendicular to it.^[65] These results are consistent with a model of screw-shaped particles that pack with interlocked

threads and grooves so as to minimize interparticle distances (Figure 1-8).^[67] In the same study, it was also postulated that the electrical double-layer of charged NCC particles may take on a screw shape that facilitates chiral interactions over larger distances in dilute suspensions.

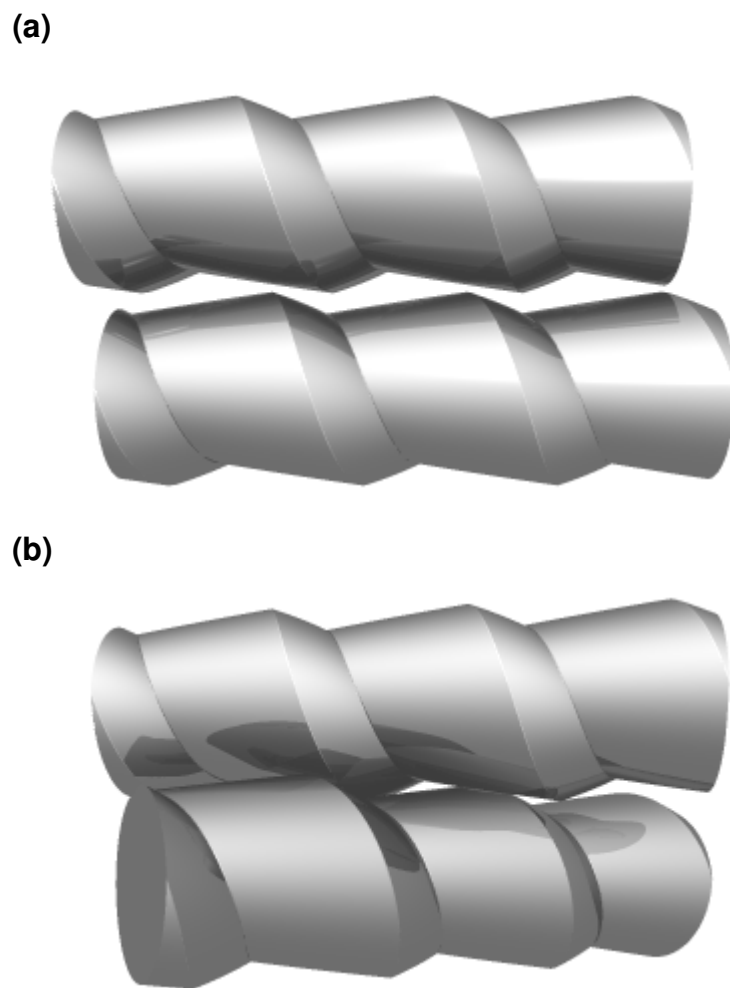


Figure 1-8. Different packing arrangements of screw-shaped rods. (a) Parallel arrangement. (b) Chiral arrangement, which can facilitate closer packing.

Although it was originally supposed that a chiral distribution of charge on the surface of NCC was required for chiral nematic phase formation,^[55] various results have indicated that surface charge is not necessary. For example, NCC coated with surfactant can form a chiral nematic phase in non-polar solvents like cyclohexane, where it is

unlikely that surface charge plays a major role.^[68] Although neutral NCC particles prepared by hydrochloric acid hydrolysis do not normally form a CN phase in water, they can form one after PEG surface grafting.^[53] The PEG grafting in this case simply provides steric stabilization and it appears that the inability of HCl-hydrolyzed NCC to form a CN phase may simply be due to its poor colloidal stability. As would be expected, the CN-LC phase of this neutral NCC is insensitive to changes in salt concentration. These results support the notion that the screw shape of NCC is the most important factor governing the chiral interactions between particles.

While surface charge may not be required for NCC to form a chiral nematic phase, it does play a large role in influencing CN-LC behaviour when it is present. For sulfated NCC, increases in ionic strength result in an increase in the critical concentration required for the CN-LC phase to form.^[56] This is due to a decrease in the effective volume of the particles at higher ionic strengths, which in turn reduces the favorable excluded volume entropy associated with forming an anisotropic phase. Increased electrolyte concentrations also cause a decrease in the helical pitch of the chiral nematic phase, which implies that the chiral interactions are greater at higher ionic strength. In fact in one study using bacterial-derived sulfated NCC, it was found that a chiral nematic phase could only form after an electrolyte was added.^[66] The authors concluded that the larger electrostatic repulsion and effective size of the particles without added electrolyte obscures their chiral morphology resulting in a nematic phase. By adding electrolyte, the electrostatic interactions are shielded thereby reducing D_{eff} and increasing the chiral interactions between particles. In contrast, high power sonication of NCC causes an increase in helical pitch due to the removal of tightly bound surface cations, which decreases charge shielding.^[62]

1.3.6 Potential Applications Involving NCC

The mechanical properties of amorphous polymers can often be improved through the addition of nanocrystalline fillers; the fact that NCC has excellent strength (comparable to that of steel) and a high surface area make it particularly attractive for this application.^[49] Different methods have been used to incorporate NCC into polymer matrices including simple solution casting, compression molding or extrusion, and in situ polymerization. The hydrophilicity of NCC makes it easiest to process in combination with water-soluble polymers like starch^[69] and polyvinyl alcohol.^[70] In these cases, NCC was found to considerably improve the mechanical properties of the materials. There is also considerable interest in combining NCC with hydrophobic thermoplastics, which has motivated the development of surface functionalization techniques to make NCC more compatible with these systems. Examples of surface functionalization reactions that have been successfully carried out on NCC include esterification, silylation, and polymer grafting reactions.^[46]

NCC has several properties that make it appealing for biomedical applications.^[71] While toxicity has been a concern for many nanomaterials, studies have shown that NCC is non-toxic and environmentally benign.^[71, 72] NCC particles are also readily dispersible in aqueous systems and their surface hydroxyl groups make them relatively easy to functionalize. One potential application for NCC is in drug delivery systems where it can be used to bind therapeutics through surface interactions and release them in a controlled manner. Electrostatic interactions have been used to facilitate the delivery of cationic drugs like doxorubicin and tetracycline, and by adsorbing surfactants to the surface of NCC, hydrophobic drugs were also delivered.^[73] NCC has also been used to image cells by conjugating it with fluorescent dyes.^[74] An interesting feature of NCC for these types of applications is that its ability to enter cells strongly depends on surface charge:

positively-charged NCC (which can be produced through surface functionalization)^[75] readily enters cells, while negatively-charged NCC does not.^[76]

NCC has been used as a template for different inorganic materials that can be used in a variety of applications. NCC is an effective host for the templation/immobilization of nanoparticles, where it can improve the nucleation of monodispersed particles and prevent aggregation.^[71] Silver NPs templated by NCC have been shown to have antimicrobial properties^[77] and to be useful for the electrochemical detection of DNA.^[78] Gold and palladium NPs formed on NCC are effective catalysts for several reactions including hydrogenation, Heck couplings, and the reduction of nitro groups.^[79, 80] NCC has also been used to template metal oxide nanostructures including shape-controlled TiO₂ cubes^[81], porous TiO₂,^[82] and porous silica.^[83]

1.4 Mesoporous Materials

1.4.1 Overview

Mesoporous materials are defined by IUPAC as having pores between 2-50 nm.^[84] As the name implies, this is an intermediate pore size regime, lying in between micropores (<2 nm) and macropores (>50 nm). Mesopores provide an excellent compromise in terms of being small enough to give high specific surface areas (>1000 m²/g in many cases) while being large enough to allow access to molecules with a range of different sizes. For specific applications involving porous materials, it is important to be able to precisely tune their pore size, pore structure, surface chemistry, and composition. Several key breakthroughs in the past 20 years have allowed mesoporous materials to be extremely versatile in this regard. In the following sections, strategies for

controlling these parameters and some specific applications of mesoporous materials will be discussed.

1.4.2 Liquid Crystal Templating

In 1992, Kresge and coworkers reported that cationic surfactants could be used to template mesoporous silica with well-defined hexagonal or cubic pore systems (termed MCM-41 and MCM-48, respectively).^[85, 86] This discovery represented a significant breakthrough; although mesoporous materials had been known for decades, they invariably had disordered structures with broad and irregular pore size distributions. In their original paper, Kresge *et al.* proposed that the individual mesopores of MCM-41 were templated by surfactant micelles while the overall hexagonal structure was determined by their further self-assembly into a lyotropic liquid crystalline phase. This allowed for both the pore size and overall structure to be tailored through simple changes in the synthetic procedure. The liquid crystal template approach for synthesizing mesoporous materials proved to be extremely versatile, and within a fairly short time period it was expanded from cationic surfactants to other templates (e.g., block copolymers, anionic surfactants, biological polymers, and colloidal particles),^[83, 87-90] as well as to inorganic materials other than silica.^[16] This has given access to mesoporous materials with a range of different compositions, pore sizes, and ordered structures.

In a typical liquid crystal templating procedure, an inorganic precursor is enriched and condensed within the aqueous domains of an organic lyotropic liquid crystal to form a composite material; the organic template is subsequently removed through thermal decomposition or solvent extraction to yield a mesoporous solid. Two generalized mechanistic pathways for liquid crystal templating are possible depending on the conditions employed. In the first pathway, the inorganic species cooperatively interacts

with the template during condensation and strongly influences its self-assembly into an ordered structure. In the second pathway, a pre-established lyotropic liquid crystal acts to direct the assembly of the inorganic species.^[91] The first mechanism explains the formation of ordered structures at mesogen concentrations that are below what is normally necessary for a liquid crystal phase to form, as was true for the original MCM-41 synthesis.^[92]

The cooperative self-assembly of inorganic species and organic templates requires favorable interactions between the two components, and the reaction conditions must be carefully selected to facilitate this. In the case of ionic surfactants, four different possibilities for favorable interactions can be considered: S^+I^- , S^-I^+ , $S^-M^+I^-$, and $S^+X^-I^+$ (where S = surfactant, I = inorganic species, M^+ = metal cation, and X^- = anion).^[87] In the first two cases (S^+I^- and S^-I^+), favorable electrostatic interactions occur directly between the surfactant and inorganic species to facilitate self-assembly. In the latter two cases ($S^-M^+I^-$ and $S^+X^-I^+$), counterions are required to mediate interactions between like-charged species. In many instances the charge of the inorganic species can be adjusted depending on the pH. In addition to ionic surfactants, neutral surfactants and block copolymers can also be used for cooperative self-assembly (e.g., SBA-15 mesoporous silica synthesized using P123 triblock copolymer as a template).^[88, 89] These syntheses are typically carried out under strongly acidic conditions where the interactions are thought to be mediated by double-layer hydrogen bonding of the type $S^0H^+X^-I^+$.

One of the limitations of the cooperative self-assembly pathway is that it can be hard to control the morphology and long range ordering of the resulting materials.^[93] In addition, because the self-assembly process is a complex balance between many different factors, it can be difficult to predict structures a priori.^[94] The use of a pre-established lyotropic liquid crystal phase (sometimes called true liquid crystal templating) as a

template for mesoporous silica was first demonstrated by Attard *et al.* by using high concentrations of nonionic surfactants.^[95] This approach has the advantages that the nanostructure is more easily predicted a priori and morphologically controlled materials with long-range ordering can be readily obtained.^[94] For example, transparent monolithic structures can be formed by condensing a silica precursor around concentrated block copolymer solutions with pre-established ordering.^[96, 97]

An extension to true liquid crystal templating is evaporation induced self-assembly (EISA), which is a very useful technique for making ordered mesoporous films.^[98] In EISA, the template and inorganic precursor are mixed at low initial concentrations to form a homogeneous solution (below the critical concentration for ordered phase formation) and allowed to self-assemble during the drying process. As the solvent evaporates, the concentration of template increases to the point where it forms a liquid crystal phase and directs the organization of the inorganic precursor. It is generally important that inorganic polymerization is suppressed to some extent during EISA so that self-assembly can proceed unimpeded and give films with long-range liquid crystal ordering. In the case of silica, this can be achieved by operating near the isoelectric point of colloidal silicate species (pH ~2). The hybrid material can be further condensed after drying (e.g., through aging, exposure to acid or base catalyst, or thermal treatment) to further solidify the structure.

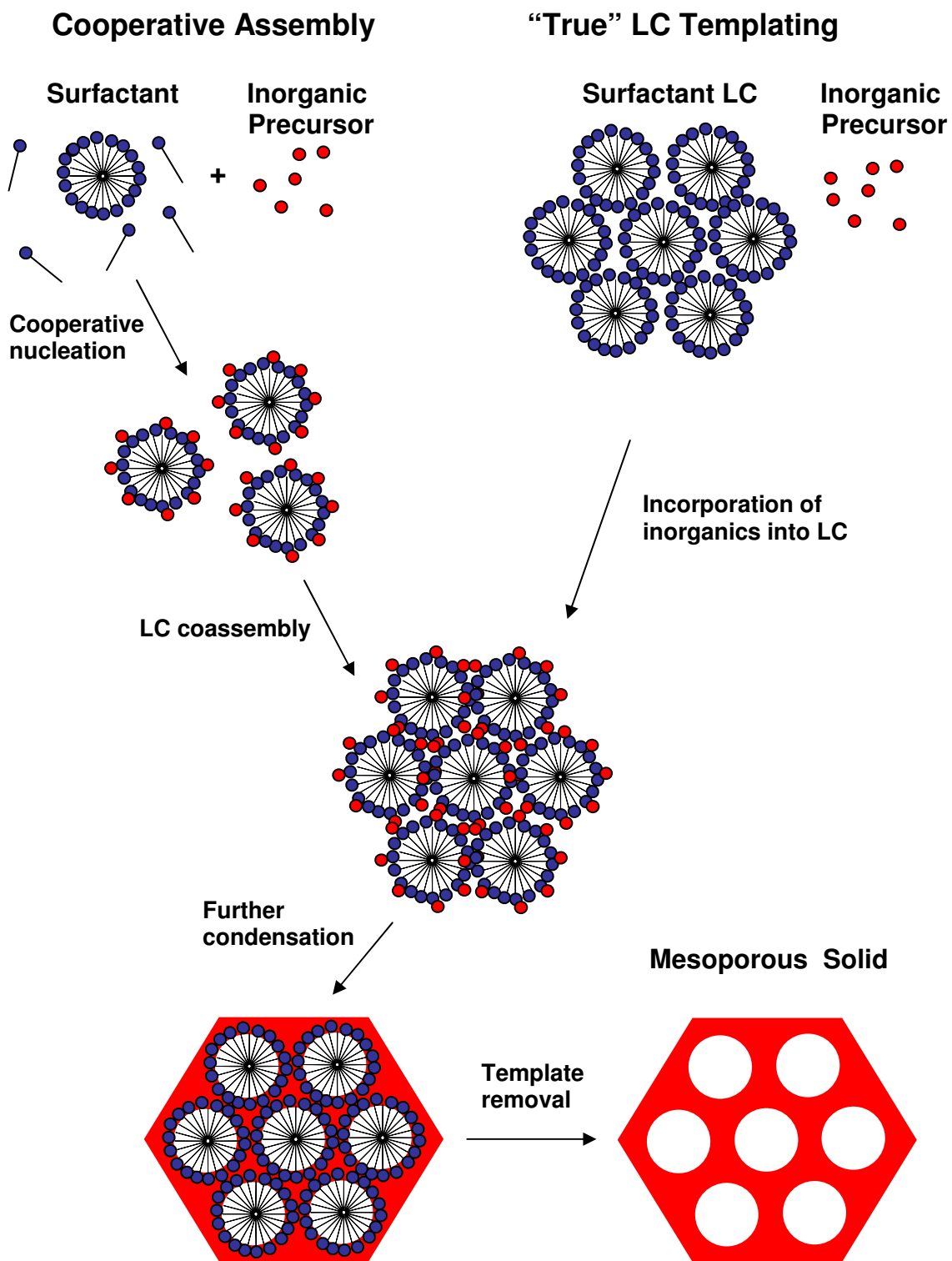


Figure 1-9. Synthesis of ordered mesoporous materials by cooperative self-assembly and “true” liquid crystal templating pathways.

1.4.3 Mesoporous Silica

As described above, mesoporous silica was the first ordered mesoporous material prepared by template synthesis. Although many other types of mesoporous materials have now been synthesized, silica has been by far the most heavily studied for reasons that include its relative ease of preparation, chemical and physical stability, and tunable surface chemistry. These properties have led to mesoporous silica being explored for a wide range of applications including catalysis,^[99] chromatography,^[100] environmental remediation,^[101] sensing,^[102] and drug delivery.^[103]

Mesoporous silica is typically synthesized under aqueous conditions through a sol-gel process that starts with an alkoxy silane, such as tetraethyl or tetramethyl orthosilicate (TEOS and TMOS, respectively). The alkoxy silane undergoes hydrolysis and poly-condensation reactions to form colloidal species that eventually condense around the organic template to form a solid silica network. The template can then be removed through calcination or solvent extraction to give mesoporous silica. Silica sol-gel chemistry is very versatile and can be carried out over a wide range of different conditions (e.g., pH, concentrations, solvent mixtures, and temperatures). This has allowed mesoporous silica to be synthesized with many different structures (e.g., hexagonal, cubic, lamellar, wormlike), pore sizes (~2-30 nm) and morphologies (e.g., powders, nanoparticles, films, monoliths, fibres), by simply using different templates and reaction/processing conditions.^[104]

One of the advantages of mesoporous silica materials is that their surface chemistry can be easily modified. This arises from the presence of free silanol groups on the mesopore surface that readily react with trialkoxyorganosilanes, trichloroorganosilanes, and other chemicals that can be used to graft organic groups onto the pore surface.^[101, 105] The introduction of organic functionality can be used for many

different purposes ranging from simply changing the polarity of the surface to introducing sites for catalysis, heavy metal scavenging, biomolecule detection, and drug loading.^[106] Along with the post-synthetic grafting of organic groups, it is also possible to incorporate them by co-condensing a trialkoxyorganosilane with a tetraalkoxysilane during self-assembly.^[107-109] This one-pot approach has the advantages that it requires fewer steps, typically results in a more even distribution of organic groups, and avoids the pore blocking that can sometimes occur with post-synthetic grafting. However, this method also has the disadvantage that it can result in less ordered mesostructures with decreased surface areas and pore volumes.^[106]

1.4.4 Mesoporous Organosilica

An alternative approach for introducing organic functionality into ordered mesoporous silica by using bridged precursors of the general type $(R_3O)_3Si-R'-Si(OR_3)_3$ was reported by three research groups in 1999.^[110-112] The synthesis of these materials follows the same basic sol-gel process that occurs for pure silica materials, which allows for the same types of templates and conditions to be employed. The resulting materials, frequently referred to as PMOs (periodic mesoporous organosilicas), have organic functionality built in as an integral component of the three dimensional cross-linked structure. This direct incorporation of organic groups into the structure guarantees a uniform, high loading of organic groups within the material, which is often difficult to achieve using other techniques. It also minimizes pore blockage and allows for physical and materials properties to be tuned along with the surface chemistry within the pores.
[113]

The first reports of PMOs involved small organic functional groups like methylene ($-CH_2-$), ethylene ($-CH_2CH_2-$), and ethene ($-CH=CH-$). Even these relatively

simple bridging groups can lead to unique properties compared to mesoporous silica such as increased hydrothermal stability, improved mechanical properties, and the ability to perform various chemical reactions within the mesopores.^[114, 115] The molecular ordering within the walls of a PMO can also be significantly influenced by the choice of the organic bridging group. For example, in contrast to the amorphous walls found in mesoporous silica, PMOs synthesized with bridging phenylene groups can have highly crystalline walls.^[116] PMOs have now been synthesized with a great diversity of bridging groups with many different applications in mind.^[117] These include chiral groups for use in chromatography and catalysis,^[118-121] electroactive groups,^[122, 123] and photoactive groups for applications involving photoluminescence and light harvesting.^[124, 125] It should be noted that there are some limitations with respect to synthesizing PMOs. In the case of larger bridging groups it is often not possible to form a highly porous and ordered material without diluting the precursor with another silica source (e.g., TEOS or bis(triethoxysilyl)ethane).^[126] This of course limits the amount of the desired functional group in the material and can lead to phase separation. Nonetheless, bridging units as large as C₆₀ fullerene have been incorporated into PMOs by using this dilution approach.^[127]

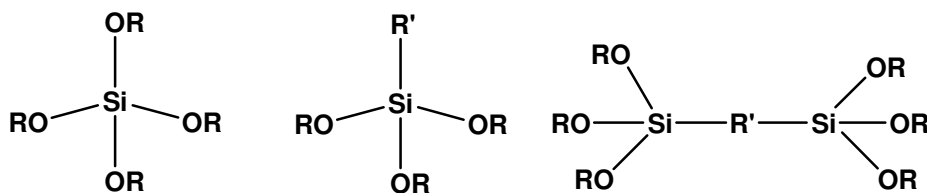


Figure 1-10. Chemical structures of typical alkoxy-silanes used to synthesize mesoporous silica and organosilica materials. R = alkyl group (typically –CH₃ or –CH₂CH₃). R' = any organic group.

1.4.5 Mesoporous Carbon

Mesoporous carbons are useful for many applications, including catalysis and energy storage, due to their extremely high surface areas ($>1400 \text{ m}^2/\text{g}$ in some cases) and excellent chemical and physical properties.^[128] The first examples of ordered mesoporous carbon were reported in 1999 by casting replica structures of MCM-48 mesoporous silica.^[129, 130] The resulting mesoporous carbon, referred to as CMK-1, has a similar cubic pore structure as the silica template. This approach, referred to as hard templating or nanocasting, involves the impregnation of a mesoporous host with a suitable precursor, followed by polymerization of the precursor, and dissolution of the template.^[131] In the case of carbon, a simple organic molecule like sucrose can be used as the precursor, which is then polymerized into a carbonaceous structure within the host by heating it (typically $\sim 900 \text{ }^\circ\text{C}$) under an inert atmosphere. While most mesoporous carbons have amorphous wall structures, it is possible to make them more graphitic by selecting an appropriate carbon precursor, such as acenaphthene.^[132] Mesoporous silica is an ideal material to use as a hard template for carbon since it is thermally stable and can be selectively removed using either HF or strong base. After removing the silica template, the resulting carbon material has an inverse structure compared to the silica template; the space that the silica walls previously occupied become the pores of the mesoporous carbon.

In order for the carbon to form a stable mesoporous structure, the template must contain three-dimensionally connected porosity.^[133] For example, when MCM-41 is used in place of MCM-48 as a hard template, a disordered microporous material is obtained.^[134] This is because the hexagonally arranged mesopores of MCM-41 are not interconnected and the carbon that forms within them essentially consists of independent rods. In contrast, a hexagonal mesoporous carbon (CMK-3) can be synthesized from

hexagonal SBA-15 mesoporous silica.^[135] The reason for this is that there are micropores within the walls of SBA-15 that connect the mesopores, allowing the carbon to form a stable three-dimensional structure.

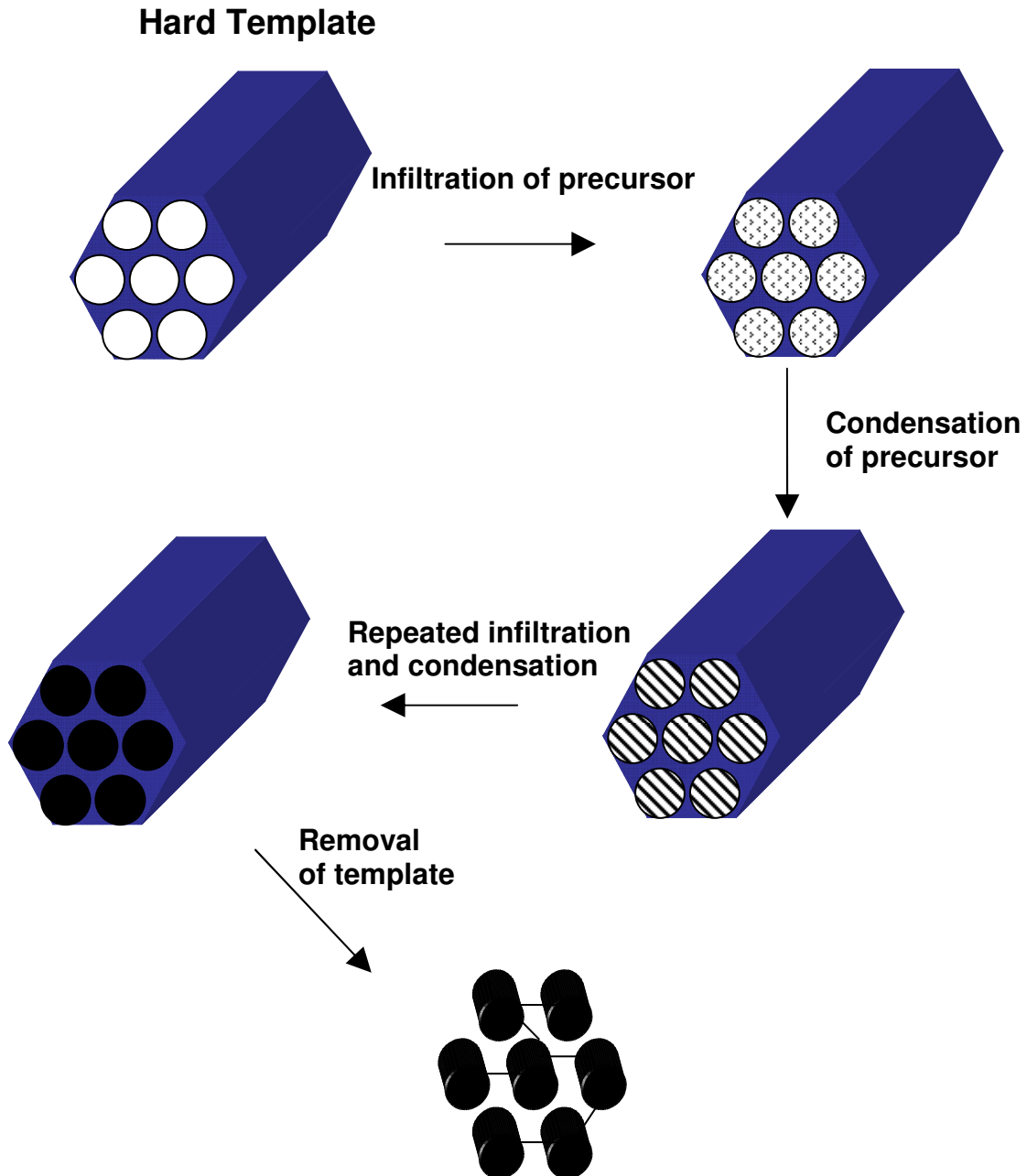


Figure 1-11. Scheme outlining the synthesis of mesoporous carbon through hard templating.

Along with the hard templating approach, methods have been developed to synthesize mesoporous carbon through direct liquid crystal templating.^[136] This has been achieved by using EISA to assemble a polymerizable carbon precursor (e.g., low molecular weight phenolic resin) around block copolymer lyotropic liquid crystals. After EISA, the phenolic resin can be thermally polymerized without disrupting the mesostructure. The template is then removed to give a mesoporous polymer that can be converted to mesoporous carbon by heating it under inert atmosphere.

The physical properties of mesoporous carbons make them excellent candidates for supercapacitor electrodes.^[137] Supercapacitors are an emerging class of energy storage device that fall in between conventional capacitors and batteries, having higher energy densities than the former and higher power capabilities than the latter.^[138] Supercapacitors can be classified into two categories depending on their charge storage mechanism: electrical double-layer capacitors (EDLCs) store charge based on the formation of an electrical double-layer at the electrode/electrolyte interface, while pseudo-capacitors store charge through fast and reversible redox reactions that occur near the electrode surface. High surface area carbons are the prototypical example of EDLCs while materials that show pseudo-capacitance include conducting polymers and transition metal oxides. On their own, mesoporous carbons can show high specific capacitances (up to ~200 F/g) based entirely on electrical double-layer formation.^[139] Pseudo-capacitive materials can also be deposited onto mesoporous carbon supports to increase their performance.^[140] In doing so, the conductivity, mechanical stability, and accessible surface area of the pseudo-capacitive material can also be enhanced.^[137, 141] In addition to supercapacitors, mesoporous carbon has shown potential as an electrode material in other energy storage devices, such as lithium ion batteries.^[142]

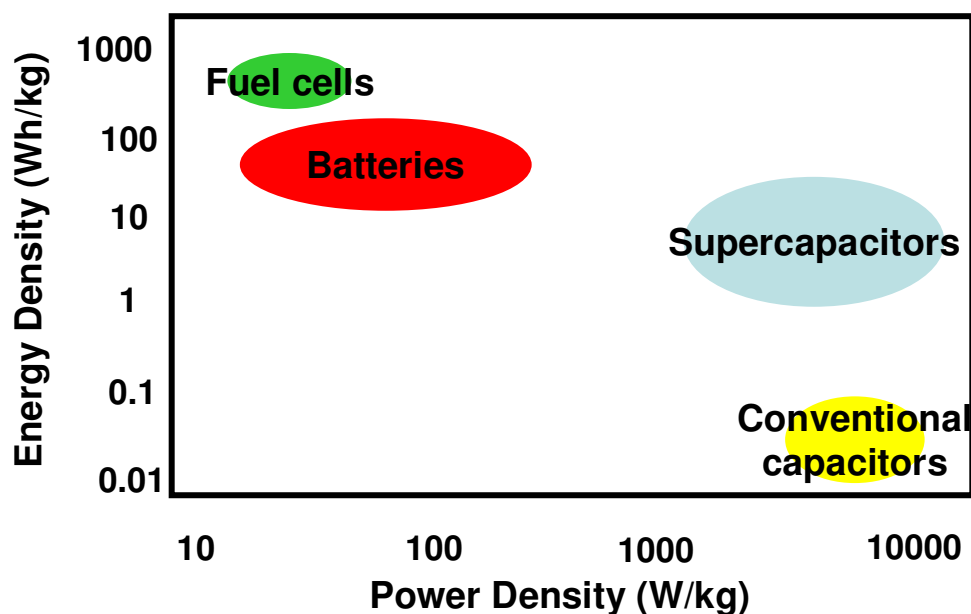


Figure 1-12. Ragone plot comparing performance of different energy storage devices.

1.4.6 Other Mesoporous Materials

In addition to silica, organosilica, and carbon, ordered mesoporous materials have been synthesized with a wide variety of other compositions. At first glance it might seem that the general liquid crystal templating approach used for silica should be applicable to many other metal oxides; unfortunately, it is in fact much more difficult to control the hydrolysis and condensation of most metal alkoxides, which often leads to poor structural ordering.^[131] However, by using modified sol-gel procedures that involve either adding chelating agents to control condensation or coordinating transition metals to surfactants prior to self-assembly, it has been possible to form different mesoporous transition-metal oxides (e.g., TiO_2 , ZrO_2 , Ta_2O_5 , Nb_2O_5) that can have many interesting properties (e.g., semiconductivity, magnetism) not observed for silica.^[143] Although the order in these materials is generally not as high as in mesoporous silica, they can still have high specific surface areas and narrow pore size distributions. Another method that has been used to synthesize mesoporous metal oxides is to use metal chloride precursors with block

copolymer templates in non-aqueous media, which slows down condensation and hinders subsequent crystallization.^[144] This approach gives mesoporous materials with thick, mostly amorphous, inorganic walls embedded with nanocrystalline domains. Forming highly crystalline materials using sol-gel self-assembly methods has proven to be difficult, since crystallization tends to disrupt mesoscopic ordering. One way to overcome this limitation is to use block copolymers to direct the self-assembly of preformed nanocrystals, which has been used to make mesoporous, nanocrystalline metal oxides including CeO₂, SnO₂, and TiO₂.^[145-147]

Other mesoporous inorganic materials have been prepared through liquid crystal templating. Some of the more well-studied examples are metal chalcogenides, which are often prepared by linking metal clusters (e.g., [MQ₄]⁴⁻ or [M₄Q₁₀]⁴⁻ with different metal salts in the presence of cationic surfactants.^[148, 149] Mesoporous semiconducting germanium has also recently been synthesized through self-assembly.^[150, 151] It is expected that these materials will show interesting quantum confinement effects dependent on the thickness of their walls. Mesoporous metal films have been synthesized by reducing metal salts around pre-formed lyotropic liquid crystals. This approach was first developed for platinum,^[152] but has been extended to other metals including Sn, Pd, Co, and Ni.^[149]

The hard templating approach that was originally developed for mesoporous carbon can also be used to synthesize many other mesoporous materials ranging from metal oxides to polymers.^[131, 153] Reaction conditions that might normally disrupt self-assembly can be used with hard templates, since their structures are preformed and fixed. As described above, silica is an excellent hard template in many cases since it is thermally stable and can be readily dissolved. In cases where the selective removal of

silica is not possible (e.g., the synthesis of some other oxides), mesoporous carbon can be used since it can be removed through combustion.^[154]

1.5 Goals and Scope of the Thesis

The premise of this thesis is the development of new mesoporous materials based on the self-assembly of nanocrystalline cellulose (NCC). This takes advantage of two important properties of NCC: its nanometer dimensions and its lyotropic liquid crystalline behaviour. There are several reasons why I chose to focus on NCC as a template. First, although many templates have been used to form mesoporous materials with different ordered structures, none had been reported with chiral nematic order. Developing an approach to access such materials could be of considerable interest given the numerous applications for both porous photonic crystals and chiral mesoporous materials. Second, the stable nanometer dimensions and hydrophilicity of NCC suggested that the standard sol-gel approaches used to synthesize templated mesoporous materials should also be applicable to it. Lastly, NCC is an extremely abundant and renewable material, it is environmentally safe, and its synthesis is currently in the process of being scaled up to industrial quantities. New technologies developed with NCC therefore have the potential to see real-world applications.

In this thesis, I present the first examples of chiral nematic mesoporous materials. These new materials have high specific surface areas, chirality, and photonic properties, and are synthesized using a simple self-assembly based approach. In Chapters 2-5, I report the synthesis and characterization of four different types of chiral nematic materials, all of which are templated either directly or indirectly by NCC. In Chapter 2, I describe my efforts to prepare and understand the properties of chiral nematic

mesoporous silica, which is the first material that I was able to successfully template with NCC. In Chapter 3, I detail the expansion of the approach used in Chapter 2 to a related class of materials, namely chiral nematic mesoporous organosilica. In Chapter 3, methods to control the porosity of both organosilica and silica materials templated by NCC are also described. In Chapter 4, the use of chiral nematic mesoporous silica as a hard template is explored for the synthesis of TiO_2 . In Chapter 5, I report the use of NCC to form chiral nematic mesoporous carbon and describe its potential application for energy storage devices. Finally, in Chapter 6, I put forward some general conclusions and outline future directions for this work.

Chapter 2

Mesoporous Silica Films with Tunable Chiral Nematic Structures*

2.1 Introduction

Lyotropic liquid-crystal templating is a powerful tool for synthesizing materials that have periodic nanostructures with features on the order of 2-50 nm. The prototypical example of this approach is the use of surfactants to template mesoporous silica, giving access to high surface area materials with well-ordered pore structures (e.g., MCM-41, MCM-48, SBA-15).^[86-88] This process takes advantage of the self-assembly of surfactant molecules into micelles that can further organize into a liquid crystalline (LC) phase. The surfactant LC phase then directs the condensation of a silica precursor through a sol-gel process to form an organic-inorganic composite material.^[91, 95] The removal of the organic template by thermal decomposition or solvent extraction generates mesoporous silica with a pore structure governed by the liquid crystalline organization of the surfactant and a pore diameter that is determined by the size of the surfactant micelles. Kresge and co-workers first demonstrated this approach in 1992 by using cetyl trimethylammonium bromide (CTAB) to template highly ordered hexagonal mesoporous silica that was coined MCM-41.^[85, 86] Since this landmark discovery, various surfactant templates including small molecule surfactants (both ionic and non-ionic) and polymeric surfactants (e.g., diblock and triblock copolymers) have been used to synthesize mesoporous silica with different pore diameters and pore structures.^[88, 89, 144, 155]

* Portions of this chapter have been previously published as: K. E. Shopsowitz, H. Qi, W. Y. Hamad, M. J. MacLachlan, "Free-Standing Mesoporous Silica Films with Tunable Chiral Nematic Structures." *Nature* **2010**, 468, 422-425.

Chirality at the molecular level is manifest in diverse biological structures, such as polysaccharides, proteins, and DNA, and is responsible for many of their unique properties. Introducing chirality into porous inorganic solids is an important endeavour for developing new types of materials that could be useful for chiral separation, stereospecific catalysis, chiral recognition (sensing), and photonic materials.^[156-159] Chirality has been introduced into hexagonal mesostructures through the use of chiral surfactant templates.^[160-162] Biological molecules could present an interesting alternative to surfactants as chiral templates due to their inherent enantiopurity and ability to form unique liquid crystal phases.

Photonic crystals are materials with periodic refractive indices that repeat on the length scale of the wavelengths of visible light.^[27] The solution of Maxwell's equations for these materials results in a range of frequencies of light that cannot propagate within the photonic crystal; light that falls within this range, termed the photonic band gap, is selectively reflected by the material giving rise to so-called structural colour. Introducing porosity into photonic crystals provides a means to tune their optical properties by infiltrating the pores with various guests. Mesoporous photonic crystals have been synthesized using a variety of approaches (e.g., electrochemical etching of silicon, alternate deposition of porous silica and titania layers, self-assembly of mesoporous silica spheres to form opals) and show promise for applications involving sensing, photovoltaics, and light emission.^[34, 35, 163-168] The self-assembly of lyotropic liquid crystals has been used to introduce mesoporosity into photonic crystals, however, multiple additional steps are generally required to build up the periodic photonic structure.^[169, 170] The development of a lyotropic liquid crystal system that could simultaneously template mesoporosity and a photonic structure would therefore be highly desirable.

Chiral nematic liquid crystals (CN-LCs) consist of rod-shaped molecules or particles arranged in a long-range helical structure that gives rise to a periodically changing refractive index with a repeating distance of a half helical pitch ($P/2$). When this distance is similar to the wavelengths of visible light, CN-LCs behave as one-dimensional photonic crystals that selectively reflect circularly polarized light with the same handedness as the chiral nematic helical structure.^[44] Thermotropic CN-LC phases were first discovered for cholesterol derivatives in the 1800s but have now been studied extensively for many different systems. These materials display temperature and electric field dependent optical properties and have been used for various applications such as thermometers, polarizing mirrors, reflective displays, and lasers.^[171-173] Lyotropic CN-LC phases have been observed for several chiral, rod-shaped biomolecules including cellulose, DNA, and chitin.^[40, 55, 174, 175] In nature, the solid-state chiral nematic organization of chitin results in the brilliant iridescent colours of beetle exoskeletons.^[22]

Stable nanocrystals of cellulose may be obtained by acid-catalyzed hydrolysis of bulk cellulose.²⁰ In water, suspensions of nanocrystalline cellulose (NCC) organize into a chiral nematic phase that can be preserved upon air-drying, resulting in iridescent films.^[55, 59, 60] This property, along with the nanometer dimensions of NCC, make it an interesting potential template for mesoporous photonic crystals. Researchers have previously attempted to use the chiral nematic phase of various cellulosic materials to template mesoporous solids. Chiral nematic liquid crystals of hydroxypropyl cellulose and ethyl-cyanoethyl cellulose have been used to template chiral nematic cellulose/silica composite materials. However, in these reports chiral nematic ordering was not retained after the cellulose was removed.^[90, 176] There is also a previous report of using NCC to template mesoporous silica, although the conditions employed resulted in materials with nematic organization, which do not display photonic properties.^[83]

In this chapter I report the first example of a purely inorganic material templated by a chiral nematic liquid crystal. Specifically, I have found that NCC is a robust template for chiral nematic mesoporous silica (CNMS), which represents a new class of porous photonic crystals that can be accessed through self-assembly.

2.2 Experimental

2.2.1 General

All solvents and reagents including TMOS (tetramethyl orthosilicate, Acros) were purchased from commercial sources and used without further purification. Thermogravimetric analysis was performed on a PerkinElmer Pyris 6 thermogravimetric analyzer. All samples were run under air. Gas adsorption studies were performed using a Micromeritics ASAP 2000. All samples were degassed for 2 hours under vacuum at 100 °C immediately prior to analysis. BJH pore size distributions were all calculated from the adsorption branch of the isotherm. IR spectra were obtained with a Nicolet 6700 FT-IR equipped with a Smart Orbit diamond ATR. Powder X-ray diffraction spectra were collected using a D8 advance X-ray diffractometer.

2.2.2 Spectroscopic Characterization

UV-visible/near-IR spectroscopy was conducted on a Cary 5000 UV-Vis/NIR spectrophotometer. Transmission spectra were collected by mounting free-standing films so that the surfaces of the films were perpendicular to the beam path. The maximum transmittance was set to 100% in a region away from the reflectance peak. CD experiments were performed using a JASCO J-710 spectropolarimeter. Spectra were collected by mounting free-standing films so that the surfaces of the films were

perpendicular to the beam path. For the dry films, small pieces were used that did not completely cover the aperture (the CD signals from larger pieces are too intense and saturate the detector). The CD signals measured for the dry films were all normalized to the same intensity for the purpose of comparison. Because the intensity for the wet films is drastically reduced compared to the dry films, films that completely covered the aperture were used allowing for quantitative comparison of CD signals between the samples.

2.2.3 Microscopy

TEM images were collected on a Hitachi H7600 electron microscope. Samples were prepared by first grinding the films into a fine powder, suspending them in ethanol, and then dropcasting them onto a carbon-coated copper TEM grid. SEM images were collected on a Hitachi S4700 electron microscope. Samples were prepared by breaking the films into small pieces and attaching them to aluminum stubs using double-sided adhesive tape. The samples were then sputter-coated with 5 nm of either gold or gold-palladium. Polarized optical microscopy was performed on an Olympus BX41 microscope. All images were taken with the polarizers in a perpendicular (crossed) arrangement unless otherwise noted.

2.2.4 Preparation of Nanocrystalline Cellulose

For the preparation of nanocrystalline cellulose (NCC) fully-bleached, commercial Kraft softwood pulp was first milled to pass through a 0.5-mm screen in a Wiley mill to ensure particle size uniformity and to increase surface area. The milled pulp was hydrolyzed in sulfuric acid (8.75 mL of a sulfuric acid solution/g pulp) at a concentration of 64 wt. % and a temperature of 45 °C with vigorous stirring for 25

minutes. The cellulose suspension was then diluted with cold de-ionized (DI) water (~10 times the volume of the acid solution used) to stop the hydrolysis, and allowed to settle overnight. The clear top layer was decanted and the remaining cloudy layer was centrifuged. The supernatant was decanted and the resulting thick white suspension was washed 3 times with DI water to remove all soluble cellulose materials. The thick white suspension obtained after the last centrifugation step was placed inside dialysis membrane tubes (12,000-14,000 molecular weight cut-off) and dialyzed against slow running DI water, for 1-4 days. The membrane tubes containing the extracted cellulose materials were placed periodically in DI H₂O, and the procedure was continued until the pH of the water became constant over a period of one hour. The suspension from the membrane tubes was dispersed by subjecting it to ultrasound treatment in a Fisher Sonic Dismembrator (Fisher Scientific) for 10 minutes at 60% power and then diluted to the desired concentration (3 wt. %). The final NCC suspension was measured to have a zeta potential of -59 mV and a pH of 2.4.

2.2.5 Preparation of NCC/Silica Composite Films

In a typical procedure, chiral nematic NCC/silica composite films were prepared by first sonicating a 3 wt. % aqueous NCC suspension for 10 minutes. TMOS was then added dropwise to the suspension and the mixture was left to stir at room temperature for 1 h to obtain a homogeneous solution.* The NCC/TMOS mixtures were then poured into polystyrene Petri dishes (5 mL / 60 mm diameter dish) and left to dry under ambient conditions (typically 18-24 h were required for complete drying). For the different ratios of NCC/TMOS used for the different chiral nematic composite samples (**Comp1-8**)

* Note that although TMOS was used throughout this chapter, TEOS can also be used. When TEOS is used in place of TMOS, either the addition of ethanol or heating is required to obtain a homogeneous mixture.

please refer to Table 2-1. Chiral nematic NCC films (**CN-NCC**) were prepared using the same procedure, except without the addition of TMOS. For the samples prepared at different initial pH (**Comp3-pHx**), the pH of the 3 wt. % NCC suspension was adjusted using either 1 M HCl_(aq) or 1 M NaOH_(aq) prior to the addition of TMOS. Otherwise, the procedure was identical to that used for the other composite samples.

2.2.6 Preparation of Mesoporous Silica

For calcination of the NCC/silica composite films, the films were heated under flowing air at a rate of 2 °C/min to 100 °C, held at that temperature for 2 h, then heated to 540 °C at 2 °C/min and held at that temperature for 6 h. After slowly cooling the samples to room temperature free-standing mesoporous silica films were recovered.

2.3 Results and Discussion

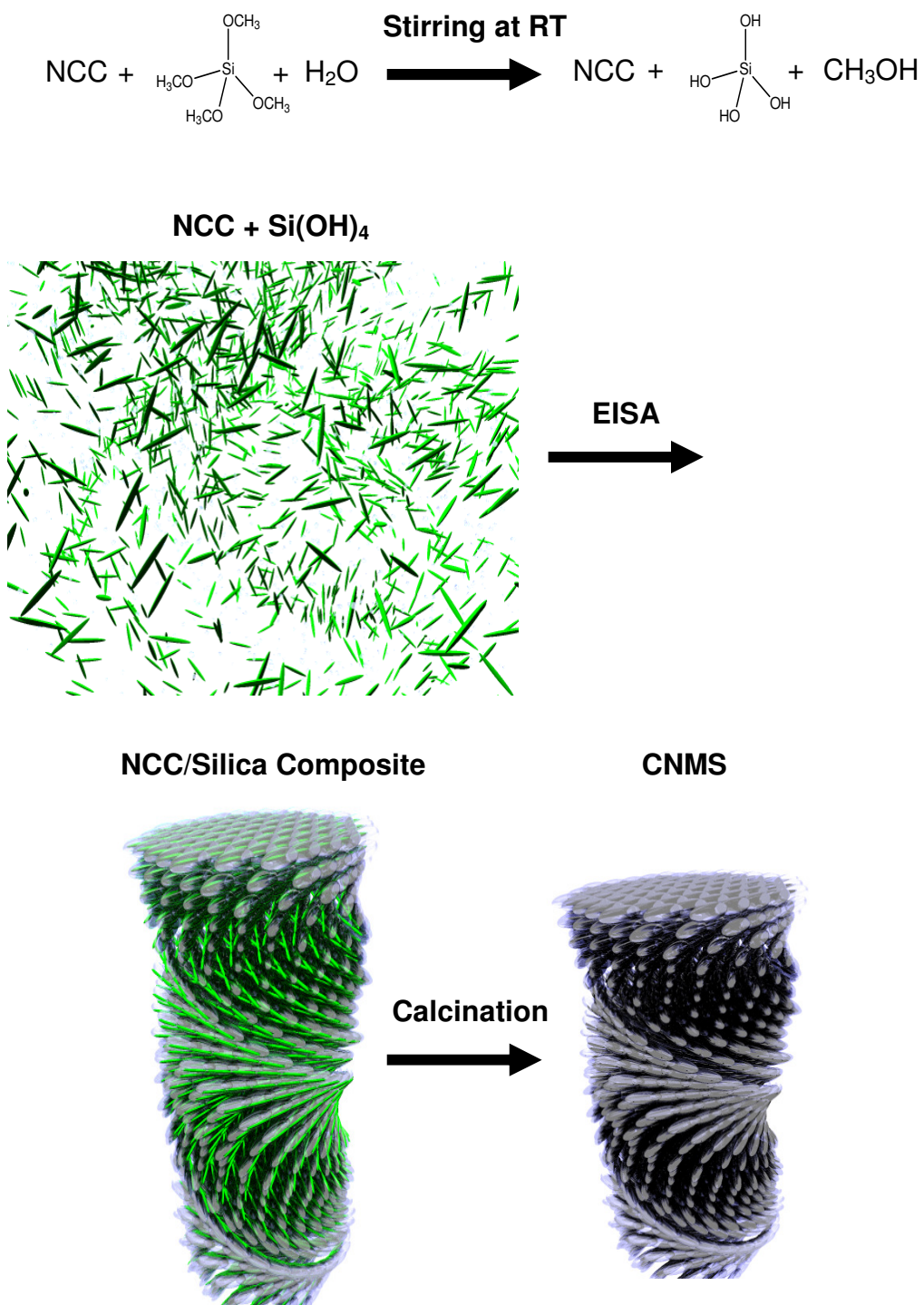
2.3.1 Preparation of Chiral Nematic NCC/Silica Composite Films

The NCC used in our experiments was prepared by sulfuric acid hydrolysis (64 wt. % H₂SO₄ at 45 °C for 25 min) of a commercial, fully-bleached Kraft softwood pulp (for TEM images of the NCC used in our experiments please refer to Appendix A). Previous work has shown that these conditions give NCC with 89% crystallinity and a crystallite size of 8.3 nm as determined by powder X-ray diffraction (PXRD).^[51] Sulfate ester groups are introduced onto the surface of NCC during this procedure (NCC-OH is converted to NCC-OSO₃H) with a conversion of ≈ 1 sulfate group per 20 glucose units* as determined by combustion analysis.^[51] This gives the NCC particles a negative surface charge when dispersed in water (zeta potential = -59 mV), which stabilizes the colloidal suspension and is also important for the formation of a chiral nematic phase.^[58, 60] A 3 wt.

* This includes both surface and internal glucose units.

% aqueous NCC suspension with a pH of 2.4 was used for all of our subsequent experiments unless otherwise noted; the acidic pH of this suspension derives entirely from H^+ associated with the surface sulfate groups of NCC (i.e., no additional acid was added).

NCC/silica composite films were prepared through evaporation-induced self-assembly (EISA) of NCC with tetramethoxysilane (TMOS) as shown in Scheme 2-1. A series of samples was prepared by varying the amount of TMOS used relative to NCC (**Comp1-Comp8**) and the compositions are reported in Table 2-1. TMOS is initially immiscible when added to an aqueous NCC suspension but quickly dissolves as it is hydrolyzed to form water-soluble silicic acid and methanol after stirring for several minutes at room temperature. I initially tested whether NCC could form a chiral nematic phase in the presence of TMOS by drop-casting the NCC/TMOS mixtures onto glass microscope slides and observing the evaporation process by polarized optical microscopy (POM, Figure 2-1). The initial concentration of the NCC suspension used (3 wt. %) is below the critical concentration for anisotropic phase formation and the drops initially appear dark when viewed under crossed-polarizers. As evaporation takes place, a fingerprint texture is established demonstrating that the chiral nematic phase of NCC can form over the range of TMOS loadings that were tested (initial [TMOS] ranged from 0.22 M to 0.74 M).



Scheme 2-1. Outline of the synthesis of chiral nematic NCC/silica composite films and chiral nematic mesoporous silica (CNMS).

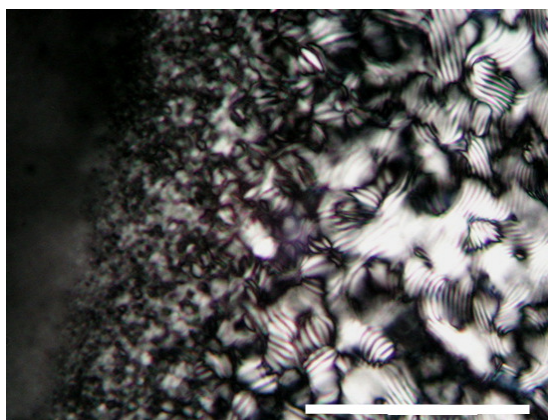


Figure 2-1. POM micrograph of a drop taken from an NCC/TMOS mixture during evaporation on a glass slide. The right side of the image (closer to the edge of the drop) displays a fingerprint texture indicative of a chiral nematic LC phase (scale bar = 100 μm).

NCC/silica composite films were formed by casting the homogeneous mixtures in polystyrene Petri dishes and allowing them to dry under ambient conditions. After complete drying, this results in transparent, free-standing films with typical thicknesses between 50-100 μm and lengths/widths of 1-3 cm. The size of the films is limited by cracking that occurs during the final stages of the drying process (more cracking tends to occur for films with higher silica loadings). The weight % of silica in the different composite samples was determined by thermogravimetric analysis (TGA) and ranges from 29% for **Comp1** to 58% for **Comp8** (see Table 2-1). It should be noted that the determination of the weight % silica is based on the assumption that the composite materials solely consist of cellulose and fully condensed SiO_2 , which likely leads to a slight overestimation of the NCC content in the samples. Measurements carried out on **Comp3** prepared at different times varied by $\sim 2\text{-}3$ wt. %, which could be due to small measurement errors along with differences in the aging time of the samples prior to running the TGA.

The presence of chiral nematic ordering in the NCC/silica composite films was confirmed by scanning electron microscopy (SEM, Figure 2-2), which shows a 1D

periodic structure perpendicular to the surface of the films that is similar to what is seen for chiral nematic NCC films without silica (CN-NCC). This ordering is indicative of a chiral nematic structure with its helical axis oriented perpendicular to the surface of the films (each repeating band corresponds to a half helical pitch of the chiral nematic structure).

Table 2-1. Compositions and peak reflected wavelengths of NCC/silica composite films.

Sample	mmol TMOS/ 150 mg NCC	Wt. % NCC ^a	λ_{\max} (nm)	P (nm) ($\lambda_{\max}/n_{\text{avg}}$)	P (nm) (SEM)
CN-NCC	0	100	475	317	350
Comp1	1.09	71	608	405	-
Comp2	1.22	68	708	472	575
Comp3	1.36	65	770	513	-
Comp4	1.69	60	838	559	-
Comp5	2.03	57	929	619	760
Comp6	2.37	51	986	657	-
Comp7	3.05	47	1172	781	-
Comp8	3.73	42	1420	947	920

a) Calculated from TGA.

Chiral nematic periodic structures are observed for all of the NCC/silica composite samples, demonstrating that the chiral nematic self-assembly of NCC is very tolerant to silica. Looking at Figure 2-2, it is also apparent that the repeating distance ($P/2$) depends on the silica loading showing a pronounced increase as the amount of TMOS added relative to NCC is increased. Average values for P of 350 nm, 575 nm, 760 nm, and 920 nm were measured for **CN-NCC**, **Comp2**, **Comp5**, and **Comp8**, respectively. The increase in helical pitch caused by increasing the amount of silica in the composite films may simply be a result of greater silica wall thickness, although modulation of the electrostatic interactions between NCC may also play a role. This behaviour is the opposite of that previously reported for the addition of salt to NCC (e.g., NaCl), which is believed to reduce the helical pitch by masking electrostatic repulsion.^[56]

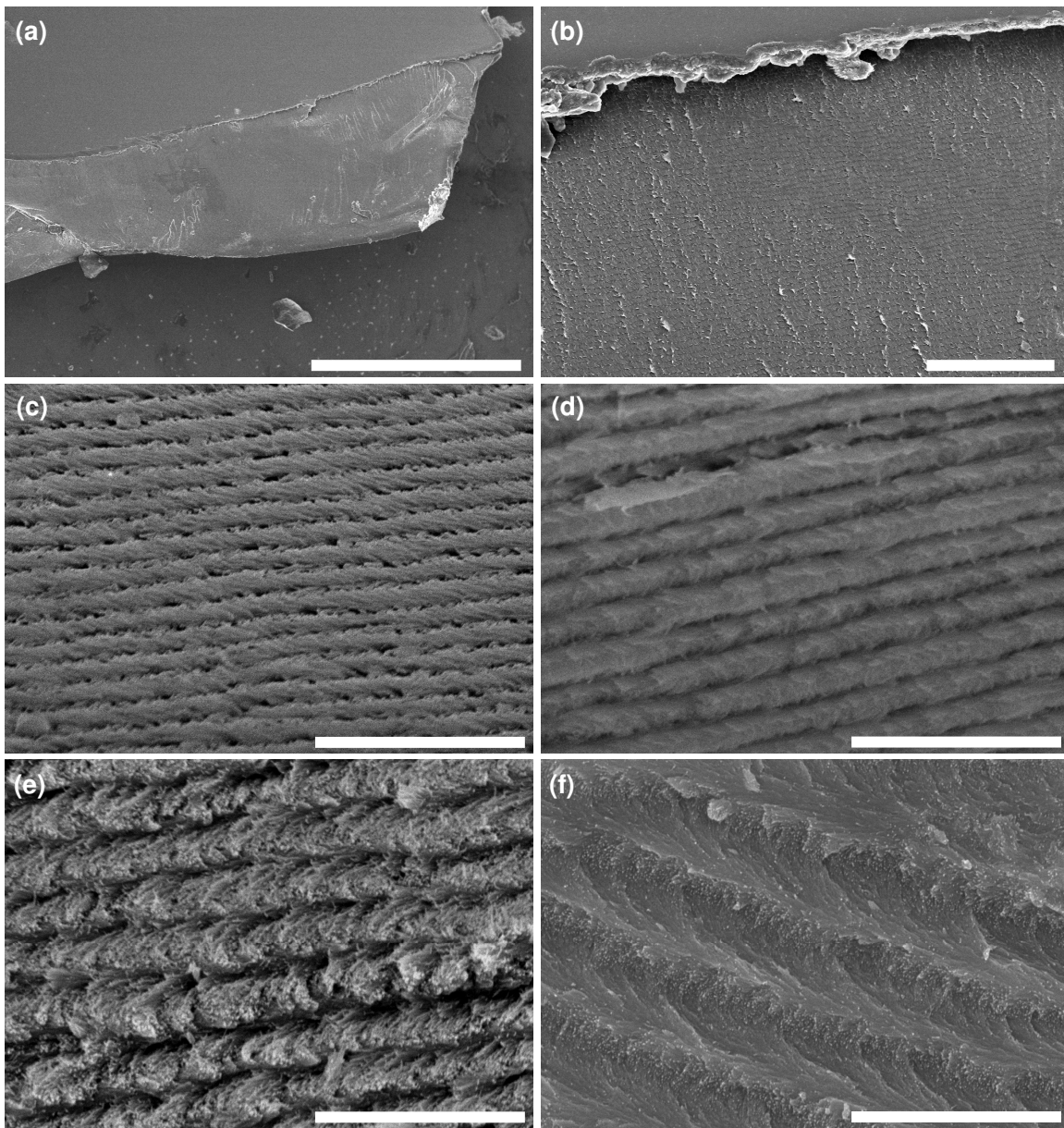


Figure 2-2. SEM images of chiral nematic NCC and NCC/silica films. (a) Low magnification image of pure NCC film **CN-NCC** (scale bar = 200 μm). (b) Cross-sectional image of **CN-NCC** shows periodic structure perpendicular to the film surface (scale bar = 10 μm). (c) Cross-sectional image of **CN-NCC** at higher magnification (scale bar = 2 μm). (d) Cross-sectional image of NCC/silica composite film **Comp2** at the same magnification as (c) shows a similar periodic structure but with a larger repeating distance (scale bar = 2 μm). (e) Cross-sectional image of NCC/silica composite film **Comp5** (scale bar = 2 μm). (f) Cross-sectional image of NCC/silica composite film **Comp8** (scale bar = 2 μm).

2.3.2 Optical Characterization of NCC/Silica Composite Films

Chiral nematic liquid crystals selectively reflect circularly polarized light with a handedness that matches that of the chiral nematic structure according to the following equation:

$$\lambda_{\max} = n_{\text{avg}} P \sin\theta \quad (1)$$

where n_{avg} is the average refractive index, P is the helical pitch, and θ is the angle between the surface of the liquid crystal and the incident light (i.e., for incident light normal to the surface/parallel to the helical axis, $\sin\theta = 1$).^[44] For a given angle of incidence, λ_{\max} may therefore be tuned by varying the helical pitch or the average refractive index of a chiral nematic liquid crystal. Figure 2-3 shows POM micrographs for **Comp3** and **CN-NCC**. The films show similar textures, but the colour of **Comp3** is red-shifted compared to the pure NCC film. UV-Vis/NIR spectra were collected for samples **Comp1-Comp8** and show a continuous red shift of λ_{\max} with increased silica loading (Figure 2-4). It should be noted that for a given sample, spectra collected from different locations on the films gave λ_{\max} values that varied by up to ~30 nm. Altogether, λ_{\max} of the composite films ranged from 475 nm (for the pure NCC film) to 1420 nm for **Comp8** by simply increasing the proportion of silica precursor relative to NCC (Table 2-1).

The values for n_{avg} of the different composite materials are essentially constant since the two components, SiO₂ and crystalline cellulose, have similar refractive indices ($n = 1.46$ and 1.54 , respectively). It can therefore be inferred that the increase in λ_{\max} for samples with higher silica content must be predominantly caused by the increase in P that was observed by SEM. Values of P were also calculated by dividing λ_{\max} for the different composite samples by n_{avg} , (assumed to be 1.5) and are reported in Table 2-1. It should be noted that although the values of P determined by UV-Vis and SEM both show the same

trend of increasing with higher silica loadings, the values do not match up very well in some cases. There are several possible reasons for this discrepancy. Accurate measurements of P by SEM require that the films are fractured very cleanly along the helical axis, which is not always the case. It is also likely that the helical axis is not perfectly perpendicular to the film surface throughout the entire sample, which would lead to peak broadening towards shorter wavelengths in the UV-Vis/NIR spectra and hence an underestimation of P .

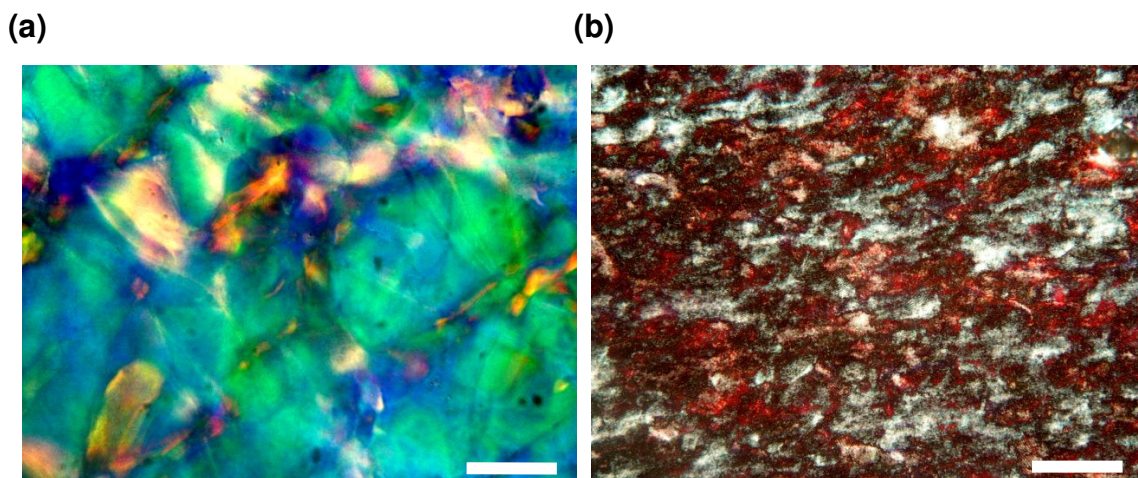


Figure 2-3. (a) POM micrograph of a free-standing chiral nematic NCC film (CN-NCC, scale bar = 100 μm). (b) POM micrograph of free-standing NCC/silica composite film **Comp3** (scale bar = 100 μm).

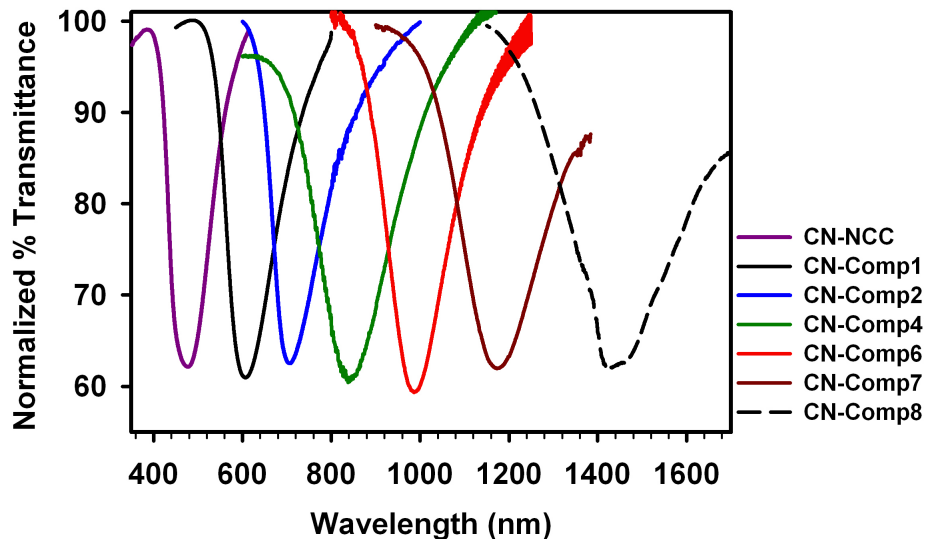


Figure 2-4. UV-Vis spectra for chiral nematic NCC and selected NCC/silica composite films.

2.3.3 Influence of pH on the Formation of NCC-Silica Composite Films

The considerable tolerance of the chiral nematic self-assembly of NCC to TMOS is likely due at least in part to the fortuitous fact that the initial pH of dilute NCC suspensions is close to the isoelectric point of colloidal silica (pH ~2). This may be important for two reasons: 1) the chiral nematic self-assembly of NCC is more sensitive to charged species than it is to neutral species and 2) operating close to the isoelectric point of colloidal silica is known to suppress silica polymerization.^[98] This allows for NCC self-assembly to occur unimpeded with silica condensation mostly occurring at the later stages of the drying process.

The influence of the initial pH of the NCC suspension on composite film formation was investigated by adding dilute HCl or NaOH to the NCC prior to the addition of TMOS (the same NCC/TMOS ratio was used as for **Comp3**) and these samples are denoted as **Comp3-pHx**. Adjusting the initial pH of the NCC suspension to 2.0 with HCl completely inhibits the chiral nematic self-assembly of NCC and results in

transparent films without photonic properties. Observations of **Comp3-pH2.0** using POM and SEM do not show any of the texture or periodic structure present in the chiral nematic films. Instead, POM shows a uniform birefringence that changes intensity when the film is rotated (Figure 2-5a) and SEM shows aligned rods organized in a disordered layer structure (Figure 2-5b). Taken together these results indicate that the addition of HCl disrupts the chiral nematic assembly of NCC and results in nematic composite films (films cast from the pH 2 NCC suspension without the addition of TMOS appear very similar and also show nematic ordering, rather than chiral nematic ordering).

NCC suspensions with more basic pH of 7.0 and 12.5 were prepared by the addition of NaOH and were also used to make NCC/silica composite films. The **Comp3-pH7.0** films are completely opaque and do not appear to show any chiral nematic ordering. In contrast to the addition of acid described above, NCC films prepared from this suspension without the addition of TMOS form chiral nematic films. The disruption of chiral nematic ordering in these samples therefore appears to be caused by a change in the silica condensation rate. **Comp3-pH12.5** appears very similar to **Comp3-pH2.0** and also does not show any chiral nematic ordering. As with **Comp3-pH2.0**, POM observation of **Comp3-pH12.5** shows birefringence indicative of nematic ordering, which is also observed for pure NCC films cast from the pH 12.5 suspension. Taken together, these results demonstrate that the formation of chiral nematic NCC/silica composite films is very sensitive to the addition of acid or base, which can disrupt self-assembly by modulating the interactions between NCC particles and influencing the rate of silica condensation.

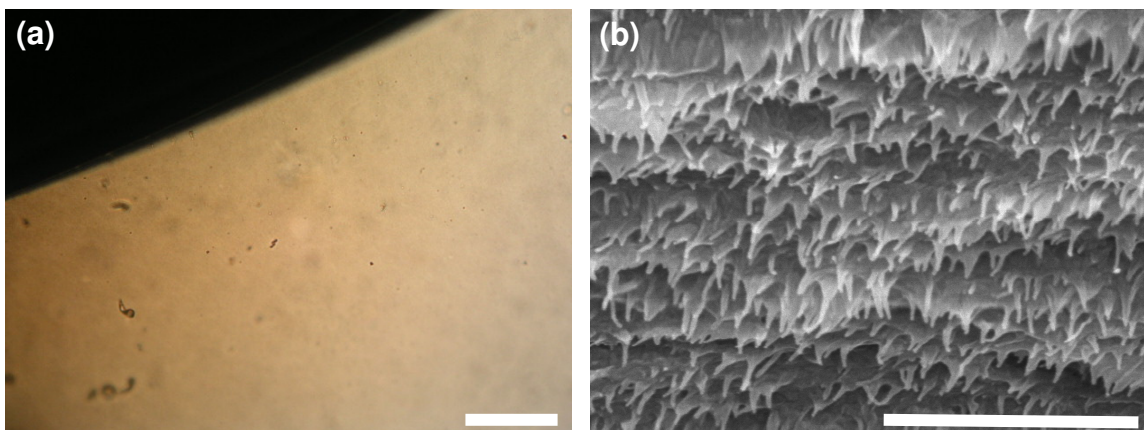


Figure 2-5. Disruption of chiral nematic ordering by the addition of HCl. (a) POM micrograph of **Comp3-pH2.0** (scale bar = 100 μm). (b) Cross-sectional SEM micrograph of **Comp3-pH2.0** (scale bar = 1 μm).

2.3.4 Removal of the NCC Template by Calcination

Removal of the cellulose template was accomplished by calcination of the NCC/silica composite films at 540 $^{\circ}\text{C}$ under air. NCC-silica composite samples **Comp1-Comp8** were calcined to give silica samples denoted as **CNMS1-CNMS8**. In addition, the composite samples **Comp3-pHx** were calcined to give corresponding silica samples labeled as **MS3-pHx**. The films remained intact during the cellulose removal yielding free-standing silica films. The removal of NCC from the composite films was confirmed by IR spectroscopy and PXRD (Figure 2-6). IR peaks characteristic of NCC at 1160 cm^{-1} (C-C stretch), 2900 cm^{-1} (C-H stretch), and 3330 cm^{-1} (O-H stretch) are no longer present after calcination, while PXRD shows the disappearance of peaks corresponding to crystalline cellulose at ~ 15 and $23^{\circ} 2\theta$. The calcined material shows IR peaks at 1020 cm^{-1} and 800 cm^{-1} that can be assigned to Si-O modes and the PXRD shows a broad peak centered at $23^{\circ} 2\theta$ characteristic of amorphous silica.

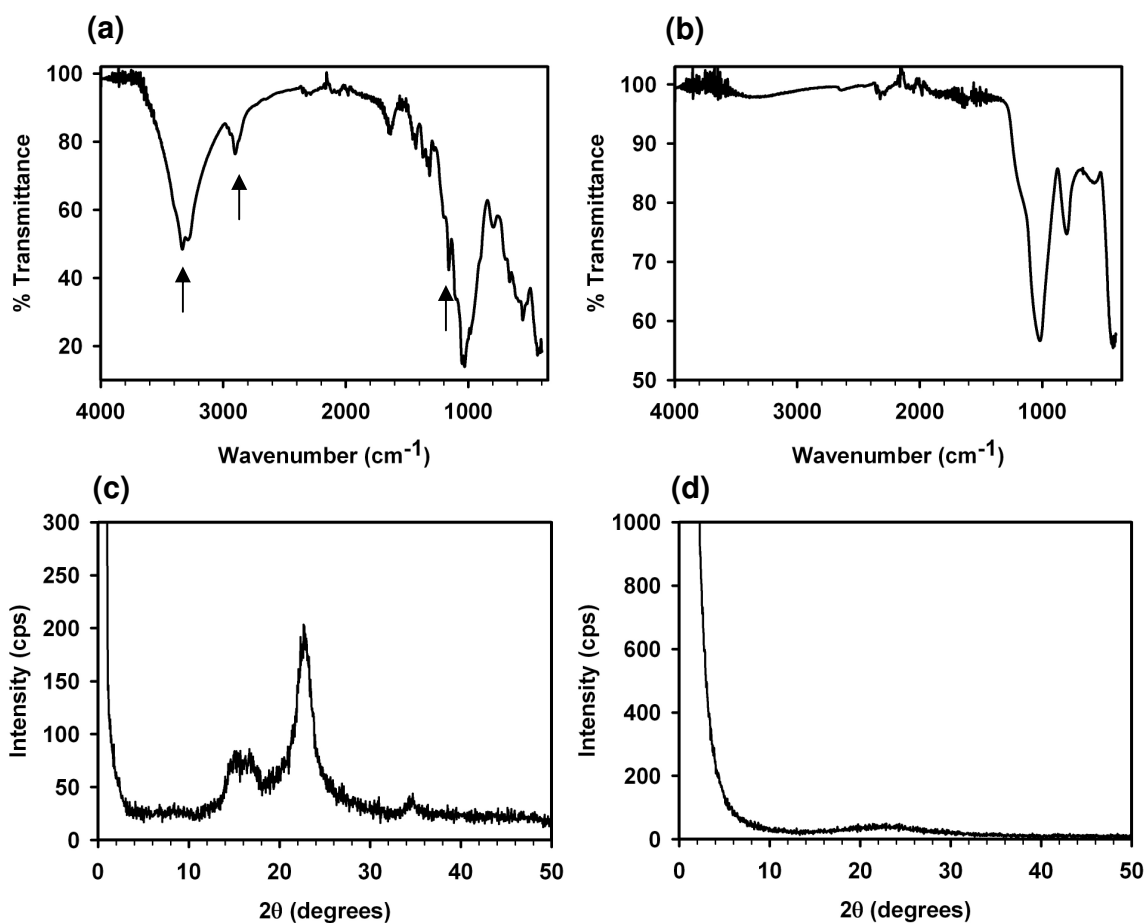


Figure 2-6. IR spectra and PXRD patterns before and after calcination of an NCC-silica composite film. (a) IR spectrum of **Comp1**. Arrows indicate characteristic NCC peaks (O-H, C-H, and C-C stretching modes, respectively, from left to right). (b) IR spectrum of **CNMS1**. (c) PXRD pattern of **Comp1**. (d) PXRD pattern for **CNMS1**.

SEM confirms the retention of chiral nematic organization in the pure silica films (Figure 2-7). The top surfaces of the films appear very smooth and perpendicular to the surface the periodic helical pitch characteristic of chiral nematic organization is observed (Figure 2-7a). In some locations defects can be seen that correspond to a condensed version of those observed by POM in the LC phase (Figure 2-7b, these defects are also observed in the composite and pure NCC films). This demonstrates that the liquid crystalline organization of NCC is locked into place and faithfully replicated in the silica samples. At very high magnification a twisting rod-like morphology is resolved, similar to what is seen for pure NCC. Throughout the sample, this twisting appears to occur in a

counter-clockwise direction when looking down the helical axis, consistent with a left-handed helical organization (Figure 2-7d).

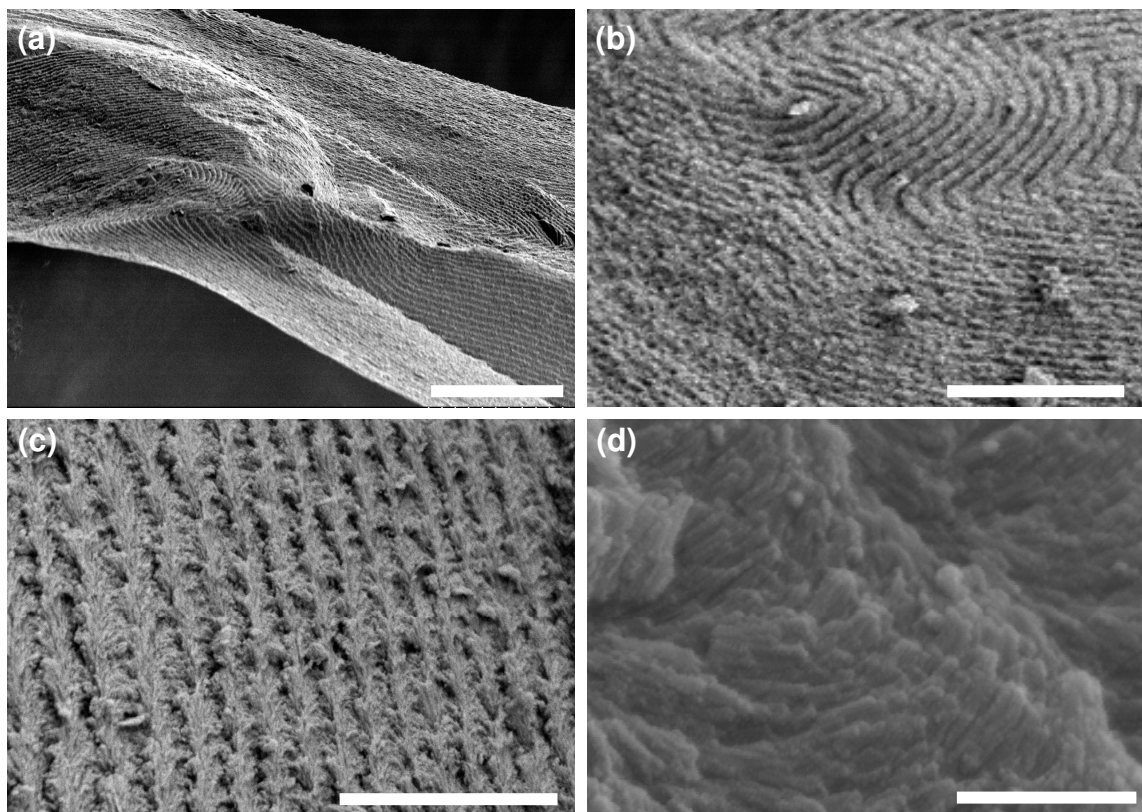


Figure 2-7. SEM images of calcined silica CNMS2. (a) Top view looking down the edge of a fractured film (scale bar = 10 μm). (b) Cross-sectional micrograph of film showing repeating structure with fingerprint defect (scale bar = 10 μm). (c) Cross-sectional view at higher magnification (scale bar = 2 μm). (d) High magnification micrograph looking down the chiral nematic helical axis (scale bar = 200 nm).

2.3.5 Mesoporosity of Calcined Silica Films

Nitrogen adsorption measurements were carried out on selected calcined samples and the data is reported in Table 2-2 and Figure 2-8. The CNMS samples display type IV adsorption isotherms, which are characteristic of mesoporous materials, and have BET surface areas ranging from 690-470 m^2/g and pore volumes of 0.63-0.42 cm^3/g , depending on the NCC/silica ratio of the starting composite samples. The hysteresis in the isotherms can be classified as type H2, which is indicative of a complex pore

structure composed of interconnected networks of pores of different size and shape.^[177] As expected, the specific surface area and pore volumes of the samples both decrease with increased silica loading (the thicker silica walls make the materials denser).

The BJH pore size distributions give peak pore diameters of ~3 nm, and show very little pore volume past 10 nm. This pore size distribution is somewhat smaller than the width measured for the NCC template by TEM, which has a distribution centered around 8 nm (see Appendix A). This indicates that considerable contraction occurs upon the removal of NCC by calcination. It appears that this contraction may depend to some extent on the silica loading since the pore size distribution for **CNMS1** is slightly broader and has a smaller peak diameter compared to **CNMS3** and **CNMS6** (Figure 2-8e and 2-8f). The contraction of the films was also confirmed by SEM. Figure 2-9 shows a comparison of cross-sectional SEM micrographs taken for **Comp2** and **CNMS2** at the same magnification. When viewed side by side, it is apparent that the repeating distance ($P/2$) for **CNMS2** is smaller than that of **Comp2**. The average helical pitch measured for **Comp2** by SEM is 575 nm while the pitch measured for **CNMS2** is 307 nm.

The porosity of **CNMS3** was also observed by TEM (Figure 2-10). Figure 2-10a shows a fragment that appears to have its helical axis oriented perpendicular to the plane of the image. Twisting silica rods are observed that are separated by fairly disordered mesopores. The pores appear locally aligned, as is anticipated for the local nematic ordering present in a chiral nematic structure. Figure 2-10b shows a fragment that appears to have its helical axis oriented in the plane of the image; regions with in-plane pores are separated by regions with pores perpendicular to the image plane. The pores seen in the TEM images have widths of ~3-5 nm, which corresponds well with the values obtained from N₂ adsorption.

Table 2-2. Nitrogen adsorption data for selected samples.

Sample	BET Surface Area (m ² /g)	Pore Volume (cm ³ /g)
CNMS1	688	0.63
CNMS3	556	0.46
CNMS6	469	0.42
MS3-pH2.0	390	0.39
MS3-pH7.0	408	0.53
MS3-pH12.5	28	0.10

Nitrogen adsorption studies were also performed on the series of calcined silica films **MS3-pH2.0** to **MS3-pH12.5**. **MS3-pH2.0** displays a type IV isotherm with a similar shape to that of **CNMS3**. The BET surface area and pore volume calculated for **MS3-pH2.0** are somewhat lower than for **CNMS3** (Table 2-2). Although it is possible that the lack of chiral nematic ordering seen for **MS3-pH2.0** may be related to its decreased porosity, it is not possible to conclude this for certain since other factors related to pH (e.g., degree of silica condensation) may also play a role. **MS3-pH12.5** has a considerably lower pore volume and BET surface area compared to the other samples and an isotherm that is characteristic of a macroporous material (Figure 2-8d), which suggests that NCC aggregation occurs at this higher NaOH loading.

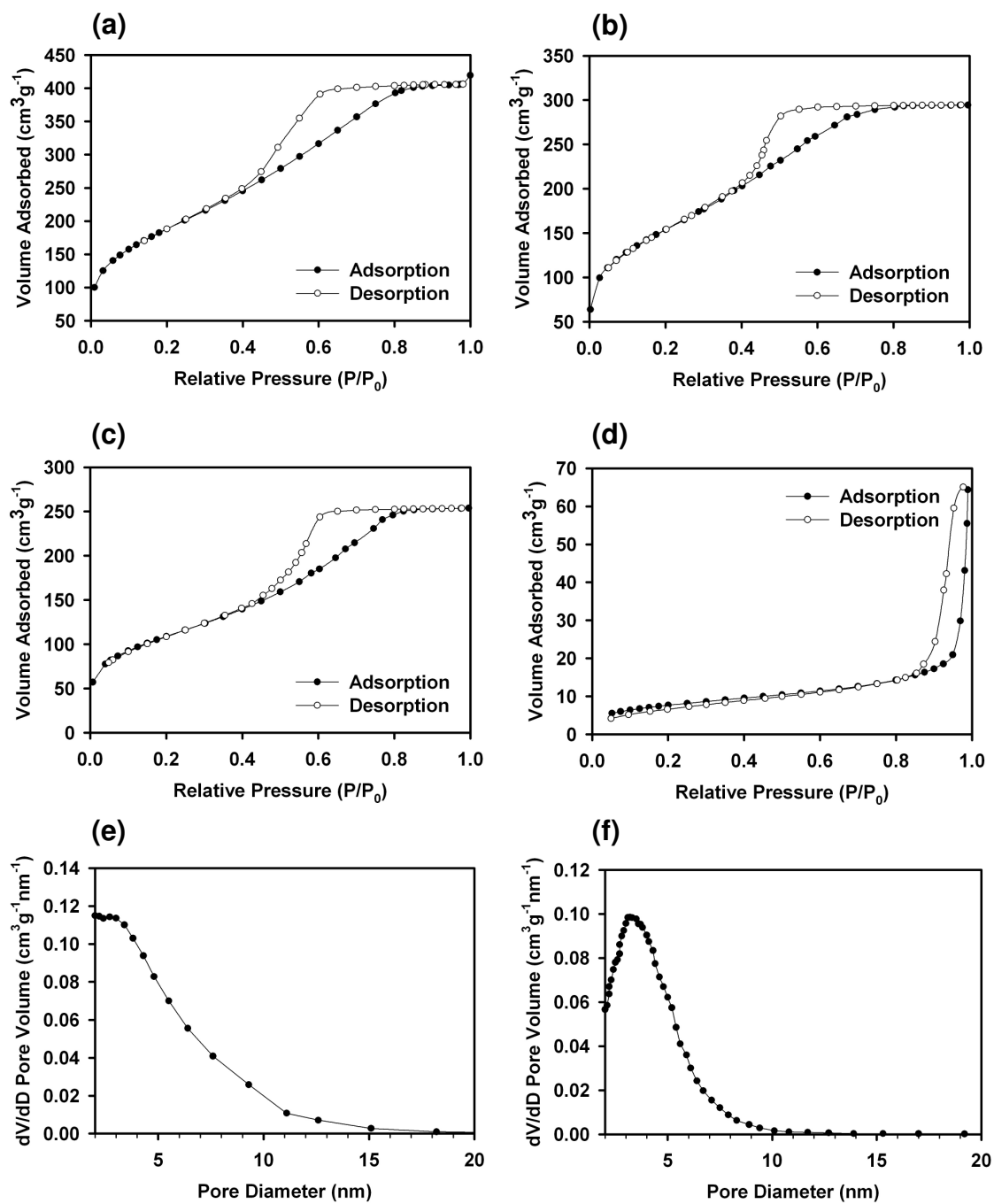


Figure 2-8. Nitrogen adsorption data for selected calcined samples (a) N₂ isotherm for **CNMS1**. (b) N₂ isotherm for **CNMS3**. (c) N₂ isotherm for **MS3-pH2.0**. (d) N₂ isotherm for **MS3-pH12.5**. (e) BJH pore size distribution for **CNMS1**. (f) BJH pore size distribution for **CNMS6**.

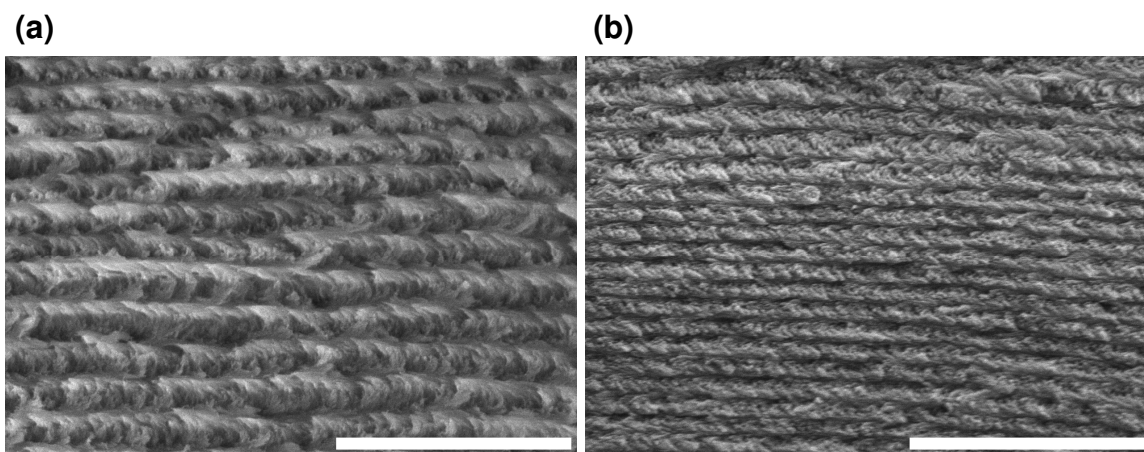


Figure 2-9. SEM comparison of chiral nematic film before and after calcination. (a) Cross-sectional micrograph of **Comp2** (scale bar = 2 μm). (b) Cross-sectional micrograph of **CNMS2** (scale bar = 2 μm).

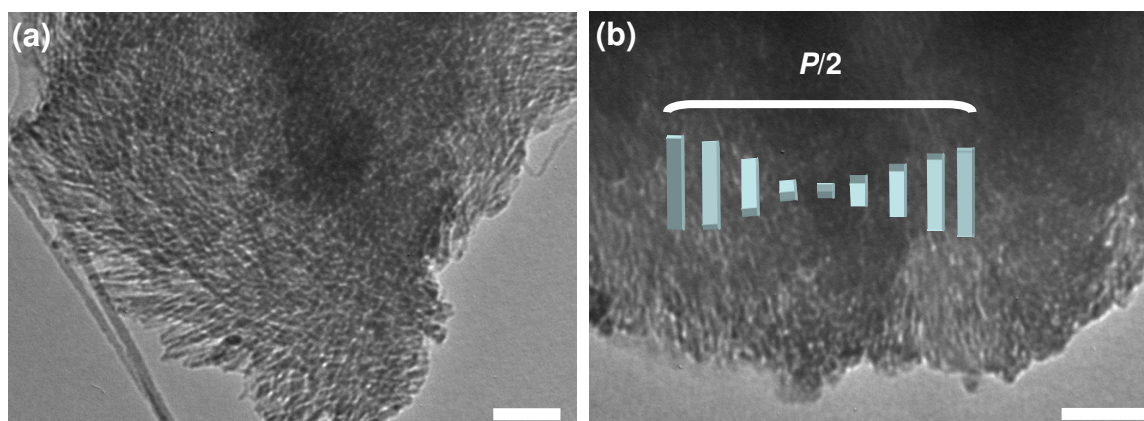


Figure 2-10. TEM micrographs of **CNMS3**. (a) View looking down the helical axis of a film fragment (scale bar = 100 nm). (b) Film fragment with the helical axis in the plane of the image as indicated (scale bar = 100 nm).

2.3.6 Optical Characterization of Mesoporous Silica Films

I was particularly interested to see if the photonic properties of the chiral nematic composite samples were retained after the removal of NCC. The calcined films show strong birefringence by POM and a texture that is very similar to that observed for the composite films (Figure 2-11), further confirming that the chiral nematic structure of the composite films is retained after NCC removal.

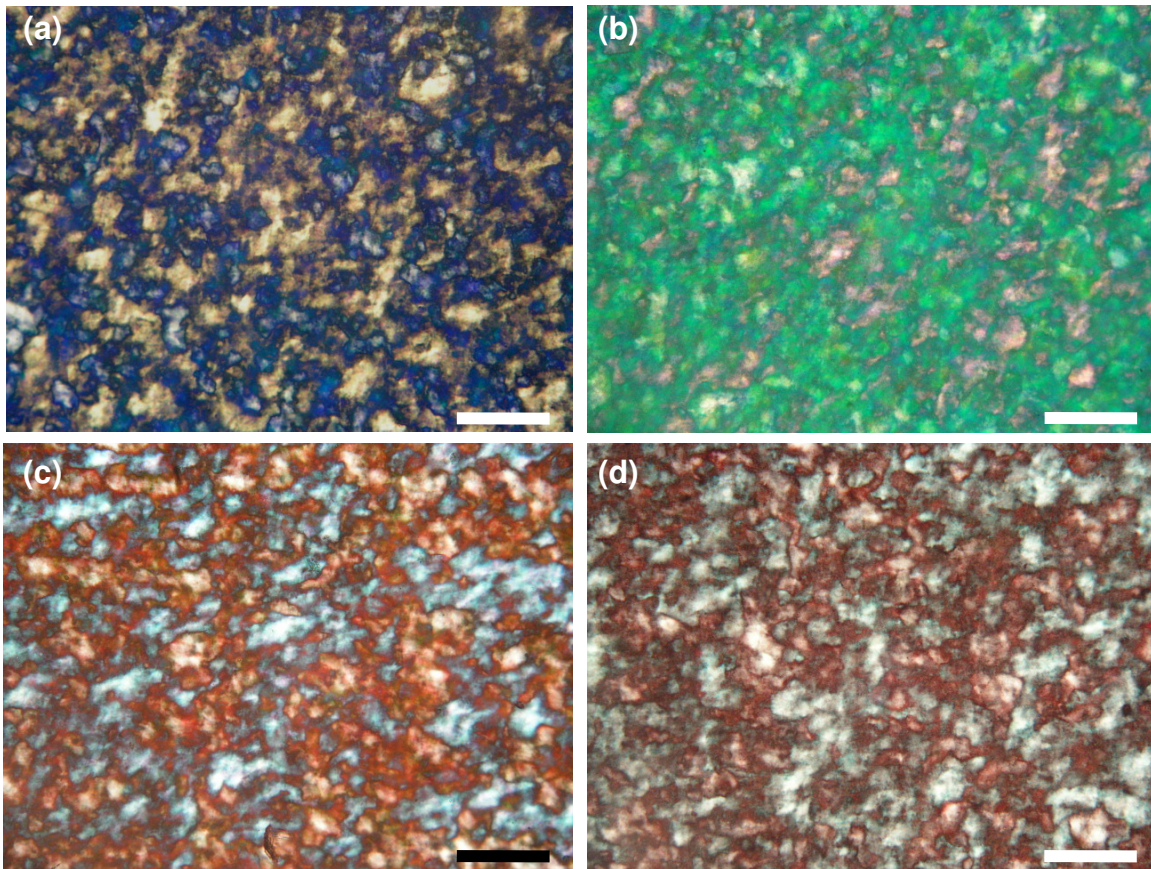


Figure 2-11. POM micrographs of chiral nematic silica films **CNMS3-CNMS6** (a-d respectively, all scale bars = 100 μm).

Table 2-3. Peak reflected wavelengths for chiral nematic mesoporous silica samples.

Sample	λ_{max} (nm)	P (nm) ($\lambda_{\text{max}}/n_{\text{avg}}$) ^a	P (nm) (SEM)
CNMS1	<300	-	-
CNMS2	350	-	307
CNMS3	450	375	-
CNMS4	545	-	-
CNMS5	610	-	415
CNMS6	700	560	-
CNMS7	890	-	-
CNMS8	1080	-	-

a) n_{avg} was calculated based on the volume weighted average of the individual refractive indices of air and SiO_2 , which were taken to be 1 and 1.46 respectively (the volume fractions were calculated based on nitrogen adsorption measurements).

The chiral nematic silica films selectively reflect light at wavelengths that are blue-shifted by $\sim 250\text{-}300$ nm compared to the corresponding NCC/silica composite films.

This blue shift results from a combination of the decrease in average refractive index that occurs upon the removal of cellulose as well as the contraction in helical pitch discussed above. Altogether, the series of silica films **CNMS1-8** have reflection peaks that range from ~300-1100 nm (Table 2-3). Starting from the composite films **Comp3-6**, mesoporous silica films **CNMS3-6** that reflect light at different wavelengths across the entire visible spectrum were obtained. The colours of the films are easily observed by the naked eye and appear iridescent (i.e., the colours are angle dependent) because of the $\sin\theta$ dependence of λ_{\max} for chiral nematic liquid crystals (Figure 2-12). Circular dichroism spectra of the coloured films give very intense positive signals with positions that closely match the peaks measured by UV-Vis spectroscopy (Figure 2-13). This demonstrates that the observed colours arise from the selective reflection of left-handed circular polarized light as is expected for a left-handed chiral nematic structure.

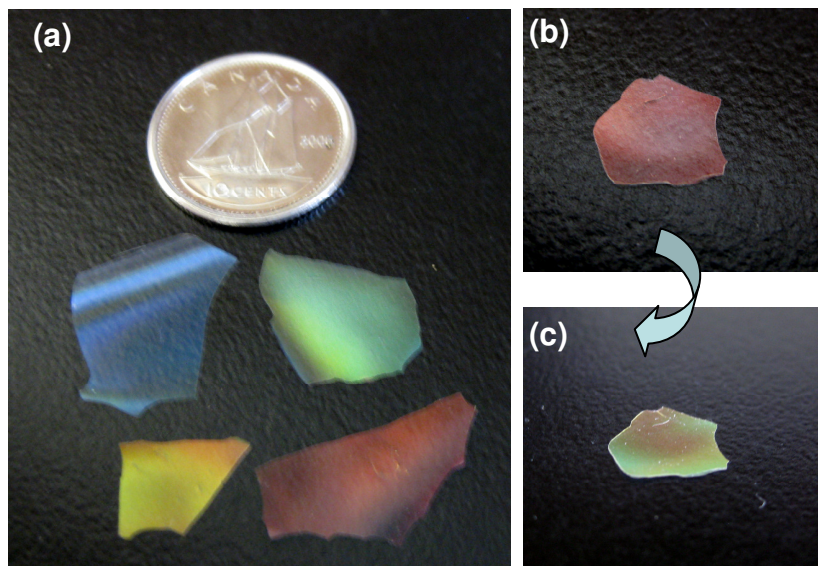


Figure 2-12. Photographs of iridescent silica films. (a) Silica films **CNMS3-6**. The dime is included for scale ($d = 18$ mm). (b) Photograph of **CNMS6** taken at normal incidence. (c) Photograph of **CNMS6** taken at oblique incidence.

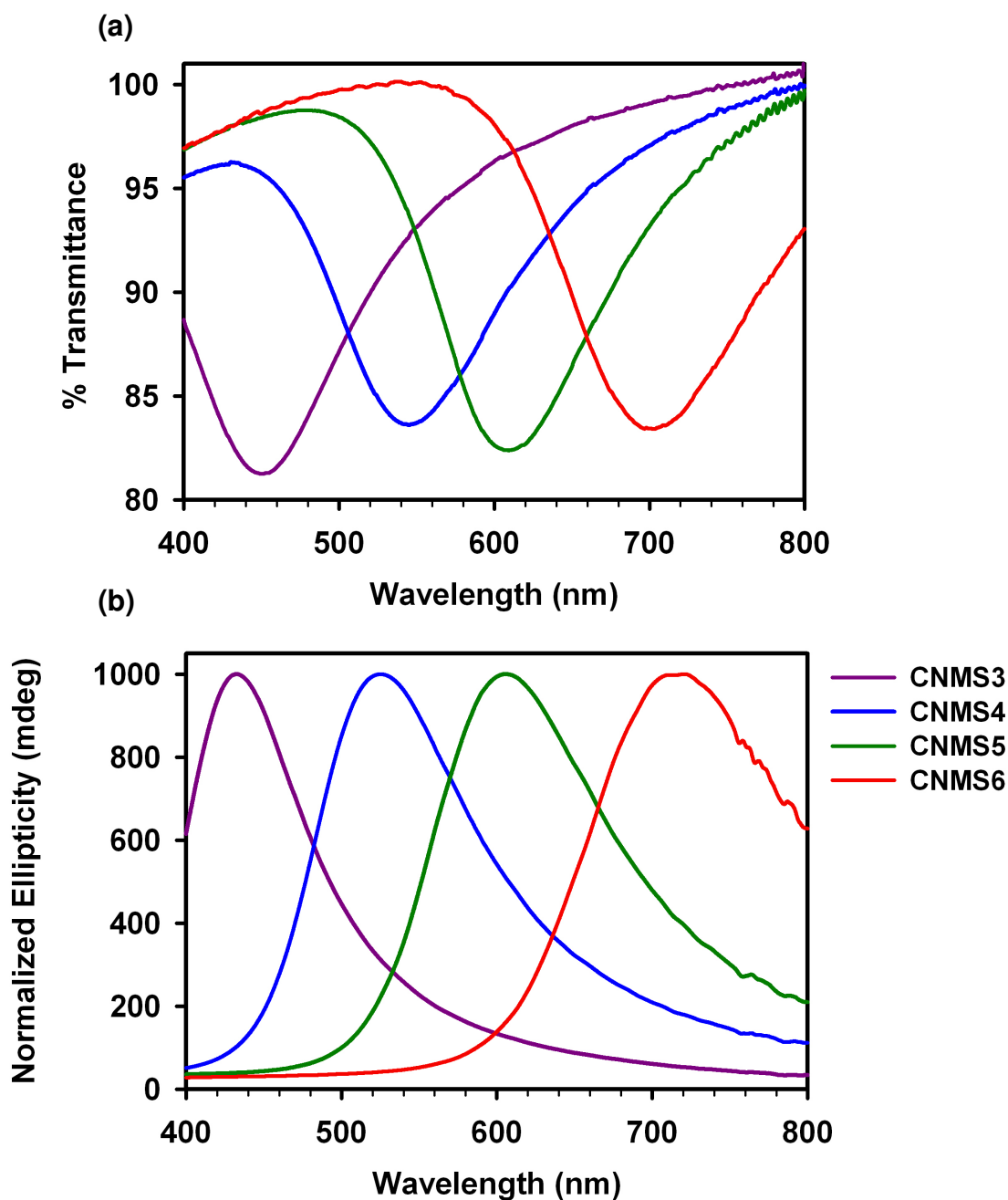


Figure 2-13. Optical characterization of iridescent silica films **CNMS3-6**. (a) UV-Vis spectra of **CNMS3-6**. (b) CD spectra of **CNMS3-6**.

2.3.7 Addition of Isotropic Liquids to Chiral Nematic Mesoporous Silica

To demonstrate a unique property of the chiral nematic mesoporous silica films, I examined their absorption of isotropic liquids. The films rapidly absorb water and other liquids and become completely transparent and colourless, which can be detected visually

as shown in Figure 2-14. A similar effect has also been reported for helical inorganic nanostructures prepared by glancing angle deposition (GLAD), and was attributed to approximate refractive index matching between the isotropic liquid in the pores and the walls of the material.^[178] The birefringence of the mesoporous films is also drastically reduced when the pores are filled with isotropic liquids (Figure 2-15b). These changes are reversible and the films fully regain their iridescence and birefringence upon drying. Because the silica in these materials is amorphous, the birefringence of the films results entirely from the anisotropic shape of the silica rods. This type of birefringence is known as form birefringence, and is dependent on the refractive index contrast between the pores and the silica walls. This is in contrast to the materials that contain NCC, since NCC has an anisotropic crystalline structure and is therefore intrinsically birefringent.

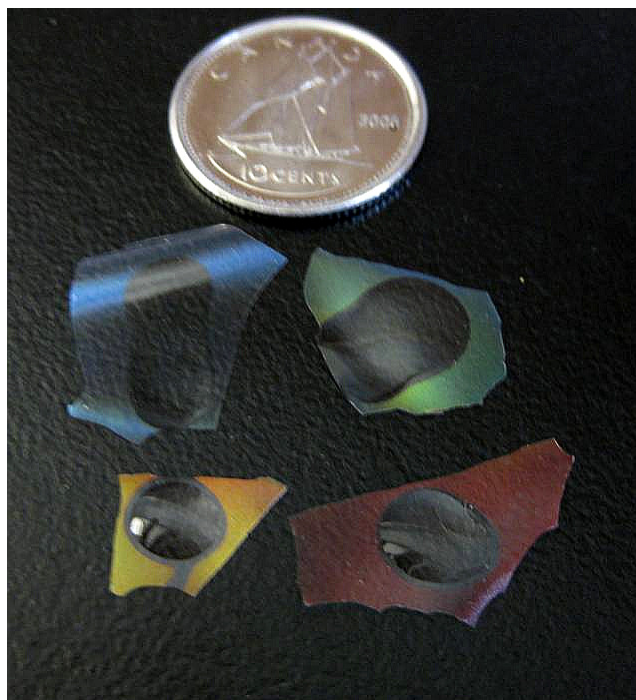


Figure 2-14. Photograph of CNMS3-6 after the addition of water.

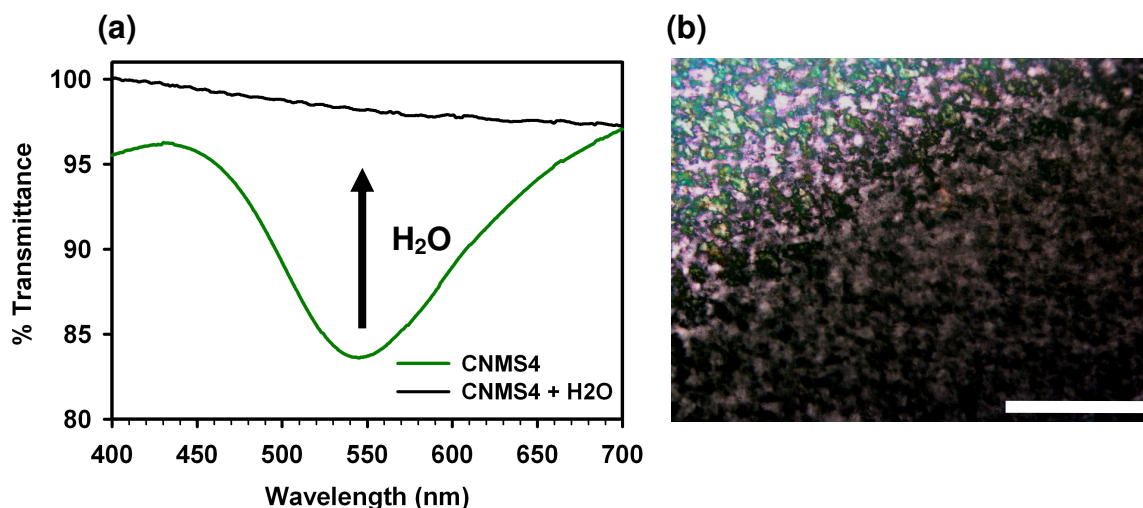


Figure 2-15. Water infiltration of **CNMS4**. (a) UV-Vis spectra of **CNMS4** before and after the addition of water. (b) POM micrograph of **CNMS4** after the addition of water (scale bar = 200 μm). The green area in the top-left region of the image is still dry.

Because the refractive index of water ($n = 1.33$) and SiO_2 ($n = 1.46$) are not perfectly matched, a small residual peak is expected after water infiltration; however, it is too small to be detected by the naked eye or in the transmission spectra of the water-soaked mesoporous films (Figure 2-14 and Figure 2-15a). The chiral origin of the reflectance peak allows optical changes in the films to be probed using circular dichroism. The CD signal of the films is reduced by two orders of magnitude to ~ 30 mdeg after infiltration with water (Figure 2-16). The CD peak is also red-shifted compared to the reflectance peak for the dry film due to the increase in n_{avg} (λ_{max} for **CNMS5** is shifted from 610 nm to 695 nm after the addition of water). Infiltration with isopropanol ($n = 1.38$) gives a CD signal that is further red-shifted and considerably less intense than that observed for water based on a small difference in refractive index. Wetting the films with DMSO ($n = 1.48$) completely eliminates the CD signal due to near-perfect refractive index matching with SiO_2 . These results suggest that there are opportunities to employ these materials in optical sensing devices where small changes in the refractive index within the pores would result in changes in both the intensity and

position of the CD peak. This takes advantage of the sensitivity of circular dichroism and the unique combination of chirality, photonic properties, and mesoporosity in these materials.

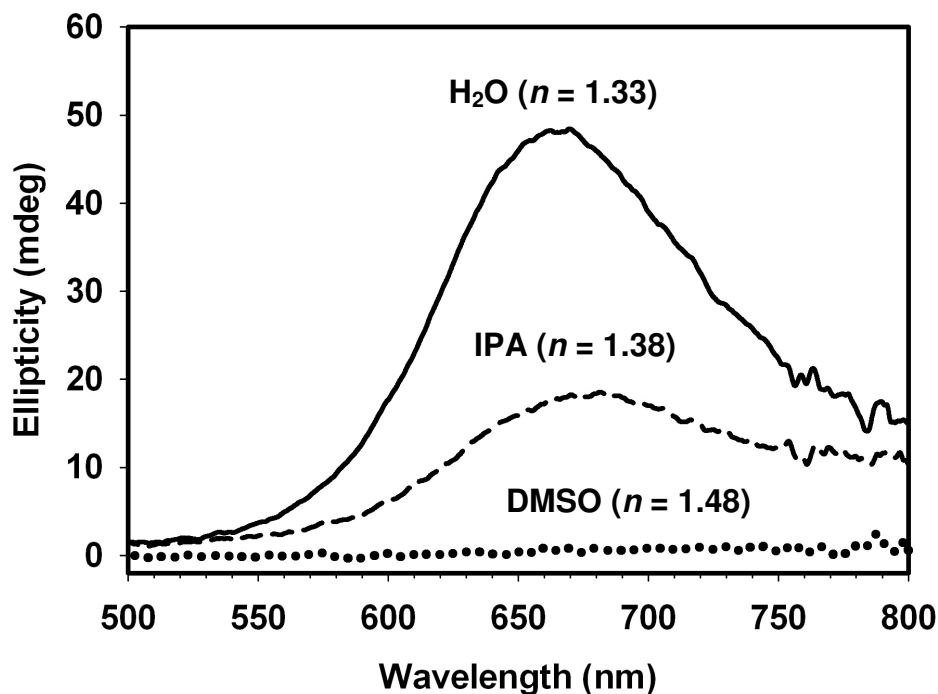


Figure 2-16. Circular dichroism spectra of CNMS5 after infiltration with different liquids.

2.4 Conclusions

I have discovered that nanocrystalline cellulose can be used to form composite materials with silica that have tunable photonic properties. These materials are formed using a simple self-assembly approach and have a left-handed chiral nematic structure. The removal of the NCC template from these materials gives free-standing mesoporous silica films where the chiral nematic organization and high surface area of nanocrystalline cellulose are accurately replicated in the inorganic solids. The helical structure of the mesoporous films results in chiral reflectance that can be tuned across the entire visible

spectrum and into the near infrared based on simple changes in the synthetic procedure. The combination of chiral nematic ordering and porosity in these materials causes their colours to respond to changes in refractive index within the mesopores, a property that could make them useful as “smart-windows” or sensors. In addition, these materials have the potential to be used as hard templates to synthesize a variety of other new materials with chiral nematic structures, which will be discussed in subsequent chapters. Future work will aim to further understand the pore structure of these materials and investigate whether their chirality makes them useful for applications such as enantioselective separation. Finally, the wide availability of cellulose combined with the simplicity of our approach make it plausible that bulk quantities of chiral nematic mesoporous silica could be produced at low cost.

Chapter 3

Chiral Nematic Mesoporous Organosilica Films*

3.1 Introduction

The incorporation of organic functionality into mesoporous silica provides a way to fine-tune its properties. An important advance in this area took place with the discovery that by using bridged silsesquioxane precursors of the general type $R(\text{Si}(\text{OR}')_3)_2$, periodic mesoporous organosilicas (PMOs) with integral organic groups could be directly synthesized using liquid crystal templating.^[110-112, 116, 179, 180] The direct use of bridged organosilica precursors provides a distinct advantage compared to post-synthetic grafting by allowing precise stoichiometric control over the relative amounts of inorganic and organic components within the hybrid material.^[108] Also, by incorporating the organic groups as integral components of the cross-linked structure, it is possible to not only change the chemical environment within the pores but also to modify material properties such as mechanical strength, hydrothermal stability, and molecular organization.^[114, 116, 181]

PMOs have been synthesized with diverse organic components providing potential applications in many areas including catalysis, chromatography, sensors, insulating materials, and fuel-cells.^[126, 182-186] PMOs incorporating chiral bridging groups have been synthesized and were shown to be effective materials for enantioselective catalysis and separation.^[118, 121, 187-190] Another approach to generate chiral PMOs is to use a chiral template.^[191] The use of abundant, naturally occurring chiral polymers as

* Portions of this chapter have been previously published as: K. E. Shopsowitz, W. Y. Hamad, M. J. MacLachlan, "Flexible and Iridescent Chiral Nematic Organosilica Films." *J. Am. Chem. Soc.* **2012**, *134*, 867-870.

templates provides an attractive route to generate enantiopure mesoporous organosilica materials. Along with the possibility of chiral imprinting into the mesopores of the organosilica, which could be useful for enantioselective recognition and separation, biological polymers can also template long-range, chiral photonic structures into mesoporous materials.^[90, 192]

Cellulose is the main structural component of plants and, being comprised entirely of D-glucose monomers, is inherently chiral. Bulk cellulose may be converted into spindle-shaped nanocrystalline cellulose that behaves as a chiral nematic lyotropic liquid crystal.^[46, 49, 55] In Chapter 2 I discussed the use of NCC as a template for chiral nematic mesoporous silica (CNMS). In this chapter, I describe the expansion of this approach to chiral nematic mesoporous organosilica materials. The first part of this chapter reports in detail the synthesis and characterization of ethylene-bridged chiral nematic mesoporous organosilica (Et-CNMO), which shows improved mechanical properties compared to CNMS. At the end of the chapter, the synthesis of several other bridged mesoporous organosilicas is presented. These materials present the first example of a new family of functional photonic materials based on organosilica chemistry and NCC.

3.2 Experimental

3.2.1 General

All solvents and reagents including 1,2-bis(trimethoxysilyl)ethane (BTMSE, Sigma Aldrich), bis(triethoxysilyl)methane (BTESM, Gelest), 1,6-bis(trimethoxysilyl)hexane (BTMSH, Gelest), 1,4-bis(triethoxysilyl)benzene (BTESB, Gelest), and tetramethoxysilane (TMOS, Acros) were purchased and used without further

purification. NCC was prepared according to the procedure described in Chapter 2, section 2.2.4.

Two different batches of NCC were used throughout this chapter. Experiments performed with a 3 wt. % NCC suspension all use the same batch of NCC that was used throughout Chapter 2. Experiments performed with a 3.5 wt. % suspension involve a different batch of NCC (preparation of organosilica films with methylene, phenylene, and hexylene bridges). To the best of our knowledge, these two batches of NCC were prepared in the same way; however, there are some differences between them that are discussed in more detail in Appendix B.

Thermogravimetric analysis was performed under air on a PerkinElmer Pyris 6 thermogravimetric analyzer. Elemental analysis was carried out by UBC microanalytical services. N₂ adsorption studies were performed using a Micromeritics ASAP 2000 at 77 K. All samples were degassed for 2 hours under vacuum at 100 °C immediately prior to analysis. BJH pore size distributions were all calculated from the adsorption branch of the isotherm. IR spectra were obtained with a Nicolet 6700 FT-IR equipped with a Smart Orbit diamond ATR. Powder X-ray diffraction patterns were collected using a D8 advance X-ray diffractometer. Tensile strength measurements were carried out on a Deben microtensile stage equipped with a 200 N load cell. Films were cut into ~15 mm x 5 mm strips and elongated at a constant rate of 0.1 mm/min until fracture occurred.

3.2.2 Spectroscopic Characterization

UV-visible/near-IR spectroscopy was conducted on a Cary 5000 UV-Vis/NIR spectrophotometer. Transmission spectra were collected by mounting free-standing films so that the surfaces of the films were perpendicular to the beam path. The maximum transmittance was set to 100% in a region away from the reflectance peak. CD

experiments were performed using a JASCO J-815 spectropolarimeter. Spectra were collected by mounting free-standing films so that the surfaces of the films were perpendicular to the beam path. For the dry films, small pieces were used that did not completely cover the aperture (the CD signals from larger pieces are too intense and saturate the detector). The CD signals measured for the dry films were all normalized to the same intensity for the purpose of comparison. Because the intensity of the wet films is drastically reduced compared to the dry films, films that completely covered the aperture were used allowing for quantitative comparison of CD signal between the samples. Solid-state NMR spectra were collected on a 400 MHz Varian Unity Inova. ^{13}C CP/MAS experiments (100 MHz, 3000 acquisitions) used glycine as a reference and ^{29}Si CP/MAS experiments (80 MHz, 16000 acquisitions) used DSS as a reference.

3.2.3 Sucrose Sensing Experiments

Sucrose sensing experiments were carried out using a JASCO J-815 spectropolarimeter. To ensure that the mesoporous organosilica film did not move during testing, the film was secured onto a piece of glass using epoxy resin, which was then further secured inside a quartz cuvette. The sucrose solutions were loaded into the cuvette containing the immobilized film (starting with the most dilute solution), which was then given 5 minutes to equilibrate before each measurement.

3.2.4 Microscopy

TEM images were collected on a Hitachi H7600 electron microscope. Samples were prepared by first grinding the films into a fine powder, suspending them in ethanol, and then dropcasting them onto a carbon-coated copper TEM grid. SEM images were collected on a Hitachi S4700 electron microscope. Samples were prepared by breaking

the films into small pieces and attaching them to aluminum stubs using double-sided adhesive tape. The samples were then sputter-coated with 5 nm of either gold or gold-palladium. Polarized optical microscopy was performed on an Olympus BX41 microscope. All images were taken with the polarizers in a perpendicular (crossed) arrangement unless otherwise noted. Helium ion microscopy was performed on a Zeiss Orion Plus Helium Microscope. Images were taken without sputter-coating at an accelerating voltage of 31 kV.

3.2.5 Preparation of NCC/Silica and NCC/Organosilica Composite Films

For the NCC/silica sample (**Comp3**) and the **Et-Comp** series of samples the following general procedure was used. Chiral nematic NCC/(organo)silica composite films were prepared by first sonicating a 3 wt. % aqueous NCC suspension for 10 minutes. TMOS or BTMSE was then added to the suspension dropwise and left to stir at room temperature for 1 h to obtain a homogeneous mixture. The NCC/TMOS or NCC/BTMSE mixtures were then poured into polystyrene Petri dishes (5 mL / 60 mm diameter dish) and left to dry under ambient conditions (typically 18-24 h were required for complete drying). The ratio of NCC/TMOS used for **Comp3** was the same as that reported for **Comp3** in Chapter 2 (1.36 mmol TMOS / 150 mg NCC). For the amounts of BTMSE used for the different chiral nematic composite samples (**Et-Comp1-4**), please refer to Table 3-1.

Chiral nematic NCC/organosilica composite films with different bridging groups were prepared using a different batch of NCC that had an initial concentration of 3.5 wt. %. The NCC/organosilica films **Me-Comp**, **Bz-Comp**, and **Hex-Comp** were prepared using the following general procedure. Ethanol was added to the 3.5 wt. % aqueous NCC suspension up to a concentration of 33% v/v for the preparation of **Me-Comp**, or

alternatively to a concentration of 50% v/v for the preparation of **Bz-Comp** and **Hex-Comp**. After 10 min sonication, the organosilica precursors were added dropwise to the NCC suspension with stirring (a ratio of 0.57 mmol precursor / 150 mg NCC was used for **Me-Comp** and **Hex-Comp**, and 0.48 mmol precursor / 150 mg NCC was used for **Bz-Comp**). Stirring of the mixtures was continued at room temperature until they appeared homogeneous (typically 2-3 h). The NCC / organosilica precursor mixtures were then transferred to polystyrene Petri dishes (7.5 mL / 60 mm dish for **Me-Comp** and 10 mL / 60 mm dish for **Bz-Comp** and **Hex-Comp**) and left to dry under ambient conditions.

3.2.6 Preparation of Mesoporous Silica and Organosilica

Et-CNMO, CNMS-H₂SO₄, Me-CNMO, and Hex-CNMO

For the removal of NCC, the composite films (~600 mg) were placed in 900 mL of 6 M sulfuric acid and heated to 100 °C for 18 h (this was done without stirring in order to avoid breaking the films). The films were then filtered, washed with 1 L of water, and alternately washed with a room-temperature solution of piranha (20 mL 30% H₂O₂ / 100 mL H₂SO₄) and water until they appeared colourless. The films were then rinsed with 2 L of water and allowed to air-dry.

CNMS-HCl

The NCC/silica composite films were placed in 12 M HCl (~500 mg / 500 mL) and heated to 85 °C for 18 h without stirring to avoid breaking the films. After cooling to room temperature and filtering, the films were washed with piranha solution as described above.

Bz-CNMO

The NCC/organosilica composite films were treated in 12 M HCl as described above. After filtration, 100 mg of films were placed in 20 mL of 30% hydrogen peroxide solution with 15 mg of silver nitrate and heated to 70-80 °C until the films appeared colourless (typically 2-3 h). The films were then filtered and heated to 70 °C in distilled water for 18 h before the final filtration and air-drying steps.

3.3 Results and Discussion

3.3.1 Preparation of NCC/Organosilica Composite Films

NCC produced through sulfuric acid hydrolysis of wood pulp was used in this study as the chiral nematic liquid crystal template while 1,2-bis(trimethoxysilyl)ethane (BTMSE) was initially tested as the organosilica precursor. When I initially set out, it was uncertain whether: a) the organosilica precursor would be compatible with the chiral nematic self-assembly of NCC and b) whether it would be possible to remove NCC from the composite materials without degrading the organic bridging group. BTMSE was first tested for its ability to form a homogeneous mixture with NCC without disrupting its chiral nematic self-assembly. When added to an isotropic NCC suspension (3 wt. % in water, pH 2.4), BTMSE is initially immiscible but dissolves after stirring for several minutes at room temperature. After stirring for 1 h at 20 °C, the NCC/BTMSE mixture was allowed to dry in polystyrene Petri dishes under ambient conditions to obtain free-standing films. The composite films show strong selective reflection of light, demonstrating that BTMSE does not negatively affect the self-assembly of NCC into a chiral nematic structure. By varying the relative amounts of BTMSE and NCC, four different composite samples were obtained with reflectance peaks ranging from 700-900

nm (**Et-Comp1-4**). A red shift in the reflectance peaks of the NCC-organosilica composite films occurs with increasing amounts of BTMSE, allowing the optical properties of the films to be easily tuned (Table 3-1, Figure 3-1). This is the same trend that was reported in Chapter 2 for increased loadings of TMOS in the synthesis of NCC/silica composites and is related to an increase in helical pitch with increased BTMSE loading. The ethylene-bridged NCC/organosilica films crack less during drying compared to NCC/silica films and films can be obtained with lengths and widths > 5 cm in some instances.

Table 3-1. Ethylene-bridged NCC/organosilica composite films.

Sample	mmol BTMSE / 150 mg NCC	λ_{\max} (nm)
Et-Comp1	0.49	695
Et-Comp2	0.67	776
Et-Comp3	0.79	837
Et-Comp4	0.99	903

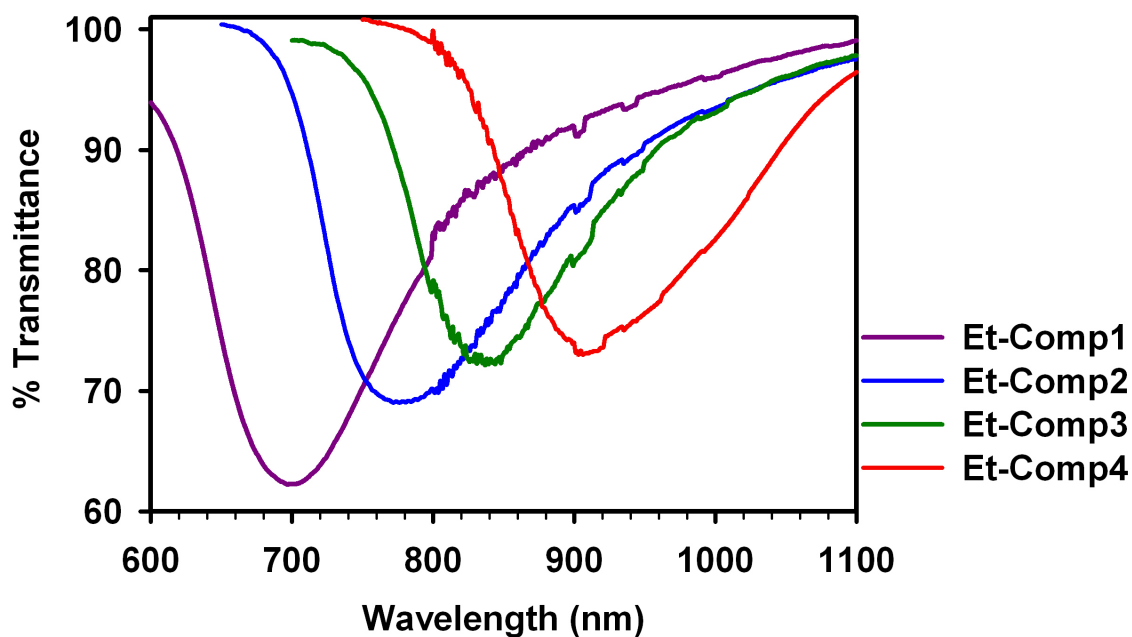


Figure 3-1. UV-Vis/NIR spectra of **Et-Comp1-4**.

3.3.2 Removal of NCC from Ethylene-Bridged NCC-Organosilica Composite Films

A new approach had to be developed to remove NCC from the organosilica composite materials to generate mesoporous organosilica since the elevated temperature required for cellulose decomposition also leads to decomposition of the organic bridging group. NCC can be hydrolyzed under strongly acidic conditions and I found that selective removal of cellulose from the NCC/organosilica composites can be achieved by heating the films to 90-100 °C in 6 M sulfuric acid. This treatment followed by a brief rinsing with piranha solution (to remove brown, insoluble cellulosic byproducts) results in transparent and colourless films that become strongly iridescent after drying. The films remain intact for the most part during the cellulose removal procedure and free-standing organosilica films with dimensions of several centimeters can be obtained. Four ethylene-bridged organosilica samples (**Et-CNMO1-4**) were prepared from composite samples **Et-Comp1-4**, respectively.

The complete removal of NCC and retention of the ethylene bridge in the organosilica films was confirmed using a variety of techniques. Solid-state ^{13}C and ^{29}Si CP/MAS (cross-polarization magic angle spinning) NMR spectroscopy were carried out before and after the acid hydrolysis procedure for **Et-Comp3**. The ^{13}C NMR spectrum of the composite sample shows peaks between 60-120 ppm, assigned to cellulose, and a single peak at 5 ppm that corresponds to the ethylene ($\text{SiCH}_2\text{CH}_2\text{Si}$) carbons of the organosilica (Figure 3-2).^[110, 111] After the acid hydrolysis treatment, only the single peak of the organosilica remains, demonstrating that cellulose is selectively removed.

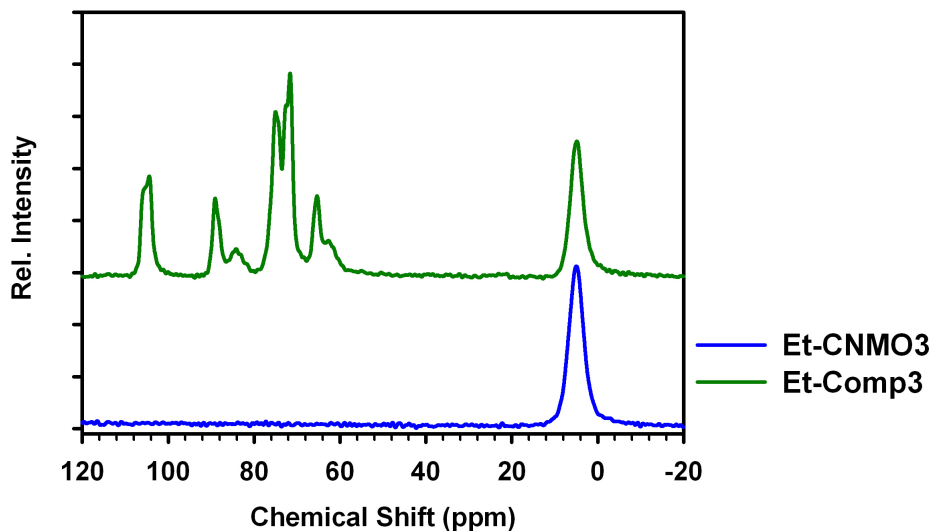


Figure 3-2. ^{13}C CP/MAS solid-state NMR of ethylene-bridged organosilica before (green) and after (blue) the removal of NCC.

Solid-state ^{29}Si CP/MAS NMR spectroscopy, both before and after NCC removal (Figure 3-3), shows peaks characteristic of ethylene-bridged organosilica at -65 and -57 ppm that can be assigned to T^3 ($\text{CSi}(\text{OSi})_3$) and T^2 ($\text{CSi}(\text{OSi})_2\text{OR}$, where $\text{R} = \text{C}$ or H) Si environments, respectively.^[110, 111] The absence of signals corresponding to SiO_4 species between -90 and -120 ppm demonstrates that Si-C bond cleavage does not occur during NCC removal. While the T^2 peak is larger than the T^3 peak before NCC removal, the relative intensities are reversed after the acid treatment. Overall, this tells us that there is a net formation of Si-O-Si bonds during the acid-catalyzed removal of NCC. A large component of the T^2 peak in the composite sample likely corresponds to Si-OH groups stabilized by hydrogen bonding with NCC and Si-O-C covalent bonds between the organosilica and NCC. The decrease in T^2 signal indicates that some of the surface Si-OH groups generated during NCC removal condense to form Si-O-Si bonds under the acidic conditions that were employed.

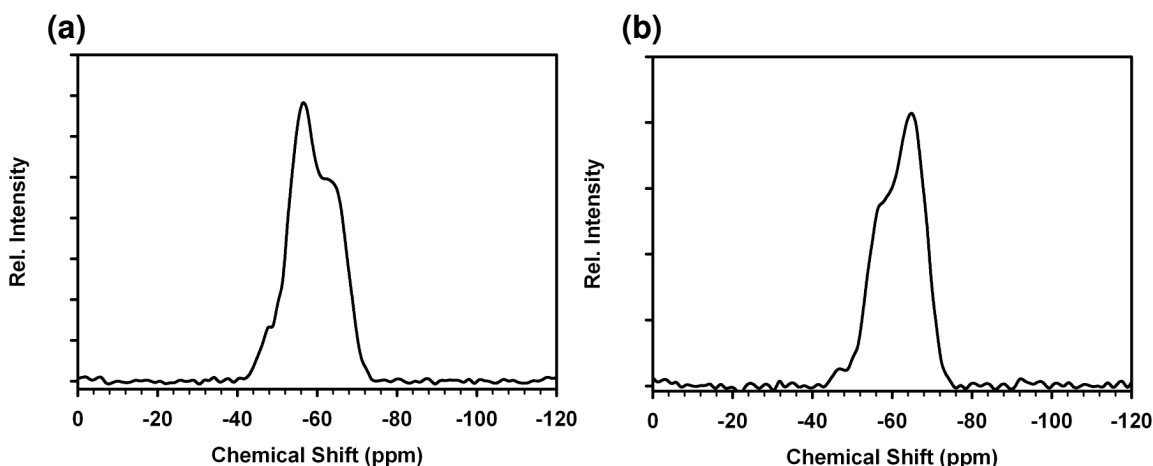


Figure 3-3. ^{29}Si CP/MAS solid-state NMR spectra of (a) **Et-Comp3** and (b) **Et-CNMO3**.

Elemental analysis of the ethylene-bridged organosilica samples shows that they contain ~14 wt. % carbon and ~4 wt. % hydrogen after the removal of NCC. For comparison, the predicted values for an organosilica with the formula $\text{Si}_2\text{C}_2\text{H}_5\text{O}_{3.5}$ (corresponding to an ethylene-bridged material with equal amounts of T^2 and T^3 silicon environments) are 17 wt. % carbon and 3.6 wt. % hydrogen. This suggests that the organosilica has slightly more uncondensed Si-OH groups than indicated by the above formula, although surface adsorbed water may also have affected the measurements. Thermogravimetric analysis (TGA) shows that the organosilica is stable up to 400 °C, after which decomposition of 14-18 wt. % occurs (Figure 3-4a). In contrast, elemental analysis and TGA of mesoporous silica control samples that were prepared using the same procedure (except with $\text{Si}(\text{OCH}_3)_4$ used in place of BTMSE, **CNMS3- H₂SO₄**) show that no residual organic material is present (Figure 3-4b), further confirming that the acid hydrolysis conditions employed are sufficient for the complete degradation and removal of cellulose.

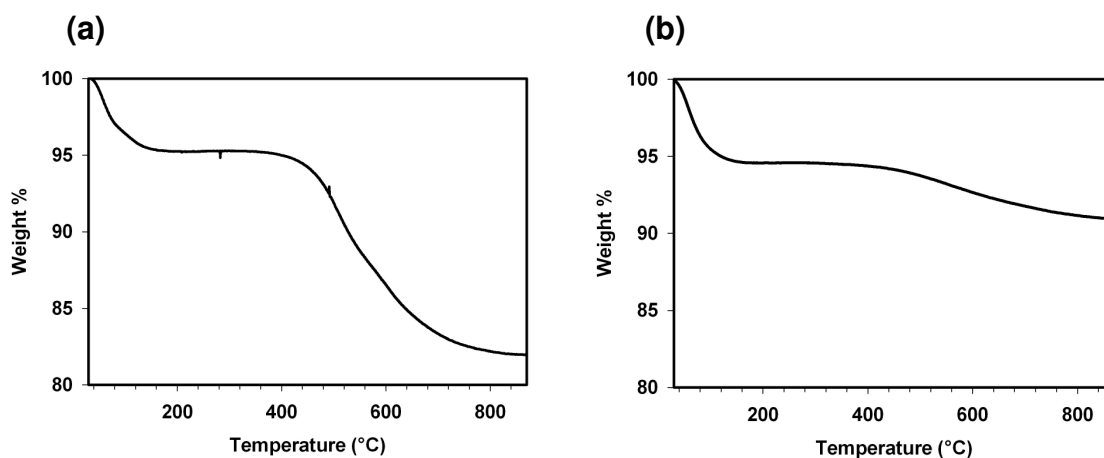


Figure 3-4. TGA of (a) Et-CNMO3 and (b) CNMS3- H₂SO₄.

3.3.3 Chiral Nematic Optical and Structural Properties of Ethylene-Bridged Organosilica

Organosilica samples **Et-CNMO1-4** show peak reflected wavelengths that cover the visible spectrum from 400-750 nm (Figure 3-5). The iridescence of the organosilica films confirms that their chiral nematic structure is retained after NCC removal. This was further confirmed by circular dichroism (CD), which shows strong positive signals with positions that match up closely with the reflectance peaks of the films, indicating that they selectively reflect left-handed circularly polarized light (note that due to the extremely large CD signal generated by these materials, small pieces of film were used to avoid saturating the detector).

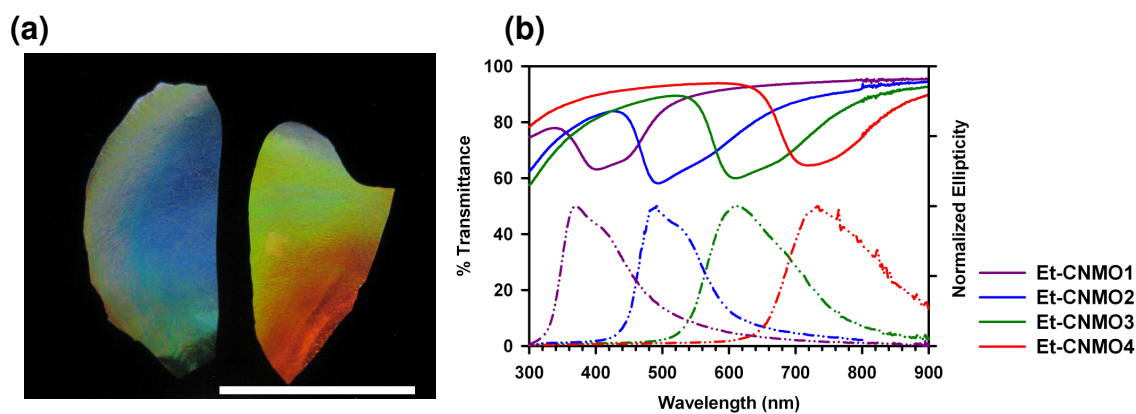


Figure 3-5. Optical characterization of Et-CNMO films. (a) Photograph of **Et-CNMO2** (left) and **Et-CNMO3** (right, scale bar = 18 mm). (b) UV-Vis/NIR (solid lines) and CD spectra (dashed lines) of **Et-CNMO1-4**.

As was reported for the silica films in Chapter 2, the colours of the organosilica films are all blue-shifted relative to the corresponding composite films. Again, this blue shift can be caused by a decrease of the helical pitch (P) or average refractive index (n_{avg}). The blue shifts seen for the organosilica films are considerably smaller than what was reported for calcined silica in Chapter 2, and can mostly be attributed to the decrease in refractive index that occurs upon the removal of NCC. This indicates that the removal of NCC by acid hydrolysis in the **CNMO** films avoids much of the contraction in helical pitch that occurs upon calcination of the **CNMS** films.

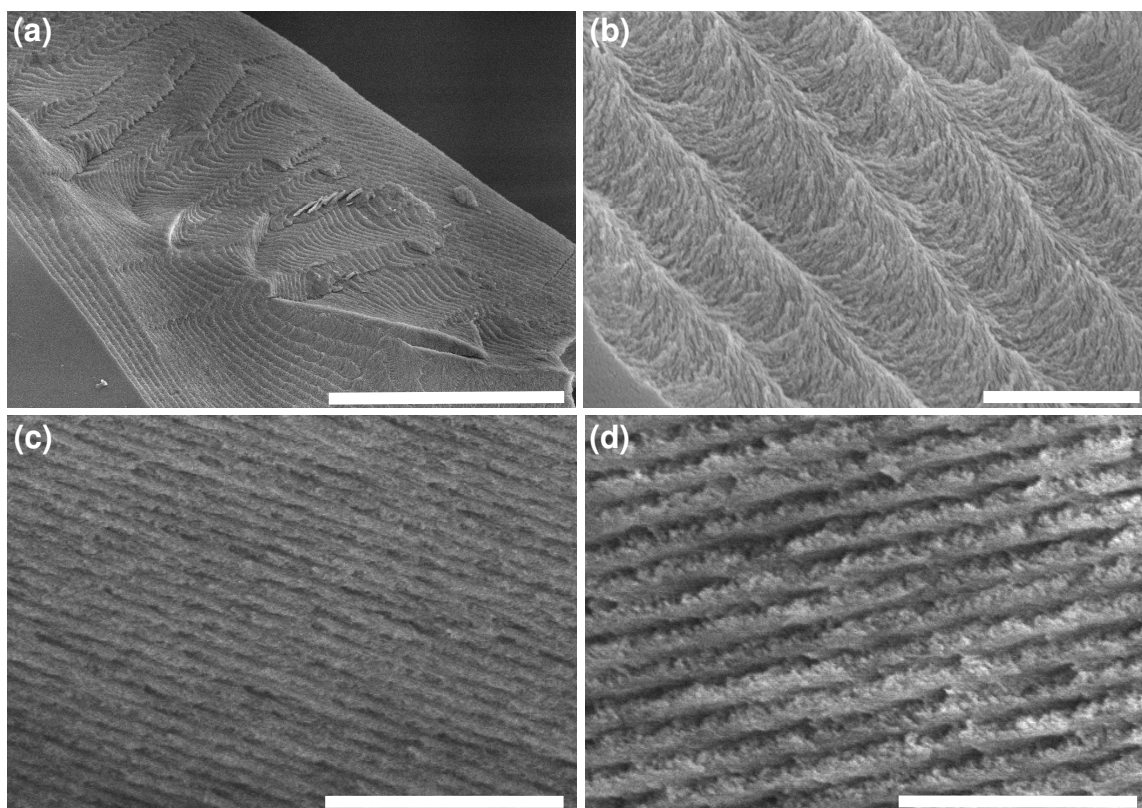


Figure 3-6. SEM images of Et-CNMO films. (a) Top view of fracture for **Et-CNMO3** (scale bar = 30 μm). (b) High magnification micrograph of **Et-CNMO3** (scale bar = 1 μm). (c) Cross-sectional micrograph of **Et-CNMO1** (scale bar = 2 μm). (d) Cross-sectional micrograph of **Et-CNMO4** (scale bar = 2 μm).

The chiral nematic organization of the **Et-CNMO** films was directly observed by scanning electron microscopy (SEM, Figure 3-6). At fractures, a periodic structure typical of chiral nematic organization is observed throughout the entire thickness of the films. At higher magnification, it is apparent that the material consists of organosilica rods with a director that rotates in a counter-clockwise direction when moving away from the viewer. This gives rise to the long-range helical structure responsible for the selective reflection of left-handed circular-polarized light. Comparing the SEM cross-sections of samples **Et-CMNO1** and **Et-CMNO4**, it is apparent that the helical pitch of **Et-CMNO1** ($P = 290 \text{ nm}$) is considerably shorter than that of **Et-CMNO4** ($P = 510 \text{ nm}$). This confirms that increasing the relative amount of BTMSE used to synthesize the films

causes an increase in their helical pitch, which in turn causes a red shift of their reflected colours. This is the same trend that was reported for TMOS in Chapter 2.

3.3.4 Porosity Characterization of Chiral Nematic Organosilica and Silica Samples Prepared by Acid Hydrolysis of NCC

The porosity of the organosilica films was investigated using nitrogen adsorption-desorption as shown in Figure 3-7. The organosilica samples **Et-CNMO1-4** display type IV isotherms with hysteresis, which is indicative of mesoporosity. BET surface areas and specific pore volumes ranging from 400-524 m²/g and 0.6-1 cm³/g, respectively, were calculated for samples **Et-CNMO1-4**. From Table 3-2 it can be seen that there is no obvious correlation between the surface area, pore volume, and the amount of organosilica precursor used. It is possible that at lower BTMSE loadings there is some structural instability that leads to pore collapse upon NCC removal. This is supported by the fact that the peak BJH pore diameter is smallest for the sample with the lowest BTMSE loading, increases from **Et-CNMO1-3**, and is identical for **Et-CNMO3-4**.

The BJH pore size distributions of the **Et-CNMO** samples are fairly broad going from ~5-20 nm with peaks ranging from 6.5-9 nm for the different samples. This is considerably larger than the pore size distributions obtained for NCC-templated mesoporous silica generated by calcination. The reason for the larger pore diameter of the organosilica films may simply be that the use of acid hydrolysis to remove NCC results in less contraction than occurs during calcination. The pore size distribution for the **Et-CNMO** samples more closely reflects the width of the NCC template measured by transmission electron microscopy (TEM), which gives a range of ~5-15 nm, and by PXRD, which gives an average crystallite width of 8.2 nm.^[51]

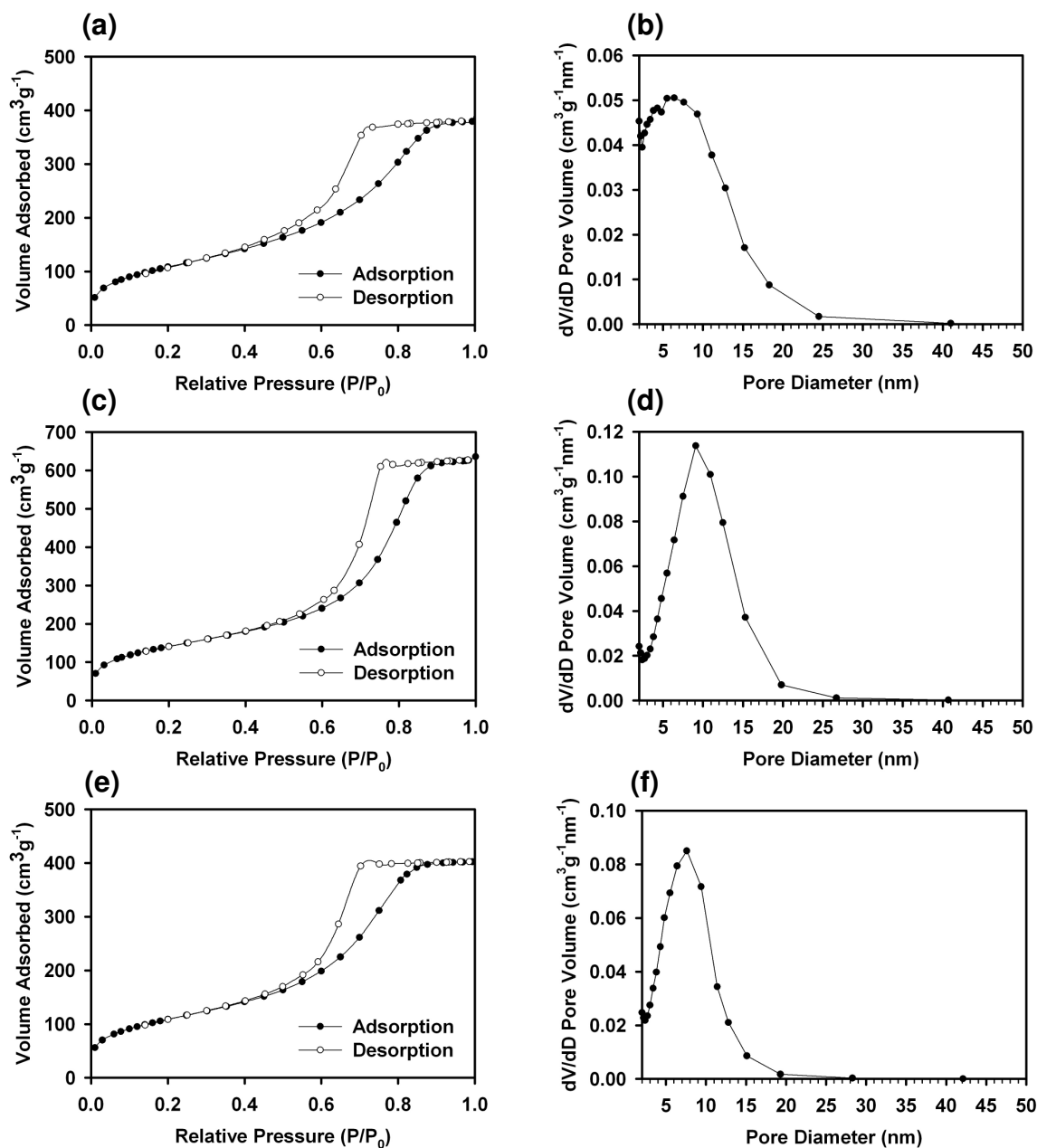


Figure 3-7. Nitrogen adsorption data for selected ethylene-bridged mesoporous organosilica samples. (a) N_2 isotherm for **Et-CNMO1**. (b) BJH pore size distribution for **Et-CNMO1**. (c) N_2 isotherm for **Et-CNMO3**. (d) BJH pore size distribution for **Et-CNMO3**. (e) N_2 isotherm for **Et-CNMO3-Cal**. (f) BJH pore size distribution for **Et-CNMO3-Cal**.

N_2 adsorption was also measured after calcining **Et-CNMO3** at 540 °C (**Et-CNMO3-Cal**) and shows that the pore diameter shrinks slightly from 9 nm to 7.5 nm due to contraction that occurs upon the removal of the ethylene bridge. In contrast, direct

calcination of NCC/organosilica composite sample **Et-Comp3** results in a material with even smaller pores than were measured for the calcined mesoporous silica samples reported in Chapter 1 (peak pore diameter <3 nm).

Table 3-2. Nitrogen adsorption characterization of acid hydrolyzed samples.

Sample	BET Surface Area (m ² /g)	Pore Volume (cm ³ /g)	BJH Pore Diameter (nm) ^a
Et-CNMO1	400	0.59	6.5
Et-CNMO2	524	0.82	8.5
Et-CNMO3	515	0.97	9
Et-CNMO4	400	0.79	9
Et-CNMO3-Cal	399	0.62	7.5
CNMS3-H₂SO₄	325	1.22	22
CNMS3-HCl	430	1.0	11
CNMS3-HCl-Cal	427	0.88	10.5

a) Calculated from the adsorption branch of the isotherm using the BJH method.

Et-CNMO3 was also investigated by helium ion microscopy, which is an imaging technique similar to SEM but has the advantage that it does not require sputter coating for non-conductive samples and can achieve higher resolution. This allowed us to clearly visualize the porous structure of **Et-CNMO3**, as shown in Figure 3-8. The organosilica rods are interconnected by small bridges and have void spaces that are generated by the removal of NCC. In Figure 3-8, the chiral nematic axis is oriented vertically in the plane of the image and the organosilica rods rotate perpendicular to the plane of the image, which allows us to see the anisotropy of the pore structure. Regions where the rods are oriented perpendicular to the plane of the image appear highly porous since we are looking down the pore channels. Regions where the rods are oriented along the x-axis of the image do not appear very porous since we are looking perpendicular to the channels. Measurements of the pores throughout the image give an average diameter of 8.4 nm, which corresponds closely to the value determined by N₂ adsorption.

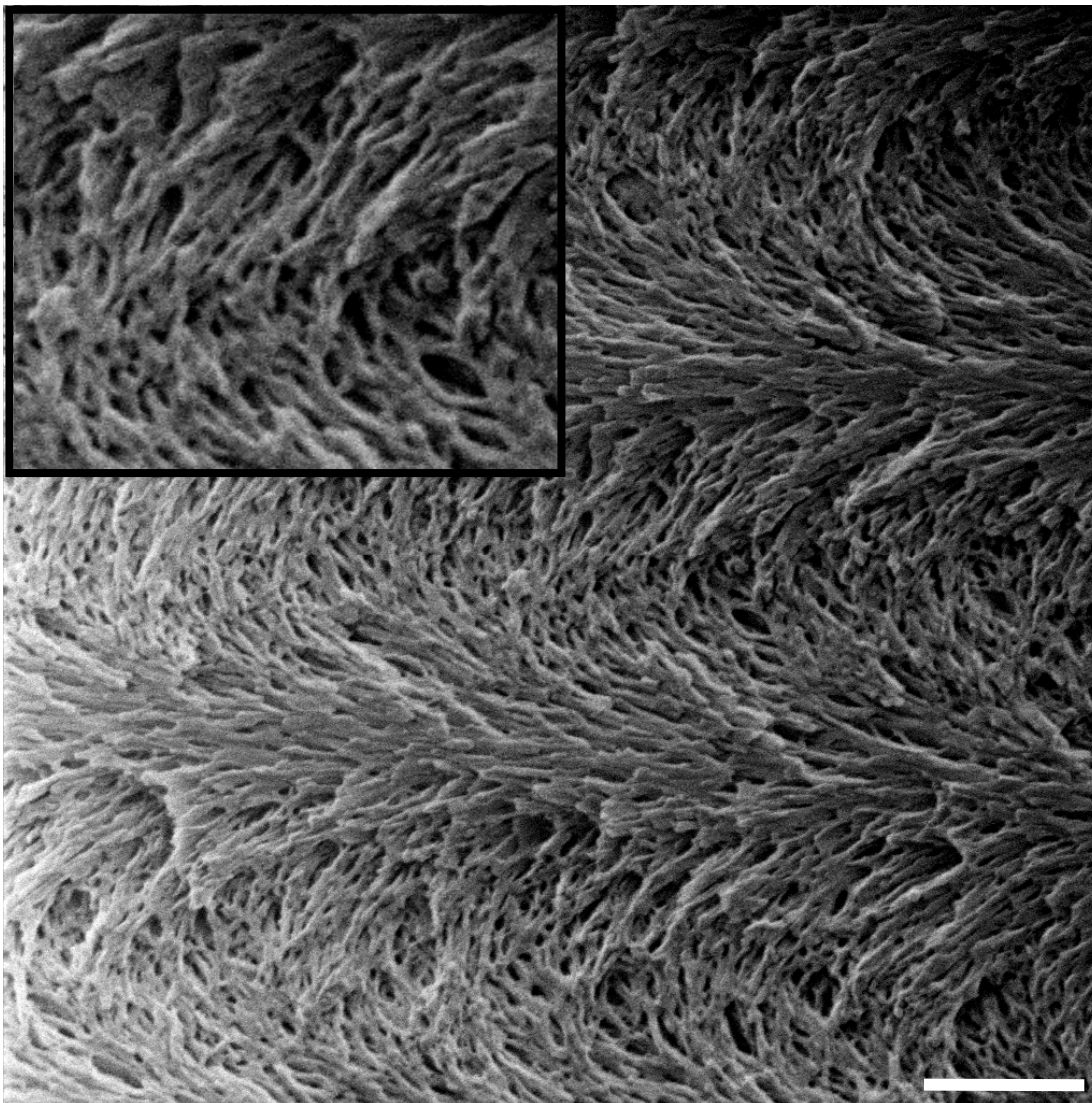


Figure 3-8. Helium ion micrograph of **Et-CNMO3** (scale bar = 200 nm). The inset shows a blown-up section taken from the middle of the image.

For comparison, the removal of NCC by acid hydrolysis was also investigated for an NCC/silica composite sample, **Comp3**, which has the same composition as **Comp3** reported in Chapter 2. I initially tested the same conditions that were used for the organosilica samples (6 M $\text{H}_2\text{SO}_4/100\text{ }^\circ\text{C}$ followed by rinsing with piranha solution), which as mentioned above gives pure silica without detectable organics present (denoted as **CNMS3- H_2SO_4**). N_2 adsorption measurements for **CNMS3- H_2SO_4** show that it has

significantly larger pores compared to the **Et-CNMO** samples (Figure 3-9a-b). Ethylene-bridged mesoporous organosilica has been shown to have greater hydrothermal stability^[111, 114] than pure silica and it appears that the larger pore size measured for **CNMS3-H₂SO₄** is caused by silica dissolution under these conditions. I also examined the removal of NCC from the NCC/silica composite **Comp3** using other strong acids and found that 12 M HCl at 85 °C (again followed by brief rinsing with piranha solution) gives mesoporous silica (denoted as **CNMS3-HCl**) with a similarly shaped isotherm and pore size distribution (although slightly larger) compared to the **Et-CNMO** samples (Figure 3-9c-d). In contrast, the acid used (H₂SO₄ vs. HCl) does not seem to significantly influence the porosity of the **Et-CNMO** samples. The pore volume of **CNMS3-HCl** is 1.0 cm³/g, which is considerably larger than the pore volume reported for calcined **CNMS3** in Chapter 2 (0.46 cm³/g). By taking the wt. % of NCC in **Comp3** (65%) and using a density for NCC of 1.6 g/cm³,^[46] one can calculate that the theoretical pore volume upon removing all of the NCC should be 1.15 cm³/g. This further confirms that there is considerable structural collapse that occurs during calcination that can be largely avoided through using acid hydrolysis to remove NCC.

The thermal stability of the larger mesopores present in **CNMS3-HCl** was investigated by measuring N₂ adsorption after heating the sample to 540 °C for 6 h (Figure 3-9e-f). There is virtually no change in the pore size distribution after this thermal treatment, which demonstrates that the smaller pores seen for the calcined **CNMS** samples are not simply caused by thermal instability. One possibility is that the structural collapse that occurs during calcination may in part be due to the build up of pressure from volatile species generated from cellulose decomposition. It is also possible that the HCl treatment used to remove NCC causes further condensation of the silica network that stabilizes it before thermal treatment. Taken together, these results demonstrate that

different pore size regimes in NCC-templated silica and organosilica can be accessed depending on the conditions used for NCC removal.

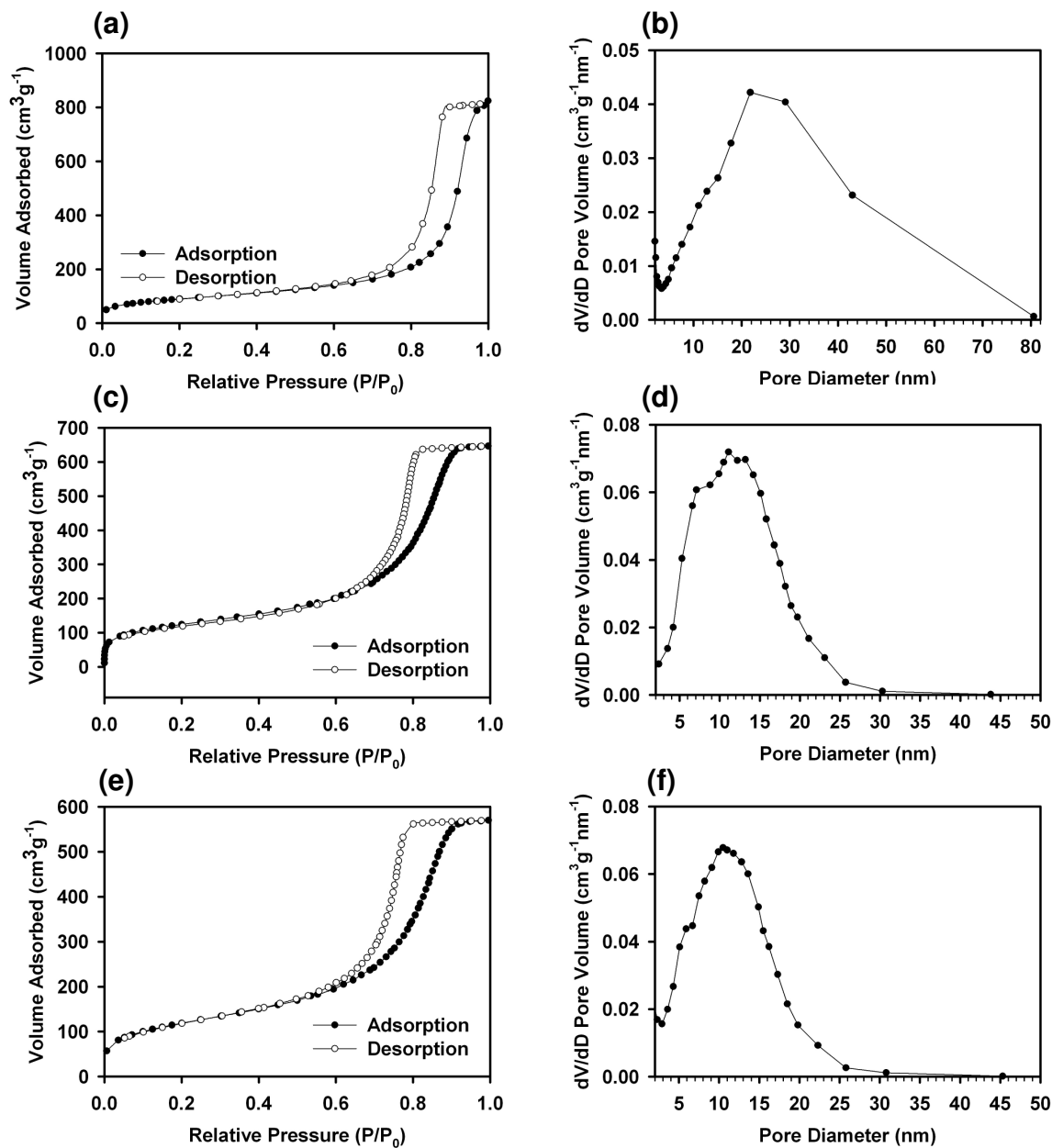


Figure 3-9. Nitrogen adsorption data for mesoporous silica films prepared by acid hydrolysis of **Comp3**. (a) N₂ isotherm for **CNMS3-H₂SO₄**. (b) BJH pore size distribution for **CNMS3-H₂SO₄**. (c) N₂ isotherm for **CNMS3-HCl**. (d) BJH pore size distribution for **CNMS3-HCl**. (e) N₂ isotherm for **CNMS3-HCl-Cal**. (f) BJH pore size distribution for **CNMS3-HCl-Cal**.

3.3.5 Mechanical Properties of Et-CNMO Films

The ethylene-bridged mesoporous organosilica films show significantly improved mechanical properties compared to pure mesoporous silica (either prepared by calcination or acid treatment of NCC-silica composites). Whereas the pure silica films are very brittle, the organosilica films are considerably less fragile and are fairly flexible. Large crack-free films can be readily prepared that can be handled with tweezers, bent, and easily attached to different substrates (Figure 3-10a). Due to their flexibility, when the mesoporous organosilica films absorb liquids, they rapidly flex towards the direction of the liquid before relaxing again.

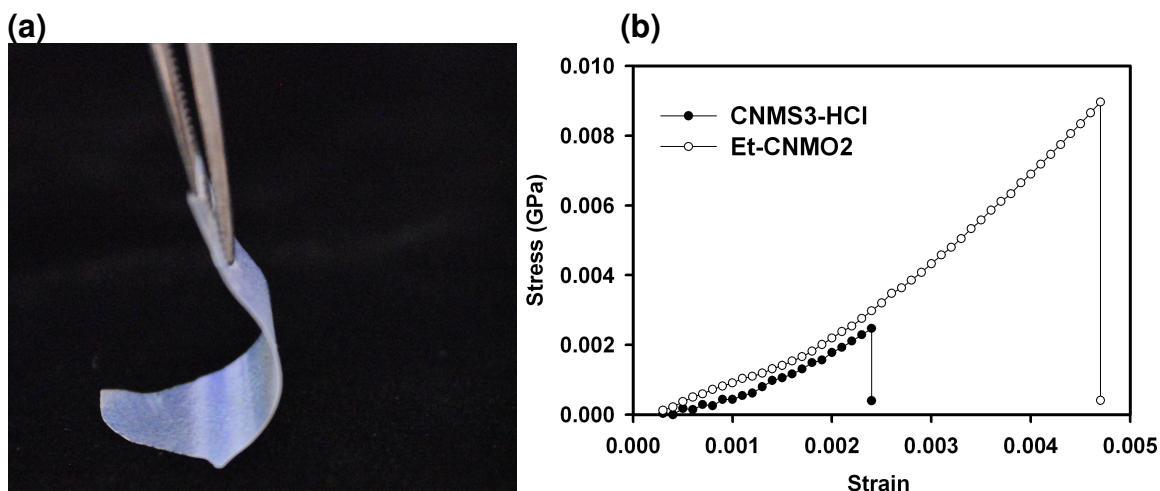


Figure 3-10. Improved flexibility of Et-CNMO films. (a) Photograph of a film from sample **Et-CNMO2** being bent with tweezers. (b) Comparison of stress-strain curves obtained from tensile testing of mesoporous silica (**CNMS3-HCl**) and organosilica (**Et-CNMO2**) samples.

Tensile strength measurements were conducted on free-standing films of mesoporous organosilica and silica (prepared by acid hydrolysis of an NCC-silica composite). Stress-strain curves confirm that the organosilica films are less brittle than their silica counter-parts and can withstand greater stress and strain before fracturing (Figure 3-10b). The improved mechanical properties of ethylene-bridged mesoporous

organosilica films were recently attributed to bond trapping phenomena that lead to superior fracture energies.^[193]

3.3.6 Refractive Index Sensing with Et-CNMO Films

Absorption of liquids into the Et-CNMO films causes a reversible loss of iridescence due to refractive index matching between the pores and walls of the material. Figure 3-11 shows POM micrographs of an organosilica film taken at different time points after wetting with acetone. Immediately after wetting the films lose their birefringence and appear dark under crossed polarizers (Figure 3-11a). The films regain their colour and birefringence as the bulk liquid evaporates from the pores over the course of a few seconds (Figure 3-11b-c). The films then gradually change back to their original colour as the remaining adsorbed acetone evaporates (Figure 3-11c-d).

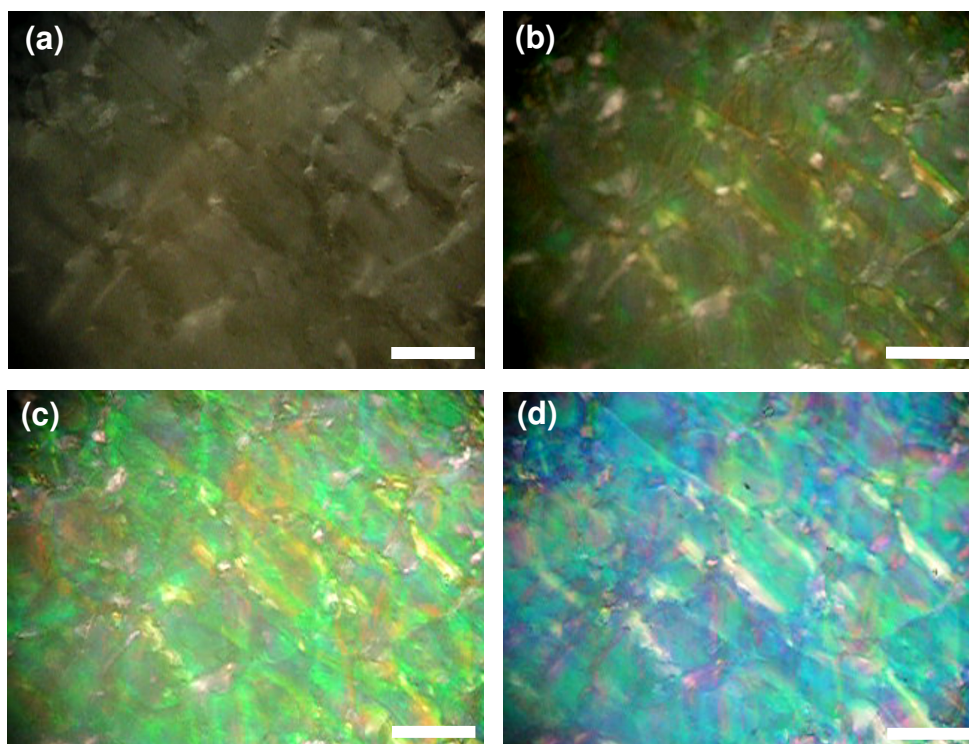


Figure 3-11. POM micrographs of Et-CNMO₂ taken at different time points after wetting with acetone. (a) Et-CNMO₂ immediately after wetting with acetone. (b) Et-CNMO₂ 15 seconds after wetting with acetone. (c) Et-CNMO₂ 17 seconds after wetting with acetone. (d) Et-CNMO₂ 30 seconds after wetting with acetone. All scale bars = 200 μm .

CD spectra were also measured for the organosilica films after soaking with different liquids (Figure 3-12). The CD spectra of the wet films show dramatically reduced intensities compared to the dry films. Because the refractive indices of the liquids used do not match perfectly with that of the organosilica walls, reflection still occurs from the wet films that, although undetectable to the naked eye, produces a strong CD signal. The residual CD signals for the **Et-CNMO** samples are considerably larger than those measured for chiral nematic mesoporous silica samples for all of the liquids that were tested, which reflects the higher refractive index of the organosilica walls compared to silica.

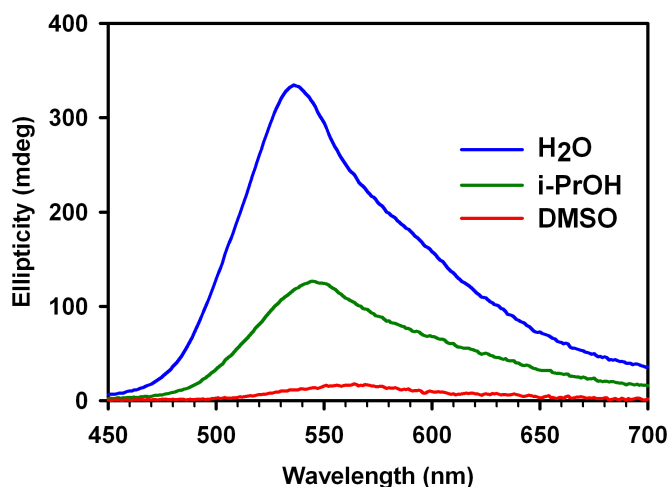


Figure 3-12. CD spectra of **Et-CNMO2** after wetting with different liquids.

The positions of λ_{\max} for the wet films are all red-shifted compared to the dry films due to the increase in n_{avg} that occurs upon wetting. As the refractive index of the infiltrating liquid increases, the position of λ_{\max} continues to shift to longer wavelengths, however, the change is not easily discernible due to the broadness of the peaks. The intensity of the CD signal on the other hand strongly depends on the refractive index of the liquid absorbed into the films. For example, the fairly small change in refractive index

going from water ($n = 1.33$) to isopropanol ($n = 1.38$) causes a very large decrease in the CD signal.

The effect of refractive index on the intensity of the CD signal was further probed by preparing a series of sucrose solutions at different concentrations. Figure 3-13a shows the CD spectra for **Et-CNMO2** after being infiltrated with aqueous sucrose solutions with concentrations ranging from 0-20% (wt. / vol.). Each 5% increase in sucrose concentration results in a change of approximately 0.01 in refractive index, which causes an easily detectable decrease in CD signal.

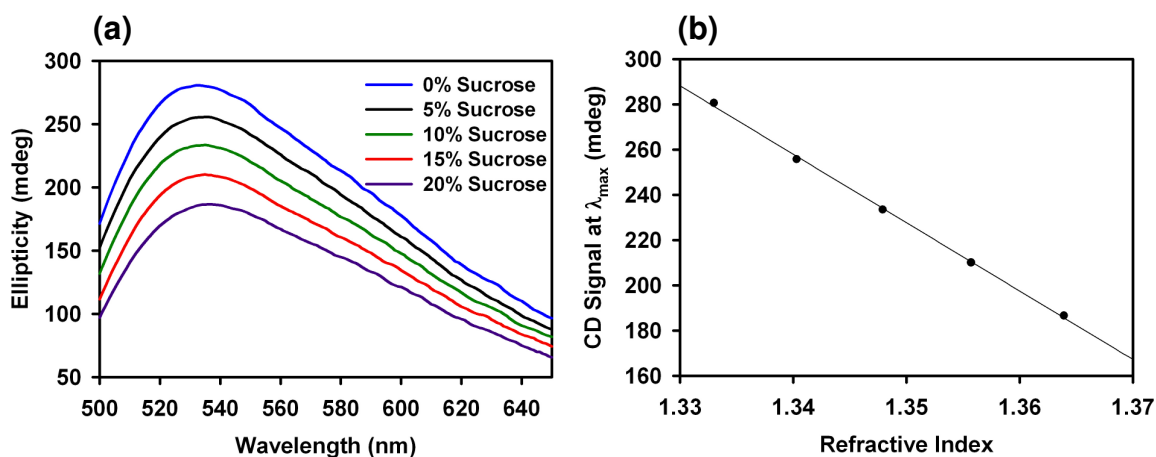


Figure 3-13. (a) CD spectra for **Et-CNMO2** after soaking with different aqueous sucrose solutions. (b) Plot of max CD signal vs. refractive index based on the spectra shown in (a).

The plot of CD signal intensity vs. refractive index gives a linear relationship for the range of sucrose solutions that were tested (Figure 3-13b) and from this a slope of $\Delta\theta/\Delta n = 3300$ was calculated. This means that assuming it is possible to resolve a change in CD signal of 1 mdeg, the minimum detectable change in refractive index would be 3×10^{-4} . This is comparable to porous silicon photonic crystal biosensors that can detect refractive index changes of as low as $\sim 2 \times 10^{-4}$ based on changes in the position of λ_{max} (assuming a resolution limit of 0.1 nm).^[194] Although the chiral nematic mesoporous silica samples can also be used for this type of sensing, the **Et-CNMO** films have the

advantage that they are easier to incorporate into a sensing device due to their superior mechanical properties.

3.3.7 Synthesis of Additional Organosilica Samples

A series of additional NCC/organosilica composite samples was prepared using a variety of precursors with different bridging groups, as shown in Figure 3-14. Initial attempts to prepare these materials used the same procedure described above for BTMSE; however, it was difficult to obtain homogeneous mixtures between NCC and the other organosilica precursors. The methylene and phenylene-bridged precursors that were commercially available are both bis(triethoxysilyl) compounds (BTESM and BTESB, respectively), which significantly decreases their rate of hydrolysis and water solubility. Although the hexylene-bridged precursor (BTMSH) is a bis(trimethoxysilyl) compound, the hydrophobic hexylene group causes it to be only sparingly soluble in water.

The colloidal stability and chiral nematic self-assembly of NCC are tolerant to large amounts of ethanol. The solubility of the different organosilica precursors is significantly improved by adding ethanol (30-50% v/v) to the NCC suspensions and homogeneous mixtures are obtained after stirring for 1-3 h at room temperature. In this way organosilica composite films were obtained in an analogous fashion as was described above for BTMSE.

New NCC/organosilica composite samples were prepared with BTMSE, BTESB, and BTMSH, and the samples are denoted as **Me-Comp**, **Bz-Comp**, and **Hex-Comp**, respectively. The **Me-Comp** films appear similar to the **Et-Comp** series and form chiral nematic films over a wide range of compositions. The **Bz-Comp** samples also form transparent chiral nematic films over a range of BTESB loadings; however, at higher loadings the films become very brittle. The **Hex-Comp** samples form cloudy films that

do not appear to have any chiral nematic ordering even at relatively low BTMSH loadings (0.5 mmol / 150 mg NCC).

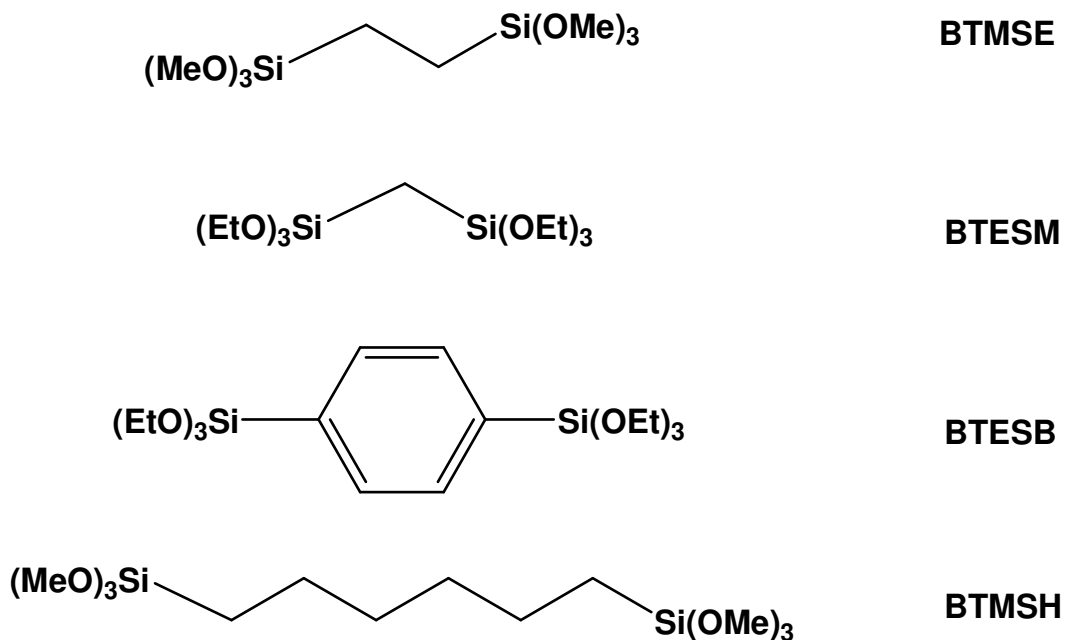


Figure 3-14. The different organosilica precursors used in this chapter.

The removal of NCC was carried out for representative samples of **Me-Comp** (0.57 mmol BTMSE / 150 mg NCC), **Bz-Comp** (0.48 mmol BTESB / 150 mg NCC), and **Hex-Comp** (0.57 mmol / 150 mg NCC). The **Me-Comp** and **Bz-Comp** samples chosen both had chiral nematic ordering while the **Hex-Comp** sample did not. Removal of NCC from the composite samples was initially attempted using sulfuric acid in the same way as previously described for the **Et-Comp** samples. After the piranha washing step, all of the samples appear completely colourless except for the phenylene-bridged material, which remains slightly yellow. Previous studies have reported that the benzene groups in phenylene-bridged organosilica can be sulfonated and we postulate that this occurred with the **Bz-Comp** sample during the sulfuric acid treatment.^[116] An alternative

procedure was therefore used to remove the NCC from **Bz-Comp** that avoids sulfuric acid. Briefly, the films were heated in 12 M HCl at 85 °C and then cleaned with 30% hydrogen peroxide/AgNO₃ catalyst in place of the piranha step, which resulted in colourless films.

The organosilica films obtained after NCC removal are denoted as **Me-CNMO**, **Bz-CNMO**, and **Hex-MO**. The **Me-CNMO** and **Bz-CNMO** films remain intact after NCC removal to give free-standing films. The **Hex-MO** films tend to fall apart after NCC removal and only a powder or very small films are recovered. **Me-CNMO** appears quite similar to the **Et-CNMO** samples and gives fairly flexible films whereas the **Bz-CNMO** films are more rigid and brittle. TGA, elemental analysis, and solid state NMR of the different organosilica films confirm the removal of NCC and show that the organic bridging groups remain intact (Table 3-3, Appendix B).

Table 3-3. Elemental analysis and N₂ adsorption data for different organosilica samples.

Sample	%C	%H	BET SA (m ² /g)	Pore Vol. (cm ³ /g)	BJH Pore Diameter (nm)
Me-CNMO	7.5	3.4	518	0.55	5.5
Bz-CNMO	31.6	3.6	740	0.74	5
Hex-CNMO	35.7	6.5	133	0.52	5.5, 30

After drying, the different organosilica samples (except for the pure hexylene-bridged material) show selective reflection peaks, confirming that chiral nematic ordering is retained after NCC removal (see Appendix B). The ordering of the samples was also observed by SEM, as shown in Figure 3-15. At the nanoscale, a rod-shaped morphology is seen for **Me-CNMO** and **Bz-CNMO** and long-range chiral nematic ordering is present throughout the samples. The hexylene-bridged sample, on the other hand, appears very disordered and consists of globular nanoparticles as opposed to nanorods. It appears that

the bridging hexane group is too hydrophobic and causes complete disruption of chiral nematic self-assembly.

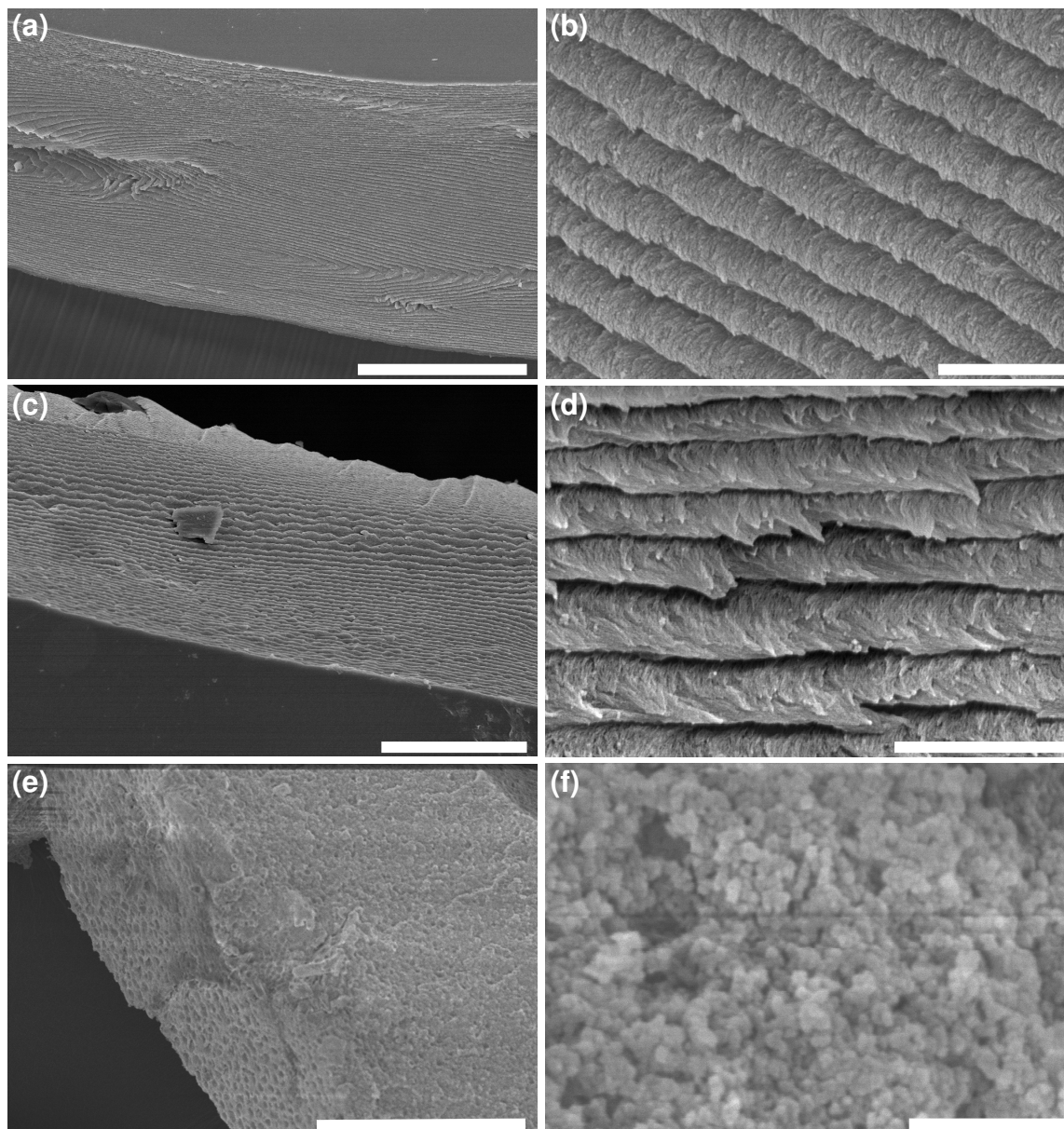


Figure 3-15. SEM images of organosilica samples with different bridging groups. (a) Side view of **Me-CNMO** film at edge (scale bar = 20 μm). (b) Edge of **Me-CNMO** film at higher magnification (scale bar = 1 μm). (c) Top view of **Bz-CNMO** film at edge (scale bar = 10 μm). (d) Edge of **Bz-CNMO** film at higher magnification (scale bar = 1 μm). (e) Low magnification image of **Hex-MO** (scale bar = 50 μm). (f) **Hex-MO** viewed at higher magnification (scale bar = 500 nm).

Nitrogen adsorption measurements were carried out for the different organosilica samples and the data is reported in Figure 3-16 and Table 3-3. Nitrogen adsorption measurements show that **Me-CNMO** and **Bz-CNMO** are mesoporous with BET surface areas of 518 and 740 m²/g, respectively. The increased specific surface area of **Bz-CNMO** is likely due to the increased carbon content of the material, which makes it less dense.

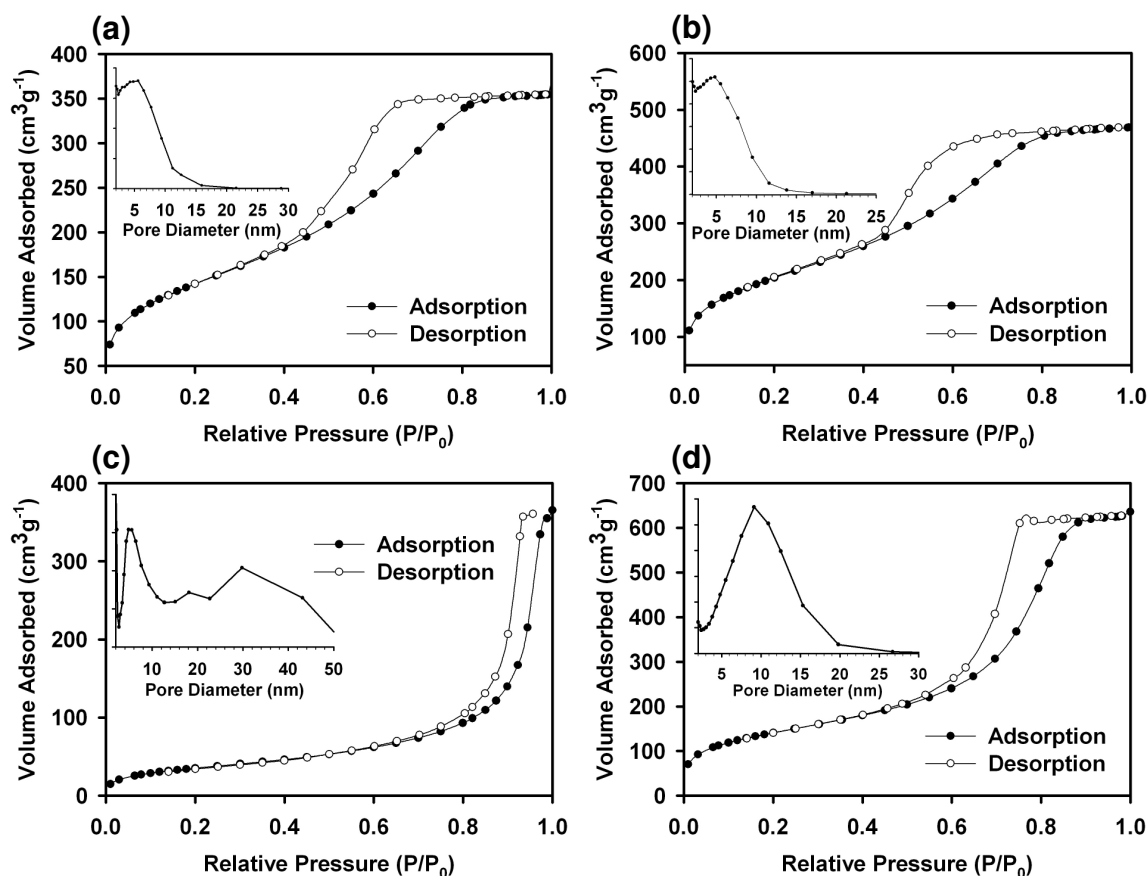


Figure 3-16. N₂ adsorption data for organosilica samples with different bridging groups. (a) N₂ adsorption isotherm and BJH pore size distribution (inset) for **Me-CNMO**. (b) N₂ adsorption isotherm and BJH pore size distribution (inset) for **Bz-CNMO**. (c) N₂ adsorption isotherm and BJH pore size distribution (inset) for **Hex-MO**. (d) N₂ adsorption isotherm and BJH pore size distribution (inset) for **Et-CNMO3**.

The BJH pore diameters of these samples are comparable to what was seen for **Et-CNMO1** and it appears that some pore collapse occurs due to the relatively low loading of organosilica precursor used in these experiments (additional experiments

performed on **Bz-Comp** samples with higher BTESB loadings show larger pore diameters). The hexylene-bridged sample **Hex-MO** has much lower porosity compared to the other samples and a BET surface area of only 133 m²/g. The pore size distribution shows a broad hump around 30 nm as well as a peak at 5.5 nm. This bimodal distribution suggests that some individual NCC rods may be acting to template mesopores while phase separation and aggregation may also be occurring.

3.4 Conclusions

I have shown that NCC can be used to template free-standing films of chiral nematic ethylene-bridged mesoporous organosilica that have improved mechanical properties and flexibility compared to pure silica. By using acid hydrolysis, it is possible to selectively remove NCC from NCC/organosilica composite materials. This new method of removing NCC also provides a way to control the pore size of NCC-templated mesoporous silica. This general approach can be expanded to the synthesis of other chiral nematic organosilica materials with bridging methylene or phenylene groups, which can result in even higher specific surface areas. There are some limitations, however; attempts to synthesize materials with a longer hexylene-bridging alkyl chain resulted in disordered materials with low specific surface area, which is attributed to the greater hydrophobicity of the precursor. Future work incorporating other bridging organic groups into these materials should provide highly tunable optical and mechanical properties. This also opens the door to introduce functional groups that could provide catalytic activity or enhanced selectivity for sensing applications.

Chapter 4

Hard Templating of Nanocrystalline TiO₂ with Chiral Nematic Ordering*

4.1 Introduction

Hard templating (also called nanocasting) has emerged as a powerful method for constructing new solid-state materials with periodic order.^[131, 154, 195] Although silica can be prepared with a variety of periodic structures (e.g., lamellar, hexagonal, cubic) and pore sizes by aqueous sol-gel methods using a surfactant template, this method cannot always be applied to other materials.^[149] This limitation stems from the fact that the required precursor for many materials either condenses too quickly, disrupts the organization of the surfactant, or is not compatible with aqueous chemistry (e.g., in the preparation of metal nitrides). Sometimes these problems can be overcome by using chelating ligands or by judicious choice of solvent and template.^[150, 196-198] On the other hand, by using porous silica as a hard template, diverse nanostructured materials may be obtained with a wide variety of compositions (e.g., carbon, polymers, noble metals, and metal oxides) after etching of the silica.^[128, 153, 199-201] The thermal stability of silica also allows for the use of high temperature treatments to generate highly crystalline mesoporous products that may be otherwise difficult to obtain.

The hard templating approach has been applied to the synthesis of a variety of mesoporous metals, metal oxides, and polymers.^[131, 153] Yue *et al.* recently reported the

* Portions of this chapter have been published as: K. E. Shopsowitz, A. Stahl, W. Y. Hamad, M. J. MacLachlan, "Hard Templating of Nanocrystalline Titanium Dioxide with Chiral Nematic Ordering." *Angew. Chem. Int. Ed.* **2012**, *51*, 6886-6890.

synthesis of mesoporous rutile and anatase TiO_2 using SBA-15 silica as the hard template,^[202, 203] and other hard templates have also been employed in the synthesis of nanostructured titania.^[204-206] High surface area nanocrystalline TiO_2 is of particular interest for applications such as dye sensitized solar cells, photocatalysts, gas sensors, and batteries.^[207-211]

The incorporation of high surface area anatase TiO_2 into photonic structures is a further challenge that has recently garnered attention.^[212-214] By using titania in colloidal crystals and inverse opals, the high refractive index of TiO_2 ($n \sim 2.5$) can impart a complete photonic band gap in these materials, which has been used to improve the efficiency of dye-sensitized solar cells and enhance photocatalytic activity.^[215, 216]

To date the synthesis of mesoporous materials has been mainly limited to the ordered pore structures obtained from the lyotropic liquid crystalline phases of surfactants and block copolymers. As described in Chapters 2 and 3, I have developed a new class of mesoporous materials with chiral nematic pore structures templated by the lyotropic liquid crystalline phase of nanocrystalline cellulose (NCC).^[192] In this chapter I describe the synthesis of mesoporous anatase TiO_2 using chiral nematic mesoporous silica films as a hard template. Structural features of the chiral nematic silica template ranging from the mesoscopic to macroscopic size regimes are retained in the product, resulting in mesoporous TiO_2 films that reflect circularly polarized light. To the best of my knowledge this is the first example of organizing a crystalline metal oxide into a chiral nematic structure, a method that may be useful for generating novel photonic and catalytic materials.

4.2 Experimental

4.2.1 General

All solvents and reagents including tetramethoxysilane (TMOS, Acros) and titanium (IV) isopropoxide (Sigma Aldrich) were purchased and used without further purification. NCC was prepared according to the procedure described in Chapter 2, section 2.2.4. Thermogravimetric analysis was performed under air on a PerkinElmer Pyris 6 thermogravimetric analyzer. N₂ adsorption studies were performed using a Micromeritics ASAP 2000 at 77 K. All samples were degassed for 2 hours under vacuum at 100 °C immediately prior to analysis. BJH pore size distributions were all calculated from the adsorption branch of the isotherm. IR spectra were obtained with a Nicolet 6700 FT-IR equipped with a Smart Orbit diamond ATR. Powder X-ray diffraction patterns were collected using a D8 advance X-ray diffractometer.

4.2.2 Microscopy

SEM images were collected on a Hitachi S4700 electron microscope. Samples were prepared by breaking the films into small pieces and attaching them to aluminum stubs using double-sided adhesive tape. The samples were then sputter-coated with 5 nm of either gold or gold-palladium. Polarized optical microscopy was performed on an Olympus BX41 microscope. All images were taken with the polarizers in a perpendicular (crossed) arrangement unless otherwise noted. EDX analyses were acquired using a Hitachi S2300 scanning electron microscope. Samples were analyzed without sputter-coating.

4.2.3 Preparation of NCC/Silica Composite Films

NCC/silica composite films were prepared by first sonicating a 3 wt. % aqueous NCC suspension for 10 min. TMOS (1.36 mmol / 150 mg NCC) was then added to the suspension dropwise with stirring. Stirring was continued for 1 h at room temperature to obtain a homogeneous mixture. The NCC/TMOS mixtures were then poured into polystyrene Petri dishes (5 mL / 60 mm diameter dish) and left to dry under ambient conditions (typically 18-24 h were required for complete drying). Note that a 6 wt. % NCC suspension was used in this chapter for the preparation of **Si-Acid** in order to obtain thicker films that were easier to handle for the subsequent TiCl_4 loading steps.

4.2.4 Preparation of Mesoporous Silica

For the preparation of **Si-Cal**, NCC/silica composite films were calcined by heating them under air at a rate of 2 °C/min to 540 °C and holding them at that temperature for 6 h.

For the preparation of **Si-Acid**, NCC/silica composite films were first heated in 12 M HCl at 85 °C for 18 h without stirring (~500 mg / 500 mL). The dark brown reaction mixture was cooled to room temperature and the films were filtered and washed with water. The films were then alternately washed with a 5:1 mixture of sulfuric acid and 30% hydrogen peroxide (piranha solution) and water until they appeared completely colourless, and were then left to air dry.

4.2.5 Preparation of TiO_2

A fresh TiCl_4 solution was prepared as follows: titanium (IV) isopropoxide (4 mL) was dissolved in ethanol (36 mL) and then water (10 mL) was added. The white

Ti(OH)₄ solid that immediately formed was filtered and dried under air. Ti(OH)₄ (1 g) was then dissolved in 2 mL of 12 M HCl to give a 4.3 M TiCl₄ solution.

The freshly prepared TiCl₄ solution was added to the mesoporous silica using the incipient wetness method. A volume of TiCl₄ solution equivalent to the pore volume of mesoporous silica used was added to the silica films. For example, **Ti-Acid** was prepared by adding 105 μL of TiCl₄ solution to 130 mg of **Si-Acid** (pore volume of **Si-Acid** = 0.81 cm³/g). The TiCl₄ loaded films were then dried at 80 °C for 30 min before heating to 200 °C for 1 h under air to induce TiO₂ formation. This procedure was repeated four times in total to ensure sufficient pore loading of the films. After the final loading step, the TiO₂/SiO₂ films were calcined at 600 °C to facilitate TiO₂ crystallization giving 202 mg of TiO₂/SiO₂ composite films. The composite films were then placed in a 2 M NaOH solution for 18 h at 20 °C to selectively remove the silica. The resulting TiO₂ films were then recovered by filtration, washed with copious amounts of water, and allowed to air dry giving 117 mg of **Ti-Acid**. **Ti-Cal** was prepared by an analogous procedure. **Ti-Control** was prepared by the same procedure in a vial that did not contain any mesoporous silica template.

4.3 Results and Discussion

4.3.1 Synthesis of Mesoporous Silica Films

Attempts to synthesize NCC/TiO₂ composite films directly using the same approach that was used for silica and organosilica all resulted in a disruption of chiral nematic ordering. When TiO₂ precursors such as titanium (IV) isopropoxide are directly added to NCC in water extremely rapid hydrolysis and condensation occurs. I therefore decided instead to use chiral nematic mesoporous silica films as a hard template for TiO₂. The NCC/silica composite samples used in this chapter were prepared using a

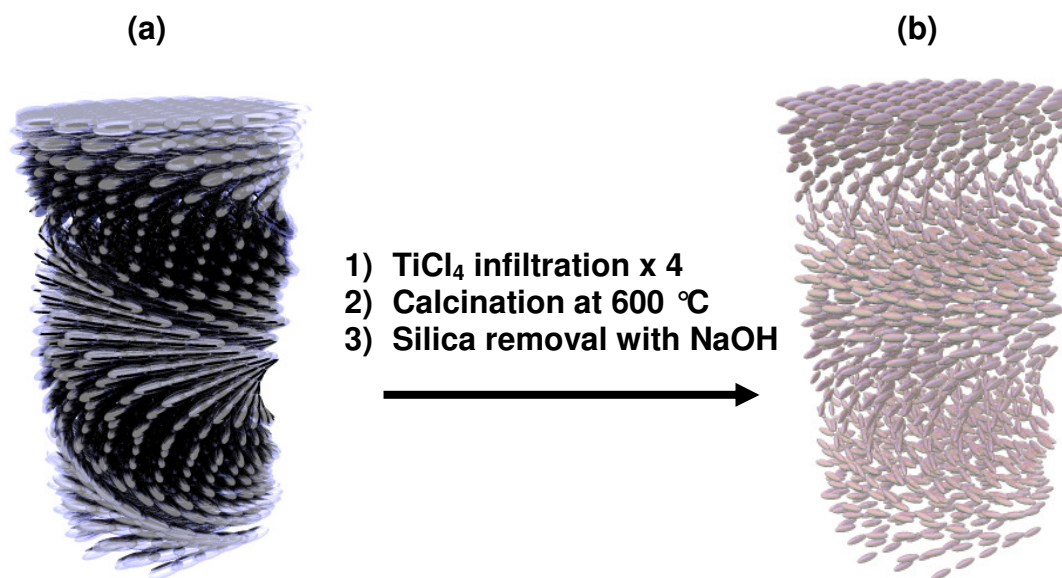
composition of 1.36 mmol TMOS / 150 mg NCC, which gives chiral nematic NCC/silica composite films with a reflectance peak at ~800 nm. NCC was removed from the NCC/silica composite films using two different methods: calcination at 540 °C to give chiral nematic mesoporous silica films (referred to in this chapter as **Si-Cal**) with a peak pore diameter of 3.5 nm and acid hydrolysis with HCl to give mesoporous silica with a peak pore diameter of 10.5 nm (referred to in this chapter as **Si-Acid**). These two chiral nematic mesoporous silica samples were used as hard templates for TiO₂ in order to investigate the effect of pore size on structural replication.

4.3.2 Synthesis of TiO₂ Replicas via Hard Templating

Previous reports of hard templating TiO₂ have shown that it is possible to replicate mesoscopic structures using this approach.^[203] I wanted to know whether hard templating could be used to organize TiO₂ nanocrystals into a macroscopic chiral assembly by simultaneously replicating features ranging over different length scales, namely mesopores (nanometers), chiral nematic organization (microns), and free-standing film morphology (mm to cm).

Titania replicas were synthesized using free-standing chiral nematic mesoporous silica films **Si-Cal** and **Si-Acid** as hard templates and the resulting TiO₂ materials are denoted as **Ti-Cal** and **Ti-Acid**, respectively. The procedure employed was a variation of that reported by Yue *et al.* and is summarized in Scheme 4-1.^[203] Briefly, an aqueous solution of TiCl₄ was loaded into the mesoporous silica films using the incipient wetness method, which involves adding a volume of liquid that corresponds to the pore volume of the material. After each loading step, the films were dried and then annealed at 200 °C. This loading procedure was repeated four times, after which the silica/titania composite films were calcined at 600 °C to obtain a crystalline product. After this final step, pore

filling fractions of 75% and 86% were found for **Si-Cal** and **Si-Acid** respectively (Figure 4-1). The silica templates were then removed by soaking the films in 2 M NaOH_(aq) at room temperature, resulting in mesoporous TiO₂. As a control, an additional sample (**Ti-Control**) was prepared using identical conditions in the absence of any silica hard template.



Scheme 4-1. Schematic representation of the synthesis of chiral nematic mesoporous titania. (a) Chiral nematic mesoporous silica used as a hard template. (b) Chiral nematic mesoporous titania replica.

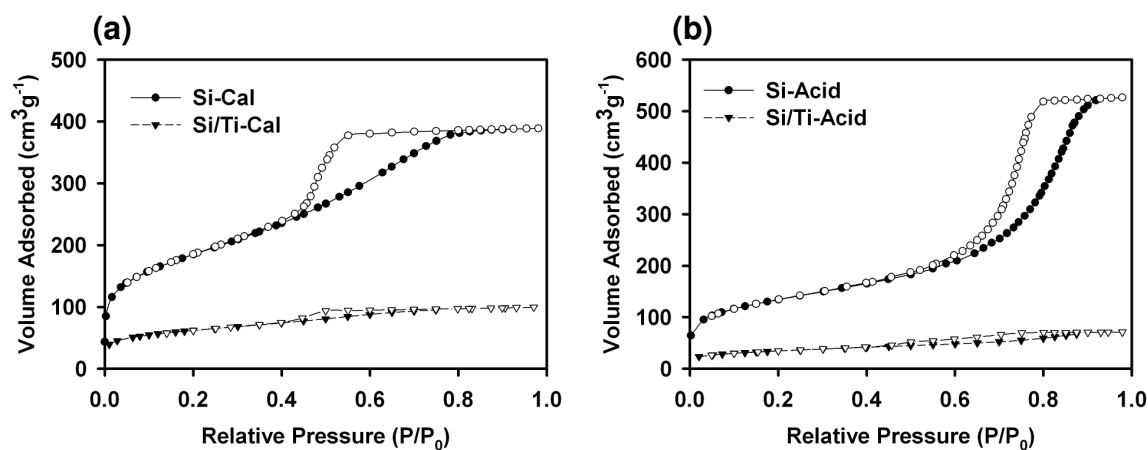


Figure 4-1. N₂ adsorption isotherms before and after TiO₂ loading. (a) Isotherms for **Si-Cal** and the corresponding silica/titania composite obtained after the final TiCl₄ loading step and calcination at 600 °C. (b) Isotherms for **Si-Acid** and the corresponding

silica/titania composite obtained after the final TiCl_4 loading step and calcination at 600°C .

The film morphology of the mesoporous silica templates is retained in the TiO_2 replicas, although the TiO_2 films are somewhat smaller than the original silica films (larger pieces are obtained for **Ti-Acid** compared to **Ti-Cal**). The removal of the silica template was confirmed by IR spectroscopy and by energy dispersive X-ray analysis (EDX, Figure 4-2). EDX analysis of the materials shows peaks corresponding to Ti, O, and a trace amount of residual Si; the Si:Ti ratio (wt. / wt.) averaged over multiple locations is $\sim 1\%$.

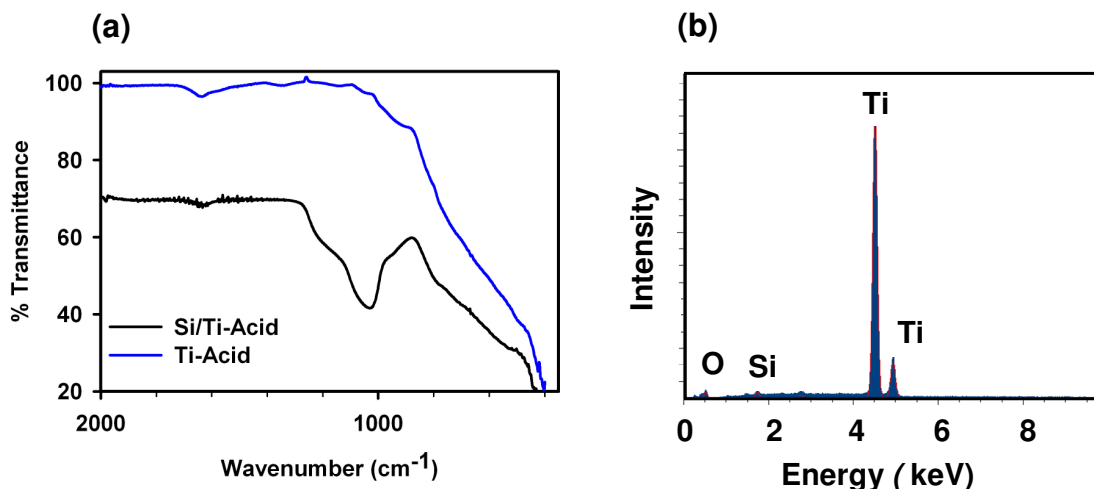


Figure 4-2. Data showing the removal of SiO_2 by NaOH treatment of $\text{SiO}_2/\text{TiO}_2$ composite. (a) IR spectra before (**Si/Ti-Acid**) and after (**Ti-Acid**) NaOH treatment of $\text{SiO}_2/\text{TiO}_2$ composite. (b) EDX spectrum of **Ti-Acid**.

Powder X-ray diffraction (PXRD) confirms that the templated TiO_2 products, **Ti-Acid** and **Ti-Cal**, are crystalline anatase with a very small amount of rutile impurity (Figure 4-3a). On the other hand, the TiO_2 synthesized without a template (**Ti-Control**) predominantly forms rutile with some anatase also present (Figure 4-3b). The grain sizes calculated for **Ti-Acid** and **Ti-Cal** (based on the integral breadth Scherrer equation) are 8.3 nm and 13 nm, respectively, whereas a grain size of 22 nm was determined for **Ti-**

Control. Although rutile is the most stable form of bulk TiO_2 , calculations have shown that anatase becomes more stable than rutile at crystallite sizes below 15 nm.^[217] Thus, for **Ti-Acid** and **Ti-Cal**, nanoconfinement within the mesopores of the silica templates induces anatase to form under conditions that otherwise favour the formation of rutile.

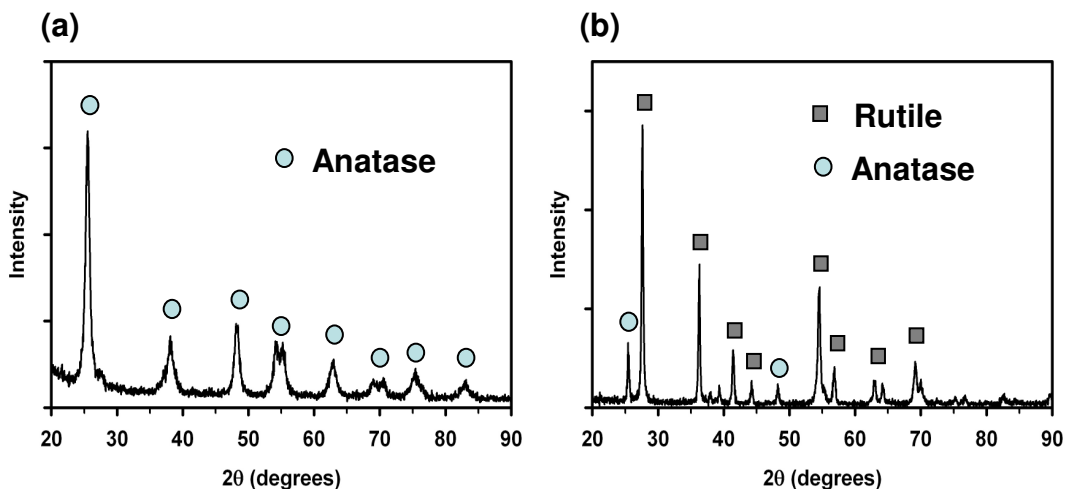


Figure 4-3. PXRD patterns for (a) **Ti-Acid** and (b) **Ti-Control**. **Ti-Cal** is not shown but gives a pattern virtually identical to **Ti-Acid**.

4.3.3 Nitrogen Adsorption Studies of TiO_2 Replicas

Nitrogen adsorption measurements were performed on the TiO_2 samples and the results are reported in Figure 4-4 and Table 4-1. The BET surface areas of **Ti-Cal** and **Ti-Acid** are 234 and 149 m^2/g , respectively, with corresponding pore volumes of 0.23 and 0.31 cm^3/g and peak pore diameters of 2.5 and 7.9 nm. In contrast, the BET surface area of **Ti-Control** is only 18 m^2/g , clearly demonstrating the importance of the hard template for obtaining a high surface area mesoporous material. It is interesting to note that the shapes of the adsorption isotherms and the relative magnitudes of surface area, pore volume, and pore size for **Ti-Acid** and **Ti-Cal** reflect those of the corresponding silica templates. This demonstrates that the mesoporosity of the hard templates affects the mesoporosity of the products. The specific surface area and pore volumes of TiO_2

templated by chiral nematic mesoporous silica compares well with TiO₂ that has been templated by other mesoporous hosts.^[203-205]

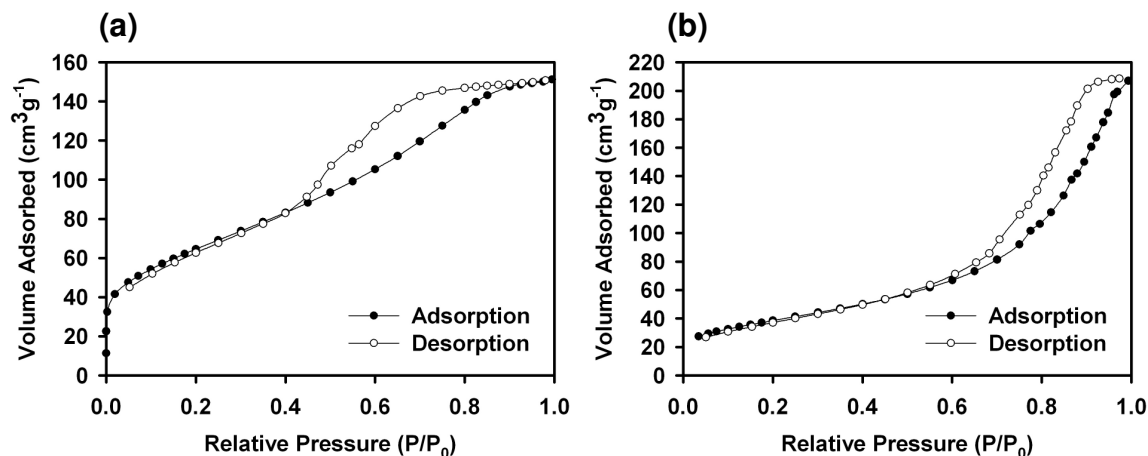


Figure 4-4. N₂ adsorption isotherms for mesoporous titania (a) **Ti-Cal** and (b) **Ti-Acid**.

Table 4-1. Nitrogen adsorption data.

Sample	BET Surface Area (m ² /g)	Pore Volume (cm ³ /g)	BJH Pore Diameter (nm)
Si-Cal	650	0.60	3.5
Si-Acid	471	0.81	10.5
Si/Ti-Cal	220	0.15	<2
Si/Ti-Acid	121	0.11	<2
Ti-Cal	234	0.23	2.5
Ti-Acid	149	0.31	8
Ti-Control	18	0.06	-

4.3.4 Chiral Nematic Optical and Structural Properties of TiO₂ Replicas

The hard-templated TiO₂ films are visibly iridescent giving a good indication that the chiral nematic structure of the mesoporous silica is retained to some degree in the TiO₂ replicas. The iridescence of the **Ti-Acid** films is more pronounced compared to the iridescence of the **Ti-Cal** films. As mentioned above, the **Ti-Acid** films are also generally larger than the **Ti-Cal** films. These observations suggest that long-range structural replication is more effective when using **Si-Acid** as the template. The larger mesopores of

Si-Acid may allow for more efficient diffusion and even loading of the titania precursor throughout the films, which in turn results in better long-range replication when compared to **Si-Cal**.

The iridescence of a chiral nematic structure results from the selective reflection of circularly polarized light with a handedness that matches that of the structure. The **Ti-Acid** films were photographed using left-handed and right-handed circular polarizing filters (LHP and RHP, respectively). The films appear strongly iridescent under an LHP filter (Figure 4-5a) while they simply appear white when viewed under an RHP filter (Figure 4-5b). This confirms the chiral nematic origin for the iridescence of the films and shows that the left-handed structure templated by NCC is preserved in the titania replicas. The iridescence of the films is still present after heating to 500 °C, demonstrating that the long-range chiral nematic structure is stable up to this temperature. However, the films lose their iridescence after heating to 900 °C, which may be due to structural rearrangement that occurs during a transition from nanocrystalline anatase to rutile (TGA of **Ti-Acid** suggests that this occurs around 600 °C, see Appendix C).

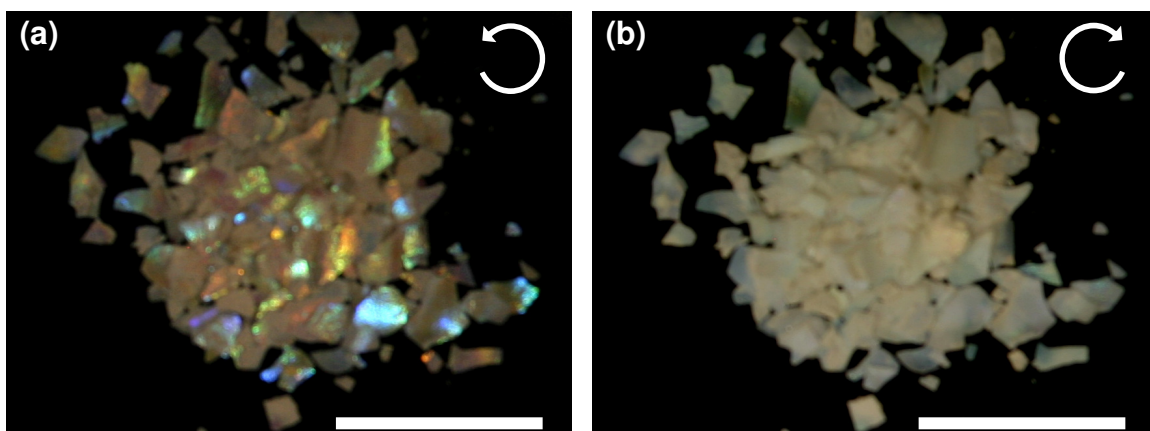


Figure 4-5. Circular polarized iridescence of **Ti-Acid**. (a) **Ti-Acid** photographed using a left-handed circular polarizing filter (scale bar = 2 cm). (b) **Ti-Acid** photographed using a right-handed circular polarizing filter (scale bar = 2 cm).

Scanning electron microscopy (SEM) further confirms the transfer of the chiral nematic structure from the chiral nematic silica templates to the TiO₂ replicas (Figure 4-6). A repeating helical structure is observed perpendicular to the surface of the films for both **Ti-Acid** and **Ti-Cal**. One major difference between the silica templates and titania replicas is that the former are amorphous while the latter are nanocrystalline. This is clearly seen when comparing the surfaces of the films, where the surfaces of the TiO₂ films appear much rougher due to the nanocrystalline morphology. The crystallization of TiO₂ drives the formation of more globular particles compared to the rod morphology of the mesoporous silica and original NCC template. This leads to the helical pitch of the TiO₂ samples appearing less ordered when compared to the silica (also **Ti-Cal** appears somewhat more disordered than **Ti-Acid**). The decreased ordering of the TiO₂ replicas may also be related to imperfect loading and structural collapse that occurs upon removing the silica template. A “crust” is seen coating some of the TiO₂ films, likely due to some of the TiCl₄ solution condensing on the surface of the silica films as opposed to within the mesopores (see Appendix C). This is due to the imperfect loading achieved using the incipient wetness technique and could likely be overcome by using an alternative technique such as atomic layer deposition

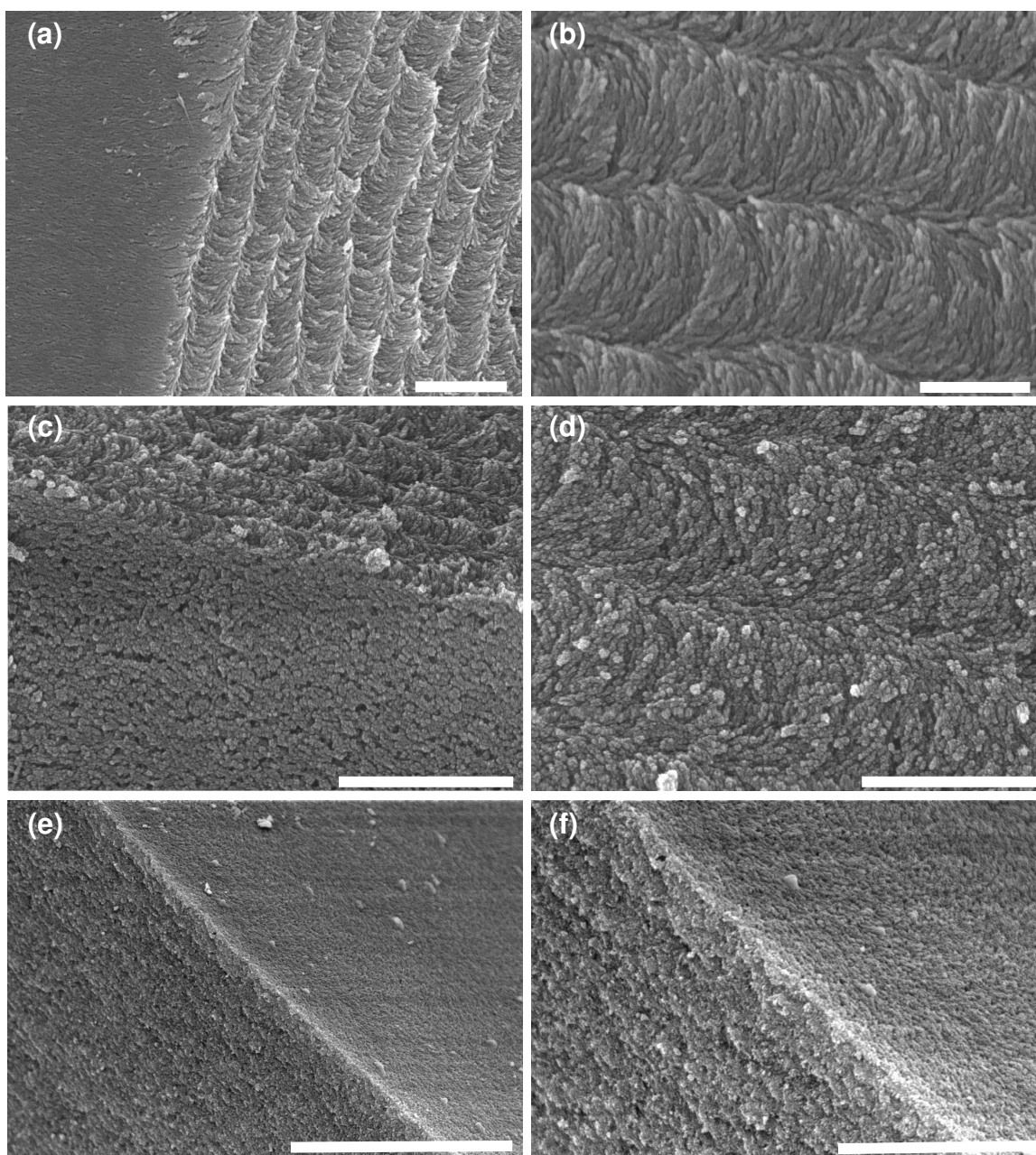


Figure 4-6. SEM images of **Si-Acid**, **Ti-Acid**, and **Ti-Cal**. (a) Top view of **Si-Acid** film at edge (scale bar = 1 μm). (b) Cross-section of **Si-Acid** at high magnification (scale bar = 500 nm). (c) Top view of **Ti-Acid** film at edge (scale bar = 1 μm). (d) Cross-section of **Ti-Acid** at high magnification (scale bar = 500 nm). (e) Side view of **Ti-Cal** film at edge (scale bar = 5 μm). (f) Edge of **Ti-Cal** film at higher magnification (scale bar = 2 μm).

Looking at **Ti-Acid** using polarized optical microscopy (POM), the films are strongly birefringent further confirming the long-range anisotropy of the materials (Figure 4-7a). Upon addition of ethanol, the films remain iridescent and birefringent but POM shows a large change in colouration (Figure 4-7b). This change is reversible and

the films regain their original colour when the ethanol has evaporated. This marked change in birefringence gives clear evidence that the pores of the mesoporous TiO₂ are accessible to guest molecules and that pore infiltration can cause a change in optical properties. The change in birefringence upon solvent loading of the TiO₂ films is markedly different than for the silica films. When isotropic liquids (e.g., water or ethanol) are added to **Si-Acid** or **Si-Cal**, the iridescence and birefringence of the films are almost completely shut off. As discussed in Chapters 2 and 3, this effect can be attributed to refractive index matching. The refractive index of TiO₂ (2.5 for anatase), however, is much higher than that of SiO₂ (1.46), and a smaller change in the optical properties of the TiO₂ films is therefore expected upon soaking with isotropic liquids.

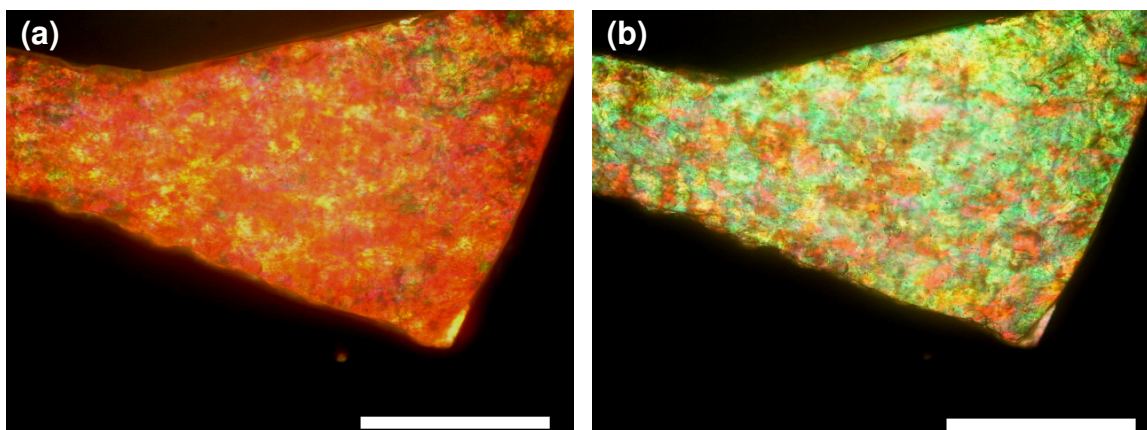


Figure 4-7. (a) POM micrographs **Ti-Acid**. (a) Micrograph of a dry **Ti-Acid** film (scale bar = 400 μm). (b) Micrograph of the same film after wetting with ethanol (scale bar = 400 μm).

4.4 Conclusions

I have demonstrated that chiral nematic mesoporous silica (CNMS) can be used as a hard template to synthesize anatase TiO₂. Using this hard templating method, structural features are replicated at several length scales: (1) the TiO₂ is mesoporous with a surface area and pore size that is determined by the porosity of the starting silica template; (2) the

material obtained selectively reflects left-handed circularly polarized light, which indicates a chiral nematic organization of the titania crystallites; and (3) the titania is obtained as films with similar dimensions as the original silica films. The ability to accurately replicate features of CNMS over macroscopic distances confirms that these materials have a highly interconnected pore structure. This approach works for silica with different pore sizes (3.5 nm and 10.5 nm); however, long-range structural replication appears to work better when using the silica template with larger mesopores. Future work will look to test these materials for various applications such as dye-sensitized solar cells, photocatalysts, sensors, and batteries. Using this hard templating method, I expect that other mesoporous metal oxide structures with chiral nematic organization may be prepared.

Chapter 5

Chiral Nematic Mesoporous Carbon Derived from Nanocrystalline Cellulose*

5.1 Introduction

Mesoporous carbon materials show considerable promise as electrodes for energy storage devices such as lithium ion batteries and supercapacitors.^[137, 142, 218, 219] In supercapacitors, the large specific surface areas of mesoporous carbons mediate electrical double layer formation leading to high specific capacitance values. In addition, mesoporous carbons can be used as hosts for pseudo-capacitive materials, like conducting polymers, to further improve their performance. Ordered mesoporous carbon materials were first synthesized using ordered mesoporous silica as a hard template.^[129, 130] In the hard templating (also referred to as nanocasting)^[131, 220] approach, mesoporous silica is repeatedly infiltrated with a suitable carbon precursor (e.g., sucrose) that is carbonized within the pores of the silica at elevated temperature. After sufficient pore loading and etching of the silica, mesoporous carbon with a structure that is the inverse of the original silica template is obtained. Despite the potential benefits of using mesoporous carbon over traditional activated carbon, the cost of making these materials may be prohibitive. Finding more economical synthetic routes both in terms of the number of steps involved and precursors used is important if mesoporous carbon is to be implemented in new technologies.

* Portions of this chapter have been published as: K. E. Shopsowitz, W. Y. Hamad, M. J. MacLachlan, "Chiral Nematic Mesoporous Carbon Derived from Nanocrystalline Cellulose." *Angew. Chem. Int. Ed.* **2011**, *50*, 10991-10995.

Direct surfactant templating approaches (soft templating) have also been developed for the synthesis of mesoporous carbon by condensing polymerizable carbon precursors (e.g., phenolic resins) around block copolymer templates.^[221] Soft templating requires fewer synthetic steps than hard templating and offers improved morphological control over the mesoporous carbon products. For example, free-standing mesoporous carbon membranes have been synthesized through evaporation-induced self-assembly coupled with soft templating.^[222, 223] The specific surface areas of these films, however, are considerably less than those of mesoporous carbons produced via hard templating. Using both hard and soft templating approaches, mesoporous carbon has been synthesized with cubic and hexagonal pore systems that are ultimately derived from the self-assembly of surfactants into ordered mesophases.^[133, 135, 136] The synthesis of mesoporous carbon templated by other liquid crystal phases, for example nematic and chiral nematic phases, has been virtually unexplored.

Chiral nematic liquid crystals, which consist of mesogens organized into a long-range helical assembly, exhibit unique properties such as the selective reflection of circularly polarized light.^[44] The incorporation of chiral nematic organization into solid-state materials could give rise to novel properties. Kyotani *et al.* have synthesized graphitic carbon with chiral nematic ordering by first polymerizing polyacetylene within a thermotropic chiral nematic liquid crystal followed by iodine-doping and pyrolysis.^[224, 225] It is expected that these materials will display interesting electromagnetic properties.

In Chapter 2, I reported that evaporation induced self-assembly of NCC with different silica precursors can result in composite films with chiral nematic structures and that the removal of NCC from these films generates chiral nematic mesoporous silica. In this chapter, I describe how NCC/silica composite films can also be used to generate mesoporous carbon with excellent retention of chiral nematic organization. This approach

gives access to high surface area free-standing mesoporous carbon films that are otherwise difficult to obtain and has the advantage of requiring relatively few synthetic steps (when compared with the usual hard templating procedure) by utilizing the structural template (NCC) directly as the carbon source. The synthesis, structural characterization, and use of these materials as supercapacitor electrodes and hosts for polyaniline electrodeposition will be discussed.

5.2 Experimental

5.2.1 General

All solvents and reagents including tetramethoxysilane (Acros) and aniline (Sigma Aldrich) were purchased from commercial sources and used without further purification. Nanocrystalline cellulose was prepared as described in Chapter 2 (section 2.2.4). Powder X-ray diffraction spectra were collected using a D8 advance X-ray diffractometer. CD experiments were performed using a JASCO J-710 spectropolarimeter. Spectra were collected by mounting free-standing films so that the surfaces of the films were perpendicular to the beam path (due to the small size of the films the aperture was not fully covered). Raman spectra were collected using a Renishaw RM1000 with a 785 nm excitation laser linked to a Leica DMLB microscope. Thermogravimetric analysis was performed on a PerkinElmer Pyris 6 thermogravimetric analyzer. All samples were run under air. Gas adsorption studies were performed using a Micromeritics ASAP 2000. All samples were degassed for 2 hours under vacuum at 100 °C immediately prior to analysis. BJH pore size distributions were all calculated from the adsorption branch of the isotherm. Elemental analysis was performed by UBC Microanalytical Services.

5.2.2 Microscopy

TEM images were collected on a Hitachi H7600 electron microscope. Samples were prepared by first grinding the films into a fine powder, suspending them in ethanol, and then dropcasting them onto a carbon-coated copper TEM grid. SEM images were collected on a Hitachi S4700 electron microscope. Samples were prepared by breaking the films into small pieces and attaching them to aluminum stubs using double-sided adhesive tape. The samples were then sputter-coated with 5 nm of either gold or gold-palladium. EDX analysis was acquired using a Hitachi S2300 scanning electron microscope (samples for EDX were not sputter-coated). Polarized optical microscopy was performed on an Olympus BX41 microscope. All images were taken with the polarizers in a perpendicular (crossed) arrangement unless otherwise noted.

5.2.3 Preparation of NCC/silica Composite Films

In a typical procedure, chiral nematic NCC/silica composite films were prepared by first sonicating a 3.5 wt. % aqueous NCC suspension for 10 min. TMOS was then added to the suspension dropwise and the mixture was stirred at room temperature for 1 h to obtain a homogeneous solution. The NCC/TMOS mixtures were then poured into polystyrene Petri dishes (5 mL / 60 mm diameter dish) and left to dry under ambient conditions (typically 18-24 h were required for complete drying). For the different ratios of NCC/TMOS used for the different chiral nematic composite samples please refer to Table 5-1.

5.2.4 Preparation of Mesoporous Carbon Films

The conversion of NCC/silica composite films to carbon/silica composite films was achieved by heating the films at a rate of 2 °C/min under flowing nitrogen to 900 °C

and holding them at that temperature for 6 h. After cooling to room temperature, the films were placed in a 2 M NaOH_(aq) solution (500 mg of composite films / 200 mL) and kept at 90 °C for 4 h. This was done without stirring in order to avoid breaking the films. After cooling to room temperature, the films were carefully filtered and washed with distilled water. For the example of **CNMC3**, 175 mg of free-standing carbon films were recovered from 1 g of NCC/silica composite films.

5.2.5 Conductivity and Electrochemical Measurements of Mesoporous Carbon Films

Electrical conductivity of the mesoporous films was measured using the standard four-probe method on rectangular strips of films. Hewlett Packard model 34401A and 3478A multimeters were used to measure voltage and current, respectively. Conductivity was calculated from the raw data according to $\sigma = 0.5 \cdot I / (V \cdot t)$, where t is the thickness of the film and the multiplication by 0.5 includes a finite width correction for the sample.

Electrochemical measurements were carried out on a Brinkmann PGSTAT12 Autolab potentiostat. Dry mesoporous carbon films were weighed and then placed in a 1 M aqueous sulfuric acid solution and allowed to soak for at least 18 h. Two films were then sandwiched in a Swagelok® two-electrode cell with a Nafion® membrane separator and stainless steel current collectors.

5.2.6 Synthesis and Electrochemical Characterization of PANI@CNMC Films

A slightly different procedure was used for the preparation of NCC/silica composite films. Instead of pouring the NCC/TMOS mixture into Petri dishes, small films were cast from 1 mL drops deposited on a polystyrene surface (otherwise, the preparation of the mesoporous carbon was identical to **CNMC3**). This was done to

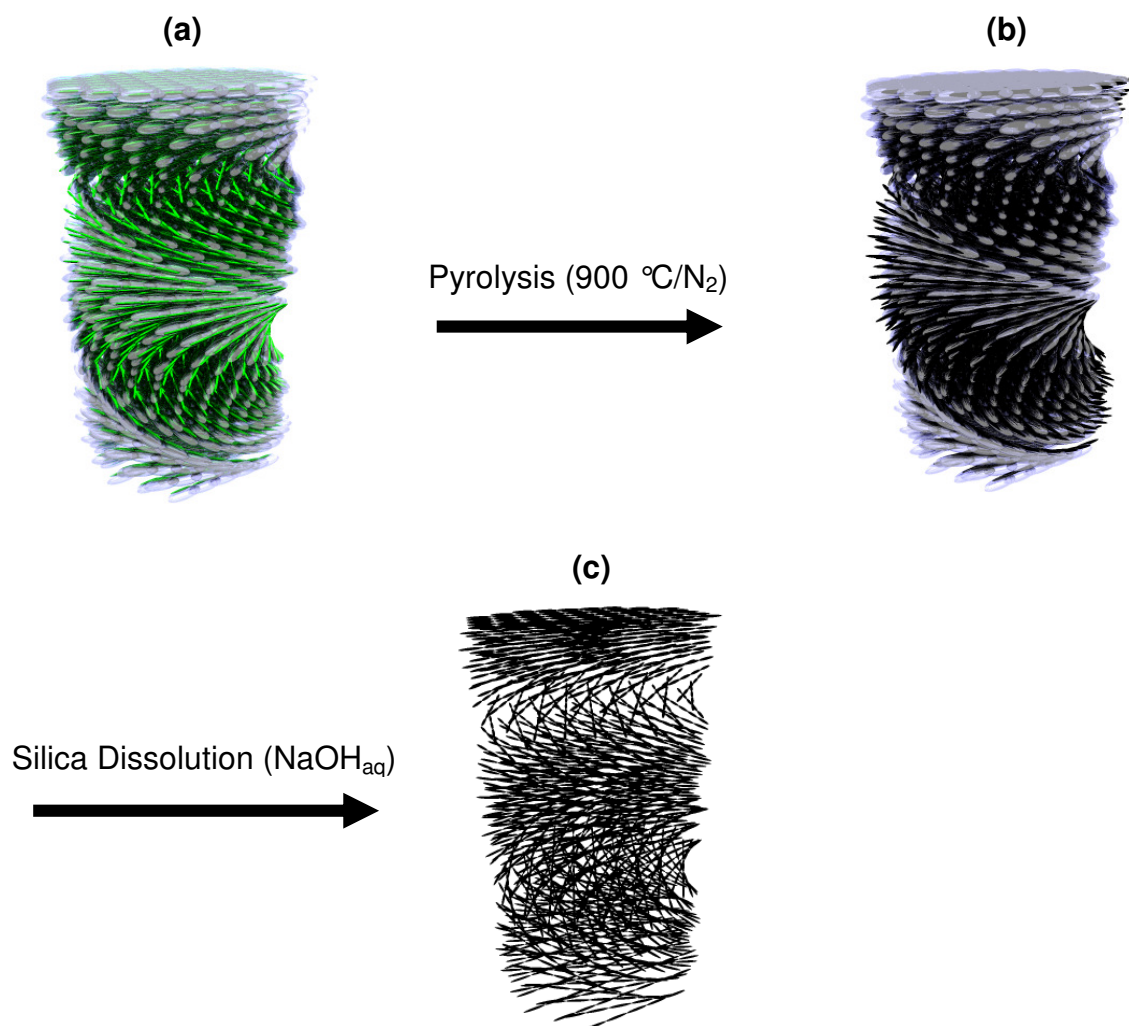
ensure uniform film sizes for the electrodeposition experiments. The electropolymerization of polyaniline was performed using a Brinkmann PGSTAT12 Autolab potentiostat configured with a three-electrode set-up (Ag/AgCl reference electrode and platinum mesh counter electrode). The mesoporous carbon film working electrodes were suspended in the electrolyte/monomer solution (0.5 M H₂SO₄ / 0.2 M aniline in water) using a copper alligator clip. A constant voltage of 0.80 V (vs. Ag/AgCl) was applied over times of 50-900 seconds to induce electrodeposition. After polymerization, the films were washed thoroughly with water and allowed to dry. Cyclic voltammograms were obtained using the same three-electrode setup with a 1 M H₂SO_{4(aq)} electrolyte solution.

5.3 Results and Discussion

5.3.1 Synthesis of Mesoporous Carbon from NCC/Silica Composite Films

A series of chiral nematic NCC/silica composite films were prepared in the same way that was reported in Chapter 2 and these samples were used as the starting point for the synthesis of mesoporous carbon (the different compositions are listed in Table 5-1). The conversion of chiral nematic NCC/silica composite films to mesoporous carbon is illustrated in Scheme 5-1. The NCC/silica composite films were heated to 900 °C under nitrogen to give carbon/silica composite films. The conversion of NCC to carbon proceeds with ~30% yield as determined by TGA (Figure 5-1, Table 5-1). These carbon yields are much higher than the typically reported yields of 10-15 wt% for carbonization of cellulose under N₂.^[226] It has been well-established that the addition of sulfuric acid prior to pyrolysis can increase the carbon yield when cellulose or glucose is used as a carbon precursor.^[129, 227] The surface of NCC utilized in these experiments is already

functionalized with sulfate groups and it is believed that this as well as the encapsulation of the NCC in the silica helps to obtain a high yield without the need for a separate sulfuric acid impregnation step.



Scheme 5-1. Conversion of a chiral nematic NCC/silica composite film to chiral nematic mesoporous carbon. (a) NCC/silica composite film. (b) Carbon/silica composite film obtained after pyrolysis of (a) at 900 °C under an N₂ atmosphere. (c) Mesoporous carbon obtained after the treatment of (b) with 2M NaOH.

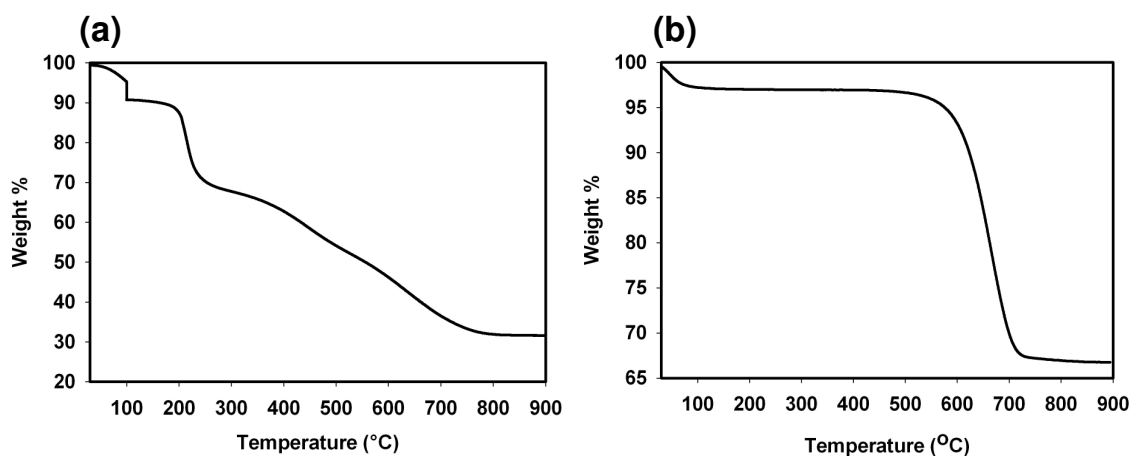


Figure 5-1. (a) TGA of **Comp3**. (b) TGA of **Comp3** after carbonization at 900 °C. Both samples were run under air.

Table 5-1. Compositions of NCC/silica and carbon/silica films.

Sample	mmol TMOS / 150 mg NCC	Wt. % NCC ^a	Wt. % Carbon ^b
Comp1	0	100	100
Comp2	0.68	76	46
Comp3	1.36	65	32
Comp4	2.43	56	20
Comp5	4.08	43	10

a) Calculated from TGA of NCC/silica composite films.

b) Calculated from TGA of NCC/carbon composite films.

Some of the carbon/silica composite samples show iridescence providing evidence for the retention of their chiral nematic organization after carbonization (Figure 5-2a). In the final step, the silica was dissolved with aqueous NaOH to yield free-standing carbon films with centimeter dimensions and a glossy black appearance (Figure 5-2b). After the NaOH treatment, the removal of silica in the samples was confirmed by TGA (run under air, Figure 5-3a), which shows decomposition of the carbon between 500 and 650 °C, and a small residual ash of ~3 wt. %. Elemental analysis of the materials showed them to generally be around 90 wt. % carbon and 1 wt. % hydrogen while EDX analysis indicates that the remaining 9 wt. % consists mostly of oxygen with trace amounts of sodium and silicon also present (<1 wt. %, Figure 5-3b).

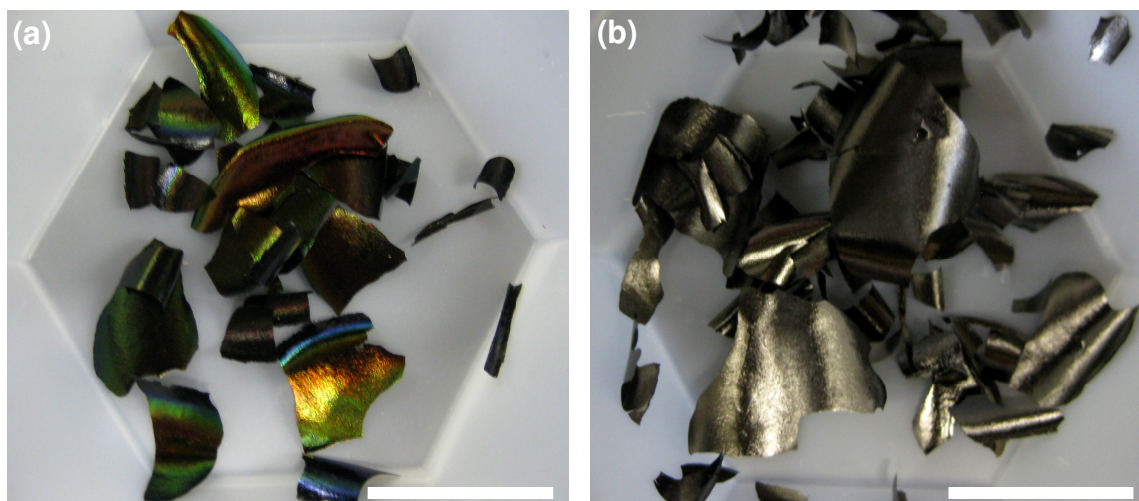


Figure 5-2. Photographs of carbon films before and after the removal of silica. (a) Carbon/silica composite films derived from **Comp3** (scale bar = 2 cm). (b) Mesoporous carbon sample **CNMC3** (scale bar = 2 cm).

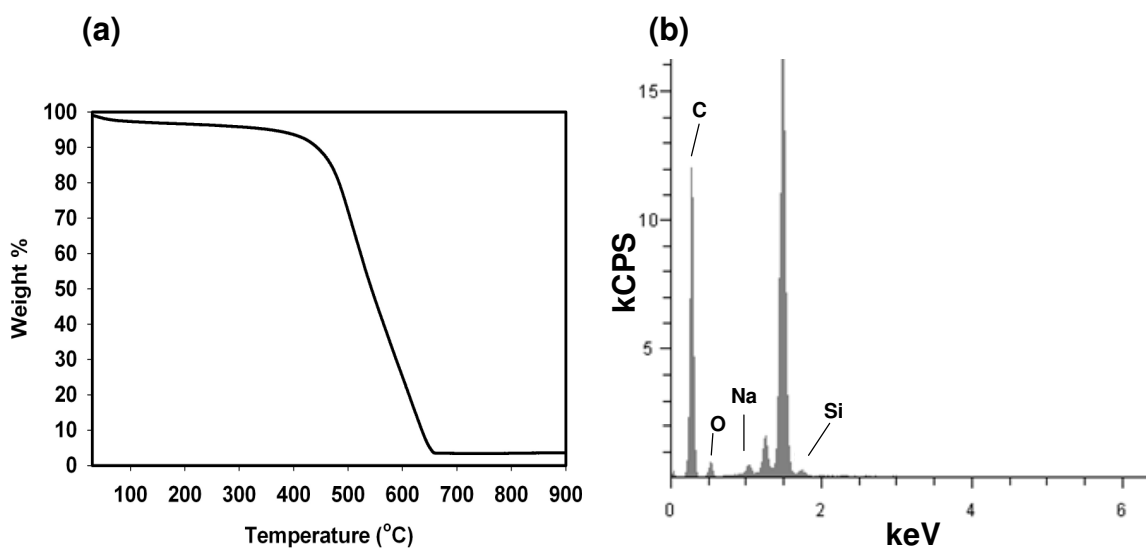


Figure 5-3. TGA and EDX characterization of mesoporous carbon. (a) TGA of **CNMC3** (10 °C/min, air). (b) EDX spectrum of **CNMC3**. The two unlabeled peaks at 1.25 and 1.5 keV correspond to Mg and Al found in the SEM stub.

The conversion of NCC to carbon was further studied by powder X-ray diffraction (PXRD) and Raman spectroscopy as shown in Figure 5-4. The Raman spectrum shows a broad D-band centered at 1320 cm^{-1} overlapping with a smaller G-band

at 1595 cm^{-1} and PXRD shows broad peaks centered at $2\theta \approx 23^\circ$ and 43° . These results are consistent with the conversion of NCC into amorphous carbon.

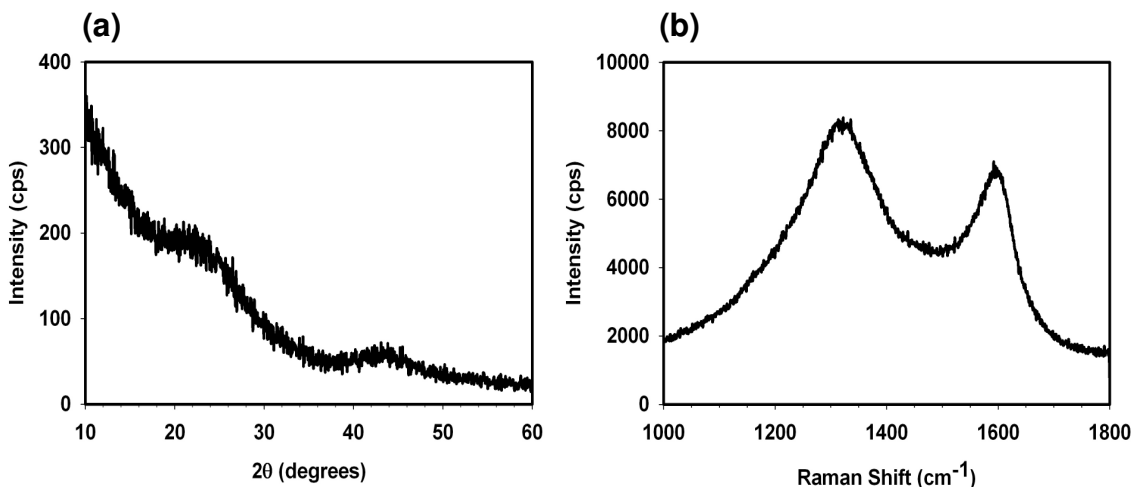


Figure 5-4. Spectroscopic characterization of mesoporous carbon. (a) PXRD pattern of CNMC3. (b) Raman spectrum of CNMC3.

5.3.2 Comparison of the Porosity of Carbon Obtained from Different NCC/Silica Compositions

The porosity of the NCC-derived carbon was analyzed by nitrogen adsorption-desorption and the results are summarized in Table 5-2. To study the influence of silica loading on the porosity of the carbon materials, samples were prepared from chiral nematic precursor films with different proportions of NCC and silica (**Comp1-5**, Table 5-1). The pyrolysis of NCC films without the addition of any silica precursor (**Comp1**) results in microporous carbon (**MC1**) as shown by a type I adsorption isotherm (Figure 5-5a). When the samples are prepared using silica as shown in Scheme 5-1, the resulting carbon materials display isotherms with more type IV character compared to **MC1**, indicating the introduction of mesoporosity into the samples (N_2 adsorption measurements performed on carbon/silica composites before the removal of silica give type I isotherms with fairly low specific surface area). A maximum BET surface area and total pore volume of $1460\text{ m}^2/\text{g}$ and $1.22\text{ cm}^3/\text{g}$, respectively, were measured for carbon

obtained from a 65% NCC/silica composite (**CNMC3**, Figure 5-5c). In addition, **CNMC3** shows very little microporosity ($11 \text{ m}^2/\text{g}$) and has a peak pore diameter of 2.9 nm. Carbon materials prepared from composites with a lower or higher fraction of silica (relative to **CNMC3**) have decreased surface areas and pore volumes compared to **CNMC3** and show more microporosity. It is apparent that a minimal amount of silica is necessary for introducing mesoporosity into the NCC-derived carbon. The decrease in mesoporosity observed at higher silica loadings may be due to thicker silica walls preventing the formation of linkages between the carbon regions during pyrolysis, which in turn causes the structure to partially collapse upon silica removal.

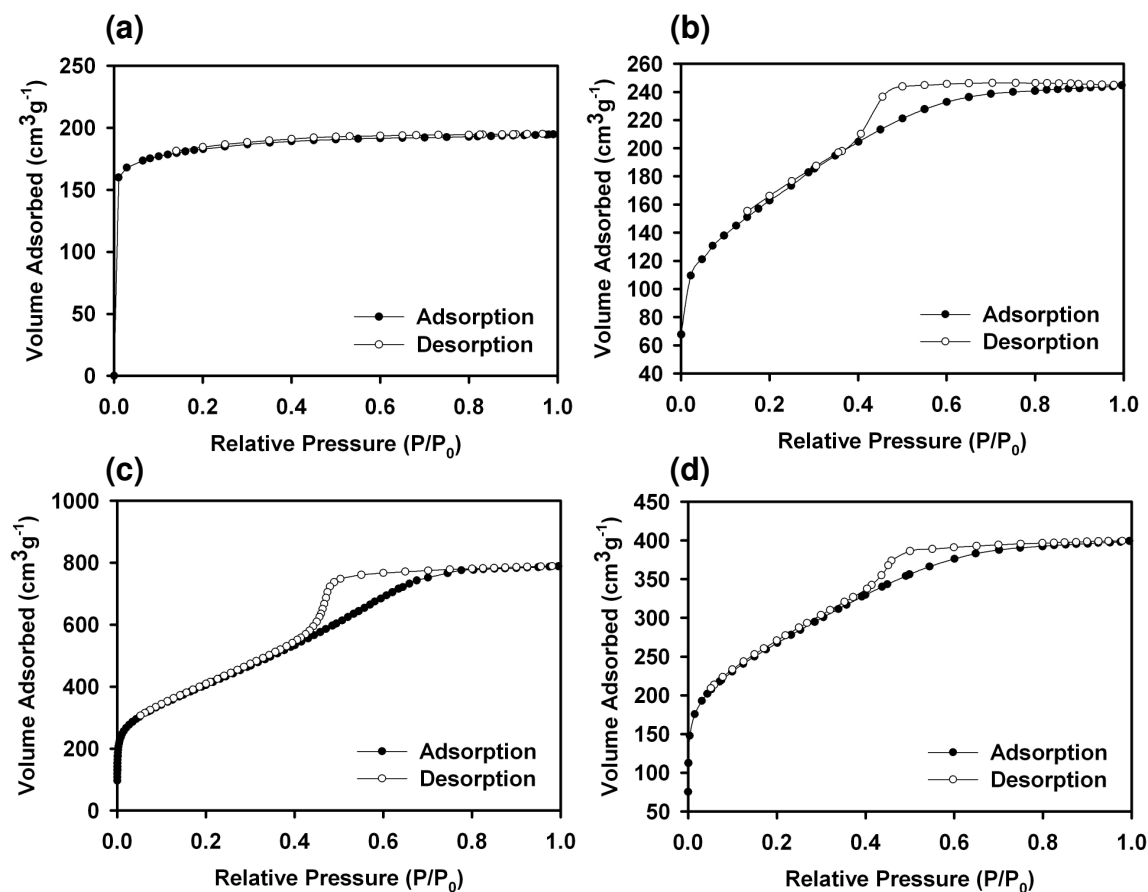


Figure 5-5. Nitrogen adsorption isotherms for selected carbon samples. (a) N₂ isotherm measured for **MC1**. (b) N₂ isotherm measured for **CNMC2**. (c) N₂ isotherm measured for **CNMC3**. (d) N₂ isotherm measured for **CNMC5**.

Table 5-2. Nitrogen adsorption data for porous carbon.

Sample	BET Surface Area (m ² /g)	Pore Volume (cm ³ /g)	Micropore Area (m ² /g) ^a
MC1	616	0.30	488
CNMC2	578	0.38	37
CNMC3	1465	1.22	11
CNMC4	1230	0.96	128
CNMC5	932	0.62	132
MC3-pH2.0	1224	1.03	74

a) Calculated from t-plot analysis of the adsorption branch of the isotherm.

In order to determine whether the chiral nematic ordering in the starting composite films has any influence on the porosity of the carbon materials, an additional sample was prepared from a nematic NCC/silica composite sample. This sample was prepared in the exact same manner as **CNMC3** except that the pH of the NCC suspension was adjusted to 2.0 with 1 M HCl prior to the addition of TMOS (see Chapter 2). Nitrogen adsorption measurements of the resulting carbon films (denoted as **MC3-pH2.0**) give a type IV isotherm that appears similar to the isotherm obtained for **CNMC3**. However, the specific surface area and pore volume of **MC3-pH2.0** are somewhat lower than the values calculated for **CNMC3** and the BJH pore size distribution for **MC3-pH2.0** is broader than the distribution calculated for **CNMC3** (Figure 5-6b). These results suggest that the connectivity between NCC required for efficient mesopore formation may be better in the chiral nematic sample.

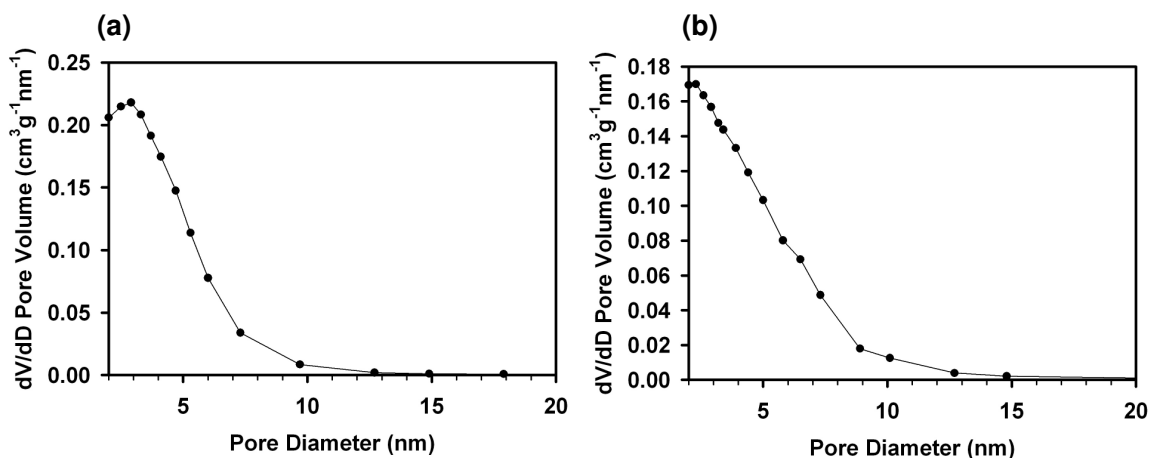


Figure 5-6. (a) BJH pore size distribution for **CNMC3**. (b) BJH pore size distribution for **MC3-pH2.0**.

The porosity of **CNMC3**, **MC3-pH2.0**, and **MC1** was also observed by TEM, as shown in Figure 5-7. TEM of **CNMC3** shows locally aligned carbon rods separated by mesopores, consistent with the local nematic organization expected for a chiral nematic pore structure. **MC3-pH2.0**, on the other hand, shows a more disordered mesopore structure. This suggests that the local ordering in the chiral nematic composite films is greater than in the corresponding nematic films. As expected, TEM images of **MC1** do not show mesoporosity and instead reveal a disordered micropore structure.

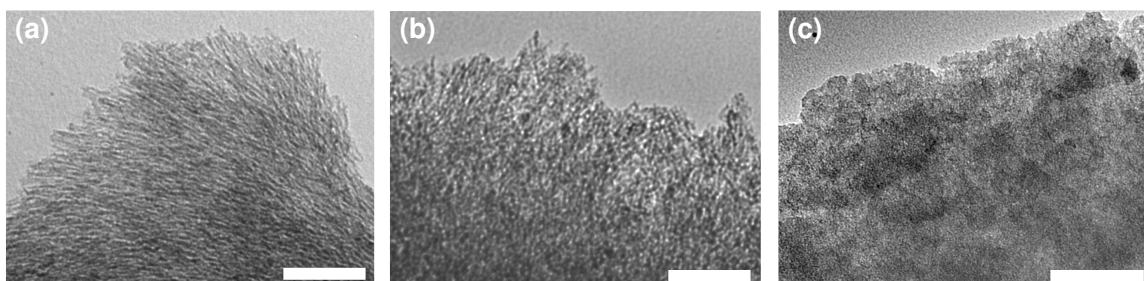


Figure 5-7. TEM micrographs of porous carbon samples. (a) TEM micrograph of **CNMC3**. (b) TEM micrograph of **MC3-pH2.0**. (c) TEM micrograph of **MC1**. Scale bars all = 200 nm.

5.3.3 SEM Structural Studies of NCC-Derived Carbon

The long-range chiral nematic organization of the various carbon samples was studied by SEM. The chiral nematic ordering of NCC was essentially perfectly retained in mesoporous carbon sample **CNMC3** (Figure 5-8). The chiral nematic mesoporous carbon films have smooth surfaces with a repeating layered structure perpendicular to the surface that appears virtually identical to what was reported for mesoporous silica and organosilica in Chapters 2 and 3. At high magnification we see the rod morphology of NCC retained in the carbon and twisting in a counter-clockwise direction is observed, consistent with the left-handed chiral nematic structure of the NCC template.

The carbon films prepared from chiral nematic NCC films without silica (**MC1**) show no retention of chiral nematic ordering (Figure 5-9a). While **CNMC3** has a highly ordered chiral nematic structure, **CNMC2** and **CNMC5** show some chiral nematic ordering but are overall more disordered (Figure 5-9b). There appears to be a window of silica loadings that works best for preserving the chiral nematic structure of NCC during pyrolysis, which is more or less the same range that provides the highest mesoporosity. This appears to be where there is a balance of having enough silica to protect the long-range structure during carbonization while still allowing linkages to form between the carbon rods that provide structural stability upon silica removal.

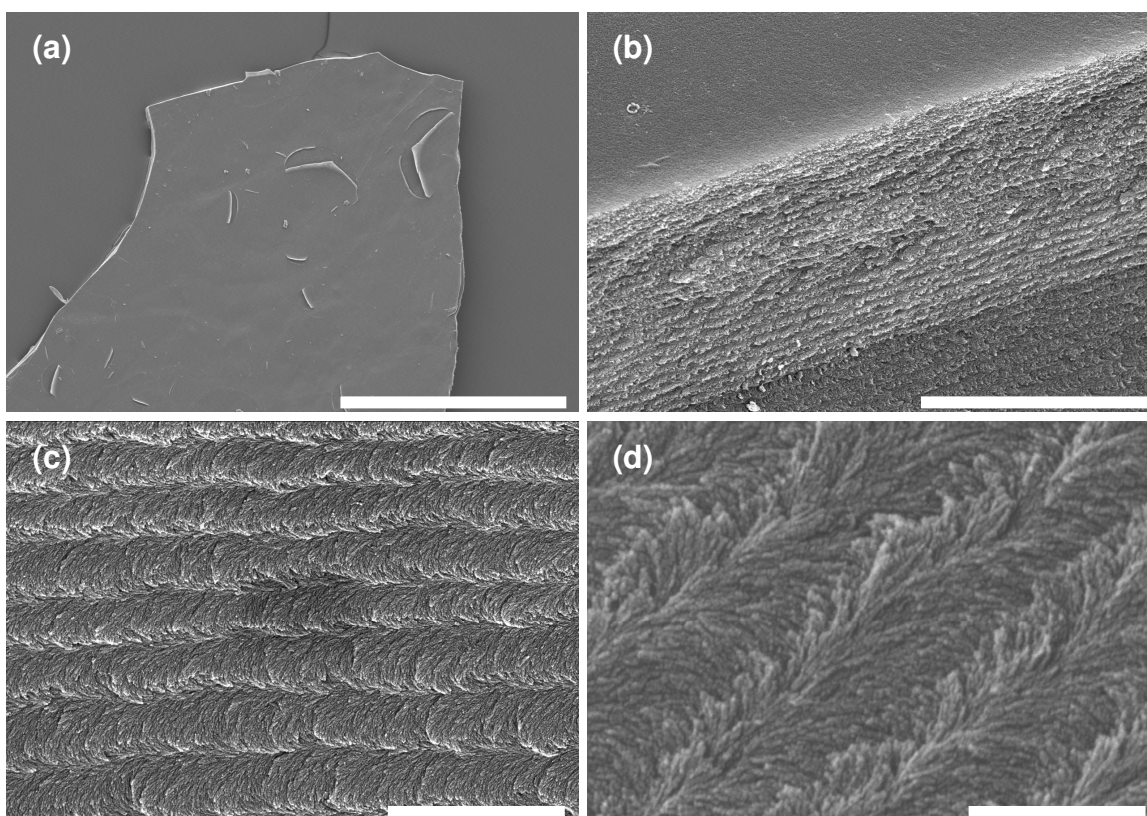


Figure 5-8. SEM micrographs of **CNMC3**. (a) Top view of film at low magnification (scale bar = 500 μm). (b) Side view at fracture (scale bar = 5 μm). (c) Cross-sectional view of film (scale bar = 2 μm). (d) High magnification image of cross-section (scale bar = 500 nm).

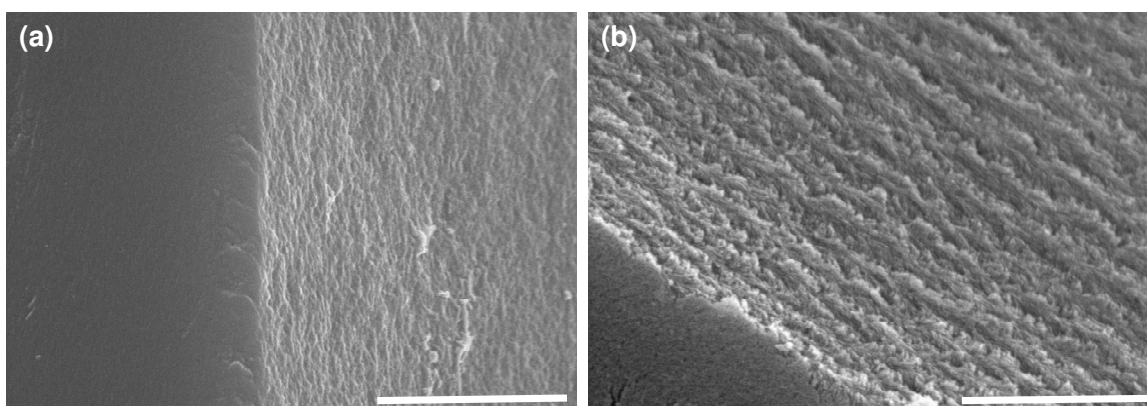


Figure 5-9. SEM micrographs of **MC1** and **CNMC2**. (a) Top view of fracture of **MC1** film (scale bar = 1 μm). (b) Top view of fracture of **CNMC2** film (scale bar = 1 μm).

5.3.4 Chiral Nematic Mesoporous Carbon as a Hard Template for Silica

The helical pitch of chiral nematic materials is often studied by optical techniques such as polarized optical microscopy (POM) and circular dichroism (CD). However, optical studies to probe the chiral nematic structure of **CNMC3** directly could not be carried out due to the opacity of the carbon films. On the other hand, mesoporous carbon has proven useful as a hard template for metal oxide replica structures due to the ease with which it can be selectively removed through thermal oxidation.^[154] As a proof of concept, I examined whether **CNMC3** could be used to template a chiral nematic silica replica that could be characterized by optical techniques.

Silica replication was achieved using an adapted literature procedure.^[228] Briefly, a mixture of TEOS, water, and HCl was loaded into the films and condensed at elevated temperature. After multiple loading steps, the carbon/silica films appear slightly iridescent. The composite films were then calcined under air to remove the carbon template yielding small pieces of colourless silica films. POM shows that the silica replicas are birefringent, which is indicative of long-range anisotropy (Figure 5-10a). A strong positive CD signal is observed from the silica replicas with a peak at 325 nm (Figure 5-10b), demonstrating that they selectively reflect left-handed circularly polarized light in the UV region. This gives further confirmation that the left-handed chiral nematic structure of NCC is preserved in the mesoporous carbon and demonstrates that it can be transferred to other materials via hard templating. The chiral nematic structure of the silica replicas can also be observed by SEM (Figure 5-11), although it is considerably more disordered than in the mesoporous carbon template (**CNMC3**) or mesoporous silica prepared directly from NCC/silica composites.

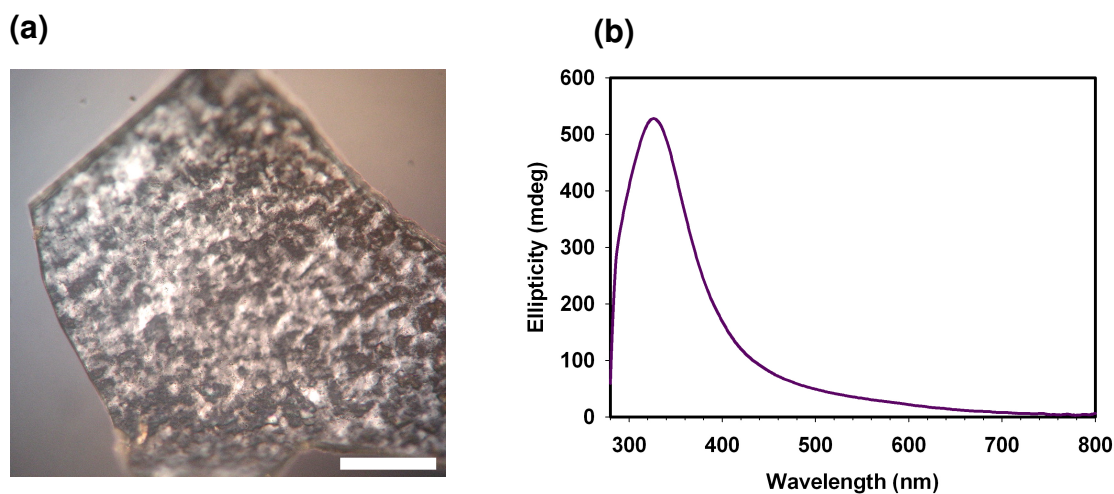


Figure 5-10. Optical characterization of silica templated by **CNMC3**. (a) POM micrograph (scale bar = 200 μm). (b) CD spectrum.

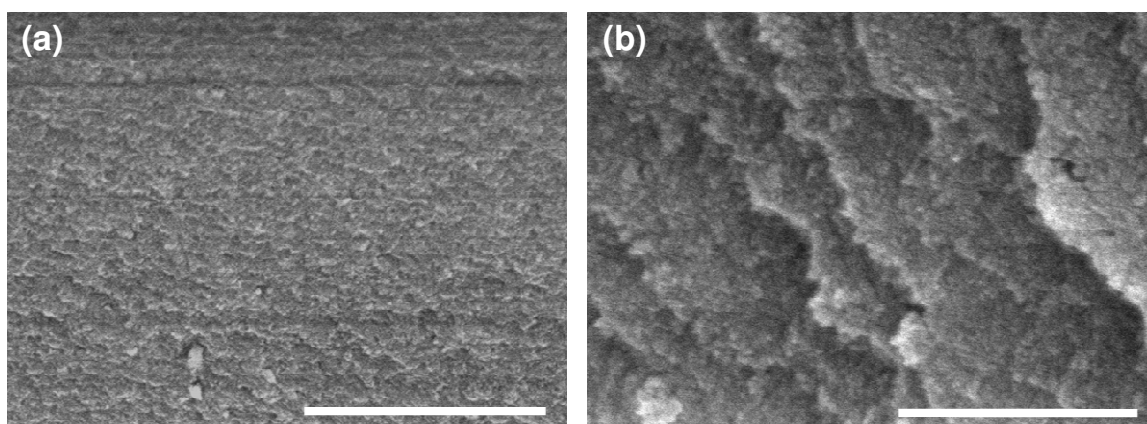


Figure 5-11. SEM micrographs of silica templated by **CNMC3**. (a) Cross-sectional view (scale bar = 2 μm). (b) Cross-sectional view at higher magnification (scale bar = 500 nm).

5.3.5 Application of Chiral Nematic Mesoporous Carbon as a Supercapacitor Electrode

An important application for porous carbon materials is in electrochemical energy storage devices, such as supercapacitors.^[138] Mesoporous carbon **CNMC3** has a conductivity of $\sim 10 \text{ S}\cdot\text{cm}^{-1}$ (measured using the four-probe method) at 25 $^{\circ}\text{C}$ that increases linearly with increasing temperature in the range of 25-170 $^{\circ}\text{C}$, which is indicative of semiconducting behaviour. To test the supercapacitor performance of chiral

nematic mesoporous carbon, a symmetrical capacitor was constructed with carbon sample **CNMC3** using a two-electrode cell and 1 M $\text{H}_2\text{SO}_{4(\text{aq})}$ as the electrolyte solution. The free-standing carbon films were used directly without the addition of any binders as shown in Figure 5-12a.

The galvanostatic charge/discharge profile of **CNMC3** (Figure 5-12b) shows a symmetrical triangular shape typical of near-ideal capacitor behaviour. The specific capacitance of **CNMC3** calculated from the discharge curve at a current load of 230 mA/g is 170 F/g, which is comparable to values reported for hard templated mesoporous carbons measured under similar conditions.^[139] The cyclic voltammogram of **CNMC3** at a scan rate of 2 mV/s is shown in Figure 5-12c. The curve has a rectangular shape with a slight slope indicating the occurrence of some Faradaic processes (i.e., redox reactions) that likely involve defect functional groups in the material. Cyclic voltammetry was further used to test the supercapacitor performance of **CNMC3** at different scan rates (Figure 5-12d). The rectangular shape of the curve is maintained up to a scan rate of 20 mV/s. At 50 mV/s some distortion of the CV curve is apparent and at 100 mV/s the curve is no longer rectangular. The decreased supercapacitor performance at higher scan rates may be due to issues with conductivity or diffusion limitations throughout the mesopore network. Future work will investigate ways to improve performance at high power loads.

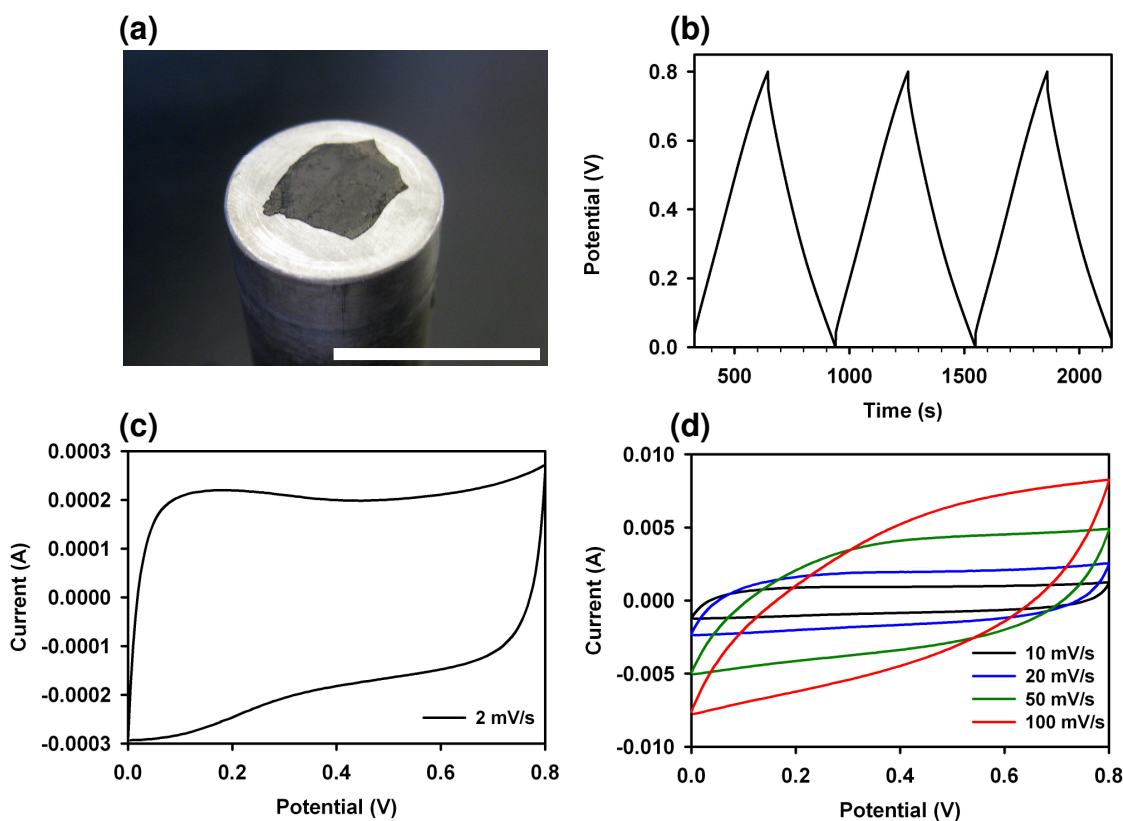


Figure 5-12. Electrochemical characterization of **CNMC3**. (a) Photograph of mesoporous carbon film on a stainless steel current collector (scale bar = 1.5 cm). (b) Galvanostatic charge/discharge curve for **CNMC3** at a current load of 230 mA/g. (c) Cyclic voltammogram of **CNMC3** at a scan rate of 2 mV/s. (d) Cyclic voltammogram of **CNMC3** at scan rates ranging from 10-100 mV/s. All measurements were carried out using a symmetrical two-electrode setup in a 1M $\text{H}_2\text{SO}_{4(\text{aq})}$ electrolyte solution.

5.3.6 Electropolymerization of Polyaniline within Chiral Nematic Mesoporous Carbon

Nanostructured carbon materials are excellent hosts for pseudo-capacitive materials such as transition metal oxides and conducting polymers.^[138, 140, 229] Nanocomposites formed between these materials can take advantage of a combination of electrical double-layer based charge storage and Faradaic charge storage to give energy densities that begin to approach those found in conventional batteries. Polyaniline (PANI) is a simple conducting polymer that has been studied extensively for energy storage applications.^[230-233] PANI can be deposited onto carbon surfaces chemically or

electrochemically to form composites that can achieve much higher specific capacitances than the initial carbon materials.^[141, 234] Electrochemical deposition of PANI is particularly attractive since it can be precisely controlled based on electropolymerization times.

Mesoporous carbon/PANI composite materials were prepared through the electrochemical polymerization of PANI onto **CNMC3**. This was achieved by using the free-standing mesoporous carbon films directly as the working electrode in a three-electrode setup. PANI was polymerized onto the **CNMC3** electrode from 0.2 M aniline dissolved in a 0.5 M H₂SO_{4(aq)} electrolyte solution at a constant potential of 0.8 V (vs. Ag/AgCl). The amount of polymer deposited is easily controlled by simply varying the duration of the electropolymerization; a series of **PANI@CNMC3** samples were prepared by varying the electropolymerization time from 50-900 seconds.

The film surfaces of the **CNMC3** films remain black after polymerization times up to 300 seconds. Figure 5-13 shows SEM images of **PANI@CNMC3** films after electropolymerization times of 100 and 300 seconds. After 100 seconds, the top surface of the films appears unchanged compared to the films without PANI. After 300 seconds, while much of the top surface is still unchanged, polymer nanofibre outgrowth is observed in some regions. The chiral nematic texture is still clearly visible at the edges of the films after 300 second PANI deposition (Figure 5-13d) demonstrating that the electropolymerization conditions do not disrupt the long-range ordering of the carbon films.

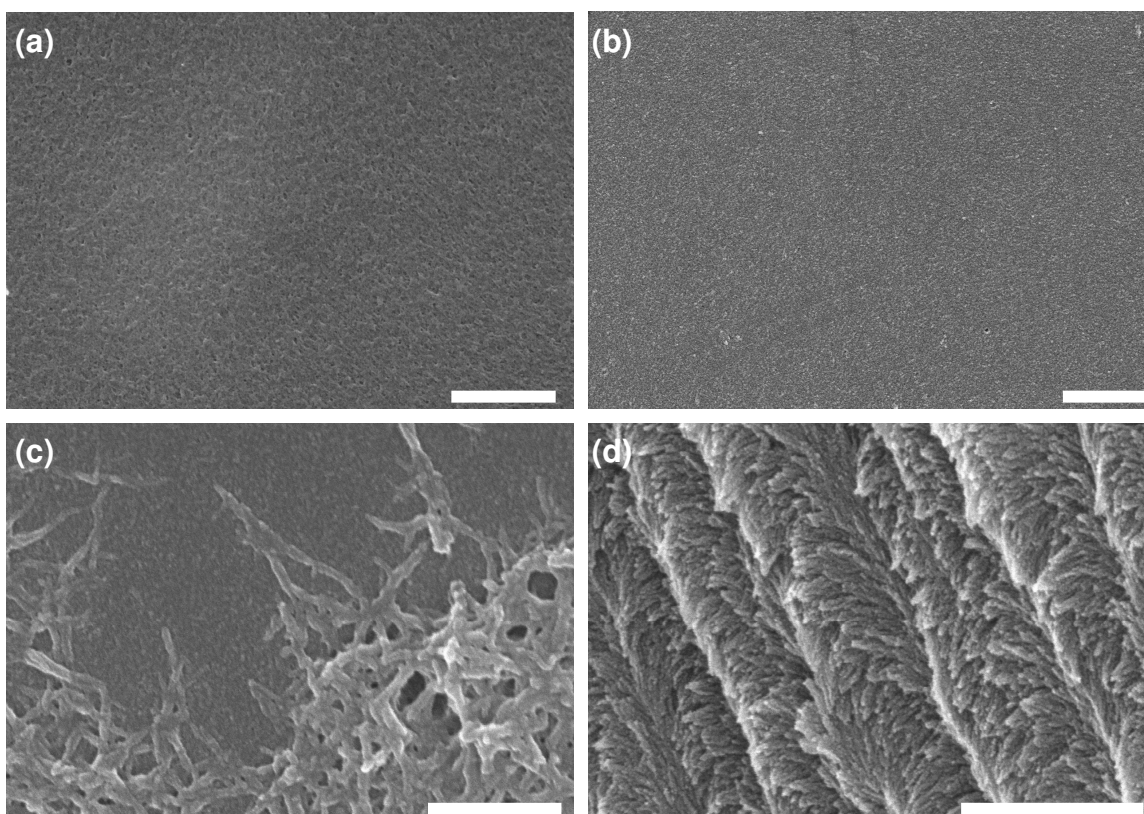


Figure 5-13. SEM micrographs of selected samples. (a) Top surface of a **CNMC3** film before PANI deposition. (b) Top surface of a **PANI@CNMC3** film after 100 second electropolymerization. (c) Top surface of a **PANI@CNMC3** film after 300 second electropolymerization. (d) Edge of **PANI@CNMC3** film after 300 second electropolymerization. Scale bars all = 500 nm.

After ~350 seconds the accumulation of PANI on the surface of the films begins to cause thin-film interference resulting in colours that depend on the electropolymerization time. Figure 5-14 shows SEM images of **PANI@CNMC3** films with copper, purple and green colours after deposition times of 350, 400, and 900 seconds, respectively.

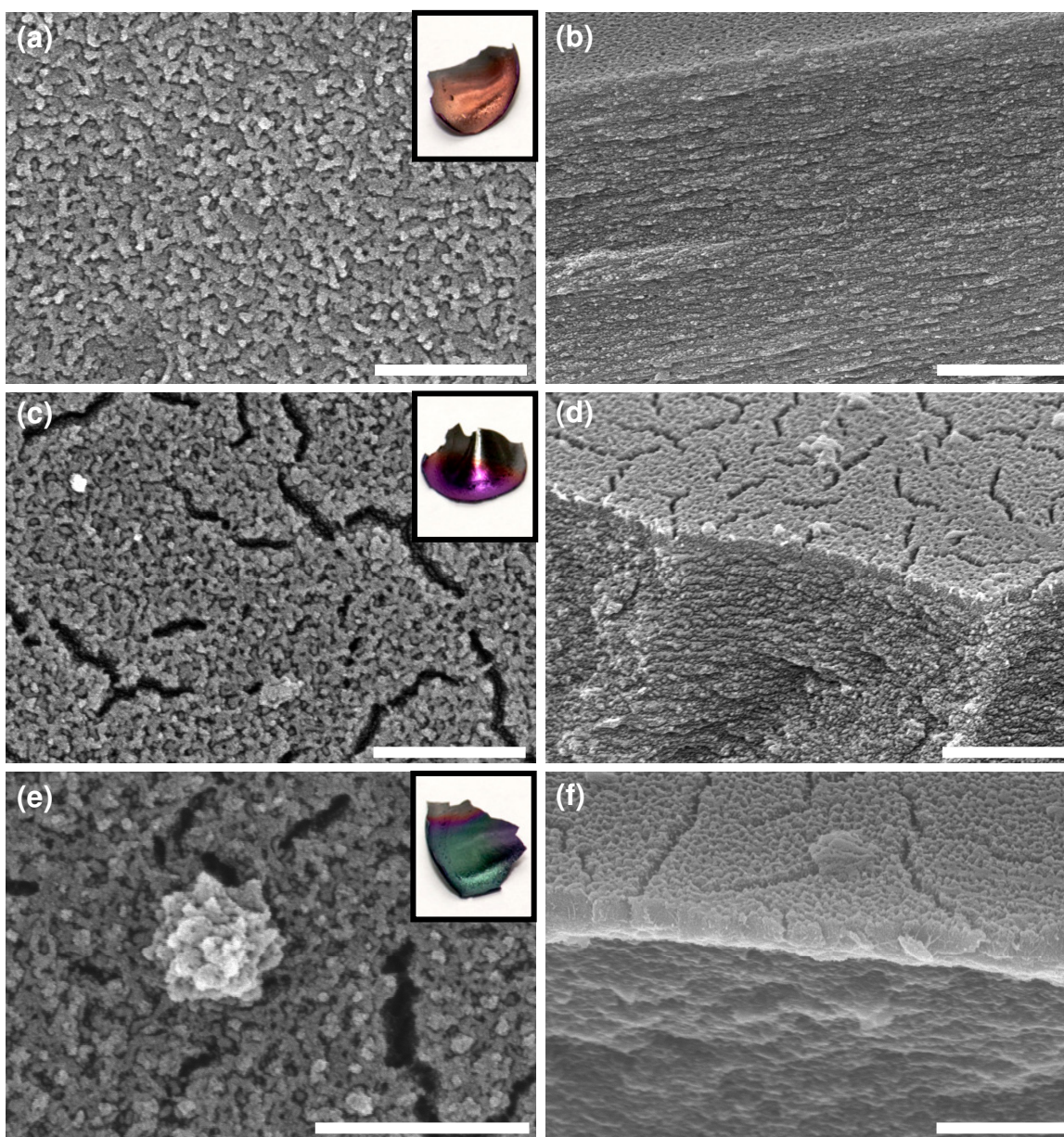


Figure 5-14. SEM images and photographs of different coloured **PANI@CNMC3** films. (a) Top view of a **PANI@CNMC3** film after 350 second electropolymerization (scale bar = 500 nm). (b) Side view of a **PANI@CNMC3** film after 350 second electropolymerization (scale bar = 1 μm). (c) Top view of a **PANI@CNMC3** film after 400 second electropolymerization (scale bar = 500 nm). (d) Side view of a **PANI@CNMC3** film after 400 second electropolymerization (scale bar = 1 μm). (e) Top view of a **PANI@CNMC3** film after 900 second electropolymerization (scale bar = 500 nm). (f) Side view of a **PANI@CNMC3** film after 900 second electropolymerization (scale bar = 1 μm). The insets show photographs of the corresponding films.

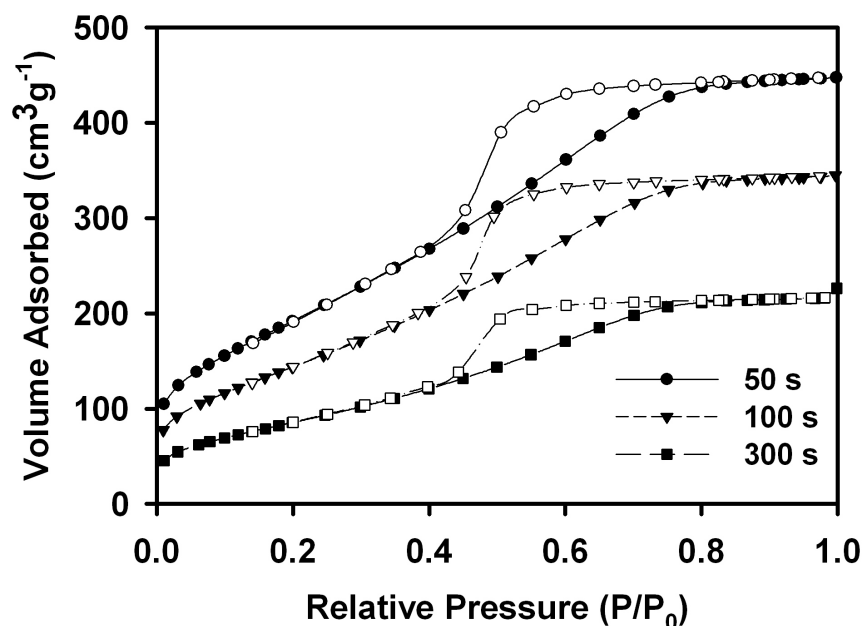
The colours of the films reversibly red shift after soaking with water; the copper films become yellow, the purple films become red, and the green films become

colourless, presumably reflecting light in the NIR. The copper films obtained after 350 seconds of PANI deposition show a uniform, nanotextured polymer coating with a thickness of < 50 nm. After a 400 second deposition time, the polymer layer is between 50-100 nm thick and shows small cracks throughout the surface. The green films obtained after 900 second deposition times have a PANI layer of ~300 nm and show outgrowths with flower-like and nanorod morphologies in some areas.

Elemental analysis of the films confirms that there is an increase in PANI loading for longer electropolymerization times. The nitrogen content increases from 0% to a maximum of 4 wt. % for the 900 second sample as reported in Table 5-3. This corresponds to a PANI loading of 27 wt. % given that the theoretical nitrogen content of PANI is 15%. In order to determine the extent of PANI polymerization within the mesopores of **CNMC3**, nitrogen adsorption measurements were carried out for the samples prepared using different electropolymerization times (Table 5-3). The surface areas and pore volumes drop dramatically between electropolymerization times of 0-300 seconds, however, the porosity is essentially unchanged going from 300 to 900 second deposition times (Figure 5-15). Combined with the SEM images shown above, these results suggests that PANI deposition mostly occurs within the mesopores up until ~300 s, after which deposition begins to occur predominantly on the film surface. The pore volume of 0.33 cm³/g measured for the 300 second sample corresponds to a 75% mesopore filling. Assuming uniform pore loading and using a value of 1.25 g/cm³ for the density of PANI,^[235] one would predict a PANI loading of 53 wt. % for this sample. However, the measured PANI loading after a 300 second electropolymerization is only 15 wt. %, which implies that the mesopore loading is not entirely uniform and that pore blockage accounts for much of the observed decrease in porosity.

Table 5-3. Characterization data for **PANI@CNMC3** samples.

Polymerization Time	%N	BET Surface Area (m ² /g)	Pore Vol. (cm ³ /g)	Max. Specific Current (A/g)
0	0	1465	1.22	0.50
50	1.1	711	0.69	1.07
100	1.5	534	0.53	1.45
300	2.2	317	0.33	1.60
900	4	352	0.32	1.84

**Figure 5-15.** Nitrogen adsorption isotherms for **PANI@CNMC3** electropolymerized for 50, 100, and 300 seconds.

Electrochemical measurements were carried out for the **PANI@CNMC3** samples using a three-electrode setup. Figure 5-16b shows the cyclic voltammograms (2 mV/s) for the **PANI@CNMC3** films prepared with 50, 300, and 900 second electropolymerization times (**CNMC3** without PANI is included for comparison). For the 50 second **PANI@CNMC3** sample redox peaks are observed at ~0.5 and 0.2 V, which is fairly typical for PANI, and the specific current is substantially increased compared to **CNMC3**. As expected, longer polymerization times lead to larger redox peaks; however,

the increase in specific current relative to the amount of PANI deposited is much greater for the shorter electropolymerization times. This suggests that the PANI deposited within the mesopores has a greater specific capacitance than the PANI deposited on the surface of the films at longer polymerization times.

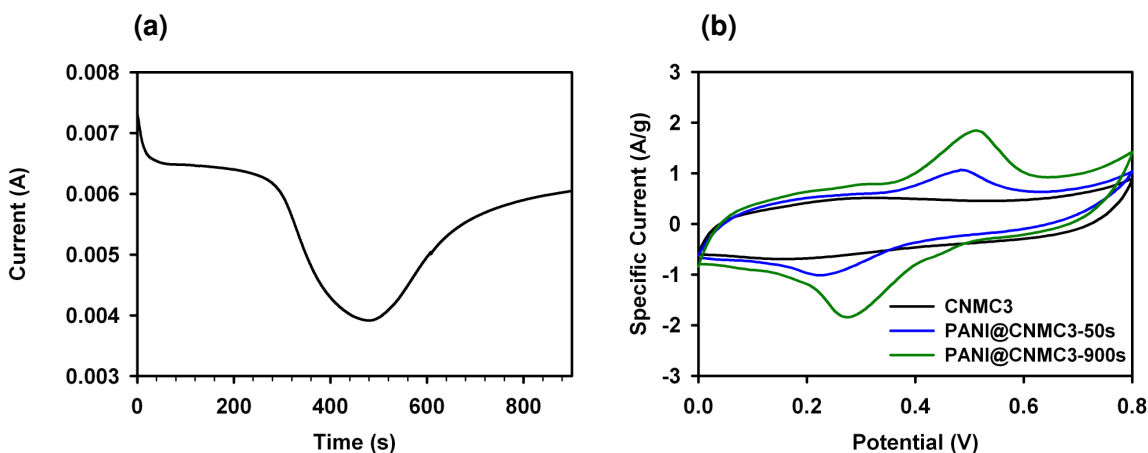


Figure 5-16. Electrochemical characterization of selected **PANI@CNMC3** samples. (a) Current vs. time curve during a 900 s PANI electropolymerization carried out at 0.8 V vs. Ag/AgCl. (b) CV curves for selected samples obtained at a scan rate of 2 mV/s (all CVs were run with a three electrode setup, potential is vs. Ag/AgCl).

5.4 Conclusions

I have demonstrated that nanocrystalline cellulose confined within a silica host is an ideal precursor for a new form of mesoporous carbon that has a chiral nematic structure. Upon pyrolysis and etching of the silica, free-standing films of chiral nematic mesoporous carbon are obtained. The chirality of the films was demonstrated by electron microscopy and by using them as a template for chiral nematic silica. As the mesoporous carbon films have a high specific surface area and good electrical conductivity, they are an effective electrode material for supercapacitors. Polyaniline can be readily electropolymerized within the mesoporous carbon films, which greatly enhances their

energy storage capacity. Future work will aim to further develop these materials for energy storage devices and try to determine whether the chiral nematic structure of the mesoporous carbon films can impart unique electrical properties.

Chapter 6

Conclusions and Future Directions

6.1 Conclusions

Since the development of liquid crystal templating in 1992, there has been intense interest in mesoporous materials.^[85] The vast majority of research in this area has used amphiphilic surfactant molecules and polymers that can form hexagonal, cubic, and lamellar structures as templates. Chiral surfactants have been successfully used to generate chiral mesoporous materials, which is of considerable interest for applications involving enantioselective separation and catalysis.^[162] With respect to introducing chirality into mesoporous materials, biological templates provide an interesting alternative to surfactants due to their inherent enantiopurity and ability to form unique liquid crystal phases.

Although colloidal nanocrystalline cellulose particles have been known for over 50 years,^[52] only recently have their self-assembly properties been fully appreciated with the discovery that they can form a chiral nematic phase.^[55] Remarkably, by simply letting the water from suspensions of nanocrystalline cellulose evaporate, chiral nematic films that behave as 1D photonic crystals can be obtained.^[60] The aim of this thesis has been to explore the use of nanocrystalline cellulose as a novel liquid crystal template for mesoporous materials. I have found that in an analogous way to surfactant micelles, NCC particles can be used to template mesopores and give rise to high surface area materials. In the same way that the liquid crystal phases formed by surfactant micelles can be replicated in mesoporous solids, I have developed methods that allow the chiral nematic structure of NCC to be replicated in diverse materials.

In Chapter 2, I described the synthesis and characterization of the first chiral nematic mesoporous material, namely chiral nematic mesoporous silica (CNMS). Through a simple evaporation induced self-assembly approach, free-standing NCC/silica composite films were obtained that display photonic properties. The helical pitch of the films, and hence their peak reflected wavelength, can be easily tuned by making very simple changes to the synthetic procedure. Remarkably, after removing the NCC template by calcination, the chiral nematic photonic structure is retained in the mesoporous silica replicas. As a result, I was able to obtain mesoporous films with different colours spanning the visible spectrum. These chiral nematic mesoporous silica films have many advantages compared to pure NCC films. NCC films are not very thermally stable, have very little accessible surface area, and their photonic properties are essentially fixed. On the other hand, CNMS is very thermally stable, has an extremely high accessible surface area, and can reversibly change colour in response to stimuli. In this last respect, I was able to demonstrate that the unique combination of a chiral nematic photonic structure and mesoporosity in CNMS films causes their circular dichroism signal to change in response to changes of the refractive index within the pores.

In Chapter 3, I demonstrated that the general approach reported in Chapter 2 can be expanded to make mesoporous organosilica films with chiral nematic structures. This required the development of an alternative method for removing NCC from the composite films so as to leave the organic bridges intact. This approach can be used to generate chiral nematic mesoporous organosilica with both aliphatic and aromatic bridging groups. Notably, mesoporous organosilica films with an ethylene-bridge show significantly improved flexibility compared to silica, which could be useful for many applications. In Chapter 3, it was also demonstrated that by selecting different methods of

removing NCC from NCC/silica composite films (calcination vs. acid hydrolysis) some control over the pore size can be achieved.

The pore structure of the chiral nematic mesoporous materials reported in Chapters 2 and 3 is substantially different than for materials prepared using conventional surfactant templates. Whereas the micelles formed by surfactants tend to have very uniform sizes, the size of NCC particles are not as monodisperse. The pore size distributions of NCC-templated mesoporous materials are therefore broader than those seen for typical surfactant-templated materials. The local ordering of the pores in NCC templated silica is also not nearly as well-defined as it is for most surfactant templated systems. The disordered local nematic organization found in chiral nematic mesoporous materials is much more difficult to study with TEM and PXRD than the hexagonal, cubic, and lamellar materials prepared from surfactant templates. Some insight into the pore structure of CNMS was gained by the work reported in Chapter 4; the ability to replicate long range chiral nematic ordering when using CNMS as a hard template clearly implies that the chiral nematic pore structure is connected in three dimensions. We are currently in the process of using less conventional methods to gain more insight into this unusual pore structure, which will be discussed in more detail in the following section.

Despite the great success of using NCC to template mesoporous silica and organosilica, there are clearly some limitations. The chiral nematic self-assembly of sulfated NCC is sensitive to factors such as pH and ionic strength, which limits the materials that can be directly templated by NCC. The results presented in Chapters 2 and 3 suggest that NCC can be used to template chiral nematic materials so long as the precursors are neutral, hydrophilic, and do not condense too rapidly. One way to get around this limitation is to use CNMS as a hard template, as discussed in Chapter 4. In addition to TiO_2 , this hard templating approach should also be applicable to the formation

of other chiral nematic materials that may be difficult to obtain through direct templating with NCC.

In Chapter 5, I reported that NCC/silica composite films can be directly converted to chiral nematic mesoporous carbon films. This provides an efficient method for obtaining mesoporous carbon and gives free-standing films with high specific surface areas. While the chiral nematic organization in mesoporous silica and organosilica clearly imparts useful properties (i.e., tunable selective reflection of light), the benefits of having chiral nematic ordering in mesoporous carbon are less obvious. Future work is necessary to investigate both theoretically and experimentally whether any unique electromagnetic properties may arise from this novel structure. Nonetheless, the film morphology and high surface area of chiral nematic mesoporous carbon makes it an excellent electrode material for supercapacitors. In addition, polyaniline can be electrodeposited onto these materials in a very controlled manner to further improve their performance.

Taken as a whole, the work presented in this thesis presents significant progress in the use of naturally-derived templates for the synthesis of high surface area mesoporous materials; the fact that cellulose is the most abundant organic material on Earth makes it particularly attractive in this regard. Furthermore, the unique self-assembly properties of NCC have opened the door to mesoporous materials with chiral nematic structures. The materials described in this thesis could provide unique opportunities in areas ranging from colour-changing coatings and sensors, to electrical energy storage devices and possibly materials for chiral separation and catalysis. This work will hopefully inspire the use of NCC to template other novel materials with chiral nematic organization and trigger the further exploration of different biologically derived templates.

6.2 Future Directions

The work presented in this thesis focused mainly on the development of synthetic methodologies for using NCC as a liquid crystal template for mesoporous solids. Extensive characterization was carried out on these materials; however, there are still many unanswered questions with respect to their structures and properties that would be useful to know to aid in the development of future applications.

Studying the pore structure of chiral nematic mesoporous materials is challenging due to their broad pore size distributions and fairly disordered local structures. This makes characterization with PXRD and TEM, two of the most common techniques used to study mesoporous materials, not particularly useful. I have recently begun to explore electron tomography as an alternative to standard TEM in order to gain more insight into the pore structure of CNMS. By taking images at different angles, electron tomography provides a way to construct 3D models from 2D TEM images, which should give us a better understanding of chiral nematic pore structures.

We are also beginning to use solid-state NMR spectroscopy to probe the diffusion of molecules within CNMS films to better understand their pore structure. Initial results with water show that diffusion can occur both laterally and perpendicularly throughout the films, but the lateral diffusion is considerably faster. These results demonstrate that the pores are interconnected and organized in an anisotropic arrangement, as would be expected based on the anisotropic shape of NCC.

NCC exhibits chirality at three different levels: the molecular chirality of individual glucose units, the chiral shape of individual crystallites, and the long-range chirality present in the chiral nematic liquid crystal phase. Although it is clear that long-range chirality exists in chiral nematic mesoporous materials, it is still uncertain whether these other levels of chirality are replicated. The optimization of short-range chirality is

likely to be important if CNMS and CNMO materials are to find use in applications such as chiral separation. We are currently developing methods to probe this, for example by studying the diffusion of enantiomers within mesoporous films by solid-state NMR spectroscopy.

There are still many opportunities to optimize the synthesis of chiral nematic mesoporous films. One issue is the cracking that occurs during drying of the films. Although the CNMO films reported in Chapter 3 provide a step in the right direction, it would be useful to develop methods to form very large crack-free films that could be applied, for example, as window coatings or used as highly porous membranes. Another area for improvement is the minimization of defects in the films. From POM and SEM analysis, it is clear that the chiral nematic films have small domains (on the order of several microns), which broadens and reduces the intensity of their reflection peaks. Developing methods to form larger domains within the films would therefore improve their optical properties.

Many exciting new directions with both CNMS and CNMO films are currently being explored. As with other mesoporous silica materials, the pores of CNMS and CNMO can be readily functionalized with trialkoxysilanes. This is of particular interest for the future development of sensors based on these materials. As a very simple example, n-octyl groups have been grafted onto the surface of CNMS and CNMO films, which make the films hydrophobic. These modified films no longer change colour in response to water, but can still be readily infiltrated by organic liquids and vapors. In a similar way that has been reported for porous Bragg stacks and inverse opals,^[236, 237] it should be possible to distinguish between many different liquids and vapors by forming arrays of films functionalized with different organic groups. The detection of biomolecules, which has been heavily explored for porous silicon photonic crystals, may

also be possible with chiral nematic mesoporous materials.^[238, 239] This could be achieved by grafting receptors to the walls of CNMS or CNMO films and monitoring the selective binding of target ligands with circular dichroism.

The materials reported in Chapter 3 provide a starting point for the incorporation of many other interesting organic bridging groups into CNMO materials. For example, photoswitchable groups (e.g., azobenzenes) have been incorporated into other mesoporous organosilica films, and can be used to control their pore size with light.^[240] In the case of CNMO films, this could provide a way to tune their selective reflection with light. Another interesting possibility would be to incorporate catalytically active sites into CNMO films and see whether the chirality of the films can aid in enantioselective catalysis.

In Chapter 4, I reported that the chiral nematic structure of CNMS can be replicated through hard templating to form TiO₂. So far I have only investigated the basic structural and optical properties of chiral nematic TiO₂, and there is still much work needed to assess its potential for applications such as photocatalysis and energy storage devices. The general procedure used to synthesize TiO₂ by hard templating could also be expanded to make other chiral metal oxides and metals and other methods for incorporating precursors into the films (e.g., chemical vapor deposition and atomic layer deposition) could be explored.

Chapter 5 describes the synthesis of chiral nematic mesoporous carbon from NCC and its application as a supercapacitor electrode material. Future work to improve the conductivity of these materials will likely be important if they are to be implemented in actual devices. The incorporation of PANI into CNMC was shown to be quite simple and improve its charge storage. It would be interesting to investigate the incorporation of different pseudo-capacitive materials into CNMC (e.g., other conducting polymers and

metal oxides) and compare their performance. It is still uncertain whether the chiral nematic structure of CNMC imparts any unique properties. One possibility is that the helical structure of CNMC films causes them to behave as inductors. This could be investigated by performing magnetic measurements while passing a current through the CNMC films.

The general approaches used in this thesis should be applicable to the templation of other chiral nematic materials, such as polymers, so long as the precursors are neutral, hydrophilic, and can be prevented from reacting until the final stages of the EISA process. On a final note, only one specific type of NCC was used in this thesis: namely sulfated NCC derived from softwood pulp. Given that NCC derived from different sources have unique shapes and sizes,^[50] and surface functionalized NCC can form a chiral nematic phase in non-aqueous systems,^[68] it would be interesting to explore their use as liquid crystal templates as well.

References

- [1] P. Moriarty, *Reports on Progress in Physics* **2001**, 64, 297.
- [2] G. A. Ozin, A. C. Arsenault, *Nanochemistry A Chemical Approach to Nanomaterials*, RSC Publishing, Cambridge, **2005**.
- [3] K. L. Kelly, E. Coronado, L. L. Zhao, G. C. Schatz, *Journal of Physical Chemistry B* **2003**, 107, 668.
- [4] A. P. Alivisatos, *Science* **1996**, 271, 933.
- [5] R. E. Morris, P. S. Wheatley, *Angewandte Chemie-International Edition* **2008**, 47, 4966.
- [6] M. E. Davis, Z. Chen, D. M. Shin, *Nature Reviews Drug Discovery* **2008**, 7, 771.
- [7] D. Astruc, F. Lu, J. R. Aranzaes, *Angewandte Chemie-International Edition* **2005**, 44, 7852.
- [8] G. M. Whitesides, B. Grzybowski, *Science* **2002**, 295, 2418.
- [9] J. D. Halley, D. A. Winkler, *Complexity* **2008**, 14, 10.
- [10] J. M. Lehn, *Science* **2002**, 295, 2400.
- [11] G. M. Whitesides, M. Boncheva, *Proceedings of the National Academy of Sciences of the United States of America* **2002**, 99, 4769.
- [12] S. G. Zhang, *Nature Biotechnology* **2003**, 21, 1171.
- [13] H. Colfen, S. Mann, *Angewandte Chemie-International Edition* **2003**, 42, 2350.
- [14] Y. N. Xia, G. M. Whitesides, *Annual Review of Materials Science* **1998**, 28, 153.
- [15] M. Eddaoudi, D. B. Moler, H. L. Li, B. L. Chen, T. M. Reineke, M. O'Keeffe, O. M. Yaghi, *Accounts of Chemical Research* **2001**, 34, 319.

- [16] U. Ciesla, F. Schüth, *Microporous and Mesoporous Materials* **1999**, 27, 131.
- [17] B. H. Ji, H. J. Gao, *Journal of the Mechanics and Physics of Solids* **2004**, 52, 1963.
- [18] R. Wolfenden, M. J. Snider, *Accounts of Chemical Research* **2001**, 34, 938.
- [19] S. Keten, Z. Xu, B. Ihle, M. J. Buehler, *Nature Materials* **2010**, 9, 359.
- [20] K. Autumn, M. Sitti, Y. C. A. Liang, A. M. Peattie, W. R. Hansen, S. Sponberg, T. W. Kenny, R. Fearing, J. N. Israelachvili, R. J. Full, *Proceedings of the National Academy of Sciences of the United States of America* **2002**, 99, 12252.
- [21] A. R. Parker, H. E. Townley, *Nature Nanotechnology* **2007**, 2, 347.
- [22] V. Sharma, M. Crne, J. O. Park, M. Srinivasarao, *Science* **2009**, 325, 449.
- [23] R. A. Potyrailo, H. Ghiradella, A. Vertiatchikh, K. Dovidenko, J. R. Cournoyer, E. Olson, *Nature Photonics* **2007**, 1, 123.
- [24] M. Sumper, *Science* **2002**, 295, 2430.
- [25] S. I. Stupp, P. V. Braun, *Science* **1997**, 277, 1242.
- [26] W. R. Hansen, K. Autumn, *Proceedings of the National Academy of Sciences of the United States of America* **2005**, 102, 385.
- [27] J. D. Joannopoulos, P. R. Villeneuve, S. H. Fan, *Nature* **1997**, 386, 143.
- [28] D. P. Puzzo, L. D. Bonifacio, J. Oreopoulos, C. M. Yip, I. Manners, G. A. Ozin, *Journal of Materials Chemistry* **2009**, 19, 3500.
- [29] D. Englund, D. Fattal, E. Waks, G. Solomon, B. Zhang, T. Nakaoka, Y. Arakawa, Y. Yamamoto, J. Vuckovic, *Physical Review Letters* **2005**, 95, 4.
- [30] K. Busch, S. John, *Physical Review E* **1998**, 58, 3896.

- [31] J. C. Knight, T. A. Birks, P. S. Russell, D. M. Atkin, *Optics Letters* **1996**, *21*, 1547.
- [32] A. Mekis, J. C. Chen, I. Kurland, S. H. Fan, P. R. Villeneuve, J. D. Joannopoulos, *Physical Review Letters* **1996**, *77*, 3787.
- [33] O. Painter, R. K. Lee, A. Scherer, A. Yariv, J. D. O'Brien, P. D. Dapkus, I. Kim, *Science* **1999**, *284*, 1819.
- [34] Y. Y. Li, F. Cunin, J. R. Link, T. Gao, R. E. Betts, S. H. Reiver, V. Chin, S. N. Bhatia, M. J. Sailor, *Science* **2003**, *299*, 2045.
- [35] S. Y. Choi, M. Mamak, G. von Freymann, N. Chopra, G. A. Ozin, *Nano Letters* **2006**, *6*, 2456.
- [36] S. Chandrasekhar, *Liquid Crystals*, 2nd ed., Cambridge University Press, Cambridge, **1992**.
- [37] G. J. T. Tiddy, *Physics Reports-Review Section of Physics Letters* **1980**, *57*, 1.
- [38] K. Hiltrop, in *Chirality in Liquid Crystals* (Eds.: H. S. Kitzerow, C. Bahr), Springer-Verlag, New York, **2001**.
- [39] H. S. Kitzerow, C. Bahr, *Chirality in Liquid Crystals*, Springer-Verlag, New York, **2001**.
- [40] D. G. Gray, *Carbohydrate Polymers* **1994**, *25*, 277.
- [41] F. Tombolato, A. Ferrarini, *Journal of Chemical Physics* **2005**, *122*.
- [42] F. Tombolato, A. Ferrarini, E. Grelet, *Physical Review Letters* **2006**, *96*.
- [43] F. Reinitzer, *Monatshefte Chemie* **1888**, *9*, 421.
- [44] H. De Vries, *Acta Crystallographica* **1951**, *4*, 219.
- [45] D. Klemm, B. Heublein, H. P. Fink, A. Bohn, *Angewandte Chemie-International Edition* **2005**, *44*, 3358.

- [46] Y. Habibi, L. A. Lucia, O. J. Rojas, *Chemical Reviews* **2010**, *110*, 3479.
- [47] A. Sturcova, I. His, D. C. Apperley, J. Sugiyama, M. C. Jarvis, *Biomacromolecules* **2004**, *5*, 1333.
- [48] H. Lichtenegger, A. Reiterer, S. E. Stanzl-Tschegg, P. Fratzl, *Journal of Structural Biology* **1999**, *128*, 257.
- [49] D. Klemm, F. Kramer, S. Moritz, T. Lindstrom, M. Ankerfors, D. Gray, A. Dorris, *Angewandte Chemie-International Edition* **2011**, *50*, 5438.
- [50] S. Elazzouzi-Hafraoui, Y. Nishiyama, J.-L. Putaux, L. Heux, F. Dubreuil, C. Rochas, *Biomacromolecules* **2008**, *9*, 57.
- [51] W. Y. Hamad, T. Q. Hu, *Canadian Journal of Chemical Engineering* **2010**, *88*, 392.
- [52] B. G. Ranby, *Acta Chemica Scandinavica* **1949**, *3*, 649.
- [53] J. Araki, M. Wada, S. Kuga, *Langmuir* **2001**, *17*, 21.
- [54] R. S. Werbowyj, D. G. Gray, *Molecular Crystals and Liquid Crystals* **1976**, *34*, 97.
- [55] J. F. Revol, H. Bradford, J. Giasson, R. H. Marchessault, D. G. Gray, *International Journal of Biological Macromolecules* **1992**, *14*, 170.
- [56] X. M. Dong, T. Kimura, J. F. Revol, D. G. Gray, *Langmuir* **1996**, *12*, 2076.
- [57] X. M. Dong, D. G. Gray, *Langmuir* **1997**, *13*, 2404.
- [58] X. M. Dong, J. F. Revol, D. G. Gray, *Cellulose* **1998**, *5*, 19.
- [59] J. F. Revol, L. Godbout, X. M. Dong, D. G. Gray, H. Chanzy, G. Maret, *Liquid Crystals* **1994**, *16*, 127.
- [60] J. F. Revol, L. Godbout, D. G. Gray, *Journal of Pulp and Paper Science* **1998**, *24*, 146.

- [61] J. Pan, W. Hamad, S. K. Straus, *Macromolecules* **2010**, *43*, 3851.
- [62] S. Beck, J. Bouchard, R. Berry, *Biomacromolecules* **2011**, *12*, 167.
- [63] L. Onsager, *Annals of the New York Academy of Sciences* **1949**, *51*, 627.
- [64] A. Stroobants, H. N. W. Lekkerkerker, T. Odijk, *Macromolecules* **1986**, *19*, 2232.
- [65] W. J. Orts, L. Godbout, R. H. Marchessault, J. F. Revol, *Macromolecules* **1998**, *31*, 5717.
- [66] J. Araki, S. Kuga, *Langmuir* **2001**, *17*, 4493.
- [67] J. P. Straley, *Physical Review A* **1976**, *14*, 1835.
- [68] L. Heux, G. Chauve, C. Bonini, *Langmuir* **2000**, *16*, 8210.
- [69] M. N. Angles, A. Dufresne, *Macromolecules* **2001**, *34*, 2921.
- [70] M. Roohani, Y. Habibi, N. M. Belgacem, G. Ebrahim, A. N. Karimi, A. Dufresne, *European Polymer Journal* **2008**, *44*, 2489.
- [71] E. Lam, K. B. Male, J. H. Chong, A. C. W. Leung, J. H. T. Luong, *Trends in Biotechnology* **2012**, *30*, 283.
- [72] T. Kovacs, V. Naish, B. O'Connor, C. Blaise, F. Gagne, L. Hall, V. Trudeau, P. Martel, *Nanotoxicology* **2010**, *4*, 255.
- [73] J. K. Jackson, K. Letchford, B. Z. Wasserman, L. Ye, W. Y. Hamad, H. M. Burt, *International Journal of Nanomedicine* **2011**, *6*, 321.
- [74] S. Dong, M. Roman, *Journal of the American Ceramic Society* **2007**, *129*, 13810.
- [75] M. Hasani, E. D. Cranston, G. Westman, D. G. Gray, *Soft Matter* **2008**, *4*, 2238.
- [76] K. A. Mahmoud, J. A. Mena, K. B. Male, S. Hrapovic, A. Kamen, J. H. T. Luong, *ACS Applied Materials & Interfaces* **2010**, *2*, 2924.

- [77] N. Drogat, R. Granet, V. Sol, A. Memmi, N. Saad, C. K. Koerkamp, P. Bressollier, P. Krausz, *Journal of Nanoparticle Research* **2011**, *13*, 1557.
- [78] H. Liu, D. Wang, Z. Song, S. Shang, *Cellulose* **2011**, *18*, 67.
- [79] C. M. Cirtiu, A. F. Dunlop-Briere, A. Moores, *Green Chemistry* **2011**, *13*, 288.
- [80] E. Lam, S. Hrapovic, E. Majid, J. H. Chong, J. H. T. Luong, *Nanoscale* **2012**, *4*, 997.
- [81] Y. Zhou, E.-Y. Ding, W.-D. Li, *Materials Letters* **2007**, *61*, 5050.
- [82] Y. Shin, G. J. Exarhos, *Materials Letters* **2007**, *61*, 2594.
- [83] E. Dujardin, M. Blaseby, S. Mann, *Journal of Materials Chemistry* **2003**, *13*, 696.
- [84] K. S. W. Sing, D. H. Everett, R. A. W. Haul, L. Moscou, R. A. Pierotti, J. Rouquerol, T. Siemieniewska, *Pure and Applied Chemistry* **1985**, *57*, 603.
- [85] C. T. Kresge, M. E. Leonowicz, W. J. Roth, J. C. Vartuli, J. S. Beck, *Nature* **1992**, *359*, 710.
- [86] J. S. Beck, J. C. Vartuli, W. J. Roth, M. E. Leonowicz, C. T. Kresge, K. D. Schmitt, C. T. W. Chu, D. H. Olson, E. W. Sheppard, S. B. McCullen, J. B. Higgins, J. L. Schlenker, *Journal of the American Chemical Society* **1992**, *114*, 10834.
- [87] Q. S. Huo, D. I. Margolese, U. Ciesla, P. Y. Feng, T. E. Gier, P. Sieger, R. Leon, P. M. Petroff, F. Schüth, G. D. Stucky, *Nature* **1994**, *368*, 317.
- [88] D. Y. Zhao, J. L. Feng, Q. S. Huo, N. Melosh, G. H. Fredrickson, B. F. Chmelka, G. D. Stucky, *Science* **1998**, *279*, 548.
- [89] D. Y. Zhao, Q. S. Huo, J. L. Feng, B. F. Chmelka, G. D. Stucky, *Journal of the American Chemical Society* **1998**, *120*, 6024.
- [90] A. Thomas, M. Antonietti, *Advanced Functional Materials* **2003**, *13*, 763.

- [91] J. C. Vartuli, K. D. Schmitt, C. T. Kresge, W. J. Roth, M. E. Leonowicz, S. B. McCullen, S. D. Hellring, J. S. Beck, J. L. Schlenker, D. H. Olson, E. W. Sheppard, *Chemistry of Materials* **1994**, *6*, 2317.
- [92] A. Monnier, F. Schüth, Q. Huo, D. Kumar, D. Margolese, R. S. Maxwell, G. D. Stucky, M. Krishnamurty, P. Petroff, A. Firouzi, M. Janicke, B. F. Chmelka, *Science* **1993**, *261*, 1299.
- [93] S. H. Tolbert, A. Firouzi, G. D. Stucky, B. F. Chmelka, *Science* **1997**, *278*, 264.
- [94] C. G. Goltner, M. Antonietti, *Advanced Materials* **1997**, *9*, 431.
- [95] G. S. Attard, J. C. Glyde, C. G. Goltner, *Nature* **1995**, *378*, 366.
- [96] C. G. Goltner, S. Henke, M. C. Weissenberger, M. Antonietti, *Angewandte Chemie-International Edition* **1998**, *37*, 613.
- [97] N. A. Melosh, P. Lipic, F. S. Bates, F. Wudl, G. D. Stucky, G. H. Fredrickson, B. F. Chmelka, *Macromolecules* **1999**, *32*, 4332.
- [98] C. J. Brinker, Y. F. Lu, A. Sellinger, H. Y. Fan, *Advanced Materials* **1999**, *11*, 579.
- [99] A. Corma, *Chemical Reviews* **1997**, *97*, 2373.
- [100] K. W. Gallis, J. T. Araujo, K. J. Duff, J. G. Moore, C. C. Landry, *Advanced Materials* **1999**, *11*, 1452.
- [101] L. Mercier, T. J. Pinnavaia, *Advanced Materials* **1997**, *9*, 500.
- [102] I. I. Slowing, B. G. Trewyn, S. Giri, V. S. Y. Lin, *Advanced Functional Materials* **2007**, *17*, 1225.
- [103] I. I. Slowing, J. L. Vivero-Escoto, C.-W. Wu, V. S. Y. Lin, *Advanced Drug Delivery Reviews* **2008**, *60*, 1278.
- [104] Y. Wan, D. Zhao, *Chemical Reviews* **2007**, *107*, 2821.

- [105] X. Feng, G. E. Fryxell, L. Q. Wang, A. Y. Kim, J. Liu, K. M. Kemner, *Science* **1997**, 276, 923.
- [106] F. Hoffmann, M. Cornelius, J. Morell, M. Fröba, *Angewandte Chemie-International Edition* **2006**, 45, 3216.
- [107] M. H. Lim, C. F. Blanford, A. Stein, *Journal of the American Chemical Society* **1997**, 119, 4090.
- [108] M. H. Lim, A. Stein, *Chemistry of Materials* **1999**, 11, 3285.
- [109] S. L. Burkett, S. D. Sims, S. Mann, *Chemical Communications* **1996**, 1367.
- [110] S. Inagaki, S. Guan, Y. Fukushima, T. Ohsuna, O. Terasaki, *Journal of the American Chemical Society* **1999**, 121, 9611.
- [111] B. J. Melde, B. T. Holland, C. F. Blanford, A. Stein, *Chemistry of Materials* **1999**, 11, 3302.
- [112] T. Asefa, M. J. MacLachlan, N. Coombs, G. A. Ozin, *Nature* **1999**, 402, 867.
- [113] W. J. Hunks, G. A. Ozin, *Journal of Materials Chemistry* **2005**, 15, 3716.
- [114] M. C. Burleigh, M. A. Markowitz, S. Jayasundera, M. S. Spector, C. W. Thomas, B. P. Gaber, *Journal of Physical Chemistry B* **2003**, 107, 12628.
- [115] A. Stein, B. J. Melde, R. C. Schrodin, *Advanced Materials* **2000**, 12, 1403.
- [116] S. Inagaki, S. Guan, T. Ohsuna, O. Terasaki, *Nature* **2002**, 416, 304.
- [117] N. Mizoshita, T. Tani, S. Inagaki, *Chemical Society Reviews* **2011**, 40, 789.
- [118] G. Zhu, H. Zhong, Q. Yang, C. Li, *Microporous and Mesoporous Materials* **2008**, 116, 36.
- [119] S. Polarz, A. Kuschel, *Advanced Materials* **2006**, 18, 1206.

- [120] P. Wang, X. Liu, J. Yang, Y. Yang, L. Zhang, Q. Yang, C. Li, *Journal of Materials Chemistry* **2009**, *19*, 8009.
- [121] A. Kuschel, S. Polarz, *Journal of the American Chemical Society* **2010**, *132*, 6558.
- [122] C. Yoshina-Ishii, T. Asefa, N. Coombs, M. J. MacLachlan, G. A. Ozin, *Chemical Communications* **1999**, 2539.
- [123] N. Mizoshita, M. Ikai, T. Tani, S. Inagaki, *Journal of the American Chemical Society* **2009**, *131*, 14225.
- [124] N. Mizoshita, Y. Goto, T. Tani, S. Inagaki, *Advanced Functional Materials* **2008**, *18*, 3699.
- [125] S. Inagaki, O. Ohtani, Y. Goto, K. Okamoto, M. Ikai, K.-i. Yamanaka, T. Tani, T. Okada, *Angewandte Chemie-International Edition* **2009**, *48*, 4042.
- [126] B. Hatton, K. Landskron, W. Whitnall, D. Perovic, G. A. Ozin, *Accounts of Chemical Research* **2005**, *38*, 305.
- [127] W. Whitnall, L. Cademartiri, G. A. Ozin, *Journal of the American Chemical Society* **2007**, *129*, 15644.
- [128] C. Liang, Z. Li, S. Dai, *Angewandte Chemie-International Edition* **2008**, *47*, 3696.
- [129] R. Ryoo, S. H. Joo, S. Jun, *Journal of Physical Chemistry B* **1999**, *103*, 7743.
- [130] J. Lee, S. Yoon, T. Hyeon, S. M. Oh, K. B. Kim, *Chemical Communications* **1999**, 2177.
- [131] A.-H. Lu, F. Schüth, *Advanced Materials* **2006**, *18*, 1793.
- [132] T. W. Kim, I. S. Park, R. Ryoo, *Angewandte Chemie-International Edition* **2003**, *42*, 4375.
- [133] R. Ryoo, S. H. Joo, M. Kruk, M. Jaroniec, *Advanced Materials* **2001**, *13*, 677.

- [134] J. Lee, S. Yoon, S. M. Oh, C. H. Shin, T. Hyeon, *Advanced Materials* **2000**, *12*, 359.
- [135] S. Jun, S. H. Joo, R. Ryoo, M. Kruk, M. Jaroniec, Z. Liu, T. Ohsuna, O. Terasaki, *Journal of the American Chemical Society* **2000**, *122*, 10712.
- [136] Y. Meng, D. Gu, F. Zhang, Y. Shi, L. Cheng, D. Feng, Z. Wu, Z. Chen, Y. Wan, A. Stein, D. Zhao, *Chemistry of Materials* **2006**, *18*, 4447.
- [137] L. L. Zhang, X. S. Zhao, *Chemical Society Reviews* **2009**, *38*, 2520.
- [138] P. Simon, Y. Gogotsi, *Nature Materials* **2008**, *7*, 845.
- [139] A. B. Fuertes, G. Lota, T. A. Centeno, E. Frackowiak, *Electrochimica Acta* **2005**, *50*, 2799.
- [140] E. Frackowiak, F. Beguin, *Carbon* **2001**, *39*, 937.
- [141] L.-Z. Fan, Y.-S. Hu, J. Maier, P. Adelhelm, B. Smarsly, M. Antonietti, *Advanced Functional Materials* **2007**, *17*, 3083.
- [142] Y.-S. Hu, P. Adelhelm, B. M. Smarsly, S. Hore, M. Antonietti, J. Maier, *Advanced Functional Materials* **2007**, *17*, 1873.
- [143] J. Y. Ying, C. P. Mehnert, M. S. Wong, *Angewandte Chemie-International Edition* **1999**, *38*, 56.
- [144] P. D. Yang, D. Y. Zhao, D. I. Margolese, B. F. Chmelka, G. D. Stucky, *Nature* **1998**, *396*, 152.
- [145] A. Corma, P. Atienzar, H. Garcia, J. Y. Chane-Ching, *Nature Materials* **2004**, *3*, 394.
- [146] J. H. Ba, J. Polleux, M. Antonietti, M. Niederberger, *Advanced Materials* **2005**, *17*, 2509.
- [147] T. Brezesinski, J. Wang, J. Polleux, B. Dunn, S. H. Tolbert, *Journal of the American Chemical Society* **2009**, *131*, 1802.

- [148] M. J. MacLachlan, N. Coombs, G. A. Ozin, *Nature* **1999**, 397, 681.
- [149] M. G. Kanatzidis, *Advanced Materials* **2007**, 19, 1165.
- [150] D. Sun, A. E. Riley, A. J. Cadby, E. K. Richman, S. D. Korlann, S. H. Tolbert, *Nature* **2006**, 441, 1126.
- [151] G. S. Armatas, M. G. Kanatzidis, *Science* **2006**, 313, 817.
- [152] G. S. Attard, P. N. Bartlett, N. R. B. Coleman, J. M. Elliott, J. R. Owen, J. H. Wang, *Science* **1997**, 278, 838.
- [153] A. Thomas, F. Goettmann, M. Antonietti, *Chemistry of Materials* **2008**, 20, 738.
- [154] M. Tiemann, *Chemistry of Materials* **2008**, 20, 961.
- [155] Q. S. Huo, D. I. Margolese, G. D. Stucky, *Chemistry of Materials* **1996**, 8, 1147.
- [156] A. Gabashvili, D. D. Medina, A. Gedanken, Y. Mastai, *Journal of Physical Chemistry B* **2007**, 111, 11105.
- [157] B. F. G. Johnson, S. A. Raynor, D. S. Shephard, T. Mashmeyer, J. M. Thomas, G. Sankar, S. Bromley, R. Oldroyd, L. Gladden, M. D. Mantle, *Chemical Communications* **1999**, 1167.
- [158] S. Fireman-Shoresh, I. Popov, D. Avnir, S. Marx, *Journal of the American Chemical Society* **2005**, 127, 2650.
- [159] I. Hodgkinson, Q. H. Wu, *Advanced Materials* **2001**, 13, 889.
- [160] S. Che, A. E. Garcia-Bennett, T. Yokoi, K. Sakamoto, H. Kunieda, O. Terasaki, T. Tatsumi, *Nature Materials* **2003**, 2, 801.
- [161] S. Che, Z. Liu, T. Ohsuna, K. Sakamoto, O. Terasaki, T. Tatsumi, *Nature* **2004**, 429, 281.
- [162] H. Jin, H. Qiu, C. Gao, S. Che, *Microporous and Mesoporous Materials* **2008**, 116, 171.

- [163] M. E. Calvo, S. Colodrero, N. Hidalgo, G. Lozano, C. Lopez-Lopez, O. Sanchez-Sobrado, H. Miguez, *Energy & Environmental Science* **2011**, *4*, 4800.
- [164] F. Cunin, T. A. Schmedake, J. R. Link, Y. Y. Li, J. Koh, S. N. Bhatia, M. J. Sailor, *Nature Materials* **2002**, *1*, 39.
- [165] J. Kobler, B. V. Lotsch, G. A. Ozin, T. Bein, *Acs Nano* **2009**, *3*, 1669.
- [166] S. Colodrero, A. Mihi, L. Haggman, M. Ocana, G. Boschloo, A. Hagfeldt, H. Miguez, *Advanced Materials* **2009**, *21*, 764.
- [167] H. Yamada, T. Nakamura, Y. Yamada, K. Yano, *Advanced Materials* **2009**, *21*, 4134.
- [168] Y. Yamada, H. Yamada, T. Nakamura, K. Yano, *Langmuir* **2009**, *25*, 13599.
- [169] M. C. Fuertes, F. J. Lopez-Alcaraz, M. C. Marchi, H. E. Troiani, V. Luca, H. Miguez, G. J. d. A. Arturo Soler-Illia, *Advanced Functional Materials* **2007**, *17*, 1247.
- [170] Y. Yamada, T. Nakamura, M. Ishi, K. Yano, *Langmuir* **2006**, *22*, 2444.
- [171] D. J. Broer, J. Lub, G. N. Mol, *Nature* **1995**, *378*, 467.
- [172] V. I. Kopp, B. Fan, H. K. M. Vithana, A. Z. Genack, *Optics Letters* **1998**, *23*, 1707.
- [173] D. K. Yang, J. L. West, L. C. Chien, J. W. Doane, *Journal of Applied Physics* **1994**, *76*, 1331.
- [174] G. Zanchetta, F. Giavazzi, M. Nakata, M. Buscaglia, R. Cerbino, N. A. Clark, T. Bellini, *Proceedings of the National Academy of Sciences of the United States of America* **2010**, *107*, 17497.
- [175] J. F. Revol, R. H. Marchessault, *International Journal of Biological Macromolecules* **1993**, *15*, 329.
- [176] W. Wang, R. Liu, W. Liu, J. Tan, W. Liu, H. Kang, Y. Huang, *Journal of Materials Science* **2010**, *45*, 5567.

- [177] F. Rouquerol, J. Rouquerol, K. Sing, *Adsorption by Powders and Porous Solids*, Academic Press, London, **1999**.
- [178] K. Robbie, D. J. Broer, M. J. Brett, *Nature* **1999**, 399, 764.
- [179] O. Olkhovyk, M. Jaroniec, *Journal of the American Chemical Society* **2005**, 127, 60.
- [180] O. Muth, C. Schellbach, M. Fröba, *Chemical Communications* **2001**, 2032.
- [181] Y. F. Lu, H. Y. Fan, N. Doke, D. A. Loy, R. A. Assink, D. A. LaVan, C. J. Brinker, *Journal of the American Chemical Society* **2000**, 122, 5258.
- [182] T. Asefa, M. Kruk, M. J. MacLachlan, N. Coombs, H. Grondey, M. Jaroniec, G. A. Ozin, *Journal of the American Chemical Society* **2001**, 123, 8520.
- [183] V. Rebbin, R. Schmidt, M. Fröba, *Angewandte Chemie-International Edition* **2006**, 45, 5210.
- [184] B. Johnson-White, M. Zeinali, K. M. Shaffer, C. H. Patterson, Jr., P. T. Charles, M. A. Markowitz, *Biosensors & Bioelectronics* **2007**, 22, 1154.
- [185] J. Du, J. Cipot-Wechsler, J. M. Lobez, H.-P. Loock, C. M. Crudden, *Small* **2010**, 6, 1168.
- [186] F. Pereira, K. Valle, P. Belleville, A. Morin, S. Lambert, C. Sanchez, *Chemistry of Materials* **2008**, 20, 1710.
- [187] C. Baleizao, B. Gigante, D. Das, M. Alvaro, H. Garcia, A. Corma, *Chemical Communications* **2003**, 1860.
- [188] A. Ide, R. Voss, G. Scholz, G. A. Ozin, M. Antonietti, A. Thomas, *Chemistry of Materials* **2007**, 19, 2649.
- [189] S. Inagaki, S. Guan, Q. Yang, M. P. Kapoor, T. Shimada, *Chemical Communications* **2008**, 202.
- [190] S. MacQuarrie, M. P. Thompson, A. Blanc, N. J. Mosey, R. P. Lemieux, C. M. Crudden, *Journal of the American Chemical Society* **2008**, 130, 14099.

- [191] X. Liu, W. Zhuang, B. Li, L. Wu, S. Wang, Y. Li, Y. Yang, *Chemical Communications* **2011**, 47, 7215.
- [192] K. E. Shopsowitz, H. Qi, W. Y. Hamad, M. J. MacLachlan, *Nature* **2010**, 468, 422.
- [193] G. Dubois, W. Volksen, T. Magbitang, R. D. Miller, D. M. Gage, R. H. Dauskardt, *Advanced Materials* **2007**, 19, 3989.
- [194] H. Ouyang, M. Christophersen, R. Viard, B. L. Miller, P. M. Fauchet, *Advanced Functional Materials* **2005**, 15, 1851.
- [195] R. A. Caruso, *Colloid Chemistry I* **2003**, 226, 91.
- [196] H. Qi, X. Roy, K. E. Shopsowitz, J. K. H. Hui, M. J. MacLachlan, *Angewandte Chemie-International Edition* **2010**, 49, 9740.
- [197] P. N. Trikalitis, K. K. Rangan, T. Bakas, M. G. Kanatzidis, *Nature* **2001**, 410, 671.
- [198] R. W. J. Scott, N. Coombs, G. A. Ozin, *Journal of Materials Chemistry* **2003**, 13, 969.
- [199] Y. J. Han, J. M. Kim, G. D. Stucky, *Chemistry of Materials* **2000**, 12, 2068.
- [200] Z. Liu, Y. Sakamoto, T. Ohsuna, K. Hiraga, O. Terasaki, C. H. Ko, H. J. Shin, R. Ryoo, *Angewandte Chemie-International Edition* **2000**, 39, 3107.
- [201] B. Z. Tian, X. Y. Liu, H. F. Yang, S. H. Xie, C. Z. Yu, B. Tu, D. Y. Zhao, *Advanced Materials* **2003**, 15, 1370.
- [202] W. Yue, X. Xu, J. T. S. Irvine, P. S. Attidekou, C. Liu, H. He, D. Zhao, W. Zhou, *Chemistry of Materials* **2009**, 21, 2540.
- [203] W. Yue, C. Randorn, P. S. Attidekou, Z. Su, J. T. S. Irvine, W. Zhou, *Advanced Functional Materials* **2009**, 19, 2826.
- [204] W. S. Chae, S. W. Lee, Y. R. Kim, *Chemistry of Materials* **2005**, 17, 3072.

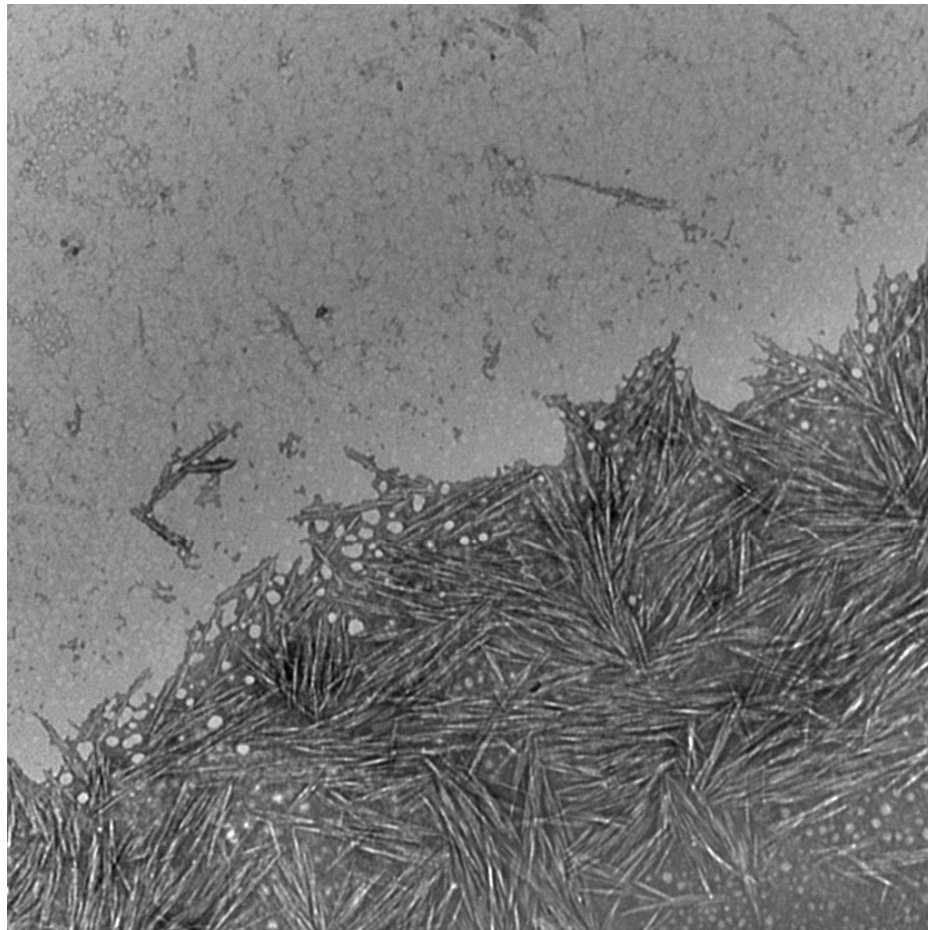
- [205] Y. D. Xia, R. Mokaya, *Journal of Materials Chemistry* **2005**, *15*, 3126.
- [206] J. C. Lytle, H. W. Yan, R. T. Turgeon, A. Stein, *Chemistry of Materials* **2004**, *16*, 3829.
- [207] B. Oregan, M. Gratzel, *Nature* **1991**, *353*, 737.
- [208] C. Aprile, A. Corma, H. Garcia, *Physical Chemistry Chemical Physics* **2008**, *10*, 769.
- [209] C. Wang, L. Yin, L. Zhang, Y. Qi, N. Lun, N. Liu, *Langmuir* **2010**, *26*, 12841.
- [210] L. Kavan, M. Gratzel, J. Rathousky, A. Zukal, *Journal of the Electrochemical Society* **1996**, *143*, 394.
- [211] M. Wagemaker, A. P. M. Kentgens, F. M. Mulder, *Nature* **2002**, *418*, 397.
- [212] J. Wijnhoven, W. L. Vos, *Science* **1998**, *281*, 802.
- [213] R. C. Schroden, M. Al-Daous, C. F. Blanford, A. Stein, *Chemistry of Materials* **2002**, *14*, 3305.
- [214] B. T. Holland, C. F. Blanford, T. Do, A. Stein, *Chemistry of Materials* **1999**, *11*, 795.
- [215] L. I. Halaoui, N. M. Abrams, T. E. Mallouk, *Journal of Physical Chemistry B* **2005**, *109*, 6334.
- [216] J. I. L. Chen, G. von Freymann, S. Y. Choi, V. Kitaev, G. A. Ozin, *Advanced Materials* **2006**, *18*, 1915.
- [217] H. Z. Zhang, J. F. Banfield, *Journal of Materials Chemistry* **1998**, *8*, 2073.
- [218] H. S. Zhou, S. M. Zhu, M. Hibino, I. Honma, M. Ichihara, *Advanced Materials* **2003**, *15*, 2107.
- [219] X. Ji, K. T. Lee, L. F. Nazar, *Nature Materials* **2009**, *8*, 500.

- [220] S. Polarz, M. Antonietti, *Chemical Communications* **2002**, 2593.
- [221] C. D. Liang, K. L. Hong, G. A. Guiochon, J. W. Mays, S. Dai, *Angewandte Chemie-International Edition* **2004**, *43*, 5785.
- [222] K. i. Kimijima, A. Hayashi, I. Yagi, *Chemical Communications* **2008**, 5809.
- [223] X. Wang, Q. Zhu, S. M. Mahurin, C. Liang, S. Dai, *Carbon* **2010**, *48*, 557.
- [224] K. Akagi, G. Piao, S. Kaneko, K. Sakamaki, H. Shirakawa, M. Kyotani, *Science* **1998**, *282*, 1683.
- [225] M. Kyotani, S. Matsushita, T. Nagai, Y. Matsui, M. Shimomura, A. Kaito, K. Akagi, *Journal of the American Chemical Society* **2008**, *130*, 10880.
- [226] O. Ishida, D. Y. Kim, S. Kuga, Y. Nishiyama, R. M. Brown, *Cellulose* **2004**, *11*, 475.
- [227] D. Y. Kim, Y. Nishiyama, M. Wada, S. Kuga, *Cellulose* **2001**, *8*, 29.
- [228] A. H. Lu, W. Schmidt, A. Taguchi, B. Spliethoff, B. Tesche, F. Schüth, *Angewandte Chemie-International Edition* **2002**, *41*, 3489.
- [229] E. Frackowiak, V. Khomenko, K. Jurewicz, K. Lota, F. Beguin, *Journal of Power Sources* **2006**, *153*, 413.
- [230] W. S. Huang, B. D. Humphrey, A. G. Macdiarmid, *Journal of the Chemical Society-Faraday Transactions I* **1986**, *82*, 2385.
- [231] F. Fusalba, P. Guerec, D. Villers, D. Belanger, *Journal of the Electrochemical Society* **2001**, *148*, A1.
- [232] Y. K. Zhou, B. L. He, W. J. Zhou, J. Huang, X. H. Li, B. Wu, H. I. Li, *Electrochimica Acta* **2004**, *49*, 257.
- [233] K. Zhang, L. L. Zhang, X. S. Zhao, J. Wu, *Chemistry of Materials* **2010**, *22*, 1392.
- [234] Y.-G. Wang, H.-Q. Li, Y.-Y. Xia, *Advanced Materials* **2006**, *18*, 2619.

- [235] J. Stejskal, R. G. Gilbert, *Pure and Applied Chemistry* **2002**, *74*, 857.
- [236] L. D. Bonifacio, D. P. Puzzo, S. Breslav, B. M. Willey, A. McGeer, G. A. Ozin, *Advanced Materials* **2010**, *22*, 1351.
- [237] I. B. Burgess, L. Mishchenko, B. D. Hatton, M. Kolle, M. Loncar, J. Aizenberg, *Journal of the American Chemical Society*, *133*, 12430.
- [238] M. M. Orosco, C. Pacholski, G. M. Miskelly, M. J. Sailor, *Advanced Materials* **2006**, *18*, 1393.
- [239] S. M. Weiss, G. Rong, J. L. Lawrie, *Physica E-Low-Dimensional Systems & Nanostructures* **2009**, *41*, 1071.
- [240] M. Alvaro, M. Benitez, D. Das, H. Garcia, E. Peris, *Chemistry of Materials* **2005**, *17*, 4958.

Appendix A

Additional Characterization for Chapter 2



B87-UA-stain036.tif
Print Mag: 11800x @ 51 mm
13:44 08/30/11

500 nm
HV=80.0kV
Direct Mag: 50000x
UBC BioImaging Facility

Figure A-1. TEM micrograph of negatively stained NCC template.

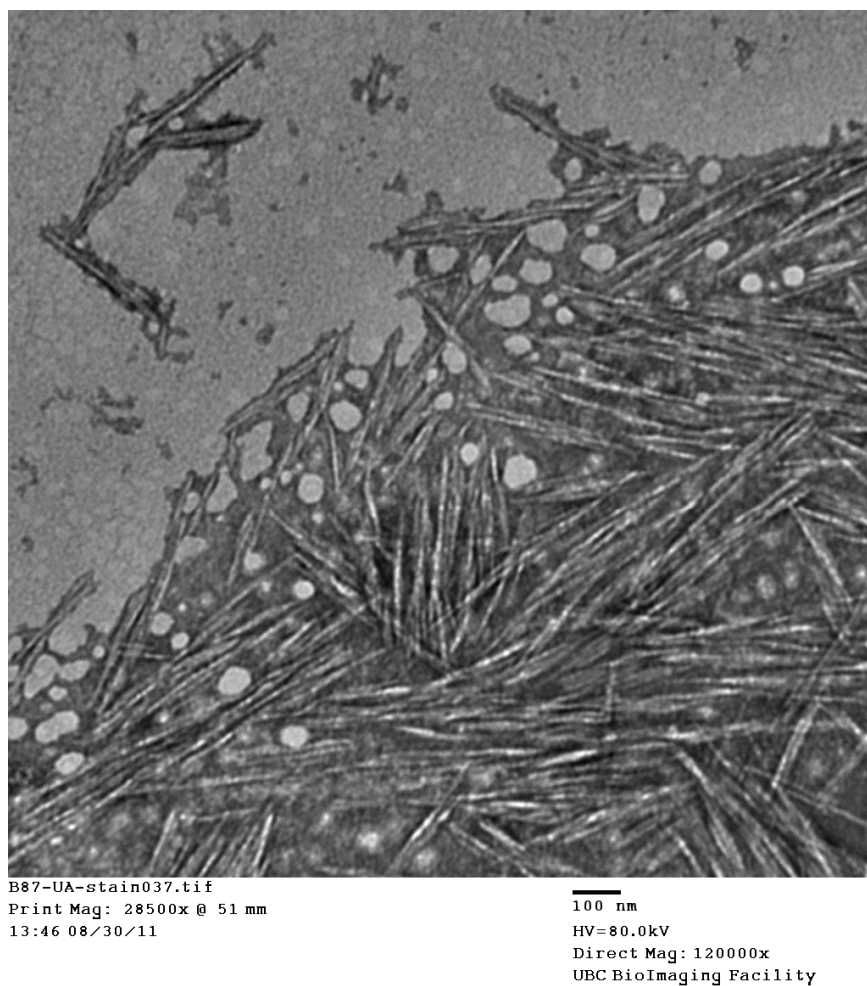


Figure A-2. TEM micrograph of negatively stained NCC template at higher magnification.

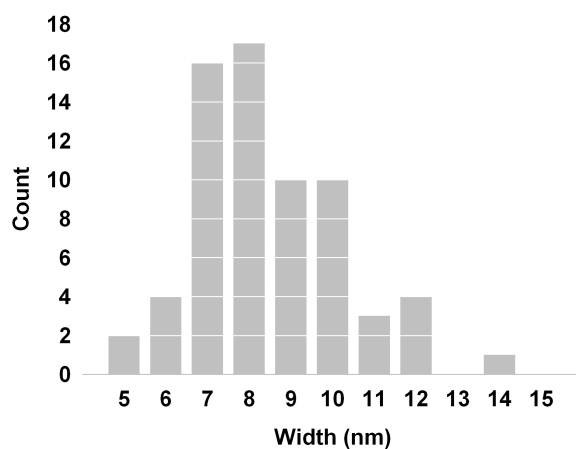


Figure A-3. Width distribution calculated from Figure A-2 (total count = 67, avg. width = 9 nm).

Appendix B

Additional Characterization and Discussion for

Chapter 3

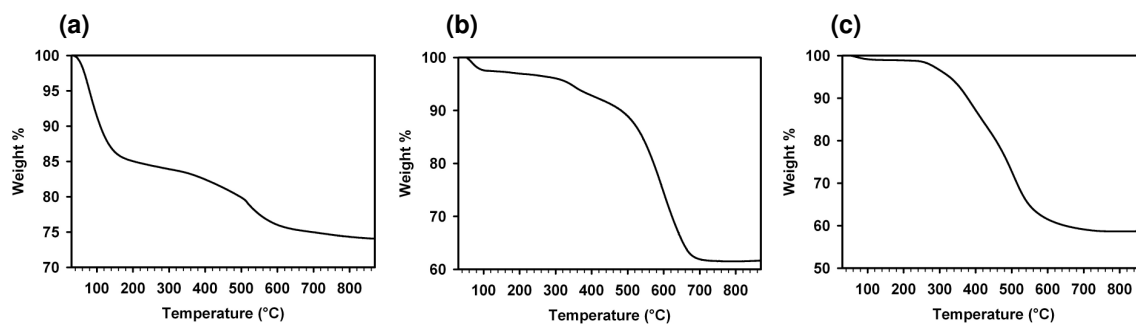


Figure B-1. TGA run under air for different organosilica samples: (a) **Me-CNMO**, (b) **Bz-CNMO**, and (c) **Hex-CNMO**.

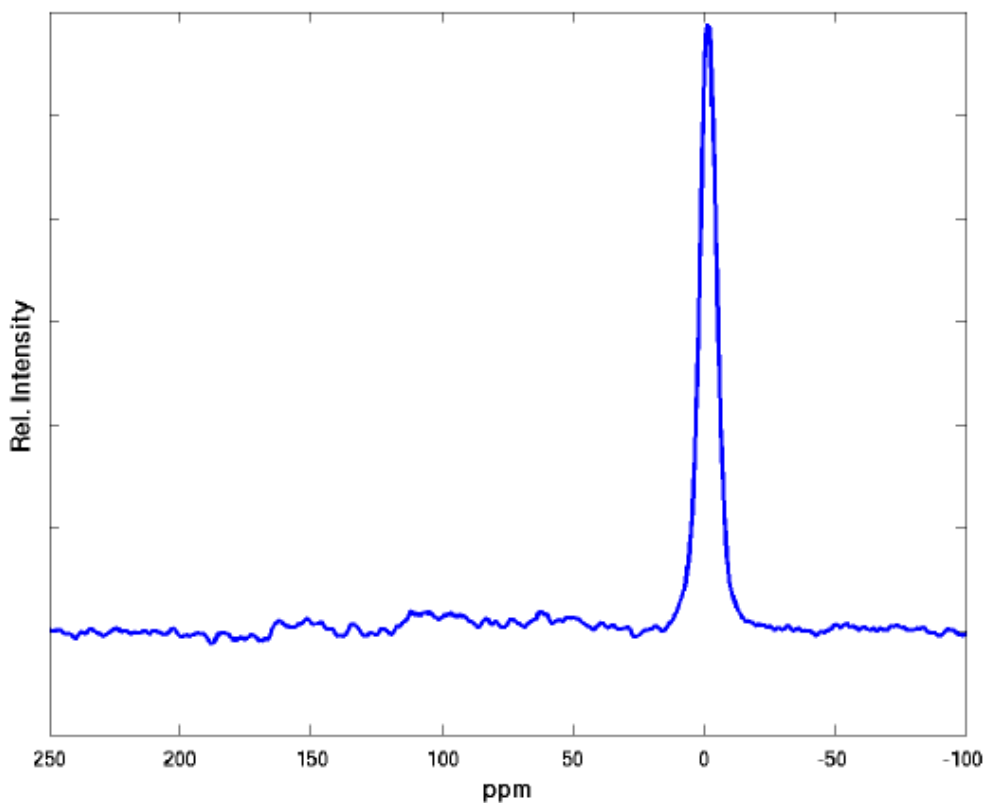


Figure B-2. ^{13}C CP/MAS solid-state NMR of **Me-CNMO**. The single peak corresponds to the methylene bridge of the organosilica.

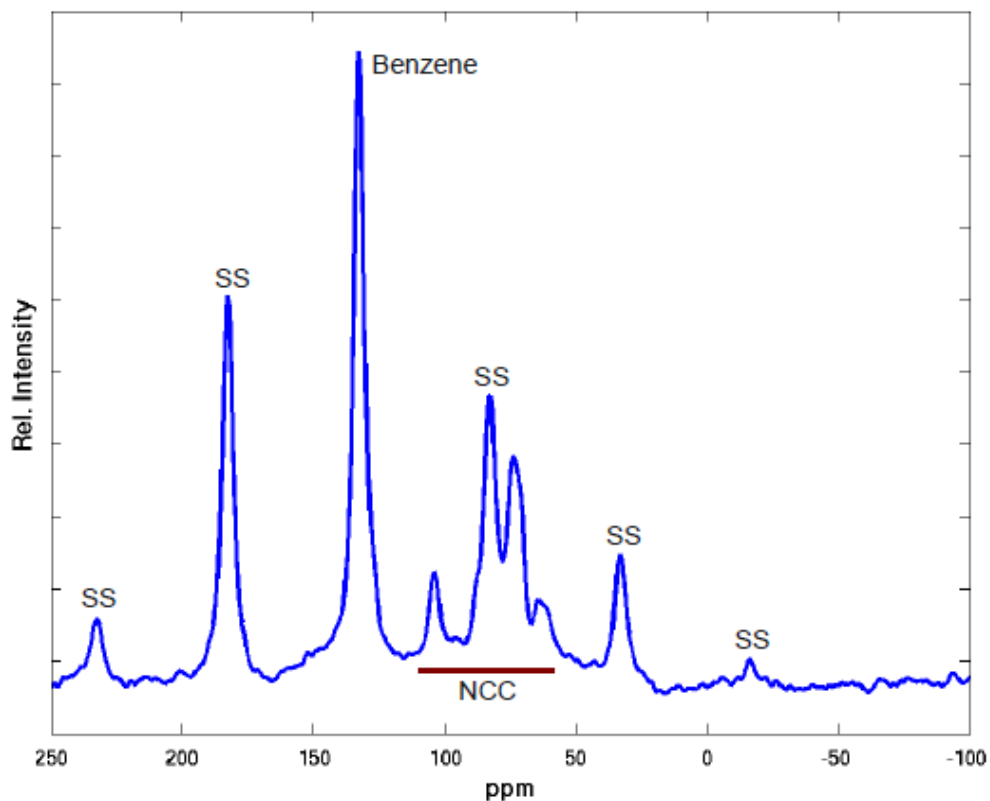


Figure B-3. ^{13}C CP/MAS solid-state NMR of **Bz-CNMO**. Peak labeled benzene corresponds to the phenylene bridge of the organosilica. Peaks labeled SS are spinning sidebands, artifacts from spinning the rotor that are often large for aromatic samples. Small additional peaks that may come from residual NCC or glucose are also present.

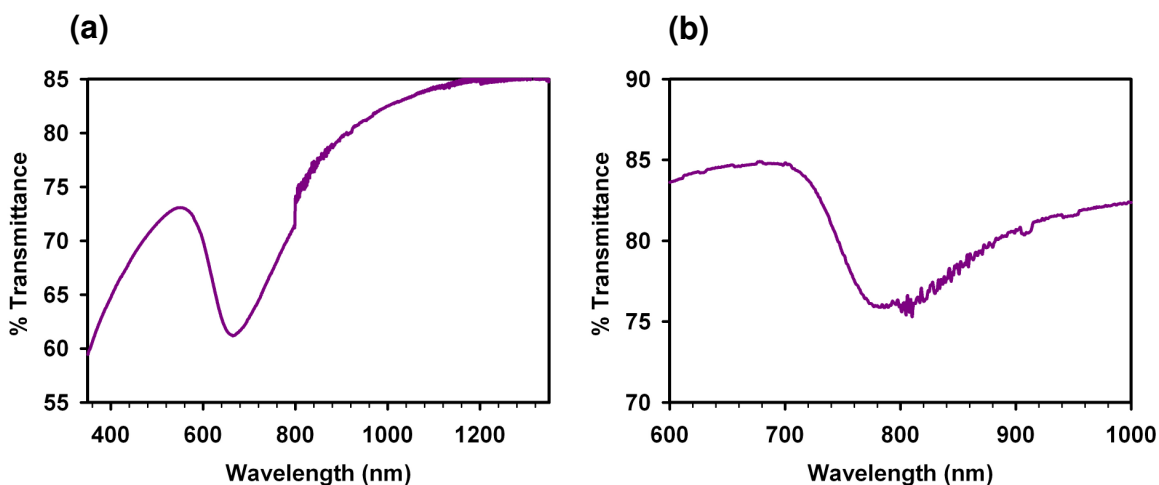


Figure B-4. UV-Vis/NIR spectra for (a) **Me-CNMO** and (b) **Bz-CNMO**.

Differences between NCC Batches Used in Chapter 3

Although to the best of our knowledge the two batches used in Chapter 3 were prepared in the same way, the 3.5 wt. % batch forms films with reflectance peaks that are red-shifted by several hundred nm compared to the 3 wt. % batch (I have confirmed that this is not simply due to the difference in concentration). Although I am not certain what causes this difference, the presence of trace electrolytes in the suspensions or the sonication power during their original preparation may play a role. By adding a small amount of NaCl, it is possible to form films from the 3.5 wt. % suspension that reflect the same wavelengths of light as films prepared from the other batch of NCC. Mesoporous films that have been prepared from the two different batches using otherwise identical conditions (this has been done with both TMOS and BTMSE) show comparable porosity (i.e., pore size distribution and BET surface area), which suggests that the particle size of NCC in the two batches is similar.

Appendix C

Additional Characterization for Chapter 4

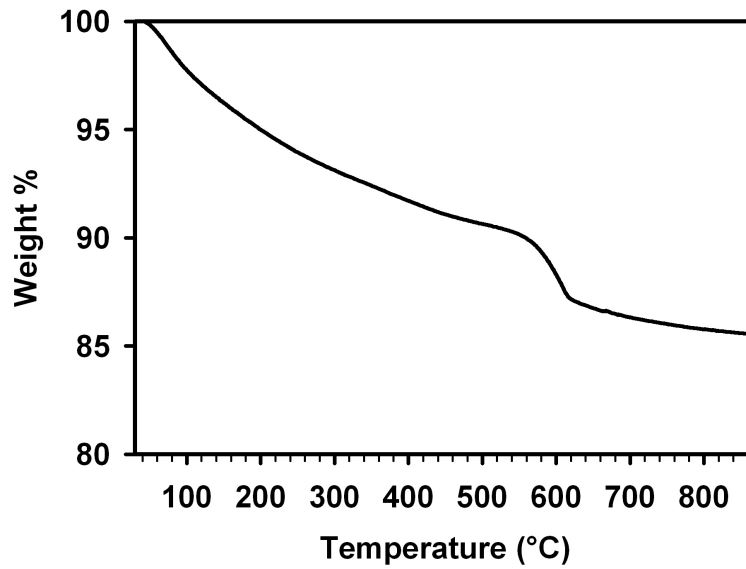


Figure C-1. TGA of **Ti-Acid** run under air.

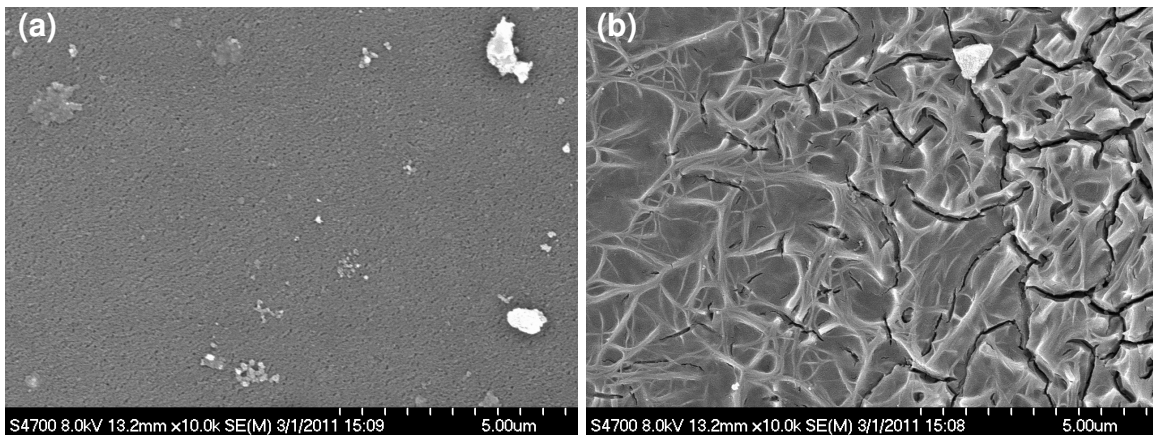


Figure C-2. SEM images showing the surface of **Ti-Acid** films. (a) Image showing a region without any surface crust. (b) Image showing a region with a surface crust.